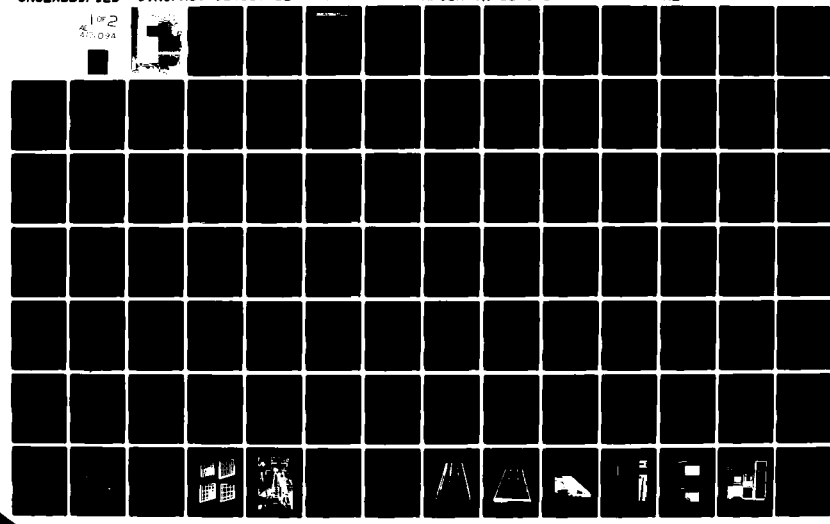


AD-A101 094

UNITED TECHNOLOGIES RESEARCH CENTER EAST HARTFORD CONN F/6 20/4
THE INFLUENCE OF FREE-STREAM TURBULENCE ON THE ZERO PRESSURE GR--ETC(U)
SEP 80 M F BLAIR, M J WERLE F49620-78-C-0064
UTRC/R80-914388-12 AFOSR-TR-81-0514 NL

UNCLASSIFIED

1 of 2
400-094



UNCLASSIFIED

SECURITY CLASSIFICATION OF THIS PAGE (When Data Entered)

REPORT DOCUMENTATION PAGE		READ INSTRUCTIONS BEFORE COMPLETING FORM
1. REPORT NUMBER AFOSR-TR-81-0514	2. GOVT ACCESSION NO. AD-A101 094	3. RECIPIENT'S CATALOG NUMBER
4. TITLE (and Subtitle) INFLUENCE OF FREE-STREAM TURBULENCE ON THE ZERO PRESSURE GRADIENT FULLY TURBULENT BOUNDARY LAYER		5. TYPE OF REPORT & PERIOD COVERED INTERIM 1 JUNE 78-1 JUNE 80
6. PERFORMING ORG. REPORT NUMBER		7. AUTHOR(s) M. F. BLAIR M. J. WERLE
8. CONTRACT OR GRANT NUMBER(s) F49620-78-C-0064		9. PERFORMING ORGANIZATION NAME AND ADDRESS UNITED TECHNOLOGIES RESEARCH CENTER EAST HARTFORD, CT 06108
10. PROGRAM ELEMENT, PROJECT, TASK AREA & WORK UNIT NUMBERS 23071A4 61102F		11. CONTROLLING OFFICE NAME AND ADDRESS AIR FORCE OFFICE OF SCIENTIFIC RESEARCH/NA BOLLING AFB, DC 20332
12. REPORT DATE SEPTEMBER 80		13. NUMBER OF PAGES 164
14. MONITORING AGENCY NAME & ADDRESS (if different from Controlling Office)		15. SECURITY CLASS. (of this report) UNCLASSIFIED
16. DISTRIBUTION STATEMENT (of this Report) Approved for public release; distribution unlimited.		
17. DISTRIBUTION STATEMENT (of the abstract entered in Block 20, if different from Report)		
18. SUPPLEMENTARY NOTES		
19. KEY WORDS (Continue on reverse side if necessary and identify by block number) TURBULENT BOUNDARY LAYERS FREE-STREAM TURBULENCE TRANSITION HEAT TRANSFER BOUNDARY LAYER PROFILES		
20. ABSTRACT (Continue on reverse side if necessary and identify by block number) Experimental research has been conducted to determine the influence of free-stream turbulence on zero pressure gradient fully turbulent boundary layer flow. During this period convective heat transfer coefficients, boundary layer mean velocity and temperature profile data, and wall static pressure distribution data were obtained for five flow conditions of constant free-stream velocity and free-stream turbulence intensities ranging from approximately 4% to 7%. Free-stream multi-component turbulence intensity, longitudinal integral scale, and		

UNCLASSIFIED

SECURITY CLASSIFICATION OF THIS PAGE(When Data Entered)

Spectral distributions were obtained for the various turbulence levels. The test results with 4% free-stream turbulence indicate that these data are in excellent agreement with classic two-dimensional low free-stream turbulence, turbulent boundary layer correlations, thus establishing the absolute accuracy of the experiment. The data obtained for the test cases with higher free-stream turbulence indicate that the turbulence has a significant effect on turbulent boundary layer skin friction and heat transfer. It has been shown that these effects are a function of the free-stream turbulence intensity, the turbulence length scale, and the boundary layer momentum thickness Reynolds number. Suggested correlations for the influence of free-stream turbulence on skin friction, heat transfer, and the Reynolds analogy factor are given.

Also during this period, a boundary layer prediction method has been assessed as to its ability to predict free-stream turbulence effects on flat plate heating and skin friction. Comparisons with the experimental data obtained here showed that adequate predictions can be made for this case with an existing turbulence model.

UNCLASSIFIED

SECURITY CLASSIFICATION OF THIS PAGE(When Data Entered)

UNITED TECHNOLOGIES RESEARCH CENTER



East Hartford, Connecticut 06108

R80-914388-12

The Influence of Free-Stream
Turbulence on the Zero Pressure
Gradient Fully Turbulent Boundary
Layer

Contract No. F49620-78-C-0064
Project-Task 2307/A4
61102 F



REPORTED BY

M. F. Blair
M. F. Blair

M. J. Werle
M. J. Werle

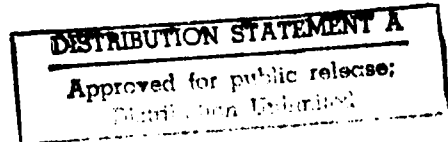
APPROVED BY

R. E. Olson
R. E. Olson

DATE September 1980

NO. OF PAGES _____

COPY NO. _____



R80-914388-12

The Influence of Free-Stream Turbulence on the Zero Pressure
Gradient Fully Turbulent Boundary Layer

TABLE OF CONTENTS

<u>Section</u>	<u>Page</u>
FOREWORD	1
ABSTRACT	2
INTRODUCTION	3
DESCRIPTION OF TEST EQUIPMENT	6
1. UTRC Boundary Layer Wind Tunnel	6
2. Uniform Heat Flux Flat Wall Model	8
3. Instrumentation	11
4. Data Acquisition System	12
DATA ACQUISITION AND ANALYSIS TECHNIQUES	13
1. Description of the Hot Film Anemometer and Signal Processing System	13
1.1 Measurement of Multi-Component Turbulence with X Hot-Film Array	13
1.2 Calibration of the Single Film and X Film Probes	16
1.3 Length Scale and Spectral Distribution Data	17
1.3.1 Length scale distributions	17
1.3.2 Spacial distributions	18
2. Boundary Layer Data Analysis	20

2.1	Background	20
2.2	Universal Velocity and Temperature Distributions	21
2.2.1	Universal Velocity Distribution-Viscous Sublayer and Buffer Zone	21
2.2.2	Universal Velocity Distribution-Logarithmic Law Region	22
2.2.3	Universal Velocity Distribution-Wake Region	23
2.2.4	Universal Temperature Distribution	24
2.2.5	Property Variations	29
2.2.6	Summary	30
2.2.7	Boundary Layer Data Reduction System	30
2.2.8	Sample Reduced Boundary Layer Profile Data	34
	WIND TUNNEL FLOW QUALITY EVALUATION TESTS	35
1.	Total Pressure Uniformity Surveys	35
2.	Flat Wall Heat Transfer Distributions (Evaluation Tests)	37
3.	Laminar Boundary Layer Profiles (Evaluation Tests)	38
	EXPERIMENTAL RESULTS	39
1.	Free-Stream Turbulence Distributions in the Wind Tunnel Test Section	39
1.1	Free-Stream Turbulence Intensity Distribution	39
1.2	Free-Stream Turbulence Length Scale Distributions	42
1.3	Free-Stream Power Spectral Density Distributions	43
2.	Heat Transfer and Boundary Layer Profile Measurements	44
2.1	Flow Condition 1 - Low Free-Stream Turbulence	44
2.2	Flow Condition 2 - Turbulence Grid No. 1	45

2.3 Flow Condition 3 - Turbulence Grid No. 2	46
2.4 Flow Condition 4 - Turbulence Grid No. 3	46
2.5 Flow Condition 5 - Turbulence Grid No. 4	47
2.6 Stanton Number as a Function of Momentum Thickness Reynolds Number	47
ANALYSIS AND DISCUSSION OF RESULTS	49
1. Influence of Free-Stream Turbulence on Skin Friction	49
2. Influence of Free-Stream Turbulence on the Velocity Profiles . . .	51
3. Influence of Free-Stream Turbulence on Heat Transfer	53
4. Influence of Free-Stream Turbulence on the Temperature Profiles .	54
5. Influence of Reynolds Number and/or Turbulence Length Scale . . .	55
ANALYTICAL PREDICTION OF FREE-STREAM TURBULENCE EFFECTS	59
1. General Statement	59
2. Turbulence Model	60
3. Finite Difference Code	62
4. Results	64
CONCLUSIONS	66
LIST OF SYMBOLS	68
REFERENCES	71
TABLE	75
FIGURES	

Accession For.	71
NTIS GRAAI	
DTIC TIR	
Undistributed	<input type="checkbox"/>
Justification	<input type="checkbox"/>
By	
Distribution	
Availability Codes	
Dist	Avail and/or Special

A

FOREWORD

This report was prepared for the Air Force Office of Scientific Research, United States Air Force by the United Technologies Corporation Research Center, East Hartford, Connecticut, under Contract F49620-78-C-0064, Project Task No. 2307/A4 61102 F. The performance period covered by this report was from 1 June 1978 to 1 June 1980. The project monitors were Dr. D. G. Samaras and Dr. James Wilson.

The experimental portions of the investigation are being conducted in the UTRC Boundary Layer Wind Tunnel. This facility was constructed during 1977 and underwent a series of flow quality evaluation tests during 1978. The UTRC Uniform Heat Flux Flat Wall Model, was also constructed, instrumented, and tested during 1978. Finally, a computer controlled data acquisition system for the UTRC Boundary Layer Wind Tunnel was designed, constructed and made operational during 1978. The construction and evaluation testing of the Boundary Layer Wind Tunnel, Uniform Heat Flux Flat Wall Model, and Data Acquisition system were conducted under UTC Corporate sponsorship.

Contract funded efforts have been devoted to the measurement and analysis of the heat transfer distributions, boundary layer profile and turbulence data presented in this report.

This report covers tasks "a" and "b" of the Statement of Work of the subject contract. A second report detailing the work conducted under tasks "c" and "d" will be prepared at the end of the contract period.

ABSTRACT

During the first two years of the contract period experimental research has been conducted to determine the influence of free-stream turbulence on zero pressure gradient, fully turbulent boundary layer flow. During this period convective heat transfer coefficients, boundary layer mean velocity and temperature profile data and wall static pressure distribution data were obtained for five flow conditions of constant free-stream velocity and free-stream turbulence intensities ranging from approximately $\frac{1}{4}\%$ to 7%. Free-stream multi-component turbulence intensity, longitudinal integral scale, and spectral distributions were obtained for the various turbulence levels. The test results with $\frac{1}{4}\%$ free-stream turbulence indicate that these data are in excellent agreement with classic two-dimensional, low free-stream turbulence, turbulent boundary layer correlations, thus establishing the absolute accuracy of the experiment. The data obtained for the test cases with higher free-stream turbulence indicate that the turbulence has a significant effect on turbulent boundary layer skin friction and heat transfer. It has been shown that these effects are a function of the free-stream turbulence intensity, the turbulence length scale, and the boundary layer momentum thickness Reynolds number. Suggested correlations for the influence of free-stream turbulence on skin friction, heat transfer, and the Reynolds analogy factor are given.

Also during this period, a boundary layer prediction method has been assessed as to its ability to predict free-stream turbulence effects on flat plate heating and skin friction. Comparisons with the experimental data obtained here showed that adequate predictions can be made for this case with an existing turbulence model.

INTRODUCTION

Improved techniques for calculating heat transfer coefficient distributions on gas turbine airfoils have been sought by engine manufacturers for the entire history of the industry. These heat transfer distributions must be known so that cooling schemes can be tailored to produce the required metal temperature. Accurate heat transfer predictions are an essential feature of gas turbine design because of the need to maximize performance through minimal use of cooling air and the need to minimize development costs through provision of adequate airfoil cooling on the initial design.

In the design of an airfoil cooling scheme the lack of any required heat transfer distribution information may be compensated for by simply overcooling the component. This overcooling may easily exist since gas turbine thermal design systems are typically not based on fundamental fluid mechanics and heat transfer data and analysis alone but rather are calibrated, or adjusted, to provide agreement with engine experience. Among the more obvious benefits that result from elimination of overcooling are reduced aerodynamic cooling penalties, increased burner and turbine mainstream mass flow rates (i.e., increased power) and potentially reduced cost for the fabrication of the airfoil cooling scheme. Furthermore, without a more complete first-principles understanding there is the likelihood that a designer will unknowingly go beyond the range of validity of the design system calibration. There is, then, a clear requirement for the development of airfoil heat transfer distribution prediction procedures which are based on fundamental fluid mechanics and heat transfer data. The great emphasis placed on the development of accurate boundary layer calculation techniques over the past few years reflects the recognition of these needs.

One particularly important topic in the general context of turbine airfoil convective heat transfer is the influence of the freestream turbulence on both transitional and fully turbulent boundary layer profile development. It has, of course, long been recognized that increasing the freestream turbulence level can cause a forward shift of the laminar to turbulent transition region. This particular phenomenon, the reduction of the boundary layer transition Reynolds number with increased freestream turbulence level, is well documented in the open literature for zero pressure gradient flows and can be accurately predicted with at least one currently available boundary layer prediction scheme. The influence of the freestream turbulence on fully turbulent boundary layers, however, is presently unclear. A number of investigators have studied the effects of free-stream turbulence level on flat wall turbulent boundary layer heat transfer rates and have all reported either negligible or very small effects. In contrast, other experiments which documented the effects of freestream turbulence on boundary layer growth, profile structure, and skin friction distribution reported very large and important influences. The current contract is being conducted in order to clarify

these contradictions. Both wall heat transfer and detailed boundary layer profile data are being obtained for fully turbulent boundary layers for a range of free-stream turbulence levels to provide data which will definitively indicate the influence that freestream turbulence level has on fully turbulent boundary layer heat transfer. In addition, these experimental data will be employed to evaluate the turbulence entrainment models currently incorporated in existing boundary layer calculation techniques.

As previously discussed, the effects of freestream turbulence on the zero pressure gradient boundary layer transition Reynolds number are well understood. The influence of the freestream turbulence on the transition process becomes considerably less well defined, however, for cases in which the boundary layer is also exposed to a pressure gradient. The net result of the combined influence of turbulence and pressure gradient is dependent upon the sign of the pressure gradient and the relative strength of the two effects. For adverse pressure gradients both the turbulence and the deceleration promote the transition process and in this case the net result is simply to hasten transition. For favorable pressure gradients, however, the flow acceleration acts to stabilize the boundary layer and tends to counteract the effect of the freestream turbulence. This interplay of pressure gradient and turbulence results in at least two effects on the transition process: (1) the location of the onset of transition is influenced and (2) the length and character of the transitional boundary layer flow region may be altered significantly. At the present time only very limited experimental data documenting these effects are available. To further complicate the matter, much of the currently available data are contradictory making it impossible to assess the relative quality of boundary layer calculation techniques for these flows. For these reasons, as part of the present contract both wall heat transfer and detailed velocity and temperature profile data will be obtained for accelerating transitional boundary layer flows exposed to high freestream turbulence levels. These data will be utilized to evaluate the current capability of existing boundary layer calculation procedures to predict boundary layer development with combined favorable pressure gradients and high freestream turbulence levels.

The present contract program will provide the wall heat transfer and detailed mean boundary layer profile development data required to determine the influence of freestream turbulence level on both fully turbulent and accelerating transitional boundary layers. These data will be fundamental in nature and could be employed by both UTRC and other workers in the field of boundary layer computation for evaluation of analytical models. In addition, the contract experiments will provide a valuable body of detailed heat transfer and boundary layer profile data directly relevant to the problem predicting heat transfer distributions on gas turbine airfoils. Possible requirements for the development of new analytical models for the entrainment of freestream turbulence into boundary layers and/or new boundary layer transition models will also be established. Finally, as mentioned above, the information could result in more accurate blade heat transfer distribution prediction techniques and thereby the more efficient use of blade cooling air.

The contract effort consists of the documentation and analysis of experimental flat wall boundary layer profile and heat transfer data to determine the influence of freestream turbulence on transitional and fully turbulent boundary layer flows. For fully turbulent, zero pressure gradient boundary layer flows the following data will be obtained for a range of freestream turbulence intensities: convective heat transfer coefficients; boundary layer mean velocity and temperature profiles; test wall static pressure distributions and freestream turbulence intensity; spectral and longitudinal integral scale distributions. These same measurements will be obtained for various combinations of favorable pressure gradients and freestream turbulence levels for transitional boundary layer flows. From these data the integral properties of the test boundary layers will be calculated and, where applicable, the profile data will be reduced to the "universal" coordinates for turbulent boundary layers U^+ , Y^+ , and T^+ . Finally, the measured heat transfer distributions and boundary layer profile development will be compared to predictions of the UTRC Finite-Difference Boundary Layer Deck. These comparisons will be employed to evaluate the computation methods currently incorporated in the UTRC deck.

DESCRIPTION OF TEST EQUIPMENT

1. UTRC Boundary Layer Wind Tunnel

All experimental data for the present investigation are being obtained in the United Technologies Research Center (UTRC) Boundary Layer Wind Tunnel. This tunnel was designed for conducting fundamental studies of two-dimensional, incompressible flat wall boundary layer flow. Incorporated in the tunnel is a versatile, adjustable test section constructed so that laminar, transitional, or turbulent boundary layers can be subjected to favorable, zero, or adverse pressure gradients. In addition, test boundary layers can be subjected to a wide range of freestream turbulence levels. Low freestream turbulence flows can be investigated in this facility since it is designed to have a very low residual test section turbulence level. Higher turbulence levels can be generated within the test section through the use of various rectangular grids.

An overall sketch of the Low Speed Boundary Layer tunnel is shown in Fig. 1. The tunnel is of recirculating design and consists of a blower, a settling chamber/plenum, a contraction nozzle, the boundary layer test section, a downstream diffuser, and a return duct. The settling chamber/plenum consists of a series of perforated part span baffles which even out gross irregularities in the flow from the blower and a honeycomb which removes large-scale flow swirl. Downstream of the honeycomb are a series of fine mesh damping screens which progressively reduce both the flow nonuniformity and the residual tunnel turbulence level. A nozzle with a 2.8:1 contraction ratio mounted downstream of the damping screens accelerates the flow to produce the required test section Reynolds numbers. Following the contraction nozzle the flow passes through the 34-in.-wide flat wall boundary layer test section. At the entrance to the test section an upstream facing scoop bleed assembly forms the leading edge of the boundary layer test surface. The purpose of this leading edge bleed scoop is to divert all the flow near the tunnel upper wall. With this arrangement the test section flow consists of the uniform "core" flow from the main contraction nozzle. A sketch showing details of the scoop assembly is presented in Fig. 2. The scoop assembly consists of a two-stage leading edge adjustable bleed and, as shown in Fig. 2, is attached to the flat wall boundary layer test surface. The upstream and by far the larger of the two scoops diverts the flow nearest the upper wall of the contraction exit duct. This large scoop is intended to trap both the two-dimensional boundary layer which develops along the contraction nozzle wall and the vortices which develop in the contraction corners. The flow rate along the scoop opening is adjusted by locally restricting portions of the perforated plate located at the scoop exit (see Fig. 2). The local scoop flow rate can be adjusted to produce uniform pressure (in the transverse direction) at the static taps along the entire scoop. The downstream and much smaller of the two scoops is mounted directly on the front edge of the Uniform Heat Flux Flat Wall Model. The test section boundary layer begins growing at the leading edge of

this smaller scoop. The purpose of this small-scale second scoop is to provide as short an unheated starting length upstream of the heated test surface as practical by bleeding off any boundary layer which develops along the large scoop lip. As with the larger upstream scoop the flow rate along the small scoop is adjusted by locally restricting portions of the perforated plate located at the small scoop exit (see Fig. 2). The leading edge of the small downstream scoop is a 4×1 ellipse shape in order to prevent a local separation bubble and premature transition of the test surface boundary layer. As shown in both Figs. 1 and 2 the flow diverted by the leading edge scoop assembly is returned to the main tunnel loop through a small duct.

The main test section of the Boundary Layer Tunnel consists of the flat upper wall test surface, a lower flexible, adjustable stainless-steel wall and transparent vertical sidewalls. The vertical sidewalls were constructed of plexiglass to facilitate positioning of boundary layer probes and for purposes of conducting flow visualization studies. Downstream of the test section a diffuser/corner combination reduces the test section velocity and delivers the flow to the return duct. Mounted in this return duct are an air filter and a liquid chilled heat exchanger which controls and stabilizes the tunnel air temperature at approximately 70°F .

Higher turbulence levels required for this investigation can be generated within the test section by installing coarse grids at the entrance to the tunnel contraction (see Fig. 1). Four rectangular bar turbulence generating grids were designed and fabricated for use in this investigation. These grids were designed, using the correlations of Ref. 1 to produce test section total turbulence levels ranging from approximately 1 to 7 percent. A diagram of the turbulence generating grid configurations including all pertinent grid dimensions is presented in Fig. 3. Photographs of the four assembled grids are presented in Fig. 4. For grid numbers 1 and 2 (small bars) a locating jig was employed to secure the grid bars at precise intervals while the bars were welded at their intersections. This step assured that the grid configurations were both permanent and uniform over their entire area. For grids number 3 and 4 (larger bars) the rectangular bars are very rigid making this unnecessary. The tunnel, then, can be operated with 5 different levels of freestream turbulence in the test section; (1) no turbulence grid installed (minimum turbulence level) and (2) through (5) with grids No. 1 through 4 installed at the contraction entrance.

A photograph of the Boundary Layer Wind Tunnel is presented in Fig. 5. Also shown in Fig. 5 are both the telescope used to position probes relative to the test wall and the computer controlled probe traverse mechanism.

2. Uniform Heat Flux Flat Wall Model

As discussed in the Boundary Layer Wind Tunnel description, the test boundary layer development begins at the leading edge of the small bleed scoop and continues along the flat test wall. For these present studies the flat wall test surface consists of an electrically heated plate instrumented for the measurement of local convective coefficients. This heated test surface is designed to produce a nearly uniform heat flux distribution over its entire surface and will be referred to as the Uniform Heat Flux Flat Wall Model. This flat wall model consists of a block of rigid urethane foam 34-in.-wide by 96-in.-long by 4-in.-thick mounted in a plexiglass frame with 6-in.-wide strips of metal foil cemented to the test surface. A sketch of the Flat Wall Model and its instrumentation is presented in Fig. 6. Rigid foam was employed for the substrate of the Flat Wall Model because of its extremely low thermal conductivity ($k = 0.025 \text{ Btu/hr ft } ^\circ\text{F}$). Because of this low foam conductivity less than $\frac{1}{2}\%$ of the heat generated on the surface of the plate is conducted through the model wall.

Electric current passing through the metal foil strips cemented to the Flat Wall Model test surface produces the surface heating. The metal foil strips are wired in series and are powered by a single low ripple, regulated dc power supply. Use of series wiring assures that precisely the same current passes through each of the metal foil surface strips. The metal foil employed for the model surface was 316 stainless, "3/4 hard" temper, 0.0012-in.-thick by 6.00-in.-wide. The temperature-resistance characteristics of three samples of this foil were determined using an Electro Scientific Industries 1701 B Precision Ohmmeter. A low temperature oven was used to control the temperature of the foil samples. Resistance data obtained for the three samples are presented in Fig. 7. The extremely small scatter for these data indicates that for any test surface temperature the local foil resistance can be calculated within an accuracy of 1% using the following expression.

$$R_{\text{foil}} = R_{\text{ref}} (1 + \alpha_{\text{ref}} (T_{\text{foil}} - T_{\text{ref}})) \quad (1)$$

where

$$T_{\text{ref}} = 71^\circ\text{F}$$

$$R_{\text{ref}} = 0.0500 \text{ } \Omega/\text{Ft} @ 71^\circ\text{F}$$

$$\alpha_{\text{ref}} @ 71^\circ\text{F} = 0.000504 \text{ } \Omega/^\circ\text{F}$$

The foil test surface is instrumented with an array of 203 Cr-Al 0.005 in. wire diameter bead welded thermocouples. The thermocouple array is shown in Fig. 6. Each thermocouple was welded to the back surface of the foil through a hole in the rigid foam plate. Welding the thermocouple beads directly to the foil insures that the local foil temperatures can be accurately measured.

In order to insure a known, constant test surface emissivity and hence a known radiation loss the completed foil test surface was coated with 3M C-101 high emissivity flat black paint ($\epsilon = 0.99$). Forty-eight surface static pressure taps were also installed in the Flat Wall Model. The locations of these static taps are shown in Fig. 6.

Photographs of the Uniform Heat Flux Flat Wall Model at various stages of completion are presented in Figs. 8, 9, and 10. Figure 8 shows the plexiglass frame for the Flat Wall Model prior to casting the rigid urethane foam wall. A photograph of the back surface of the Flat Wall Model is presented in Fig. 9. This photograph shows the leading edge scoop lip mounted on the front edge of the model and the routing of the thermocouple and static pressure leads. Figure 10 shows the test surface of the model before it was coated with high emissivity black paint. In Fig. 10 the surface foil strips have been connected to their respective buss bars. The buss bar/strip circuit is arranged in series so that the total power current passes through each individual strip.

The dc power current passing through the surface strips is measured using two precision shunt resistors and a digital voltmeter. The temperature of the test surface thermocouples are measured relative to a single test section free-stream reference junction using a digital voltmeter.

The local generated power on the test surface is determined by measuring the local wall temperature, T_w , and calculating the local dissipation.

$$q_{\text{power}} = I^2 R_{\text{foil}} = I^2 R_{\text{ref}} (1 + \alpha_{\text{ref}} (T_w - T_{\text{ref}})) \quad (2)$$

The local convective coefficient can then be determined by ignoring the negligible conduction losses, subtracting that power lost through thermal radiation, and dividing by the temperature difference from the wall (T_w) to the freestream (T_e).

$$h = \frac{q_{\text{power}} - q_{\text{radiation}}}{T_w - T_e} \quad (3)$$

As an example to illustrate the magnitude of the radiation losses from the test surface, for $U_e = 100$ fps, for turbulent boundary layer flow with $T_w - T_e = 25$ °F, the radiation loss is approximately 4% of the total surface power. Aside, then, from the small differences in local dissipation and radiation reflected by Eqs. (2) and (3), respectively, the test surface produces uniform convective heat flux for turbulent flow test cases.

3. Instrumentation

Boundary layer mean velocity profile data were measured using United Sensor Model BA-0.020 impact probes with flattened tips. A photograph of a typical probe is presented in Fig. 11. The probes used in the program were inspected using both a Nikon Model II toolmakers microscope and a Jones and Lamson Model PC14 Shadowgraph. Probe dimensions obtained with these instruments are included in Fig. 11.

Mean temperature data were measured with miniature thermocouple probes designed using the results of Ref. 2. Photographs of thermocouple probes No. 1 and 2 are presented in Fig. 12. The thermocouple sensing element for these probes was constructed from 0.001 in. dia Chromel-Alumel bead welded wires. The thermocouple bead (≈ 0.003 in. dia) is located at the center of the probe support prongs which are fabricated of heavier Chromel and Alumel wire. The results of Ref. 2 indicate that a probe of this design will be virtually free of wire conduction errors and is capable of measuring boundary layer mean temperature profile data into the viscous sublayer region.

4. Data Acquisition System

Experimental data for the UTRC Boundary Layer Wind Tunnel is recorded using a data acquisition system specifically designed for this facility. This data acquisition system is capable of recording time mean analog signals from the various pressure, temperature and hot wire/hot film probes and test section transducers used in the facility. In addition, the system controls the movement of the various boundary layer probes through the use of an L.C. Smith ball/screw traverse drive linked to an InterData Model 6/16 computer. Signals from the various probes are recorded using InterData magnetic disks. The data system consists of two units (1) a console containing the InterData computer and disk recording unit and a Perkin-Elmer Model 1100 scope/keyboard control terminal, and (2) a remote cabinet unit, linked by cables to the console unit, which contains the sensor transducers and traverse controls. The computer cabinet is relatively mobile and can be moved to convenient locations near the tunnel test section. A photograph of Units 1 and 2 of the data acquisition system is presented in Fig. 13. Also, in Fig. 5 (tunnel test section photograph) the remote unit can be seen at the downstream end of the test section.

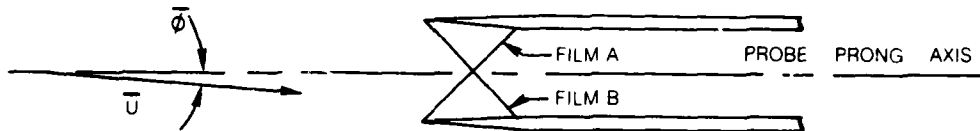
DATA ACQUISITION AND ANALYSIS TECHNIQUES

1. Description of the Hot Film Anemometer and Signal Processing System

Measurements of the turbulence quantities downstream of the various generating grids were obtained with single and X hot film probes and their associated anemometry. These data include measurements of the multi-component (u' , v' , and w') distributions of turbulence intensity and measurements of the streamwise component (u') distributions of the integral scale and power spectral density. The following are descriptions of the anemometer and signal processing equipment used to obtain these data. Also included are descriptions of the techniques employed to reduce and interpret the measured quantities.

1.1 Measurement of Multi-Component Turbulence With X Hot-Film Array

Consider an X hot-film array exposed to a mean velocity whose vector lies in the plane of the array:



In the following analysis it is not assumed that the individual films are perpendicular to each other or that they form any idealized effective angle to the mean flow direction. The angle $\bar{\phi}$ is the inclination between the mean flow direction and the nominal probe prong axis. Note that in the above sketch the flow is not assumed to be bisecting the angle between the films in the X array.

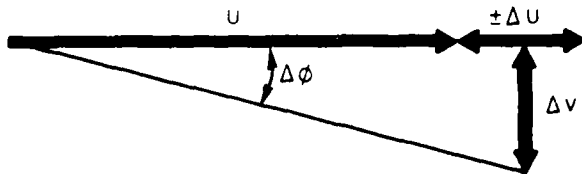
The linearized mean voltage from each of the films (i) in the array is given by:

$$E_{L_i} = E_{L_i}(\bar{U}, \bar{\phi}) = a_i \bar{U} \Big|_{\phi = \text{const.}} \quad (4)$$

where a_i is the mean velocity sensitivity coefficient of the linearized film. Differentiating with respect to time yields:

$$\frac{\partial E_{L_i}}{\partial t} = \frac{\partial E_{L_i}}{\partial U} \frac{\partial U}{\partial t} + \frac{\partial E_{L_i}}{\partial \phi} \frac{\partial \phi}{\partial t} \quad (5)$$

For the case when the mean velocity vector is aligned with the probe prong axis ($\phi = 0$) there are two components of fluctuating velocity (Δu & Δv) in the plane of the X hot-film array



$$\frac{\Delta v}{\bar{U}} \approx \tan \Delta \phi \approx \Delta \phi \quad (6)$$

$$\frac{\partial \phi}{\partial t} \approx \frac{1}{\bar{U}} \frac{\partial v}{\partial t}$$

combining Eqs. (5) and (6) yields

$$E_{L_i}' = \left(\frac{\partial E_{L_i}}{\partial U} \right) U' + \left(\frac{1}{\bar{U}} \frac{\partial E_{L_i}}{\partial \phi} \right) V' \quad (7)$$

where the prime superscript denotes differentiation with respect to time.

$$E_{L_i}' = \frac{\partial E_L}{\partial t} \quad U' = \frac{\partial U}{\partial t} \quad V' = \frac{\partial V}{\partial t}$$

If α_i is defined as the ratio of the sensitivity of V' fluctuation to U' fluctuations for the inclined wire (i)

$$\alpha_i = \frac{\frac{1}{\bar{U}} \frac{\partial E_{L_i}}{\partial \phi}}{\frac{\partial E_{L_i}}{\partial U}} = \frac{1}{\bar{U} \alpha_i} \frac{\partial E_{L_i}}{\partial \phi} = \frac{1}{E_{L_i}} \frac{\partial E_{L_i}}{\partial \phi} \quad (8)$$

Combining Eqs. (7) and (8) yields

$$E_{L_i}' = \alpha_i U' + \alpha_i \alpha_i V' \quad (9)$$

The coefficients α_i (Eq. (4)) and α_i (Eq. (8)) are to be experimentally determined for both films of each probe. A detailed description of the calibration procedure and sample calibration data are presented in the following section. The following paragraphs describe how these calibrated probes were employed to determine the various required turbulence quantities.

The fluctuating linearized voltages of films A and B in the probe array are given by Eq. (9). The fluctuating signals can be measured using a "true mean square" or true "root mean square" (RMS) voltmeter. For the case of the fluctuating linearized voltage from a single hot film a true mean square voltmeter measures

$$\overline{E_{L_i}^{'2}} = \frac{1}{T} \int_{-T/2}^{T/2} E_{L_i}'^2 dt$$

where T is the time period over which the fluctuating signal is to be averaged (typically 1 to 10 sec). In addition, the fluctuating signals from films A and B can be added or subtracted using a "sum and difference" circuit and measured using the "true mean square" voltmeter.

$$\text{true mean square of SUM} = \frac{1}{T} \int_{-T/2}^{T/2} \overline{(E_{L_A}' + E_{L_B}')^2} dt$$

$$\text{true mean square of DIFFERENCE} = \frac{1}{T} \int_{-T/2}^{T/2} \overline{(E_{L_A}' - E_{L_B}')^2} dt$$

Squaring, adding, subtracting, and averaging the terms of Eq. (9) for films A and B yields the following set of linear simultaneous equations for the unknown fluctuating velocities \bar{U}' , \bar{V}' , and $\bar{U}'\bar{V}'$.

$$\overline{(E_{L_A}' + E_{L_B}')^2} = (\alpha_A + \alpha_B)^2 \bar{U}'^2 + 2(\alpha_A + \alpha_B)(\alpha_A \alpha_A + \alpha_B \alpha_B) \bar{U}\bar{V}' + (\alpha_A \alpha_A + \alpha_B \alpha_B)^2 \bar{V}'^2$$

$$\overline{(E_{L_A}' - E_{L_B}')^2} = (\alpha_A - \alpha_B)^2 \bar{U}'^2 + 2(\alpha_A - \alpha_B)(\alpha_A \alpha_A - \alpha_B \alpha_B) \bar{U}\bar{V}' + (\alpha_A \alpha_A - \alpha_B \alpha_B)^2 \bar{V}'^2$$

(10)

$$\overline{E_{L_A}^{'2}} = \alpha_A^2 \bar{U}'^2 + 2\alpha_A^2 \alpha_A \bar{U}\bar{V}' + \alpha_A^2 \alpha_A^2 \bar{V}'^2$$

$$\overline{E_{L_B}^{'2}} = \alpha_B^2 \bar{U}'^2 + 2\alpha_B^2 \alpha_B \bar{U}\bar{V}' + \alpha_B^2 \alpha_B^2 \bar{V}'^2$$

The quantities $\overline{E_{L_A}^2}$, $\overline{E_{L_B}^2}$, $(\overline{E_{L_A}} + \overline{E_{L_B}})^2$ and $(\overline{E_{L_A}} - \overline{E_{L_B}})^2$ can all be measured using true RMS voltmeters while the coefficients (α_A , α_B , a_A , a_B) are all determined through probe calibration. Equation (10) constitutes an over-determined set (4 equations, 3 unknowns) of simultaneous, linear equations. A standard International Mathematical and Statistical Libraries, Inc. subroutine (LLSQAR) was employed to determine the "least squares" best solution for the unknowns for each set of data.

A block diagram of the varicus anemometers, signal processing circuits, and voltmeters used to obtain these measurements is presented in Fig. 14. For measurements of the U' and V' components (streamwise and vertical fluctuations) the X film array was oriented in a plane parallel to the streamwise direction and perpendicular to the horizontal test wall. For measurements of the U' and W' components (streamwise and transverse fluctuations) the X film array was oriented in a plane parallel to the streamwise direction and parallel to the horizontal test wall.

1.2 Calibration of the Single Film and X Film Probes

Mean flow velocity sensitivity coefficients, a_i (Eq. (4)), were determined for all single film and X film probes using a DISA Model 55044/45 calibration jet. For both the single film and right angle X film probes mean flow calibration data were obtained with the probe support axis perpendicular to the axis of calibration jet. For the right angle (TSI Model 1243) X hot-film probes the probe prong axis is then parallel to the jet axis. Mean flow calibration data were obtained for all probes over a range of jet velocities from $0.1 \leq U_{jet}/U_{etunnel} \leq 1.3$. TSI Model 1052 4th order polynomial linearizers were employed to transform the raw calibration data into the form of Eq. (4).

The angular sensitivity coefficients, α_i (Eq. (8)), for the X film probes were determined by measuring the voltage output of the linearized films while pitching the probes relative to the calibration jet axis. Pitch data were obtained over a range of $-20^\circ \leq \phi \leq +20^\circ$ in 10° increments. For purposes of improved accuracy, for each calibration pitched probe data were measured at three jet speeds $U_{jet}/U_{etunnel} = 0.85, 1.0$, and 1.15 . Figure 15a presents sample data obtained from one film of a typical X film probe (probe code #E303). Sensitivity coefficients a_i were determined graphically from plots such as Fig. 15a and plotted in the form shown in Fig. 15b. For the probe support oriented perpendicular to the jet flow direction ($\phi_{nom} = 0$) a precise mean value of the angular sensitivity coefficient can be determined from Fig. 15b.

1.3 Length Scale and Spectral Distribution Data

The irregular and random motions inherent to turbulent flows are produced by arrays of eddies with widely varying characteristic dimensions. Associated with this range of eddy size, the fluctuating velocities in the turbulent flow are distributed over a range of frequencies. As part of the present investigation the eddy-size/frequency-distribution properties of the Boundary Layer Wind Tunnel freestream flows were studied in detail. The purposes for documenting these turbulence properties were threefold: (1) the present turbulent flows can be compared to similar "grid turbulence" flows documented by other researchers; (2) the turbulence characteristics measured for the present flows can be compared with theoretical predictions for isotropic turbulence; and (3) provide details of freestream turbulence are available for use in the analysis of the boundary layer data.

For the present program, measurement of turbulent (eddy) length scales was accomplished by generating autocorrelations of the signals from single-sensor hot-film probes. For all these data the hot-film probes were powered by a TSI Model 1050 Constant Temperature Anemometer, the output of which was linearized using a TSI Model 1052 4th order polynomial linearizer. The autocorrelations of the linearized hot-film signal were generated using a Saicor Model SAI-42 Correlator and Probability Analyzer. A block diagram of the instrument arrangement used to document these autocorrelations is presented in Fig.16. The following paragraphs describe the methods used to analyze and interpret these data.

1.3.1 Length scale distributions

A correlator unit such as the Saicor SAI 42 can be used to generate the autocovariance of a fluctuating signal. For some input signal, $E(t)$, the autocovariance is defined as

$$R_E(\tau) \equiv \overline{E(t) \times E(t+\tau)}$$

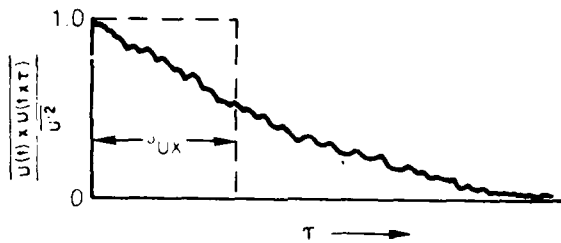
where τ is a variable "delay" time and the product is averaged over time (t). The autocovariance is usually written as a dimensionless quantity and is referred to as the autocorrelation coefficient. For our case, with the signal from the hot-film sensor, $E(t)$ is proportional to $U(t)$ the autocorrelation coefficient of interest is

$$R_U(\tau) = \frac{\overline{U(t) \times U(t+\tau)}}{\overline{U^2}}$$

A single time scale characteristic of the longest correlation distance in the entire fluctuating turbulent field can be extracted from such autocorrelation data. This time scale, the "Eulerian Longitudinal (streamwise) Integral Time Scale" (J_{UX}), is defined as

$$J_{UX} \equiv \int_{\tau=0}^{\tau=\infty} R_U(\tau) d\tau \quad (11)$$

The following sketch represents a typical freestream turbulence autocorrelation coefficient plot such as those produced by the SAICOR Correlator/Plotter unit used for these measurements (see Fig. 16).



Integration of such curves was accomplished using a planimeter with the area (of unit length) being the longitudinal integral scale.

From Taylor's (see Hinze, Ref. 3) hypothesis, if $U'/U \ll 1$ then the turbulent eddies retain an approximately constant shape as they pass by the fixed hot-film sensor. The autocorrelation then is approximately equal to a space correlation with separation $-U\tau$ in the X direction.

$$R(X) = R(-\tau \bar{U}) \quad (12)$$

Using Eqs.(11) and (12), a "characteristic" length scale, the Longitudinal (streamwise) Integral Scale (Λ_f), can be determined for a given turbulent flow.

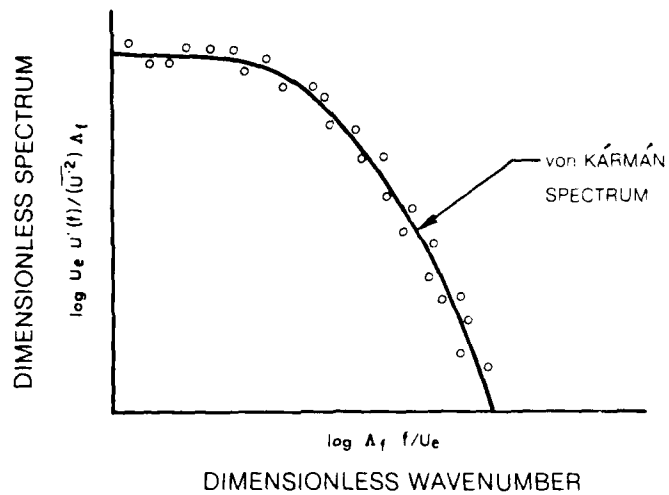
$$\Lambda_f = \bar{U} J_{UX}$$

3.2 Spectral distributions

The fluctuating velocities in a turbulent flow can be examined to determine the distribution, as a function of frequency, of the various contributions to the overall turbulence level. For the present program, these frequency related data were obtained using a Spectral Dynamics Model SD 340 MICRO FFT Analyzer (see Fig. 16). A spectral analyzer, such as the SD 340, processes a signal to determine the fluctuation level within particular intervals or bandwidths of

frequency. The distribution of these narrow band fluctuation levels over a wide range of frequencies is referred to as the spectrum. The contribution of the square of the fluctuation levels within particular unit bandwidths to the overall fluctuation level squared is called the power spectral density. Knowing the overall level, the spectral analyzer output can be used to construct a power spectral density distribution (power spectrum).

Power spectral density distributions are usually presented in dimensionless form with the Dimensionless Spectrum, $u_e u'(f)/(U^2) A_f$, as a function of the Dimensionless Wavenumber, $A_f, f/u_e$. In addition to previously defined symbols, these expressions contain $U'(f)$, the fluctuating velocity within a bandwidth of 1 Hz (U')/Hz), and the frequency f (Hz). The following sketch represents a typical free-stream turbulence power spectral density distribution.



Included in the above sketch is the von Karman theoretical spectrum for one-dimensional isotropic turbulence, the form of turbulence expected to result in the tunnel freestream "far" from the turbulence generating grids. A presentation of the analysis used to predict this spectrum can be found in Hinze (Ref. 3).

2. Boundary Layer Data Analysis

Boundary layer flow has been examined as extensively and thoroughly as any subject in fluid mechanics. As a result of these investigations, both experimental and analytical, there exists a wealth of information on the topic in the open literature. As the subject area has developed and evolved a number of "standard" or "traditional" methods have arisen for evaluating and examining mean, or time-averaged, profile data. The following section consists of a brief summary of the bases of these "standard" evaluation methods. An explanation of the mean profile data analysis system employed in the present study is also provided. This data analysis system provides an accurate and consistent method of inferring the wall shearing stress from the mean velocity profiles and, also, by reducing the profiles to "universal" velocity and temperature coordinates, allows the present results to be compared with other data. Only those aspects of boundary layer flow directly applicable to the present program are discussed within this section (specifically, turbulent incompressible flat wall boundary layer flow). For additional information, generally of a much broader scope, the reader is urged to consult the articles which formed the bases of this summary (Clauser (Ref. 4), Coles (Refs. 5 and 6), Schubauer and Tchen (Ref. 7), Rotta (Ref. 8), Blom (Ref. 9), and Deissler (Ref. 10)).

2.1 Background

Turbulent boundary layer flows are generally viewed as a composite of four regions, each with its own distinct character. Starting at the wall and moving progressively outward, the first of these four regions consists of an extremely thin layer in which the normal velocity gradients are very large and shearing stresses result only from molecular viscosity ($\tau = \mu \frac{\partial u}{\partial y}$). This extremely thin region immediately adjacent to the wall is usually referred to as the viscous sublayer. Beyond the viscous sublayer is the second region, usually called the buffer zone, in which turbulent (Reynolds) stresses produced by velocity fluctuations in the flow provide an increasingly important contribution to the effective total shear. The total shear stress relationship is commonly written as:

$$\tau = (\mu + \rho \epsilon_m) \frac{\partial u}{\partial y} \quad (13)$$

where τ is the total shear stress, μ is the molecular viscosity, and ϵ_m is the coefficient of eddy diffusivity of momentum.

At the outer edge of the buffer zone the molecular contribution to the total effective shearing stress is negligible. Bradshaw (Ref. 11) presented a comparison of the relative contributions of the molecular and turbulent shearing stresses within the buffer zone. McDonald (Ref. 12) gave a comprehensive analysis of the buffer zone region, including the effects of streamwise pressure gradient. Above the buffer zone in the largest of the three regions yet discussed, the molecular shear stresses are negligible and the turbulent stresses dominate the total effective stress. This third region can be described using the so-called "law-of-the-wall", to be discussed below. This region will be extensively examined with the present data reduction system and will subsequently be referred to as the "logarithmic law" portion of the boundary layer.

The fourth and last region of the turbulent boundary layer lies between the "logarithmic law" portion and the edge of the shear layer (typically, 80% of the overall shear layer thickness). Within this "outer" region the mean velocity gradients gradually diminish until asymptotically approaching zero at the edge of the shear layer. The turbulent shearing stresses also decrease across this outer region but may persist for some small distance beyond the edge of the mean velocity gradient.

2.2 Universal Velocity and Temperature Distributions

In the following sections "universal" mean velocity and temperature distributions laws will be presented. As previously discussed, these "universal" laws will permit comparison of the present data with that obtained in numerous earlier studies.

2.2.1 Universal velocity distribution - viscous sublayer and buffer zone

In the viscous sublayer turbulent shearing stresses are negligible in Eq. (13) and:

$$\tau = \mu \frac{\partial U}{\partial y} \quad (14)$$

Within the sublayer the shear stress is constant and equal to the wall value, τ_w . By integration and rearrangement of Eq. (14):

$$U = \frac{\tau_w}{\mu} y$$

or in dimensionless form

$$U^+ = y^+$$

where

$$U^+ \equiv \frac{U}{U_\tau} \quad \text{and} \quad y^+ \equiv \frac{yU_\tau}{\nu}$$

$$U_\tau \equiv \sqrt{\tau_w/\rho} = \text{the friction velocity}$$

It has been experimentally established by numerous investigators that the viscous sublayer extends from the wall to a dimensionless distance of approximately $y^+ = 5$. Figure 17 is a composite velocity distribution for the entire boundary layer and includes the viscous sublayer for $y^+ \leq 5$.

The derivation of velocity distribution laws within the buffer zone is extremely complex and will not be given here. A summary and comparison of many of the buffer zone velocity distribution laws available in the open literature is presented in Ref. 9. For the present program buffer zone velocity data will be compared with the velocity distribution proposed by Burton (Ref. 13). This formulation fulfills all known boundary conditions for the buffer zone, matches all available data well, and blends asymptotically with the well known "law-of-the-wall" (see following section). Burton's proposed buffer zone distribution law is given as follows:

$$y^+ = U^+ + \left(\frac{U^+}{8.74} \right)^7 \quad (15)$$

This distribution law will be employed in the region from $y^+ > 5$ to the outer edge of the buffer zone which is commonly observed to end at approximately $y^+ = 30$ (see Fig. 17).

2.2.2 Universal velocity distribution - logarithmic-law region

Prandtl introduced the argument that for a region extending for some unknown distance from the wall the velocity distribution is a function of the wall shear stress, the distance from the wall and the fluid density and viscosity.

$$U = f(\tau_w, y, \mu, \rho)$$

or in dimensionless form

$$\frac{U}{U_\tau} = f_1 \left(\frac{U_\tau y}{\nu} \right) \quad \text{where} \quad U_\tau \equiv \sqrt{\tau_w/\rho} \quad (16)$$

For that portion of the shear layer in which the viscous forces are relatively small, von Karman suggested the concept of the velocity defect law. He showed that within this region the reduction in velocity below the freestream value ($U - U_e$) is a function only of the wall shear, the distance from the wall, and the overall thickness of the boundary layer

$$U_e - U = f(y, U_\tau, \delta)$$

or in dimensionless form

$$\frac{U_e - U}{U_\tau} = f_2\left(\frac{y}{\delta}\right) \quad (17)$$

Clauser (Ref. 4) has demonstrated the universal validity of Eq. (17) for constant pressure boundary layers using data obtained for various Reynolds numbers and wall roughnesses.

It has been experimentally demonstrated by numerous investigators that for a significant fraction of the overall shear layer thickness both Eq. (16) and Eq. (17) are valid. Millikan (Ref. 14) was the first to show that if these functions have a region of overlapping validity then the functions f_1 and f_2 must be logarithms. This can be seen by writing the functions in the following form

$$\frac{U}{U_\tau} = f_1\left[\left(\frac{y}{\delta}\right) \left(\frac{U_\tau \delta}{\nu}\right)\right] \quad (18)$$

$$\frac{U}{U_\tau} = \frac{U_e}{U_\tau} - f_2\left(\frac{y}{\delta}\right) \quad (19)$$

The functions f_1 and f_2 must be logarithms since a comparison of Eqs. (16) and (17) shows that the effect of multiplying factor $(\frac{U_\tau}{\nu})$ inside the function of f_1 must be equivalent to the additive term U_e/U_τ outside the function f_2 . This observation has led to the expression commonly referred to as the "law-of-the-wall".

$$\frac{U}{U_\tau} = \frac{1}{\kappa} \ln \frac{y U_\tau}{\nu} + C \quad (20)$$

where κ and C are constants to be experimentally determined.

Taking an alternate approach Prandtl formulated the "law-of-the-wall" employing the following assumptions. If the turbulent mixing length near the wall is assumed to be proportional to the distance from the wall, $\ell = \kappa y$, and Prandtl's mixing length

hypothesis, for the purely turbulent shearing stress, $\tau_t = \rho \ell^2 \left(\frac{\partial U}{\partial y} \right)^2$ is utilized.

Then

$$\frac{\tau}{\rho} = \kappa^2 y^2 \left(\frac{\partial U}{\partial y} \right)^2 \quad (21)$$

(assuming that for this region eddy viscosity \gg molecular viscosity then $\tau_t \approx \tau$). Assuming further that shear stress is constant in this region and equal to the wall shear $\tau = \tau_w$ and integrating

$$U = \frac{U_\tau}{\kappa} \ln y + C$$

The constant of integration is determined from the condition that the turbulent velocity distribution must merge with the viscous sublayer velocity distribution near the wall. For details see Schlichting (Ref. 15). Upon rearrangement this yields

$$\frac{U}{U_\tau} = \frac{1}{\kappa} \ln \frac{y U_\tau}{\nu} + C$$

which is identical to Eq. (20).

It has been experimentally established that the logarithmic "law-of-the-wall" applies, for flows with mild adverse, zero, and mild favorable streamwise pressure gradients, from $30 < \frac{y U_\tau}{\nu} < 100$ to 800 with the upper limit dependent upon the magnitude and sign of the streamwise pressure gradient (see Fig. 17).

2.2.3 Universal velocity distribution - wake region

As previously discussed, beyond the logarithmic law region of the boundary layer the effects of both molecular and eddy viscosity become decreasingly important. This outermost section of the boundary layer is commonly referred to as the wake region because of its jet-like or wake-like shape (see Coles, Ref. 16). Coles (Ref. 6) has extensively examined wake region flow and has developed a comprehensive wall-wake analysis. In Coles' approach, the outer wake region flow is viewed as a deviation from the "law-of-the-wall" and the entire mean velocity profile from $y^+ \approx 30$ to the edge of the shear layer is described by the composite equation

$$\frac{U}{U_\tau} = \frac{1}{\kappa} \ln \frac{y U_\tau}{\nu} + C + \frac{2\pi}{\kappa} \sin^2 \left(\frac{\pi}{2} \frac{y}{\delta} \right) \quad (22)$$

where the wake strength, Π , is a measure of the maximum deviation of the dimensionless velocity from the "law-of-the-wall".

A composite velocity distribution can now be constructed for all four regions of the turbulent boundary layer (see Fig. 17). This universal distribution spans the entire shear layer, from the wall to the free stream.

2.2.4 Universal temperature distribution

To this point the development of the universal velocity distribution equations has been concerned with only constant property, isothermal flows. For flows with wall heat transfer a similar set of equations for a universal temperature distribution can be developed and employed for two purposes. First, as with the universal velocity distribution laws, they provide a method for comparing mean temperature profile data from the present program with the data from many other earlier studies. Second, the "temperature-law-of-the-wall" can be employed to infer an average value of the turbulent Prandtl number (Pr_t) for the boundary layer.

For turbulent flow the total effective shear and heat flux are the sum of the molecular and turbulent eddy contributions.

$$\tau = (\mu + \rho \epsilon_m) \frac{\partial u}{\partial y}$$

$$q = - \left(k + \rho c_p \epsilon_h \right) \frac{\partial t}{\partial y}$$

where ϵ_m and ϵ_h are the coefficients of eddy diffusivity of momentum and heat, respectively.

Written in dimensionless form these equations become

$$\frac{\tau}{\tau_w} = \left(\frac{\mu}{\mu_w} + \frac{\rho \epsilon_m}{\rho_w \mu_w / \rho_w} \right) \frac{\partial u^+}{\partial y^+} \quad (23)$$

and

$$\frac{q}{q_w} = \left(\frac{k}{k_w} \frac{1}{Pr_w} + \frac{\rho}{\rho_w} \frac{c_p}{c_{p_w}} \frac{\epsilon_h}{\mu_w / \rho_w} \right) \frac{\partial t^+}{\partial y^+} \quad (24)$$

where

$$\dot{t}^+ = \frac{(t_w - t) \rho_w c_p \sqrt{\tau_w / \rho}}{q_w} = \frac{t_w - t}{t_\tau}$$

$$t_\tau \equiv \frac{q_w}{\rho_w c_p U_\tau}$$

and $\text{Pr} = \frac{\mu c_p}{k}$ = the molecular Prandtl number. For near constant properties (i.e., $k \approx k_w$, $\rho \approx \rho_w$, $c_p \approx c_{p_w}$), Eqs. (23) and (24) can be written as

$$\frac{\tau}{\tau_w} = \left(1 + \frac{\epsilon_m}{\nu}\right) \frac{\partial U^+}{\partial y^+} = \frac{\epsilon_m}{\nu} \frac{\partial U^+}{\partial y^+} \quad (25)$$

where $\epsilon_m = \epsilon_v + \epsilon_h$ = the effective or total viscosity and

$$\frac{q}{q_w} = \left(\frac{1}{\text{Pr}} + \frac{\epsilon_h}{\nu}\right) \frac{\partial t^+}{\partial y^+} = \frac{\epsilon_{h_e}}{\nu} \frac{\partial t^+}{\partial y^+} \quad (26)$$

where $\epsilon_{h_e} (\frac{1}{\text{Pr}} + \epsilon_h)$ = the effective or total thermal diffusivity. If the effective Prandtl number is defined as $\text{Pr}_e = \frac{\epsilon_{h_e}}{\epsilon_{v_e}}$ then Eq. (26) can be written as:

$$\frac{q}{q_w} = \frac{\epsilon_{h_e}}{\nu} \frac{1}{\text{Pr}_e} \frac{\partial t^+}{\partial y^+} \quad (27)$$

In Eq. (27) the heat flux is written in terms of the eddy diffusivity of momentum. Equation (22) can be combined with Eq. (20) to yield

$$\frac{\tau_w q}{\tau q_w} \text{Pr}_e \frac{\partial U^+}{\partial y^+} = \frac{\partial t^+}{\partial y^+} \quad (28)$$

If it is assumed that for at least some distance from the wall the shear stress and heat flux are constant and equal to the value near the wall, $\frac{\tau_w q}{\tau q_w} \approx 1$ then Eq. (28) can be written as

$$t^+ = \int_0^{U^+} \text{Pr}_e dU^+ \quad (29)$$

Equation (29) is an important result, indicating that if $Pr_e(U^+)$ can be obtained then the temperature distribution can be determined. This functional relationship will be developed below. From the definition of the effective Prandtl number and the turbulent Prandtl number ($Pr_t = \frac{\epsilon_m}{\epsilon_h}$)

$$Pr_e = \frac{\epsilon_{m_e}}{\epsilon_{h_e}} = \frac{1 + \frac{\epsilon_m}{\nu}}{\frac{1}{Pr} + \frac{\epsilon_m}{\nu Pr_t}} \quad (30)$$

Using Eqs. (30) and (25) and the assumption that $\tau_w \approx \tau$

$$Pr_e = \frac{\left(\frac{\partial U^+}{\partial y^+} \right)^{-1}}{\frac{1}{Pr} + \frac{\left(\left(\frac{\partial U^+}{\partial y^+} \right)^{-1} \right)}{Pr_t}} \quad (31)$$

Thus an approximation to the functional relationship $Pr_e(U^+)$ has been established. Equation (31) can now be substituted into Eq. (29) to yield an expression for the temperature distribution in terms of the molecular and turbulent Prandtl numbers, and the dimensionless velocity and distance from the wall, or:

$$t^+ = f(Pr, Pr_t, y^+, U^+(y^+))$$

At this point the temperature distribution can be determined for certain portions of the boundary layer. The first solution will be for the temperature distribution in the viscous sublayer ($y^+ < 5$). For this region $y^+ \ll 1$ so Eq. (31) yields $Pr_e = Pr$.

Substituting into Eq. (29) and integrating:

$$t^+ = \int_0^{U^+} Pr du^+ \quad (32)$$

$$t^+ = Pr U^+$$

Equation (32) then gives the temperature distribution within the viscous sublayer.

The second region of the boundary layer for which a temperature distribution can be determined is that portion for which the velocity "law-of-the-wall" applies. The "temperature law-of-the-wall" begins at approximately $y^+ = 30$ and extends for some distance dependent upon the particular flow.

The first step required is to integrate Eq. (29) across the boundary layer to some height Δ

$$t_{\Delta}^+ = \int_0^{u_{\Delta}^+} Pr_e du^+ = \int_0^{u_{\Delta}^+} Pr_t du^+ + \int_0^{u_{\Delta}^+} (Pr_e - Pr_t) du^+ \quad (33)$$

Equation (33) will be solved by assuming that Pr_t is a constant across the entire boundary layer.

$$t_{\Delta}^+ = Pr_t (u_{\Delta}^+ + P_s)$$

where

$$P_s = \int_0^{u_{\Delta}^+} \left[\frac{(Pr_e - Pr_t)}{Pr_t} \right] du^+ \quad (34)$$

Equation (30) can be combined with Eq. (34) to eliminate Pr_e and yield

$$P_s = \left(\frac{Pr}{Pr_t} - 1 \right) \int_0^{u_{\Delta}^+} \left(1 + \frac{Pr}{Pr_t} \frac{\epsilon_m}{\nu} \right)^{-1} du^+ \quad (35)$$

In order to evaluate Eq. (35) for P_s all that is required is a model for the distribution of $\epsilon_m(y^+)/\nu$. Using Eq. (35) expressions for P_s have been determined for various universal velocity distributions.

A. von Karman (Ref. 17)

$$P_s = 5 \ln \left(1 + 5 \frac{Pr}{Pr_t} \right) + 5 \frac{Pr}{Pr_t} - 2.5 \ln 30 - 5.5 \quad (36)$$

B. Spaulding (Ref. 18)

$$P_s = 13.4 \left[\left(\frac{Pr}{Pr_t} \right)^{3/4} - 1 \right] \quad (37)$$

C. Jayatilleke (Ref. 19) has compiled an extensive review of proposed distributions of $\epsilon_n(t^*)/\nu$ and he gives

$$P_s = \frac{A_1}{Pr_t} \left[\left(\frac{Pr}{Pr_t} \right)^{3/4} - 1 \right] \left[1 + 0.28 \exp \left(-0.007 \frac{Pr}{Pr_t} \right) \right] \quad (38)$$

with $A_1 = 8.22$ for $Pr_t = 0.9$ and $A_1 = 9.00$ for $Pr_t = 1.00$. Equations (36), (37), and (38) give nearly identical results. For example, for $Pr = 0.71$ and $Pr_t = 0.9$ for Eq. (36) $P_s = -2.07$, for Eq. (37) $P_s = -2.18$, and for Eq. (38) $P_s = -1.926$.

With P_s determined the universal temperature distribution in the logarithmic region can be evaluated from Eqs. (20) and (34)

$$t^+ = Pr_t \left(\frac{1}{k} \ln y^+ + C + P_s \right) \quad (39)$$

For a constant turbulent Prandtl number, Pr_t , Eq. (39) gives the boundary layer temperature distribution from $y^+ \approx 30$ to some value of y^+ dependent on the particular flow. Equation (39) can be employed, then, to infer an average boundary layer turbulent Prandtl number from that portion which has a constant slope when plotted in t^+ vs. $\ln y^+$ coordinates.

2.2.5 Property variations

In the preceding sections only cases with approximately constant fluid properties have been considered. Deissler (Ref. 10), using the von Karman similarity principal and the assumption that the eddy diffusivities of momentum and heat are equal, has developed the following variable property expressions for y^+ and t^+ .

$$y^+ = \frac{26 \bar{e} \frac{2K}{\beta} \sqrt{1-\beta(U^+ - A + B)}}{\left[\frac{2K}{\beta} \sqrt{1-\beta(U^+ - A + B)} + 1 \right]} e^{-\frac{2K}{\beta} \sqrt{1-\beta\beta} \left(\frac{2K}{\beta} \sqrt{1-\beta\beta} + 1 \right)} \quad (40)$$

$$t^+ = U^+ - B + A$$

where $A = U^+$ at $y^+ = 26$

$B = t^+$ at $y^+ = 26$

and $\beta = \frac{q_w \sqrt{\tau_w / \rho_w}}{c_p \tau_w t_w}$

For the profile data to be obtained in the present program, $\beta = 0.002$ and Eq. (40) agrees within 1% with Eq. (20) for $\kappa = 0.41$ and $C = 5.0$. Because of the near identity between the constant property and variable property solutions to the universal velocity distributions the much simpler constant property approximation will be employed for this program.

2.2.6 Summary

As previously stated, the analytical relationships documented above provide the basis for the boundary layer data reduction system presented in the following paragraphs. Based on these analytical relationships, the data analysis system serves two purposes: (1) it provides an accurate and consistent method for inferring wall-shearing stresses from the mean profile; and (2) by reducing the profiles to "universal" velocity and temperature coordinates, it allows the present results to be compared with other data.

2.2.7 Boundary layer data reduction system

A computer program has been written which reduces, plots, and tabulates the velocity and temperature boundary layer profile data obtained by the UTRC Boundary Layer Wind Tunnel Data Acquisition System. Following is a brief description of this reduction program.

(a) Mean velocities (U) are measured with miniature flattened pitot probes. These velocities are corrected for probe Reynolds number and wall blockage effects using the results of Refs. 20, 21, and 22. Except for those measurements extremely close to the wall ($y \sim 0.010$ in.) the corrections were less than 1% of the measured velocity. The maximum velocity correction (5%) resulted for the case of the probe touching the wall.

(b) Friction velocities (U_τ) for each profile are determined by a least squares fit of the velocity profile data from $50 \sim y^+ \sim 500$ to the "law-of-the-wall" (Eq. 20).

$$\frac{U}{U_\tau} = \frac{1}{\kappa} \ln \frac{yU_\tau}{\nu} + C \quad (41)$$

where $\kappa = 0.41$

$C = 5.0$

as recommended by Coles (Ref. 5).

Using this value of U_τ , the velocity and temperature data are plotted in universal coordinates $y^+ = \frac{y}{U_\tau}$ and $\tau^+ = \frac{(1-w)}{U_\tau} \rho_w C_p \sqrt{\tau_w / \rho}$ vs. y^+ . The velocity profile data are compared with Eq. (41) and the temperature data with Eq. (42).

$$\tau^+ = \text{Pr}_t \left(\frac{1}{\kappa} \ln y^+ + C + P_s \right) \quad (42)$$

where $\text{Pr}_t = 0.9$

$$\kappa = 0.41$$

$$C = 5.0$$

$$P_s = -2.0$$

(c) The following integral properties are determined

(i) displacement thickness

$$\delta^* = \int_0^\delta \left(1 - \frac{\rho U}{\rho_e U_e} \right) dy$$

(ii) momentum thickness

$$\theta = \int_0^\delta \frac{\rho U}{\rho_e U_e} \left(1 - \frac{U}{U_e} \right) dy$$

(iii) energy-dissipation thickness

$$\delta^{**} = \int_0^\delta \frac{\rho U}{\rho_e U_e} \left(1 - \frac{U^2}{U_e^2} \right) dy$$

(iv) enthalpy thickness

$$\delta_H = \int_0^{\delta_t} \frac{\rho U}{\rho_e U_e} \left(\frac{T - T_e}{T_e} \right) dy$$

(v) kinematic displacement thickness

$$\delta_K^* = \int_0^\delta \left(1 - \frac{U}{U_e} \right) dy$$

(vi) kinematic momentum thickness

$$\theta_K = \int_0^\delta \frac{U}{U_e} \left(1 - \frac{U}{U_e} \right) dy$$

(vii) Clauser delta

$$\Delta = \int_0^\delta \left(\frac{U_e - U}{U_\tau} \right) dy$$

(viii) Clauser shape parameter

$$G = \frac{1}{\Delta} \int_0^\delta \left(\frac{U_e - U}{U_\tau} \right)^2 dy$$

Measurement of velocity profile data very close ($y^+ < 30$) to a wall is difficult because of the extremely large local velocity gradients and the finite probe tip size. For the velocity profiles measured in this program a flattened impact probe with a probe tip height of approximately 0.007 in. (see instrumentation section) is employed. This tip height corresponds to $\Delta y^+ \approx 10$ for most of the profiles (depending on the individual profile U_τ). Because the true distance from the wall to the effective center of the probe tip is uncertain (uncertainty of approximately ± 0.001 in.) the recommendation of Coles (Ref. 16) has been followed and the integral thicknesses are evaluated using standard sublayer functions very close to the wall. For values of $y^+ < 35$ (approximately three probe tip heights) the integral thicknesses are evaluated using the standard velocity sublayer and buffer zone function (Eq. (15)) of Burton (Ref. 13).

$$y^+ = U^+ + \left(\frac{U^+}{8.74} \right)^7$$

The thermocouple boundary layer probes, as described in the instrumentation section, are constructed with 0.001-in.-dia sensing elements. Because of this design, accurate temperature data can be obtained very close to the wall (for some profiles even within the viscous sublayer). For this reason it has been possible to use measured temperature data for evaluation of the integral thicknesses from $y^+ = 5$ to the edge of the boundary layer. For $y^+ < 5$ (viscous sublayer) the integral thicknesses are evaluated using Eq. (32).

$$t^+ = \text{Pr} U^+$$

(d) The profile "wake strength" (Π) is determined from an iterative solution of two "local friction law" formulations from Coles (Ref. 16)

$$(i) \quad \frac{U_e}{U_\tau} = \frac{1}{\kappa} \ln \frac{\delta U_\tau}{\nu} + C + \frac{2\Pi}{\kappa}$$

$$(ii) \quad \left(\frac{\frac{\delta U_e}{\nu} - 65}{\frac{\delta U_\tau}{\nu}} \right) = 1 + \Pi$$

Since the term $\frac{\delta}{\nu}$ can be eliminated from Eqs. (i) and (ii) all that is required to solve for Π are values of U_e , U_τ , and δ^*

The wake component

$$w = \frac{\kappa}{\Pi} \left[\frac{U}{U_\tau} - \left(\frac{1}{\kappa} \ln y^+ + c \right) \right] \quad (43)$$

is plotted vs. $\frac{y}{\delta}$ and compared to Coles (Ref. 16) zero pressure gradient wake function

$$w = 2 \sin^2 \left(\frac{\pi}{2} \frac{y}{\delta} \right) \quad (44)$$

(e) Defect velocities are calculated using the value of U_τ determined in (b).

$$\text{Velocity defect} = \frac{U - U_e}{U_\tau}$$

The velocity defect distribution is plotted vs. $\frac{y}{\delta}$ and compared with inner and outer region defect correlations.

(i) In the inner region ($\frac{y}{\delta} < 0.2$) with the correlation of Schubauer and Tchen (Ref. 7)

$$\frac{U - U_e}{U_\tau} = \frac{1}{\kappa} \ln \left(\frac{y}{\delta} \right) - 2.35 \quad (45)$$

(ii) in the outer region ($\frac{y}{\delta} > 0.2$) with the correlation of Hama (Ref. 23)

$$\frac{U - U_e}{U_\tau} = -9.6 \left(1 - \frac{y}{\delta} \right)^2 \quad (46)$$

(f) The following is a list of all plots constructed, including those discussed in parts (b), (d), and (e):

i) $\frac{U}{U_e}$ vs $\frac{y}{\delta}$

ii) $\frac{T_w - T}{T_w - T_e}$ vs $\frac{y}{\delta}$

iii) U^+ vs Y^+ (see b)

iv) T^+ vs Y^+ (see b)

R80-914388-12

v) $\frac{U-U_e}{U_\tau}$ vs $\frac{Y}{\delta}$ (see d)

vi) w vs $\frac{y}{\delta}$ (see e)

g) The following boundary layer values are tabulated

$$y, \frac{y}{\delta}, U, T, \frac{U}{U_e}, \frac{T_w - T}{T_w - T_e}, \frac{U - U_e}{U_\tau}, U^+, Y^+, T^+$$

2.2.8 Sample reduced boundary layer profile data

Typical mean velocity and temperature boundary layer profile data obtained in the UTRC Boundary Layer Wind Tunnel with the test section adjusted for zero pressure gradient flow are presented in Figs. 18A, 18B and 19. Following are test conditions for which the data were obtained and the various computed boundary layer integral properties.

Test Conditions

distance from leading edge - 36.4 in.
free stream density - 0.0720 lbm/ft³
free-stream temperature - 85.0° F
wall temperature - 106.7° F
free-stream velocity - 101.1 fps
convective wall heat flux - 0.0749 Btu/sec-ft²
unheated length upstream of heat flux - 1.7 in.
boundary layer trip location - 1.5 in.

Measured and Calculated Boundary Layer Values

Re_x	-	1.791×10^6
θ	-	0.0689 in.
δ^*	-	0.0997 in.
δ^{**}	-	0.1213 in.
δ_h	-	0.00271 in.
Re_θ	-	3389
Re_{δ^*}	-	4901
δ^*/δ	-	1.446
δ^{**}/δ^*	-	1.760
C_f	-	0.003080
Π	-	0.559

WIND TUNNEL FLOW QUALITY EVALUATION TESTS

1. Total Pressure Uniformity Surveys

Surveys of the total pressure distribution in the tunnel test section core flow were obtained for all 5 tunnel turbulence configurations using a traversing impact probe. These distributions were measured at both the tunnel contraction exit plane (12 in. upstream of the test wall leading edge) and near the test section exit plane (88 in. downstream of the test wall leading edge). Total pressure measurements were obtained over each survey plane at 1 in. intervals (vertical and horizontal). At the tunnel contraction exit (upstream survey location) this resulted in a 300 point, 1 in. x 1 in., matrix of measurements for each turbulence configuration. At the test section exit plane the extent of tunnel core flow is reduced by boundary layer growth along the test section walls. The thickness of the boundary layers at the exit plane is a function of the free-stream turbulence level and depending upon which grid was installed the 1 in. x 1 in. measurement matrix resulted in from a 75 to 125 point array. In Figs. 20 through 24 local total pressure measurements are presented in the form of the nonuniformity parameter $P_T - \bar{P}_T/q$ for all 5 tunnel turbulence configurations. Checks made on the repeatability of these total pressure measurements indicated that multiple sets of measurements at identical locations were highly consistent and reproducible. Examination of Figs. 20 through 24 reveals that there are no large scale (of the order of the test section dimensions) "cells" of high or low total pressure for any of the turbulence configurations.

The ranges (maximum to minimum) of total pressure measured within the tunnel test section core flow for the 5 turbulence configurations are presented as $P_{T_{MAX}} - P_{T_{MIN}}/2q$ ($\approx \pm \Delta P_T/q$) in Fig. 25. The data presented in Fig. 25 represents a conservative measure of test section total pressure nonuniformity in that all the boundary layer profile data measured for this program were obtained within the center 12 in. of the tunnel span. If pressures measured within the center 12 inches of the tunnel span only were included in Fig. 25 the indicated non-uniformities would be reduced by approximately 1/3. An examination of Fig. 25 reveals that for all 5 configurations core flow mixing results in decreasing total pressure nonuniformity with increasing distance from the grids. In addition, for all configurations and measurement planes, except grid No. 2 - downstream, core flow nonuniformities increase directly with increased grid coarseness. This almost certainly results from the fact that the wakes generated by the individual bars of particular grid configurations are approximately the width of the grid bars themselves, b (see Fig. 3). At a fixed distance from the grid location larger bars would be expected to have stronger residual wakes than smaller bars. For grid No. 2 the nonuniformities measured at the downstream plane were found to be extremely low, lower than for any other case including the "no grid" configuration.

Assuming that the static pressure across the measurement planes is uniform, the above total pressure measurements indicate that the following maximum non-uniformities in core flow velocity were associated with the various grids:

% NONUNIFORMITIES AT THE TEST WALL LEADING EDGE

Grid Number	$\frac{P_{TMAX} - P_{TMIN}}{2q}$ (%)	$\frac{\approx \pm U}{\bar{U}}$ (%)
no grid	0.5	0.25
1	1.0	0.5
2	1.0	0.5
3	3.4	1.7
4	4.0	2.0

The conclusion reached from Figs. 20 through 25 is that, on the scale of the tunnel test section, the flow through the various grid configurations is extremely uniform. The turbulence grids appear to have been fabricated precisely (even bar spacing) and to produce uniform flow resistance over their surfaces.

2. Flat Wall Heat Transfer Distributions (Evaluation Tests)

Stanton number distributions measured on the Uniform Heat Flux Wall for constant nominal free-stream velocities of 40 and 100 fps are presented in Fig. 26. Examination of Fig. 26 reveals that for the nominally 100 fps test case the measured heat transfer distribution, upstream of boundary layer transition ($Re_x < 1.2 \times 10^6$, $x < 23$ in.), agrees very well with the analytical solution of Ref. 34 (Equation 47 below) for zero pressure gradient, laminar boundary layer flow with a uniform convective heat flux wall and an unheated starting length ξ . For this test plate $\xi = 1.69$ in.

$$St \Pr^{2/3} = 0.453 \ Re_x^{-1/2} \left[1 - (\xi/x)^{3/4} \right]^{-1/3} \quad (47)$$

For the 40 fps test case the measured heat transfer distribution agreed with Eqn. 38 within approximately 5 percent from the beginning of wall heating ($x = \xi = 1.69$ in) to $Re_x \approx 5 \times 10^5$ ($x = 25$ in.). Between $Re_x \approx 5 \times 10^5$ and $Re_x \approx 1.1 \times 10^6$ (where the test boundary layer underwent transition), the measured heat transfer was up to 10 percent less than was calculated by the uniform heat flux prediction of Equation 47. This deviation from Equation 47 is a result of significant surface radiation heat losses present for the 40 fps test case. Unlike the example of high speed turbulent boundary layer flow cited earlier, for the case of low speed laminar boundary layer flow the convective coefficient drops to extremely low values and surface radiation losses become large. For the 40 fps test case at $Re_x = 1 \times 10^6$ nearly 50 percent of the power being generated on the test surface was lost through thermal radiation. Because of these relatively large test wall radiation losses in the 40 fps test case, the convective heat flux progressively and significantly decreases with increasing x . As a result of these radiation losses, the uniform convective heat flux solution (Eqn. 47) is inappropriate for the 40 fps test case. A prediction of the Stanton-number distribution for the 40 fps test case was computed using the UTRC Finite-Difference Boundary Layer Computation code. The code was used to predict a laminar boundary layer flow with the convective wall heat flux distribution present for the actual experimental test case. A comparison of this prediction, also shown in Fig. 26, and the measured distribution shows excellent agreement.

Downstream of $Re_x \approx 1.2 \times 10^6$ the test wall boundary layers passed through transition for both the 40 and 100 fps cases. From $Re_x \approx 1.8 \times 10^6$ to the downstream end of the plate the measured heat transfer data agreed within approximately ± 3 percent with the fully turbulent correlation of Ref. 24.

$$St \Pr^{0.4} = 0.0307 \ Re_x^{-0.2} \ (Tw/Te)^{0.4} \quad (48)$$

The conclusion reached from Fig. 26 is that there is excellent agreement, even at very low freestream velocities, between low freestream turbulent heat transfer data measured in this facility and the appropriate analytical predictions or established data correlations.

3. Laminar Boundary Layer Profiles (Evaluation Tests)

Mean velocity and temperature profile data were measured in the laminar flow upstream of boundary layer transition for the 100 fps test case of the preceding section. Profile data were obtained at three transverse positions at equal distance from the plate leading edge. These profiles, presented in Fig. 27, were obtained on the tunnel centerline and at stations 6 in to the east and west of the tunnel centerline at $x = 12$ in, $Re_x = 0.63 \times 10^6$. The measured velocity and temperature profile data agree extremely well with the laminar boundary layer profile solutions of Blasius (velocity, Ref. 15) and Levy (temperature, Ref. 25) and show negligible transverse variations. The conclusion reached from Fig. 27 is that these profile data are consistent with the wall heat transfer data of the preceding section. Both the heat transfer and profile data indicate that the test boundary layer was highly two-dimensional at that at $X = 12$ in it was still laminar.

EXPERIMENTAL RESULTS

1. Free-Stream Turbulence Distribution in the Wind Tunnel Test Section1.1 Free-Stream Turbulence Intensity Distribution

As previously described, turbulence intensity measurements were obtained with X film probes and an associated anemometry system. The U' (streamwise) and V' (vertical) components of the turbulence were measured with the X film array oriented in a plane parallel to the streamwise direction and perpendicular to the horizontal test wall. For measurements of the U' (streamwise) and W' (transverse) components the X film array was oriented in a plane parallel to the streamwise direction and parallel to the horizontal test wall. Turbulence distributions were obtained for all five tunnel turbulence configurations: (1) no turbulence grid installed (minimum turbulence level); (2)-(5) with grid Nos. 1 through 4 installed at the contraction exit. Surveys of the turbulence distributions were obtained over six planes located at the following streamwise distances from the test wall leading edge: $X = -12$ (the plane of the contraction exit), 4, 16, 40, 64, and 88 inches. For each survey plane data were obtained at 2 in. vertical intervals for the following three transverse locations: $Z = C_L$ and ± 6 in. At the contraction exit ($X = -12$ in.) where the sidewall boundary layers were still very thin these spacings resulted in a 12 point matrix of measurements for each turbulence configuration. At survey planes further downstream the extent of the freestream flow was reduced by boundary layer growth along the test section walls and the number of measurement locations was restricted accordingly. For most of the streamwise location/turbulence grid combinations, turbulence measurements were obtained at six locations.

The multi-component (U' , V' , and W') turbulence intensity distributions for the various grids are presented in Figs. 28 through 32. A composite plot showing the total turbulence intensity distributions for all five turbulence configurations is presented in Fig. 33. Prior to examining the results measured for the individual configurations, the following details common to Figs. 28 through 33 should be noted: (1) the U' (streamwise) turbulence levels plotted in these figures are the average of the U' values determined with the X probe oriented in the vertical and horizontal directions; and (2) for all three components (U' , V' , and W') of turbulence the levels plotted are the average of all values measured at that data plane. For cases when all the turbulence levels over the data plane did not fall within the plotting symbol uncertainty bars indicate the range of the measured results.

Figure 28 presents the turbulence intensity distributions measured with no turbulence generating grid installed. For this turbulence configuration a wire damping screen (0.007 in. wire, 24 mesh) was located at the plenum exit/contraction entrance. As can be seen from an examination of this figure, the turbulence

levels in the tunnel test section were $<\frac{1}{4}\%$. For applications related to internal flows and turbomachinery, $\frac{1}{4}\%$ turbulence is extremely low. Turbulent boundary layer heat transfer and profile data obtained for this "no grid" configuration can be considered as having negligible effects from the free-stream turbulence. Figure 28 indicates, as would be expected far downstream of a fine screen such as this, that all three components decay only slightly over the entire length of the test section. Also shown is that for the entire test section the streamwise component of turbulence was approximately 50% larger than both the transverse and vertical components. The relationship between the various turbulence components for this minimum turbulence configuration is believed to be the result of combined and interacting effects of the turbulence control devices in the plenum and the main tunnel contraction.

The turbulence intensity distributions measured in the tunnel test section with grids 1 through 4 installed are presented in Figs. 29 through 32. For all four grid configurations the relationship between the magnitudes of the three turbulence components in the test section was $V' > W' > U'$ with the difference between the various components decreasing with increasing distance from the grids. For grid Nos. 3 and 4 (Figs. 31 and 32) the turbulence was nearly isotropic ($U' = V' = W'$) for $X > 40$ in. The anisotropy of the turbulence in the tunnel test section results from combined effects of flow through coarse grids and the influence on the grid turbulence of the main tunnel contraction. As shown by Comte-Bellot and Corrsin (Ref. 26), lattice-type turbulence generating grids such as those used for the present study produce turbulence with $V' = W'$ and $U' \approx 5/4$ of the other components. For the present test facility (see Fig. 1) the main tunnel nozzle is located just downstream of the turbulence generating grids. Prandtl (Ref. 27) has provided a well known semiquantitative theory for predicting the influence of a contraction on the various components of turbulence. Prandtl's theory has been verified as being at least qualitatively correct by a large number of experiments (e.g., Uberoi, Ref. 28). Applying Prandtl's arguments to the present contraction shape, it would be expected that in passing through the nozzle U' would decrease ($\approx 1/\text{contraction ratio}$), and V' and W' would increase (less than the decrease in U'). Because the contraction is two-dimensional (no contraction in the W' direction), the increase of the W' component should be less than the increase of the V' component. The measured turbulence intensity levels for the various components are arranged as expected ($V' > W' > U'$). The streamwise component (U') which should have had a slightly greater intensity than the other components at the grid location was significantly reduced as the flow passed through the contraction. The vertical and transverse (V' and W') components should have been approximately equal at the grid location and as the flow passed through the contraction the V' component was increased and the W' component was slightly increased.

For all locations with grid Nos. 1 and 2 and for the far downstream locations for grid Nos. 3 and 4 the turbulence data over the various survey planes were extremely uniform with all data falling within the plotting symbols.

The largest nonuniformities in measured turbulence resulted for $X \gtrsim 20$ for grid No. 3 and for $X \gtrsim 40$ for grid No. 4. These regions are within 10 grid mesh spacings (M) from the respective grid locations. This result is in agreement with Ref. 1 which indicates that a distance of approximately 5 to 10 mesh lengths downstream of a grid are required to establish uniform flow. It should be noted here that the specific reason for locating the turbulence grids at the contraction entrance instead of at the test section entrance was to minimize turbulence nonuniformities in the test section. If the turbulence grid station had been located at the test section entrance, most of the test section would have fallen within the 5 to 10 mesh length flow establishment region and the test section turbulence would have been much less uniform.

Total turbulence distributions for the various grid configurations were calculated from the multi-component turbulence data and are presented in Fig. 33. The nonuniformity of the turbulence very near grid Nos. 3 and 4 is again evident. Figure 33 shows that the downstream decay rate of the turbulence decreased progressively with increasing distance from the grids. A quantitative comparison can be made between the present results and those of Baines and Peterson (Ref. 1) in which the decay of turbulence downstream of bar lattices was documented. Although the grid configurations of Baines and Peterson were very similar to those employed for the present study, there was one important difference in the experimental arrangement. Baines and Peterson employed a constant velocity section downstream of the turbulence grids while the present study includes the additional complexity of the tunnel contraction.

Two different methods (see Fig. 34) have been used to relate the present results to those of Ref. 1. In Fig. 34a the present turbulence intensity measurements are plotted as a function of dimensionless distance from the grid location ($X_G/\text{bar width}$). In this form the present data are seen to have a lower intensity than the data of Baines and Peterson when compared at similar locations. The turbulence decay rate, however, is identical. In this format the reduction of the turbulence level for similar distances from the grids is interpreted to be the overall effect of the contraction on the total turbulence intensity. In Fig. 34b the test section turbulence data are compared to the results of Baines and Peterson on the basis of "equivalent" turbulence decay time. The time required for the flow to pass from the grid location to the test section entrance was calculated from the known nozzle velocity distribution. If the flow is considered to have been at the test section velocity at all stations, this total flow time corresponds to a new longer "effective" distance from the grid to the measurement stations. For the present nozzle configuration this "effective" distance is $X'_G = X_G + 40$. Figure 34b shows that by plotting the present results as a function of distance from this "effective" grid location both the absolute turbulence intensity levels and the turbulence decay rate agree with the results of Ref. 1. The two different interpretations of the turbulence distributions presented in Figs. 34a and 34b are both physically reasonable. These comparisons between the data of the present study and those of Baines and Paterson indicate that there was excellent agreement between the results of the two studies.

In summary, the conclusions reached from the free-stream turbulence intensity distribution measurements are:

(1) The relationship between the three components of the free-stream turbulence measured in the test section for all four turbulence grids was $V' > W' > U'$. This anisotropy resulted from the turbulence generating grids and the specific shape of the main tunnel contraction nozzle and can be predicted using the theory of Ref. 27.

(2) The turbulence intensity measurements were very uniform over all transverse survey planes for grid Nos. 1 and 2 and for the downstream survey planes for grid Nos. 3 and 4. At the near-grid survey planes (less than 10 grid mesh lengths) for grid Nos. 3 and 4 some slight nonuniformities were detected.

(3) The turbulence intensity levels and decay rates measured for the various grids and survey locations are in excellent agreement with the results reported in Ref. 1.

1.2 Free-Stream Turbulence Length Scale Distributions

Measurements of the longitudinal integral scale of the free-stream turbulence downstream of the various turbulence grids were obtained using single sensor hot film probes and the previously described anemometer system. Integral scale measurements were obtained for the four grid configurations over the same survey plane locations as described in the previous section (Turbulence Intensity Distributions). Integral length scale growth is usually assumed to obey a power law of the form $\Lambda_f = A_i (X_\Lambda)^m$ where X_Λ is the distance from the apparent origin of the growth and A_i is a constant related to the scale of the turbulence source. A best power law fit was determined for the present data by constructing logarithmic plots with a series of assumed apparent origins and selecting the one which produced the longest straight line fits. A single apparent origin (30 in. upstream of the test wall leading edge) common to all four turbulence grids was selected. The integral scale measurements plotted as a function of distance from their apparent origin are presented in Fig. 35. For this figure the symbols are plotted at the average of the integral scale measurements obtained at each survey plane. The vertical bars indicate the range of the individual measured values. The power law exponent ($M = 0.34$) determined from these logarithmic plots is in excellent agreement with the values determined by Comte-Bellot and Corrsin in Ref. 26. The integral scale data are also presented in a composite linear plot in Fig. 36. The graphically determined growth power laws determined in Fig. 35 are included in this figure. Figure 36 clearly shows that the uncertainty in the measured data increased with increasing grid bar size. The conclusion reached from Figs. 35 and 36 is that the streamwise growth of the integral scales was in excellent agreement with the growth rate determined for a similar flow in Ref. 26.

1.3 Free-Stream Power Spectral Density Distributions

Spectral distribution data were obtained along the tunnel centerline at tunnel mid-height for the following streamwise locations: $X = -12, 4, 16, 40, 64$, and 88 in. These data were obtained using a single sensor hot-film probe and the previously described anemometer/spectrum analyzer system. Figures 37 through 40 present these measured spectral distribution data for grid Nos. 1 through 4, respectively. For all four grids the measured data were in excellent agreement with the von Karman one-dimensional spectrum (Ref. 3). This result indicates that the test section turbulence has the classic characteristics of grid generated turbulence. Note that there were no significant spikes of higher or lower contributions to the overall turbulence level from discreet or narrow frequency bands. An examination of Figs. 37 through 40 reveals that the data scatter was considerably more severe for the fine grids than for the more coarse grids, a result attributed to measurement accuracy effects. The absolute level of the electronic signals associated with the narrow band width measurements for the low turbulence configurations was much reduced from those measured for higher turbulence cases and could not be measured as precisely. The conclusion reached from the Power Spectral Density Distribution Data is that the free-stream turbulence in the tunnel test section is behaving as classic grid-generated turbulence.

2. Heat Transfer and Boundary Layer Profile Measurements

Surface heat transfer data and boundary layer mean velocity and temperature profile data were obtained for five test cases. For all five test cases there was a constant free-stream velocity of nominally 100 fps and natural transition of the test wall boundary layer. The five test cases were as follows:

1. low free-stream turbulence (1/4 percent - no grid installed)
2. turbulence generating grid No. 1 (3/16 in bars)
3. turbulence generating grid No. 2 (1/2 in bars)
4. turbulence generating grid No. 3 (1 $\frac{1}{2}$ in bars)
5. turbulence generating grid No. 4 (2 in bars)

2.1 Flow Condition 1 - Low Free-Stream Turbulence

The data obtained for flow condition 1 can be compared directly to correlations available in the open literature. In Fig. 4la the measured Stanton number distribution data, which were previously presented as part of Fig. 26, are compared with well established laminar and fully turbulent correlations. Upstream of boundary layer transition ($Re_x < 1.2 \times 10^6$, $x < 23$ in.), these data agree very well with the analytical solution of Ref. 24 for zero pressure gradient, laminar boundary layer flow with a uniform convecting heat flux wall and an unheated starting length. Downstream of $Re_x \approx 1.2 \times 10^6$ the boundary layer passed through transition. The data presented in Fig. 4la were obtained along the tunnel centerline. Stanton numbers measured at locations off the tunnel centerline indicated that for this low free-stream turbulence case the transition process was dominated by the tunnel sidewall and corner flows. Premature transition began at both test wall edges and progressively encroached on the centerline flow. From $Re_x \approx 1.8 \times 10^6$ to the downstream end of the plate the measured heat transfer data agreed within ± 2 percent with the fully turbulent correlation of Ref. 24. In Fig. 4lb skin friction coefficient measurements inferred from the mean velocity profile data are compared to the well known incompressible turbulent boundary layer skin friction law formulations of Coles (Ref. 5) and Rotta (Ref. 8). These correlations, which apply for isothermal incompressible turbulent boundary layer flow have been corrected for density variations due to wall heating using Coles' "law of corresponding stations" (Ref. 5). As can be seen from Fig. 4lb the measured skin friction coefficients are bracketed by the two correlations.

Fig. 42a presents accuracy and consistency checks calculated for the measured profile data. The momentum balance of Fig. 42a consists of a ratio of the experimentally measured terms of the two-dimensional von Karman Momentum Integral equation. Coles (Ref. 5), in a comprehensive turbulent boundary layer survey article, selected 10 studies as having produced the "best" available two dimensional profile results. A direct comparison can be made between the momentum balance results of Fig. 42a and the results from these "best available" profiles presented by Coles in Fig. 12 of Appendix A in Ref. 5. For the comparable Reynolds number range the present results deviate from an exact momentum balance approximately one-half as much as these "best" selected data. This favorable comparison indicates a high degree of flow two-dimensionality for the present experimental apparatus.

The thermal energy balance data of Fig. 42a is a ratio of the total convective heat generated per unit tunnel width upstream of any profile location to the measured thermal energy contained in the boundary layer at the location. Fig. 42a reveals that this thermal energy balance is also within approximately 5 percent of unity for all the measured profiles. The conclusion reached from Fig. 42a is that the profile data forms an accurate, consistent set and that the flow is highly two-dimensional.

The measured momentum and displacement thicknesses for the various boundary layer profiles are presented in Fig. 42b. As can be seen from an examination of this figure, there is negligible variation between profiles measured at various transverse but fixed streamwise locations on the test surface.

Finally, the transverse and streamwise pressure distributions on the test surface leading edge scoop and on the test surface itself are presented in Figs. 43 and 44 respectively. Figs. 43 and 44 indicate that both transverse and streamwise pressure gradients were negligible. The conclusion reached for Figs. 41 through 44 is that the data obtained for this low free-stream turbulence, natural transition case are in excellent agreement with classic two-dimensional correlations.

2.2 Flow Condition 2 - Turbulence Grid No. 1

The profile and heat transfer data obtained for flow condition C are presented in Figs. 45 through 48. An examination of Fig. 45a reveals that upstream of boundary layer transition the measured Stanton numbers agree very well with the analytical solution of Ref. 24 for zero pressure gradient, laminar boundary layer flow with a uniform convective heat flux wall and an unheated starting length. For Fig. 45a the location of the beginning of transition has moved considerably upstream from the location observed for the low free-stream turbulence tunnel configuration (see Fig. 41). For the low free-stream turbulence configuration (flow condition 1) boundary layer transition was observed at approximately $Re_x = 12 \times 10^5$ while for the slightly higher free-stream turbulence associated with Grid No. 1 transition moved upstream to approximately 4.2×10^5 . Downstream of the

transition zone ($Re_x > 11 \times 10^5$) the measured heat transfer distribution slightly exceeds ($\sim 2\%$) the fully turbulent correlation of Ref. 24. Note that the fully turbulent heat transfer data for the low free-stream turbulence test case 1 (Fig. 41) closely bracketed this fully turbulent correlation. An examination of Fig. 45b reveals that the measured skin friction coefficients are bracketed by the correlations of Coles and Rotta and are only slightly increased from those measured for the low free-stream turbulence test case (Fig. 41). The conclusion reached from Figs. 45a and b is that, compared with classic low free-stream turbulence correlations, only small increases of skin friction and heat transfer resulted from the relatively low levels of free-stream turbulence generated by Grid No. 1.

Figs. 46a and b indicate that for flow condition 2 the test boundary layer was two-dimensional while Figs. 47 and 48 indicate that the transverse and streamwise pressure gradients along the leading edge scoops and test wall were negligible.

2.3 Flow Condition 3 - Turbulence Grid No. 2

The profile and heat transfer data obtained for flow condition 3 are presented in Figs. 49 through 52. The turbulence generating grid (No. 2) employed for flow condition 3 was coarser than the grid employed for condition 2 above (Grid No. 1) and produced somewhat more pronounced effects. The increased free-stream turbulence levels associated with Grid No. 2 resulted in a further upstream movement of the beginning of the boundary layer transition zone to $Re_x \approx 2.4 \times 10^6$. In addition, the fully turbulent heat transfer and skin friction data were increased to slightly higher levels ($\approx 4\%$ above the minimum turbulence results) than were measured for Grid No. 1 above. The conclusion reached from Figs. 49a and b is that progressively increasing turbulent heat transfer and skin friction results as the free-stream turbulence level is raised. Figs. 50a and b indicate that for flow condition 3 the test boundary layer was two-dimensional while Figs. 51 and 52 indicate that the transverse and streamwise pressure gradients along the leading edge scoops and test wall are negligible.

2.4 Flow Condition 4 - Turbulence Grid No. 3

The profile and heat transfer data obtained for flow condition 4 are presented in Figs. 53 through 56. An examination of Fig. 53a reveals that Stanton numbers measured with this free-stream turbulence distribution were about 12 percent in excess of the low free-stream turbulence correlation of Ref. 24. Fig. 53b reveals a similar increase in measured skin friction coefficients above the classic skin friction laws for low free-stream turbulence. Figs. 54a and b indicate that for flow condition 4 the test boundary layer was two-dimensional while Figs. 55 and 56 indicate that the transverse and streamwise pressure gradients along the leading edge scoops and test wall were negligible.

2.5 Flow Condition 5 - Turbulence Grid No. 4

The profile and heat transfer data obtained for flow conditions 5 are presented in Figs. 57 through 60. An examination of Fig. 57a reveals that Stanton numbers measured with this free-stream turbulence distribution were approximately 14 percent in excess of the low free-stream turbulence correlation of Ref. 24. Figure 57b reveals a similar increase in measured skin friction coefficients above an average of the classic skin friction laws of Refs. 5 and 8 for low freestream turbulence. Figs. 58a and b indicate that for flow condition 5 the test boundary layer was two-dimensional while Figs. 59 and 60 indicate that the transverse and streamwise pressure gradients along the leading edge scoops and test wall were negligible.

2.6 Stanton Number as a Function of The Momentum Thickness Reynolds Number

Fig. 61 presents a composite plot of the local Stanton number determined for all 5 grid configurations. Each Stanton number is plotted as a function of the momentum thickness Reynolds number calculated from the profile data obtained at that location. An examination of Fig. 61 reveals that at any given Reynolds number the local Stanton numbers increase progressively and significantly with increasing coarseness of the turbulence grids.

Included for comparison with the measured data of Fig. 61 are four analytical predictions of the turbulent heat transfer. These analyses assume various relationships between the turbulent heat and momentum transfer to predict a heat transfer distribution from a prescribed skin friction distribution. The predicted distributions of Fig. 61 were all calculated using the skin friction distribution measured for the minimum free-stream turbulence configuration (no grid - see Fig. 41). As such, these predictions can only be compared directly with the heat transfer data measured for the minimum turbulence case. The four predictions presented in Fig. 61 are as follows:

1. Reynolds analogy

$$S_f = C_f / 2 \quad (49)$$

2. Prandtl's laminar sublayer-fully turbulent region solution ($Pr_t = 1$)

$$S_f = \frac{C_f / 2}{1 + 11 (C_f / 2) (Pr - 1)} ; \quad (Pr = 0.71) \quad (50)$$

3. von Karman's laminar sublayer-transition zone - fully turbulent region solution ($Pr_t = 1$)

$$S_f = \frac{C_f / 2}{1 + 5 \sqrt{C_f / 2} \left[Pr - 1 + \ln \left(\frac{5}{6} Pr + \frac{1}{6} \right) \right]} ; \quad (Pr = 0.71) \quad (51)$$

4. Jayatilleke's solution for $Pr_t \neq 1$ (Ref. 19)

$$S_t = \frac{c_f/2}{Pr_t \sqrt{2/c_f} + (Pr_t \cdot P_s)} \quad (52)$$

where

$$P_s = \frac{8.23}{Pr_t} \left[\left(\frac{Pr}{Pr_t} \right)^{3/4} - 1 \right] \left[1 - 0.28 \exp \left(-0.007 \frac{Pr}{Pr_t} \right) \right]$$

Clearly the best agreement between the various predictions and the "no grid", minimum free-stream turbulence heat transfer data resulted for the Jayatilleke solution. The prediction from this analysis agreed within about 3% with the present data for $Re_\theta > 3000$. The largest discrepancy resulted for the simplest model, the classic Reynolds' analogy. The Jayatilleke solution incorporates the results of a very large number of experiments. Because of the excellent agreement with the Jayatilleke solution, it has been concluded that the present low free-stream turbulence skin friction and heat transfer data are both self-consistent and free of anomalies.

ANALYSIS AND DISCUSSION OF RESULTS

Analyses of the mechanisms through which the free-stream turbulence could influence the turbulent boundary layer have been given by Bradshaw (Ref. 29) and McDonald and Kreskovsky (Ref. 30). Bradshaw has demonstrated that the effects of the turbulence on the skin friction, heat transfer, and velocity and temperature profiles will depend primarily upon the free-stream turbulence velocity scale and, to a secondary extent, upon the turbulence length scale. McDonald and Kreskovsky have reasoned that for low ($Re_\theta < 5000$) Reynolds number boundary layers the influence of the free-stream turbulence should also depend on the boundary layer momentum thickness Reynolds number. Dependence on the Reynolds number should vanish if $Re_\theta \geq 5000$. Combining these analyses we can write a general expression for the effects of free-stream turbulence on turbulent boundary layers.

$$\Delta(c_f, S_1, U(y), T(y)) = f \left(\frac{U_e'}{U_\tau}, \frac{\Lambda_f}{\delta}, Re_\theta \right) \quad (53)$$

Bradshaw (Ref. 29) has justified the use of the free-stream turbulence intensity ($U'/U|_e$) to replace the more cumbersome parameter U_e'/U_τ of Eqn. (53). This simpler turbulence intensity parameter will be used throughout this present data analysis. Also, it should be noted that for all existing aircraft gas turbine engines, turbine airfoil boundary layers are in the low Re_θ category ($Re_\theta < 5000$) and for most cases $Re_{\theta \max} < 3000$. For this reason particular attention has been paid during the present program to exploring the importance of the influence of Reynolds numbers in Eqn. (53).

1. Influence of Free-Stream Turbulence on Skin Friction

The ratios of the measured skin friction coefficients to the low free-stream turbulence values for the same Re_θ are presented in Fig. 62 as a function of the local free-stream turbulence intensity. Skin friction coefficients are presented for all 5 grid configurations as ratios to the mean of the Coles and Rotta low free-stream turbulence skin friction- Re_θ correlations. Also included in Fig. 62 are the results of studies by four other investigators (Refs. 31, 32, 33 and 34). The data and correlations of Fig. 62 cover wide ranges of the secondary parameters Re_θ and Λ_f/δ . The skin friction measurements of Huffman et al (Ref. 31) have been plotted using their multi-component turbulence measurements at the boundary layer edge (k in their notation) to infer free-stream total T . Integral boundary layer thickness data were not presented by Charnay et al (Ref. 32). For these data boundary layer momentum thicknesses were calculated from the measured δ_{99} values using the data correlation of Robertson and Holt (Ref. 35) for the influence of T on δ_{99}/θ . It should be noted that by using this interpretation technique, excellent agreement resulted between the low free-stream turbulence test case of Charnay et al. and the low free-stream turbulence C_f vs Re_θ correlation of Coles (Ref. 5). For the results of Meier and Kreplin (Ref. 33) and Simonich and Bradshaw (Ref. 34) the free-stream turbulence was assumed to be isotropic ($T = U'/U \times 100$).

R80-914388-12

The skin friction measurements for the present experiment exhibit the same general trend found for the earlier studies. For zero pressure gradient, turbulent boundary layer flow the skin friction coefficient is clearly correlated to the local free-stream turbulence intensity. The data of Fig. 62 exhibit considerable scatter in these coordinates suggesting possible interplay of the turbulence length scale and/or the boundary layer Reynolds number.

2. Influence of Free-Stream Turbulence on the Velocity Profiles

Sample mean velocity profile data demonstrating the effect of free-stream turbulence are presented in Figs. 63A, B and C. Each of these figures presents, in universal coordinates, a group of profiles with nearly equal Reynolds numbers but different free-stream turbulence levels. The momentum thickness Reynolds numbers are 1400, 3000, and 6000 for Figs 63A, B, and C respectively. These data indicate that the influence of the free-stream turbulence on the velocity profile is limited to the depression of the boundary layer wake. Apparently no effect of the free-stream turbulence is felt in the logarithmic region in that the profile data agree very well with the zero pressure gradient law of the wall for $30 \lesssim y^+ \lesssim 200$ for all Re_θ and turbulence combinations. This result is in agreement with the data of Refs. 31 through 34 all of which indicate negligible effects in the logarithmic region. The most dramatic evidence of influence on the wake by the free-stream turbulence can be seen in Fig. 63C. At this high Reynolds number ($Re_\theta = 6000$) a strong wake, approximately equal to the Coles equilibrium value, is observed for the minimum turbulence case. In contrast, with 4% free-stream turbulence the wake has nearly vanished.

Figs. 64 and 65 present plots of the influence of the free-stream turbulence on the boundary layer integral parameters. The effect of turbulence intensity on the kinematic shape factor at a fixed Re_θ is given in Fig. 64a. In this figure H_0 is determined from Coles (Ref. 5) low free-stream turbulence correlation. Kinematic shape factor was employed for Fig. 64a in order to eliminate the influence of the wall heating and focus on changes to the velocity profile. Also shown in Fig. 64a are the correlation of Robertson and Holt (Ref. 35) and Green's (Ref. 36) analysis of the data of Ref. 32. For the present data the change of the shape factor with free-stream turbulence agrees more closely with Green's analysis than the correlation of Ref. 35. Note that the kinematic shape factors measured in the present study for $T = 0.2\%$ were about 1% larger than would have been predicted from Coles' correlation. It is unclear if there is any evidence from the present data to support the asymptotic behavior at high turbulence levels suggested by the Robertson and Holt correlation.

Reduction of the Clauser shape parameter, G , with increasing free-stream turbulence level is indicated by the data of Fig. 64b. Note that the Clauser parameter measured for the $T = 0.2\%$ test case was slightly larger ($\approx 3\%$) than the value of 6.8 recommended by Clauser (Ref. 4) for zero pressure gradient, equilibrium, low free-stream turbulence boundary layers.

Fig. 65a presents a comparison between the present data and an analysis by Green (Ref. 36). Green, using the data of Refs. 31 and 32, determined that the influence of the free-stream turbulence on the Clauser shape parameter could be represented by

$$G = G_0 \left(1 - \frac{1}{3} \sqrt{2/c_f} \frac{u'}{U_e} \right) \quad (54)$$

where G_0 is the low free-stream turbulence equilibrium boundary layer Clauser shape parameter. The value $G_0 = 6.8$, as suggested by Clauser, was used to compute G for the present data. Green's analysis and the present results are substantially in agreement with nearly equal slopes. If the experimentally measured value of $G_0 \geq 7$ (see Fig. 64b) instead of Clauser's recommended $G_0 = 6.8$ was employed for Fig. 65a the agreement between the present data and Green's analysis could be improved.

The wake component of Coles' equilibrium, zero pressure gradient, low free-stream turbulence, universal turbulent boundary layer profile can be related to the Clauser parameter as shown in Ref. 16. A comparison of the present profile results and the Clauser-Coles profile (Fig. 65b) indicates reasonably close agreement with the increase of G with Π slightly larger for the present results.

Bradshaw, in Ref. 29, has shown that for boundary layers with the same $U_\infty \delta / \nu$ differences in wall skin friction can be inferred from changes in the profile wake strength as follows:

$$\left. \frac{c_f}{c_{f0}} \right|_{Re_\theta = \text{CONST}} = 1 - \frac{4}{\kappa} (\Pi - \Pi_0) \left(1 - \frac{1}{\kappa} \sqrt{c_{f0}/2} \right) \sqrt{c_{f0}/2} \quad (55)$$

where C_{f0} and Π_0 are the skin friction and wake strength for a boundary layer with the same Re_θ in a low free-stream turbulence flow. Changes in the skin friction have been calculated from the wake strengths measured for the present profiles using Bradshaw's analysis and are presented in Fig. 66. Both Fig. 62 and 66 present the effect of free-stream turbulence on the skin friction. For Fig. 62 the absolute values of the skin friction coefficients were determined using data from the logarithmic region of the velocity profiles. For Fig. 66 changes in skin friction were determined from changes of the profile wake strength from the low free-stream turbulence values. Figs. 62 and 66 both indicate that increases of the free-stream turbulence significantly increase the skin friction. Data correlation equations and additional comparisons for these skin friction - free-stream turbulence effects will be presented in a later section.

3. Influence of the Free-Stream Turbulence on Heat Transfer

Stanton numbers measured for the present program are presented in Fig. 67 as a function of the local free-stream turbulence intensity. This figure presents the ratio of the measured Stanton numbers to the level expected for the same Re_θ for low free-stream turbulence intensity as predicted by Jayatilleke (see Fig. 61). Also included in Fig. 67 is the correlation of Simonich and Bradshaw (Ref. 34). Both the present data and the correlation of Ref. 34 indicate that there is a significant increase in the heat transfer coefficient as the free-stream turbulence intensity increases. As with the skin friction data of Fig. 62 there is considerable scatter in the present data in these coordinates. Again this suggests the influence of the secondary variables length scale and/or Reynolds number. It should be noted that the data upon which the correlation of Ref. 34 is based show even greater scatter than the present results in these coordinates.

4. Influence of Free-Stream Turbulence on the Temperature Profiles

Figs. 68a, b, and c present sample data demonstrating the influence of the free-stream turbulence on the mean temperature profiles. These temperature profiles were obtained along with the previously presented velocity profiles (Figs. 63a, b and c) and are presented in the same order and format. It should be noted that these temperature profile data have not been forced to agree with the "temperature law of the wall". The plotted values of T^+ are calculated from the measured wall, free-stream, and profile temperatures, the inferred wall shear stress and the measured heat flux. Because so many experimentally determined quantities are incorporated into the dimensionless temperature (each with inherent inaccuracies) some slight discrepancies can be seen between the level of the data and the universal log law. Using the same format as the previously presented velocity profiles (Figs. 63a, b, and c) each figure contains a group of profiles with nearly equal Reynolds numbers but different free-stream turbulence intensities. As with the velocity profiles the temperature data indicate that the influence of the free-stream turbulence is felt only in the wake region, the logarithmic region being left unaltered. The depression of the wake component by the free-stream turbulence is clearly shown in Fig. 68c. While there is a prominent wake for $T = 0.2\%$ there is no wake in evidence for $T = 4.0\%$.

The ratio $2 St/C_f$ is commonly referred to as the Reynolds analogy factor. Fig. 69 presents two separate sets of evidence from the present program that this factor increases with increasing free-stream turbulence intensity. For Fig. 69a the measured Stanton numbers and skin friction coefficients inferred from the fits of the velocity profile data to the law of the wall are plotted as a function of free-stream turbulence intensity. Also given in Fig. 69a are three values of the Reynolds analogy factor for low free-stream turbulence turbulent boundary layers recommended by other sources as follows; (A) 1.21, Spaulding (Ref. 38), (B) 1.19, Simonich and Bradshaw (Ref. 34), and (C) 1.16, Chi (Ref. 37). Reynolds analogy factor is seen to increase with increasing free-stream turbulence level with the following expression representing the results within reasonable accuracy.

$$2S_f/C_f = 118 + 1.3 T \quad (56)$$

Simonich and Bradshaw (Ref. 34), extending an earlier analysis by Kader and Yaglom (Ref. 39), have shown that the Reynolds analogy factor can be determined from relative changes between the wake strengths of the velocity and temperature profiles. Their analysis gives the following relationship:

$$2S_f/C_f = \frac{\kappa/\kappa_\theta}{1 + \sqrt{C_f/2} \left[\frac{C_\theta \kappa_\theta - C\kappa + 2(\Pi_\theta - \Pi)}{\kappa} \right]} \quad (57)$$

where C_θ and κ_θ are coefficients in the "temperature law of the wall"

$$T^+ = \frac{1}{\kappa_\theta} \ln \gamma^+ + C_\theta$$

and Π is the wake strength of the temperature profile. In the notation of Eqn. 42 of this report

$$\kappa_\theta = \kappa / Pr_t \quad \text{and} \quad C_\theta = Pr_t (C + P_s)$$

Using the measured values of Π , Π_θ , C_f and St and assumed values of $\kappa = 0.41$, $C = 5.0$ and $P_s = -2.0$ and $Pr_t = 0.9$, the left and right hand sides of Eqn. 57 have been calculated and plotted for Fig. 69b. Agreement between the present results and the analysis of Simonich and Bradshaw is shown to be very good, generally within about 20%. It can be concluded from Fig. 69b that the "wall inferred" and "wake inferred" Reynolds analogy factors are self-consistent. This consistency in turn leads credibility to the conclusion that increases of the Reynolds analogy factor result from increased free-stream turbulence intensity.

5. Influence of Reynolds Number and/or Turbulence Length Scale

As previously discussed, the analysis of McDonald and Kreskovsky (Ref. 30) indicates that if $Re_\theta \gtrsim 5000$ the momentum thickness Reynolds number should impact upon the influence of the free-stream turbulence on turbulent boundary layers. In addition, Bradshaw (Ref. 29) has reasoned that the impact of the free-stream turbulence should reach a maximum for $\Lambda_f/\delta \approx 1$. For cases in which Λ_f/δ is either significantly larger or smaller than unity the influence of the free-stream turbulence would be expected to diminish. All the experimental data currently available on this subject, including the present work, were conducted downstream of turbulence generating grids with the effective origins of the test turbulent boundary layers located some distance downstream of the grids. With this arrangement the turbulence intensity decays while the boundary layer Reynolds number and the length scale of the turbulence grow with increasing X . All the experiments have used roughly the same experimental scale with about the same free-stream velocities. The resulting experimental data cover only a narrow range of Λ_f/δ (data range $0.2 \lesssim \Lambda_f/\delta \lesssim 1$) while most contain potential low Re_θ effects (data range $1000 \lesssim Re_\theta \lesssim 6000$). Because of this situation it is currently very difficult to separate the low Re_θ from the length scale effects. (A recent Ph.D. thesis "Effect of Free-Stream Turbulence on Turbulent Boundary Layers" by Hancock, P. E. (Ref. 40) examines length scale effects but details of this work are not yet available.) The following paragraphs present an attempt to determine the relative importance of the low Re_θ and Λ_f/δ effects.

Bradshaw (Ref. 29) has shown that the influence of free-stream turbulence on the boundary layer can be related to changes in the wake strength Π . Reynolds number dependence could be expected, then, to vanish for $Re_\theta > 5000$ where, for low free-stream turbulence, the wake strength remains constant. For $Re_\theta \sim 5000$, however, the strength of the wake in low free-stream turbulence flow is strongly dependent upon Re_θ with $\Pi = 0$ at $Re_\theta = 500$ and growing rapidly in a non-linear fashion to approximately half the high Re_θ wake strength at $Re_\theta = 1000$ (see Ref. 5). The capacity of the free-stream turbulence to influence low Re_θ boundary layers could be assumed to be related to this non-linear growth of the wake strength. Following this reasoning a correlation of the influence of the free-stream turbulence was sought using a nonlinear Re_θ dependent relationship. For Fig. 70 the skin friction vs turbulence intensity data of both the present study and four earlier experiments are presented using a simple Re_θ dependent power law relationship. Fig. 70a presents the influence of the free-stream turbulence on the skin friction for boundary layers with the same Re_θ and should be compared with Fig. 62. Fig. 70b shows the influence of the free-stream turbulence on the skin friction (inferred from changes of the wake strength) for equal Re_θ and should be compared with Fig. 66. Comparison of these 4 figures reveals that the data scatter has been significantly reduced by incorporating Re_θ dependence into the correlations. Only the correlation of Ref. 34 shows a trend significantly different from the other data sets. It is

suggested that the following relationships correlate both the present data and the data of the other experiments with reasonable accuracy.

$$c_f/c_{f0} \Big|_{Re_\theta = \text{CONST}} = 0.98 + 1.92 \left(\frac{Re_\theta}{1000} \right)^{0.4} T \quad (58)$$

$$c_f/c_{f0} \Big|_{Re_\theta = \text{CONST}} = 0.98 + 2.15 \left(\frac{Re_\theta}{1000} \right)^{0.4} T \quad (59)$$

The difference in the slopes of these suggested correlations is somewhat less than calculated by Bradshaw in Ref. 29. This result suggests that for the present data the influence of the free-stream turbulence on δ/θ was less than reported by Robertson and Holt (Ref. 35).

Hancock (Ref. 40) has recently conducted an experiment designed so that the influence of free-stream turbulence on skin friction could be examined for wide ranges of A_f/δ . Unfortunately Hancock's data was obtained for low Re_θ boundary layers and so contains low Re_θ effects. He has developed a length scale dependent correlation based upon a streamwise turbulence dissipation length scale defined as follows:

$$L_d = \frac{\left[\frac{ue}{d} \right]^{3/2}}{U \frac{d ue}{dx}} \quad (60)$$

For grid generated turbulence this dissipation scale and the longitudinal integral scale are related as

$$L_d \approx 15 A_f$$

Figure 71 presents the skin friction coefficient data of the present study plotted on Hancock's length-scale dependent coordinates (P. Hancock has kindly made this correlation available to us prior to the publication of his thesis). Agreement between the data and the suggested correlation is seen to be very good.

The scatter of the data taken in the present program is about the same for the Re_θ dependent correlation of Fig. 70 and the length scale dependent correlation of Fig. 71. All of the data used to produce these correlations contain both length scale and low Re_θ effects. Since there is no clear superiority for either of these correlations it is not possible to conclude at this time which, if either, is the more important parameter.

Figure 72 presents the heat transfer data of the present study in the same Re_θ dependent coordinates used for the skin friction results. Fig. 72 should be compared to Fig. 67 which presents the same data without regard to Re_θ . As with the skin friction data it is clear that the scatter of Fig. 72 is

considerably less than that of Fig. 67. In addition in these coordinates the heat transfer correlation of Ref. 34 agrees very well with the present data. The following relationship correlates both the present data and the data of Ref. 34 with reasonable accuracy.

$$S_t/S_{t0} \Big|_{Re_\theta = \text{CONST}} = 0.98 + 2.50 \left(\frac{Re_\theta}{1000} \right)^{0.4} T \quad (61)$$

ANALYTICAL PREDICTION OF FREE-STREAM TURBULENCE EFFECTS

1. General Statement

This section presents results of the initial phase of the effort aimed at providing an assessment of a finite difference technique for predicting free-stream turbulence effects on boundary layers. The focus to date has been on zero pressure gradient flows and the use of the McDonald et al. (Refs. 30, 42, and 43) turbulence model and boundary layer code to predict surface heating and skin friction effects. The turbulence model has been assessed in its ability to represent the direct influence of typical gas turbine free-stream turbulence levels on the forward transition process and the fully turbulent flow structure.

2. Turbulence Model

Two turbulence models presented by McDonald et al. (Refs. 30 and 42) are employed in the boundary layer code being assessed here (see Ref. 44 for a comprehensive summary of this boundary layer model and code). These are both based on the integral form of the turbulence kinetic energy equation, with the model of McDonald and Kreskovsky (Ref. 30) containing a modification of that given by McDonald and Fish (Ref. 42) to account for the approach of the turbulence level in the outer portion of the boundary layer to the local edge value.

The principle features of the turbulence model are:

1. The Reynolds stress contribution to the momentum equation shear stress level is written in terms of a mixing length as

$$\tau = \rho (\nu + \nu_T) \frac{\partial u}{\partial y} = \rho \left[\nu + l^2 \left| \frac{\partial u}{\partial y} \right| \right] \frac{\partial u}{\partial y} \quad (62)$$

2. The local mixing length, l , is taken to be a function of the local free-stream mixing length, l_∞ , through the relation

$$\frac{l}{\delta} = \mathcal{D} \left\{ \frac{l_\infty}{\delta} \left[\tanh \left[\frac{\tilde{k}y}{\delta} \frac{\delta}{l_\infty} \right] \right] + \frac{1}{2} \left[1 - \tanh \left(\frac{\tilde{k}\delta}{l_\infty} \right) \right] \left[1 - \cos \left(\frac{\pi y}{\delta_T} \right) \right] \right\} \quad (63)$$

where \mathcal{D} is a wall damping function and δ_T is a measure of the "stress thickness" defined in terms of local boundary layer properties. The above relation is only employed up to $y = \delta_T$. For $y > \delta_T$, $l = l_\infty$.

3. The local value of l_∞ is established through solution of the integral form of the turbulence kinetic energy equation. This is given as

$$\frac{d}{dx} \left[\frac{\rho_e u_e^3 \delta_r}{2 a_1} \phi_1 \right] = \rho_e u_e^3 (\phi_2 - \phi_3) + E \quad (64)$$

where

$$E \equiv q_e^2/2 \left[\rho_e u_e \frac{d\delta_r}{dx} - (\bar{\rho}v)_e \right] \quad (65)$$

$$\phi_1 = \int_0^{\delta_r/\delta_r} \frac{\rho u}{\rho_e u_e} \left[\left[\frac{l}{\delta_r} \frac{\partial (u/u_e)}{\partial \eta} \right]^2 + a_1 f(y/\delta_r) \frac{q_e^2}{u_e^2} \right] d\eta \quad (66)$$

$$\phi_2 = \int_0^{\delta_r/\delta_r} \frac{\rho}{\rho_e} \left(\frac{l}{\delta_r} \right)^2 \left[\frac{\partial (u/u_e)}{\partial \eta} \right]^2 \left[1 - \frac{l}{L} \right] d\eta \quad (67)$$

$$\phi_3 = \int_0^{\delta_r/\delta_r} \frac{\rho}{\rho_e} \left(\frac{a_2 - a_3}{a_1} \right) \left[\left[\frac{1}{\delta_r} \frac{\partial(u/u_e)}{\partial \eta} \right]^2 + a_1 f(y/\delta_r) \frac{q_e^2}{u_e^2} \right] \frac{\delta_r}{u_e} \frac{\partial u}{\partial x} d\eta \quad (68)$$

Note that the free-stream turbulence level influences these equations through the terms containing q_e defined as

$$q_e = \sqrt{\overline{U_e'}^2 + \overline{V_e'}^2 + \overline{W_e'}^2} \quad (69)$$

Throughout these studies, isotropic turbulence is assumed to be present (see Figs. 28 through 32 and Section 4.1.1 for discussion) and the free-stream turbulence level is taken from the analytical expression of Figure 34. For the case of natural transition, a constant level of turbulence is used at a level of 0.002 U_∞ , see Figure 33.

Also, in the above relation, L is a dissipation length function, a_2 and a_3 are constants, and a_1 is a variable "structural" coefficient. The important function of interest here is $f(y/\delta_r)$, defined as

$$f(y/\delta_r) = \zeta/2 \left[1 - \cos \left(\frac{\pi y}{\delta_r} \right) \right] \quad (70)$$

This function was introduced by McDonald and Kreskovsky (Ref. 30) to specify the turbulence level in the outer portions of the boundary layer. It has been constructed such that the total turbulence level equals the specified edge value q_e at $y = \delta_r$.

Taking $\zeta = 0$ gives the turbulence model of McDonald and Fish (Ref. 43) while $\zeta = 1$ produces the modified model of McDonald and Kreskovsky (Ref. 30). In the current application of the boundary layer code, numerical predictions were obtained both with $\zeta = 0$ and $\zeta = 1$.

3. Finite Difference Code

The numerical code assessed here is that discussed by McDonald et al. (Refs. 30 and 43), representing an expanded version of that technique originally developed by Mellor and Gibson (Ref. 45). The current code employs an implicit finite difference solution of the classical boundary layer equations written in a surface coordinate system. A stream function formulation is used to combine the continuity and momentum equation into a single third order partial differential equation while a total enthalpy form of the energy equation is employed to represent the thermodynamic state in terms of a second order partial differential equation.

A two point backward difference law is used to give a first order accurate representation of the longitudinal convective terms. Second order accurate differences are written for the derivatives across the boundary layer in terms of a finite-difference mesh stretched with a geometric progression. The resulting nonlinear difference equations are solved iteratively with a Gaussian elimination scheme after using quasilinearization techniques to provide accelerated convergence.

Two options for initializing the flow profiles were exercised in the present study. Solutions were either initialized in the fully-turbulent region using a version of Cole's profiles (Ref. 6) or they were set in the laminar leading edge region with transition established by the turbulence model as the solution was marched aft along the surface. It was found here that initialization in the fully turbulent region produced less satisfactory results due to a less accurate representation of the profile shape factor. Thus, in all results reported here, only solutions initiated at the laminar leading edge region are reported. The outer edge conditions were held constant at their free-stream state while the wall conditions were set by the zero slip condition along with the experimentally measured wall temperature distributions. The measured wall temperature levels are tabulated in Table 1, with the free-stream temperature set at 540°R for all calculations. These temperature distributions were numerically smoothed to eliminate spurious variations in the computed wall results due to minor experimental measurement error. A typical comparison of the measured and smoothed wall temperature distributions is presented in Fig. 73 for the case of grid number 4. The smoothing routine used was a simple 19 point polynomial fit available in most computer scientific subroutine packages and it was found completely adequate for current purposes.

The finite difference grid spacing along the length of the boundary layer development was taken at exactly the spacing of the surface thermocouples so that experimental and analytical results could be compared directly. The grid spacing and extent across the boundary layer is largely set by the code with minimal control through the input parameters. The current calculations were initiated at a distance of 0.1 ft from the leading edge using 200 mesh points to represent the initial profile. The initial profile itself is generated as a member of the laminar self similar solutions - in this case for a zero pressure gradient flow. As the solution scheme marches downstream along the surface through transition and into the fully turbulent regime, mesh points are automatically added to capture the boundary layer growth

R80-914388-12

(growing to approximately 300 points at $X = 8$ ft). It was found here that the automatic (the normal) grid generation scheme encountered difficulty when a grid packing option was implemented. By attempting to pack grid points close to the surface for high resolution, the outer edge condition was compromised and solutions were found to display anomalous variations of surface heating aft of transition. The current results were obtained with the maximum level of grid packing that allowed calculations to proceed smoothly over the entire extent of the plate.

For the current calculations, the computer time required was approximately 0.004 seconds per grid point on the Univac 1110 computer (approximately 3 minutes of CPU time to compute the length of the flat plate of 8 feet).

4. Results

Comparisons of the numerically predicted results with the experimental results of Section 4.1.2 are presented in Figures 74 through 78. In all cases the results were obtained with both the turbulence model given by McDonald and Fish (Ref. 42) as given in equation 70 with $\zeta = 0$ and that used by McDonald and Kreskovsky (Ref. 30) obtained with $\zeta = 1$.

Results for the case of minimum turbulence corresponding to the turbulence level of 0.002 of Figure 41 are given in Figures 74a and 74b. In general, the results compare well in the laminar region, encounter complications in transition, and are fair in the fully-turbulent region. The surface heat transfer levels in the laminar region ($Re_x < 10^6$) provide an excellent track of the experimental results. The predicted transition process produces heating levels slightly different than the experimental results giving rise to large errors in Stanton number due to the very low level of overheating used in this study. As Table 1 shows, the measured wall temperature difference decreases rapidly aft of the 25 inch station down to levels of 15°R . Therefore, small errors in the predicted results would be expected to be magnified in this critical region. Also, as pointed out in Section 4.2.1, this extremely long run of laminar flow experiences a three-dimensional transition process that penetrates from the side walls toward the centerline. Thus it is not surprising to see the two dimensional turbulence model encounter difficulty in accurately predicting the details of the local flow. Aft of transition, both the experimental Stanton number and skin friction distributions are reasonably well predicted especially in light of the possible residual effects of the three-dimensional transition process discussed above.

The comparisons with the experimental data for the remaining four turbulence grids are shown in Figures 75 through 78. For all of these cases, the laminar region Stanton number is predicted well while the fully turbulent Stanton number and skin friction levels are all predicted within 5% or better except for $\zeta = 0$ at the high turbulence level. Both the $\zeta = 0$ and 1 models show a steady migration of the transition process forward on the surface as the free-stream turbulence level is raised. In light of the complicated nature of this flow field, and the transition process, this good qualitative and fair quantitative prediction of the transition process is considered very encouraging.

In an attempt to provide a more general basis for assessing the current theoretical model for predicting free-stream turbulence effects, additional calculations have been made with the current code. Calculations have been performed for parameter levels typical but not duplicative of the experimental test state in order to isolate the influence of the edge turbulence level itself. To this end, flat plate solutions were obtained using the model of McDonald and Kreskovsky (Ref. 30) for a free-stream velocity of 100 ft/sec., a free-stream temperature of 540°R , and a wall temperature of 560°R . Solutions were first obtained with constant levels of edge turbulence over the extent of the plate, and then with edge turbulence varying precisely as in the cases presented above (Fig. 34).

The skin friction levels for these cases have been compared with the data base of Figure 62 in Figures 79 and 80. Here the results are again normalized in terms of the analytical prediction of zero turbulence level constant velocity skin friction at the same value of momentum thickness Reynolds number. Comparison of Figs. 79 and 80 clearly show that history effects, as felt through varying edge turbulence, have a very significant effect on the predicted skin friction levels. As shown in Figure 80, the model presented by McDonald and Kreskovsky (Ref. 30) gives very good prediction for constant velocity flows once history effects are accounted for. Conversely, Figure 79 indicates that improper accounting for history effects could lead to significant error in the skin friction prediction.

The calculated Stanton number levels on the flat plate have been presented in terms of the correlation of Figure 72 in Figure 81. Again, these results have been normalized with the analytical prediction of zero turbulence level Stanton number at the same momentum thickness Reynolds number. The results are presented in this fashion because it provides a very effective means of comparing with a wide data base. As shown in Figure 81, the current calculations consistently underpredict the observed influence of free-stream turbulence on the flat plate heating over the entire range studied. This point is more clearly delineated in Figure 82 where the predicted Reynolds analogy factor for all calculations was found to be virtually constant at a level of approximately 1.14. Thus, unlike the experimental results, there seems to be no tendency in the predictions to show any significant increase of this factor with increasing turbulence level. The overall implication of these results then is that while the turbulence model presented by McDonald and Kreskovsky (Ref. 30) does apparently well represent the momentum mechanisms for constant velocity flows, there is a significant weakness in its ability to represent the energy mechanisms in the boundary layer.

CONCLUSIONS

The conclusions reached regarding the work described above are summarized in the following paragraphs. The first task consisted of an experimental study of the influence of free-stream turbulence on fully-turbulent boundary layers in zero pressure gradient flow. Numerous data quality checks and measurements to insure data consistency were obtained during the course of this experiment. In addition, for applicable cases, comparisons were made between data obtained in the present program and the results of other workers. This in-depth examination of the present data indicates that they are of extremely high quality and free of anomalies. Analysis of the present data indicates that the heat transfer, skin friction, velocity and temperature mean profile, and free-stream turbulence data form a self-consistent set of information.

1. For zero pressure gradient, turbulent boundary layer flow the skin friction coefficient increases with increasing free-stream turbulence level. As an example, increases of approximately 14% above the low free-stream turbulence skin friction coefficient for the same Re_{θ} were measured for a turbulence intensity of 5%.
2. The Stanton number increased at a somewhat higher rate with increasing free-stream turbulence than did the skin friction. For 5% turbulence intensity the measured heat transfer coefficients were approximately 18% greater than the low free-stream turbulence values.
3. Although the above effects are primarily a function of the local free-stream turbulence intensity it has been shown that the turbulence length scale and, for $Re_{\theta} < 5000$, the momentum thickness Reynolds number also exert some influence.
4. The wake strengths of both the mean velocity and temperature profiles were shown to be significantly depressed with increasing free-stream turbulence. Changes in the skin friction and Stanton numbers have been inferred from these wake depressions using an analysis by Bradshaw. These "wake inferred" changes were shown to be consistent with the "wall inferred" changes of conclusions (1) and (2).
5. Suggested correlations for the influence of free-stream turbulence on skin friction, heat transfer and the Reynolds analogy factor can be found in the body of the report.

The second task undertaken here consisted of an assessment of a boundary layer code and turbulence model for predicting free-stream turbulence effects on flat plate heat transfer and skin friction levels. Two versions of the turbulence model have been applied to data comparisons and options in the boundary layer code operation have been exercised. From this work two conclusions can be established.

1. With regard to the turbulence model study it is clear from the comparisons given above, that the model of McDonald and Kreskovsky works reasonably well for the zero

R80-914388

pressure gradient cases studied here. This model gives good quantitative prediction of the free-stream turbulence level's influence on the fully-developed turbulent boundary layer skin friction levels, showing a steady increase with increasing turbulence. The model also provided a qualitatively realistic and quantitatively acceptable prediction of the transition process' dependence on free-stream turbulence. Both the extent and position of the process were reasonably well represented, providing a strong endorsement of this model for flat plate flows. However, with regard to the predicted heat transfer levels, the model appears to have the significant deficiency of a predicted Reynolds analogy factor with considerably less dependence on free-stream turbulence level than the existing data base.

2. With regard to the boundary layer code operation, it is felt that several code limitations have been encountered that indicate directions for future improvements.

The computer times were quite large for boundary layer calculations and it is felt that improvement could be made by a) eliminating the iterative solution loops at each station at no loss of formal accuracy, b) use of similarity type variables as suggested by Blottner (Ref. 46) and Werle and Verdon (Ref. 47) to inherently capture boundary layer growth in the computational domain, and introduction of state-of-the-art strategies for improving the establishment of the finite difference mesh across the boundary layer (see Ref. 48 for one possible new such approach).

LIST OF SYMBOLS

a_1, a_2, a_3	-	turbulence model structural coefficients
C_f	-	skin friction coefficient, $\frac{2\tau_w}{\rho U_e^2}$
c_p	-	specific heat at constant pressure
D	-	turbulence model wall damping function
E	-	turbulence kinetic energy equation source term
I	-	strip current
k	-	thermal conductivity
\tilde{k}	-	turbulence model constant
λ	-	mixing length
L	-	turbulence model dissipation length
Pr	-	molecular Prandtl number
Pr_t	-	turbulent Prandtl number, $\frac{\epsilon_m}{\epsilon_h}$
Pr_e	-	effective Prandtl number, $\frac{\epsilon_m}{\epsilon_h} = \frac{1 + \frac{\epsilon_m}{\nu}}{\frac{1}{Pr} + \frac{\epsilon_m}{\nu Pr}}$
q	-	heat flux
q_e	-	free-stream turbulence
R_{foil}	-	unit resistance of heater foil
Re_x	-	Reynolds number based on distance from leading edge
Re_θ	-	Reynolds number based on boundary layer momentum thickness
St	-	Stanton number, $\frac{h}{\rho U c_p}$
t	-	temperature
t^+	-	dimensionless temperature, $\frac{(t_w - t)}{q_w} \rho_w c_p \sqrt{\tau_w / \rho}$
U	-	velocity
U^+	-	dimensionless velocity, $\frac{U}{U_r}$

LIST OF SYMBOLS (Cont'd)

U_T	- friction velocity
W	- wake function, $\frac{u' - \frac{1}{\kappa} \ln y' + c}{\Pi}$
x	- distance from leading edge
y	- distance from wall
y^+	- dimensionless distance from wall, $\frac{y U_T}{\nu}$
α	- temperature coefficient of resistance
δ	- boundary layer thickness
δ^*	- displacement thickness, $\int_0^{\delta} \left(1 - \frac{\rho u}{\rho_e u_e}\right) dy$
δ^{**}	- energy dissipation thickness, $\int_0^{\delta} \frac{\rho u}{\rho_e u_e} \left(1 - \frac{u^2}{u_e^2}\right) dy$
δ_T	- shear stress layer thickness
δ_H	- enthalpy thickness, $\int_0^{\delta_1} \frac{\rho u}{\rho_e u_e} \left(\frac{T - T_e}{T_e}\right) dy$
δ_r	- reference thickness
ϵ	- surface emissivity
ϵ_h	- coefficient of eddy diffusivity of heat
ϵ_{h_e}	- coefficient of effective thermal diffusivity
ϵ_m	- coefficient of eddy diffusivity of momentum
ϵ_{m_e}	- coefficient of effective viscosity
ζ	- selection code for use in Eq. 70
η	- y/δ_r
θ	- momentum thickness, $\int_0^{\delta} \frac{\rho u}{\rho_e u_e} \left(1 - \frac{u}{u_e}\right) dy$
κ	- von Karman constant
μ	- molecular viscosity
ν	- kinematic viscosity

LIST OF SYMBOLS (Cont'd)

ξ	-	unheated starting length
Π	-	wake strength
ρ	-	fluid density
τ	-	shearing stress
τ_t	-	turbulent shearing stress
ϕ_1, ϕ_2, ϕ_3	-	turbulence energy integrals

Subscripts

e	-	freestream
w	-	wall
T	-	turbulent

REFERENCES

1. Baines, W. D. and E. G. Peterson: An Investigation of Flow Through Screens. Trans. of ASME, Vol. 73, pp. 467-480, July 1951.
2. Blackwell, B. F. and R. J. Moffat: Design and Conduction of a Low Velocity Boundary-Layer Temperature Probe, AIAA Paper No. 74-709, ASME Paper No. 74-HT-29, July 1974.
3. Hinze, J. O.: Turbulence. McGraw-Hill, New York, 1959.
4. Clauser, F. H.: The Turbulent Boundary Layer, Advances in Applied Mechanics, Vol. IV, 1956.
5. Coles, D. E.: The Turbulent Boundary Layer in a Compressible Fluid, Rand Report, R-403-PR, 1962.
6. Coles, D. E.: The Law of the Wake in the Turbulent Boundary Layer, JFM, Vol. 1, 1956.
7. Schubauer, G. B. and Tchen, C. M.: "Turbulent Flow" in Turbulent Flows and Heat Transfer, High Speed Aerodynamics and Jet Propulsion, Vol. 5, Princeton University Press, Princeton, N. J., 1959.
8. Rotta, J. C.: Turbulent Boundary Layers in Incompressible Flow, Progress in Aeronautical Sciences, Vol. 2, Pergamon Press Ltd., London, 1962.
9. Blom, J.: An Experimental Determination of the Turbulent Prandtl Number in a Developing Temperature Boundary Layer, Ph.D. Thesis, Technological University, Eindhoven, The Netherlands, 1970.
10. Deissler, R. G.: Heat Transfer and Fluid Friction for Fully Developed Turbulent Flow of Air and Supercritical Water With Variable Fluid Properties, Trans. ASME 76, 1954.
11. Bradshaw, P.: An Introduction to Turbulence and Its Me^{sure}ment. Pergamon Press Ltd., Oxford, 1971.
12. McDonald, H.: The Effect of Pressure Gradient in the Law of the Wall in Turbulent Flow, JFM, 35, 1969.
13. Burton, R. A.: A Simple Universal Velocity Profile Equation, AIAA Journal 3, 1965.
14. Millikan, C. G.: A Critical Discussion of the Turbulent Flows in Channels and Circular Tubes, Proc. Fifth Intern. Congress Appl. Mech., Cambridge, MA, 1938.

15. Schlichting, H.: Boundary Layer Theory, 6th Edition, McGraw-Hill Book Company, New York, pp. 125-133 and 544-556, 1968.
16. Coles, D.: Proceedings, Computations of Turbulent Boundary Layers - 1965, AFOSR-IFP, Stanford Conference, Vol. II, 1968.
17. von Karman, T.: The Analogy Between Fluid Friction and Heat Transfer, Trans. ASME 61, 1939.
18. Spaulding, D. B.: A Single Formula for the Law of the Wall, J. Appl. Mech., 28, 1961.
19. Jayatilleke, C. L. V.: The Influence of Prandtl Number and Surface Roughness on the Resistance of the Laminar Sublayer to Momentum and Heat Transfer, Progress in Heat and Mass Transfer, Vol. 1, Pergamon Press Ltd., London, 1969.
20. MacMillan, F. A.: Viscous Effects in Flattened Pitot Tubes at Low Speeds, Journal of Royal Aeronautical Society, Vol. 58, 1954.
21. Quarmby, A. and H. K. Das: Displacement Effects on Pitot Tubes With Rectangular Mouths, The Aeronautical Quarterly, May 1969.
22. MacMillan, F. A.: Experiments in Pitot Tubes in Shear Flow, A.R.C. R&M 3028, 1957.
23. Hama, F. R.: Boundary-Layer Characteristics for Smooth and Rough Surfaces, Trans. Soc. Naval Architects Marine Engrs. 62, 1954.
24. Kays, W. M.: Convective Heat and Mass Transfer. McGraw-Hill Book Company, N. Y., pp. 222 and 244, 1966.
25. Levy, S.: Heat Transfer to Constant-Property Laminar Boundary-Layer Flows with Power-Function Free-Stream Velocity and Wall-Temperature Variation, J. Aeronautical Sciences, Vol. 19, pp. 341, 1952.
26. Comte-Bellot, G. and S. Corrsin: The Use of a Contraction to Improve Isotropy of Grid Generated Turbulence. J. Fluid Mech., Vol. 25, 1966, pp. 657-682.
27. Prandtl, L.: Attaining a Steady Air Stream in Wind Tunnels. NACA TM 726, 1933.
28. Uberoi, M. S.: Effect of Wind-Tunnel Contraction on Free-Stream Turbulence. J. of Aeronautical Sci., August 1956.
29. Bradshaw, P.: Effect of Free-Stream Turbulence on Turbulent Shear Layers. ARC, Paper 35648, 1974.

30. McDonald, H. and Kreskovsky, J. P.: Effect of Free-Stream Turbulence on the Turbulent Boundary Layer, *Int. J. of Heat and Mass Transfer*, Vol. 17, 1974.
31. Huffman, G. D., D. R. Zimmerman, and W. A. Bennet: The Effect of Free-Stream Turbulence Level in Turbulent Boundary Layer Behavior. *AGARD AG164*, pp. 91-115, 1972.
32. Charnay, G., G. Compte-Bellot, and J. Mathiew: Development of a Turbulent Boundary Layer on a Flat Plate in an External Turbulent Flow, *AGARD, CP 93*, Paper No. 27, 1971.
33. Meier, H. V. and Kreplin, H. P.: Influence of Freestream Turbulence on Boundary Layer Development. *AIAA Journal*, Vol. 18, No. 1, January 1980.
34. Simonich, J. C. and Bradshaw, P.: Effect of Free-Stream Turbulence on Heat Transfer through a Turbulent Boundary Layer. *ASME Journal of Heat Transfer*, Vol. 100, No. 4, November 1978.
35. Robertson, J. M. and Holt, C. F.: Stream Turbulence Effects on Turbulent Boundary Layers. *J. Hydraulics Div., Proc. ASCE*, Vol. 98, HY6, 1972.
36. Green, J. E.: On the Influence of Free-Stream Turbulence on a Turbulent Boundary Layer, as it relates to Wind Tunnel Testing at Subsonic Speeds, *AGARD Report 602*, 1973.
37. Chi, S. W.: Friction and Heat Transfer in a Compressible Turbulent Boundary Layer on a Smooth Flat Plate, Ph.D. Thesis, Imperial College, University of London, 1965.
38. Spaulding, D. B.: Contribution to the Theory of Heat Transfer Across a Turbulent Boundary Layer, *Int. J. Heat and Mass Transfer*, Vol. 7, 1964.
39. Kader, B. A. and Yaglom, A. M.: Heat and Mass Transfer Laws for Fully Turbulent Wall Flows, *Int. J. Heat and Mass Transfer*, Vol. 15, 1972.
40. Hancock, P. E.: Effect of Free-Stream Turbulence on Turbulent Boundary Layers. Ph.D. thesis, Imperial College, London University, 1980.
41. Scharnhorst, R. K., Walker, J. D. A. and Abbot, D. E.: Comparison of Theoretical Profiles for a Two-Dimensional Time-Mean Turbulent Boundary Layer with Experimental Data, *Purdue Univ. Tech Report CFMTR-77-1*, June 1977, also AFOSR TR-77-0877.
42. McDonald, H. and Fish, R. W.: Practical Calculations of Transitional Boundary Layers, *Inter. J. of Heat and Mass Transfer*, Vol. 16, No. 9, pp. 1729-1744, September 1973.

43. McDonald, H. and Camarata, F. J.: An Extended Mixing Length Approach for Computing the Turbulent Boundary Layer Development, appearing in Proceeding of the AFOSR-IFP-Stanford Conference on Turbulent Boundary Layer Prediction, Stanford, California 1968.
44. Walker, J. D. A., and Werle, M. J.: Summary and Critique of a Turbulence Model for Free Stream Turbulence Effects on Boundary Layer Characteristics, UTRC Report in preparation, 1980.
45. Mellor, G. L. and Gibson, D. M.: Equilibrium Turbulent Boundary Layers, *Journal of Fluid Mechanics*, Vol. 24, p. 255, 1966.
46. Blottner, F. G.: Finite Difference Methods of Solution of the Boundary Layer Equations, *AIAA J.*, Vol. 8, No. 2, pp. 193-205, February 1970.
47. Werle, M. J. and Verdon, J. M.: Viscid/Inviscid Interaction Analysis for Symmetric Trailing Edges, United Technologies Research Center, Report R79-914493-5, East Hartford, CT, January 1980.
48. Carter, J. E., Edwards, D. E. and Werle, M. J.: A New Coordinate Transformation for Turbulent Boundary Layer Flows, paper to be presented at the NASA Workshop on Numerical Grid Generation Techniques for Partial Differential Equations, October 1980, NASA Langley Research Center, Hampton, Virginia.

Table I
Measured Wall Temperature Distributions

X (inches)	No Grid	T _{WALL} - T _E (°K)			
		Grid #1	Grid #2	Grid #3	Grid #4
2.19	9.32	14.68	14.50	10.46	9.87
2.69	12.46	19.16	18.50	12.95	11.50
3.19	14.35	21.91	20.85	13.21	12.28
3.69	16.35	25.36	23.71	13.61	12.61
4.19	18.30	27.19	26.03	13.39	12.63
4.69	19.56	29.22	26.91	13.72	12.94
5.19	21.00	31.58	28.02	14.06	13.34
5.69	22.22	33.96	27.13	14.28	13.61
6.19	23.77	35.06	27.13	14.28	13.70
6.69	24.32	36.71	24.92	14.39	14.27
7.19	26.09	38.09	23.82	14.72	14.59
8.19	27.76	38.80	20.49	15.39	14.27
9.19	28.82	40.56	18.28	15.08	14.67
10.19	29.77	39.02	17.17	15.39	14.87
11.19	31.39	37.92		15.61	15.61
13.19	33.93	31.09	17.57	16.85	16.40
15.19	36.35	24.69	17.78	16.88	16.36
17.19	38.86	21.60	18.50	17.29	17.42
19.19	41.22	19.83	19.16	17.97	17.75
21.19	42.34	19.16	19.17	17.96	17.91
23.19	43.71	19.53	19.46	18.27	18.12
25.19	42.17	20.49	20.10	18.85	18.93
27.19	33.82	20.82	21.05	19.38	19.26
29.19	23.22	21.23	20.94	19.73	19.86
31.19	18.12	21.52	21.46	19.67	19.52
33.19	15.90	21.82	21.83	20.53	20.26
35.19	15.01	22.11	21.97	20.71	20.19
37.19	15.23	22.26	22.36	20.93	20.89
39.19	15.01	21.82	21.83	20.12	20.19
41.19	15.06	22.73	22.54	21.00	21.15
43.19	15.31	22.85	22.93	21.07	20.93
46.19	15.46	23.01	23.02	21.59	21.24
49.19	15.75	23.37	23.67	22.18	21.66
52.19	15.63	23.50	23.68	21.99	21.67
55.19	15.79	24.10	24.26	22.25	21.81
58.19	15.90	24.03	24.39	22.39	21.95
61.19	16.34	24.32	24.70	22.48	22.33
64.19	16.71	24.47	24.66	22.78	22.46
67.19	16.57	24.91	25.07	22.28	22.77
70.19	16.57	25.27	25.10	23.23	22.83
73.19	16.71	24.91	24.92	22.99	22.40
76.19	16.56	24.84	25.00	22.98	22.62
79.19	16.86	25.14	25.07	22.92	22.55
82.19	16.70	25.09	24.92	22.83	22.61
85.19	16.94	25.28	25.29	23.21	22.77
88.19	17.04	25.14	25.18	23.51	23.07
91.19	17.04	26.02	25.66	23.95	23.50
94.19	17.36	25.71	26.03	23.98	23.63

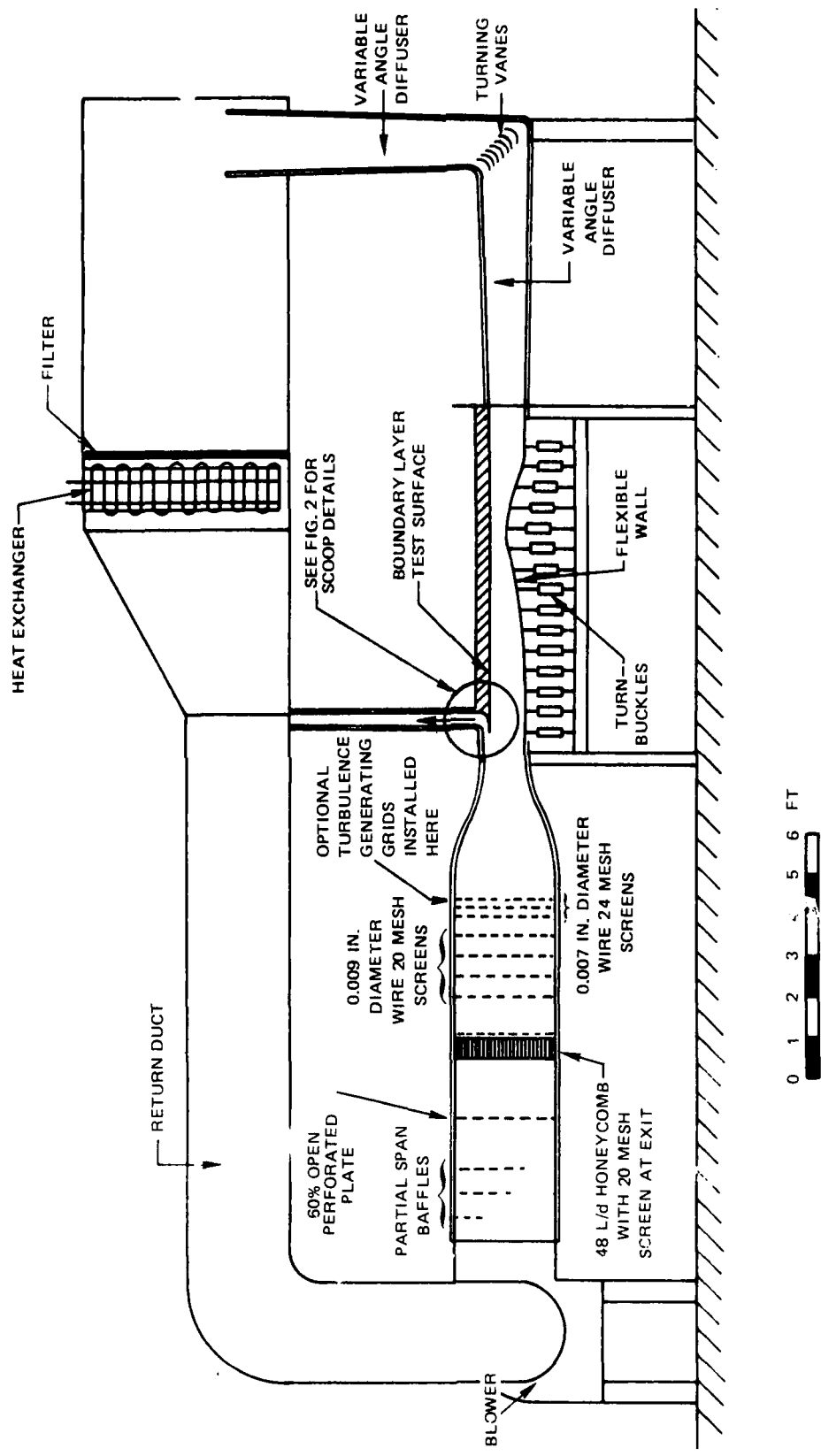


Figure 1. United Technologies Research Center Boundary Layer Wind Tunnel

R80-914388-12

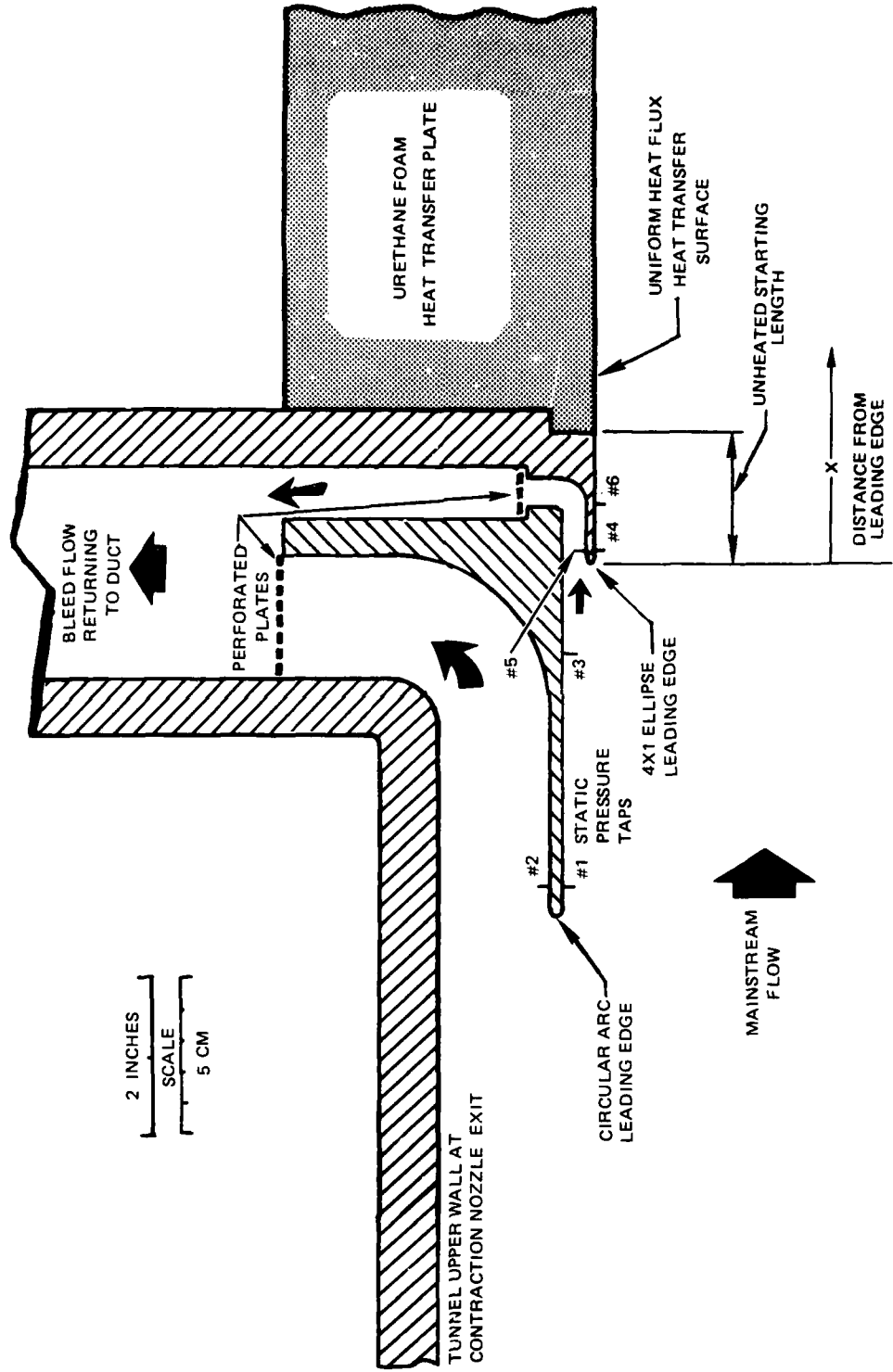
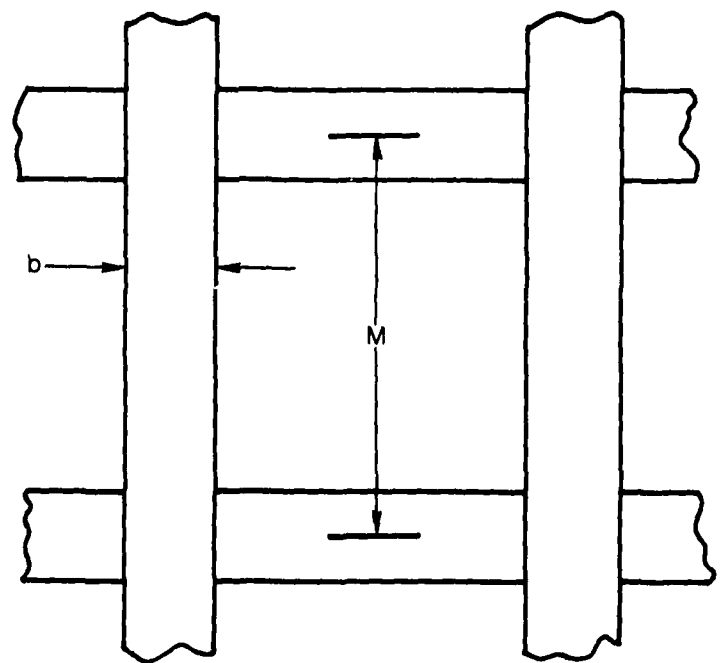


Figure 2. Detailed Sketch of Test Wall Leading Edge Bleed Scoop

78-09-102-1

R80-914388-12

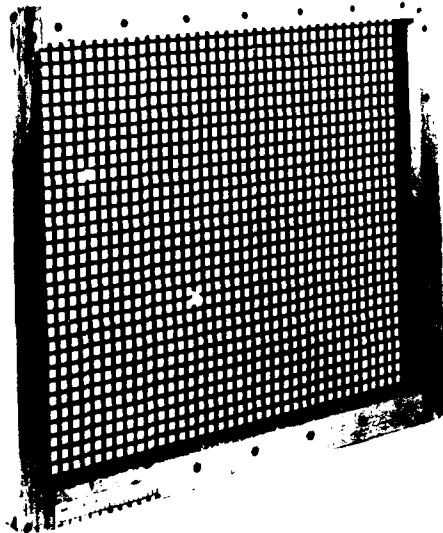


GRID NUMBER	b (inches)	M (inches)	t (inches)	M/b	% OPEN AREA
1	3/16	7/8	3/16	4.67	62
2	1/2	2 9/16	3/8	5.13	65
3	1 1/2	7	1/2	4.67	62
4	2	9	1/2	4.50	61

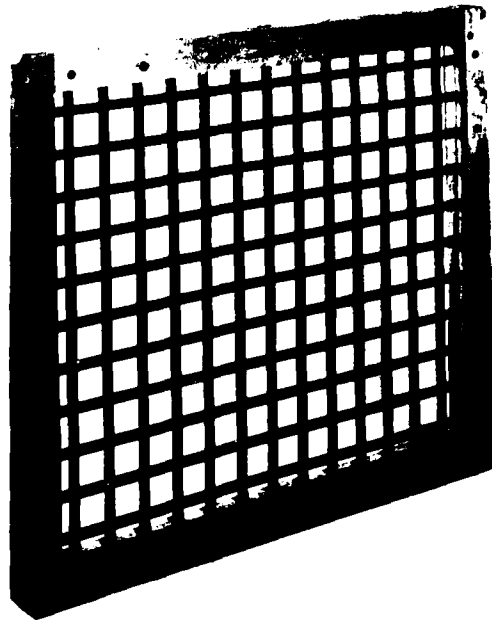
Figure 3. Turbulence Generating Grid Configurations for the Boundary Layer Wind Tunnel

R80-914388-12

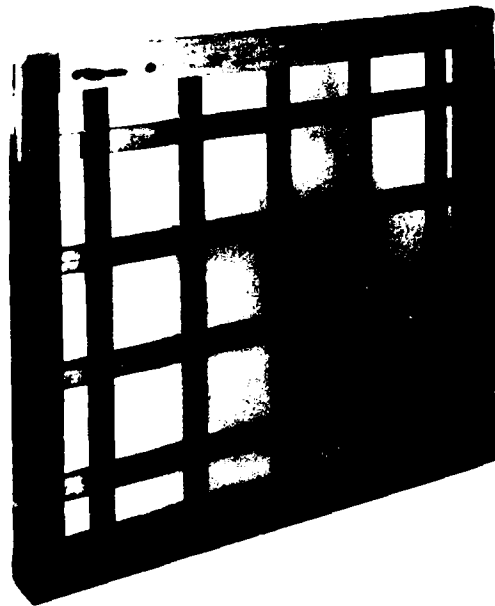
GRID NUMBER 1



GRID NUMBER 2



GRID NUMBER 3



GRID NUMBER 4

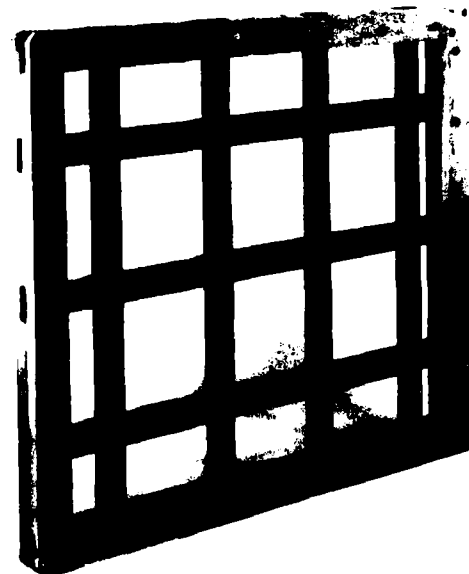


Figure 4. Photographs of Turbulence Generating Grids For The Boundary Layer Wind Tunnel

R80-914388-12

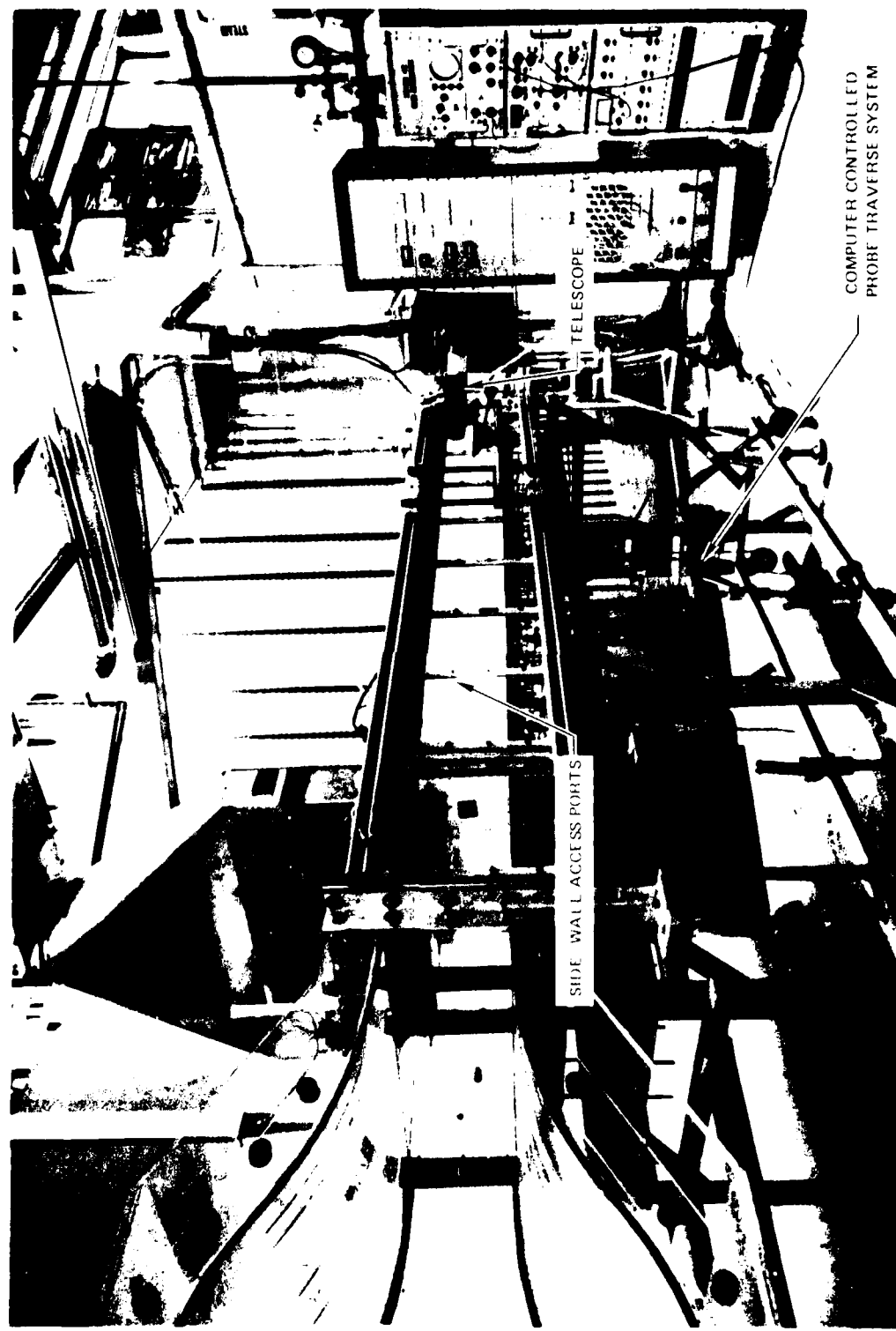


Figure 5. Photograph of UTRC Boundary Layer Wind Tunnel Test Section

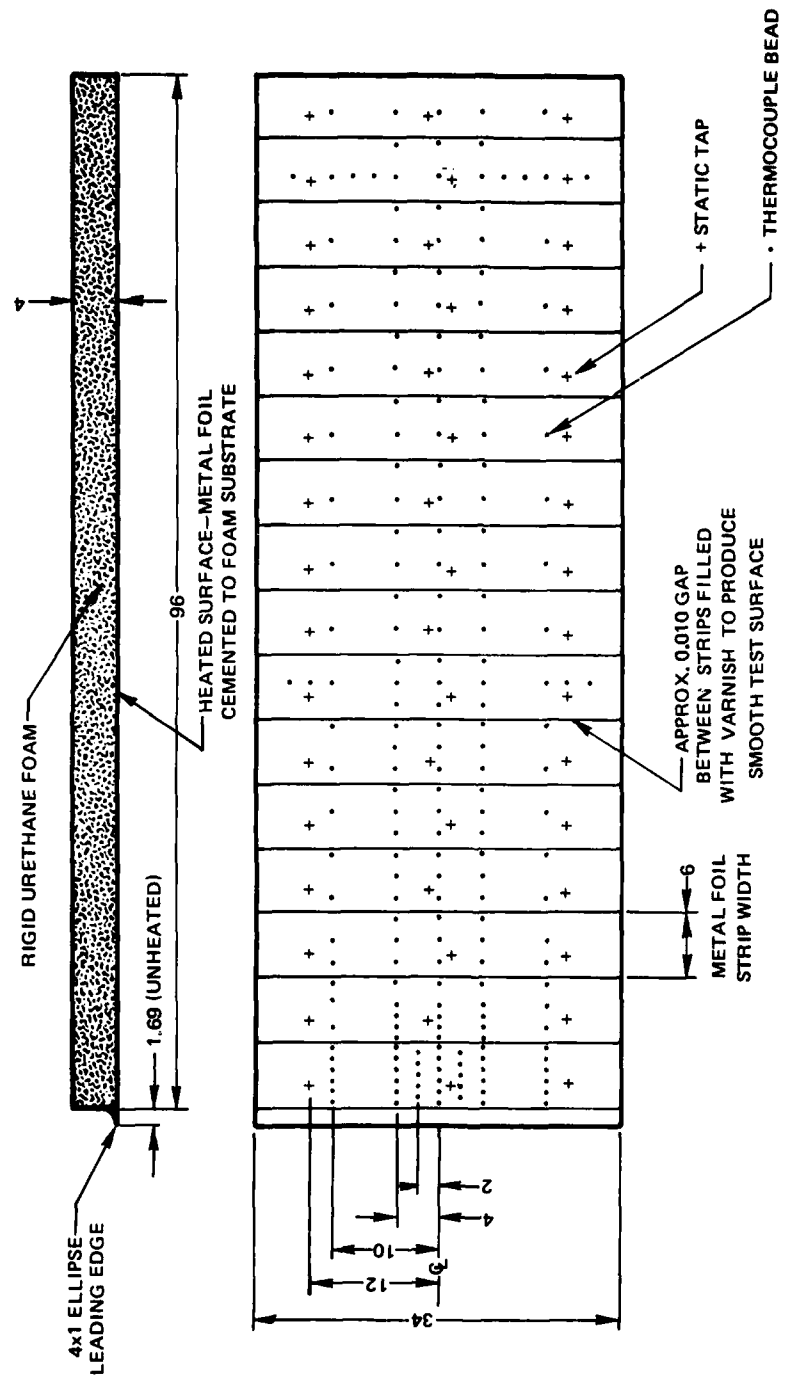
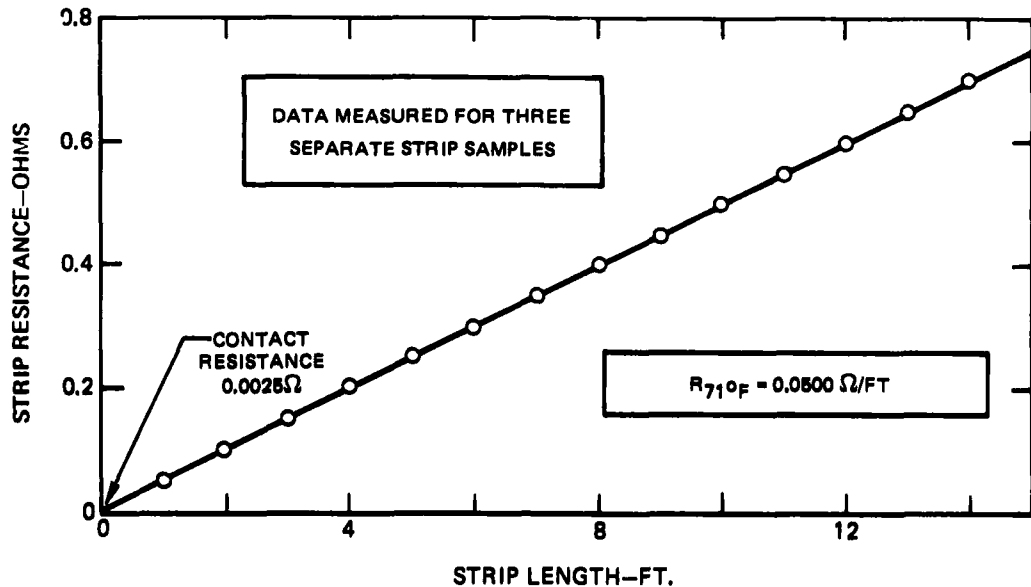
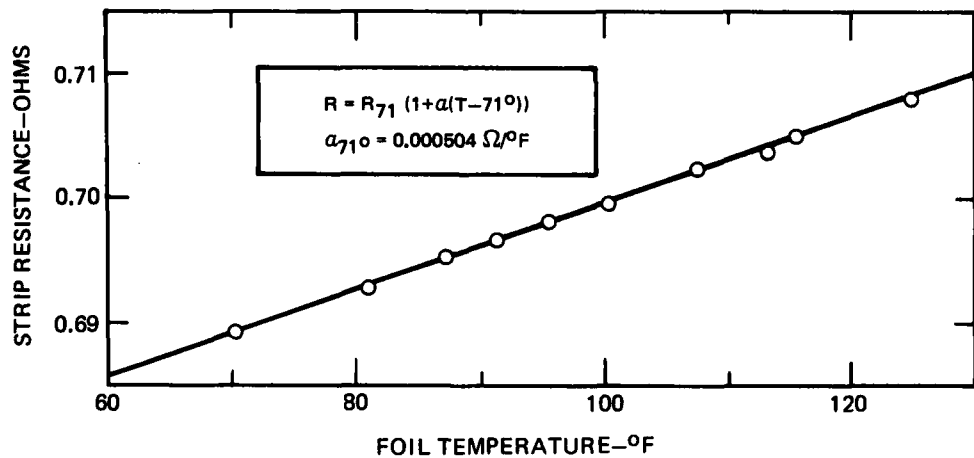


Figure 6. Instrumentation Diagram for the Uniform Heat Flux Flat Wall Model

a. 316 STAINLESS STEEL FOIL RESISTANCE AT 71°F 

b. 316 STAINLESS STEEL FOIL TEMPERATURE RESISTANCE COEFFICIENT

Figure 7. Electrical Resistance Characteristics of the 316 Stainless Steel Foil Strip Used for the Heated Test Surface of the Uniform Heat Flux Flat Wall Model

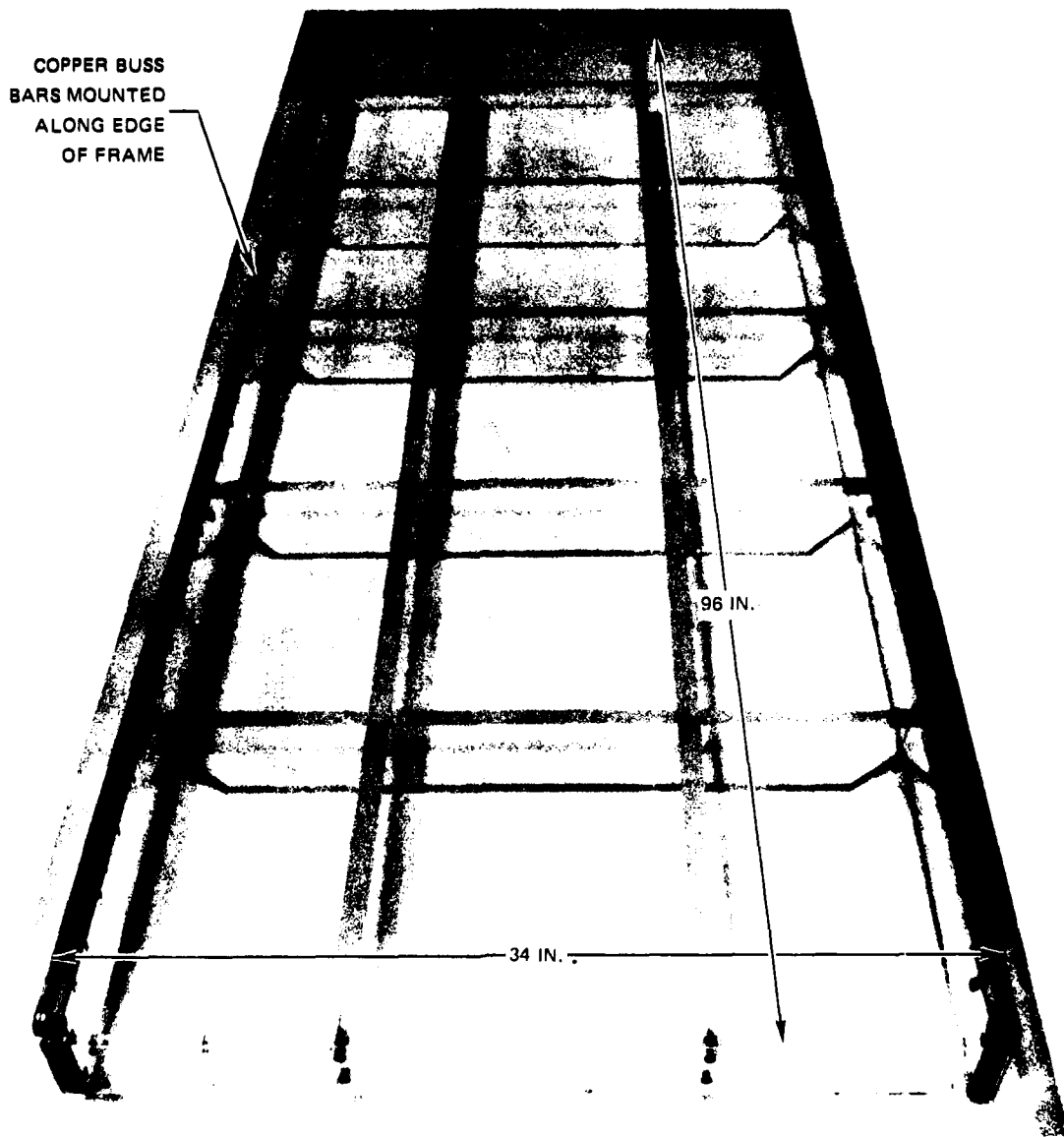


Figure 8. Photograph of the Assembled Plexiglas Frame for the Uniform Heat Flux Flat Wall Model with the Buss Bars Installed

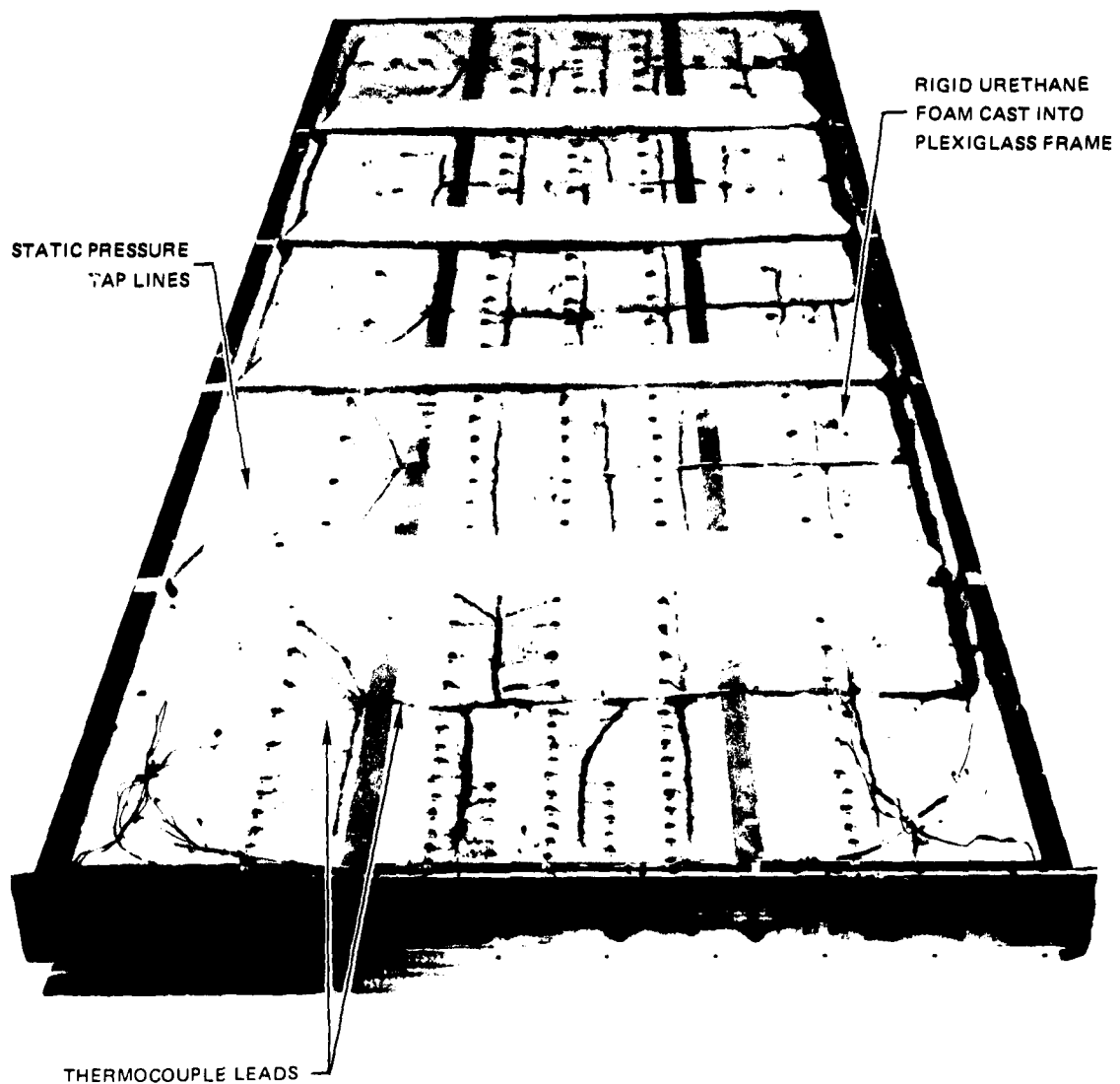


Figure 9. Photograph of the Backside of the Completely Assembled and Instrumented Uniform Heat Flux Flat Wall Model Showing the Routing of the Instrumentation Leads

R80-914388-12

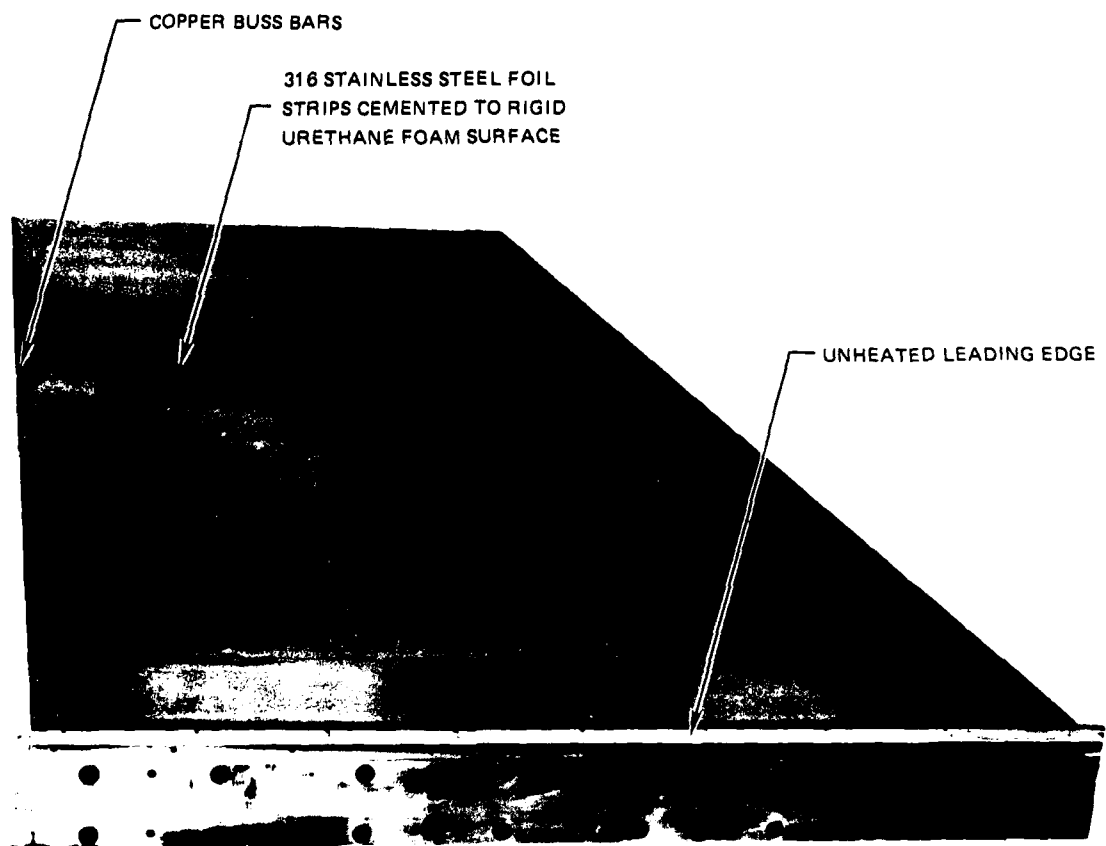
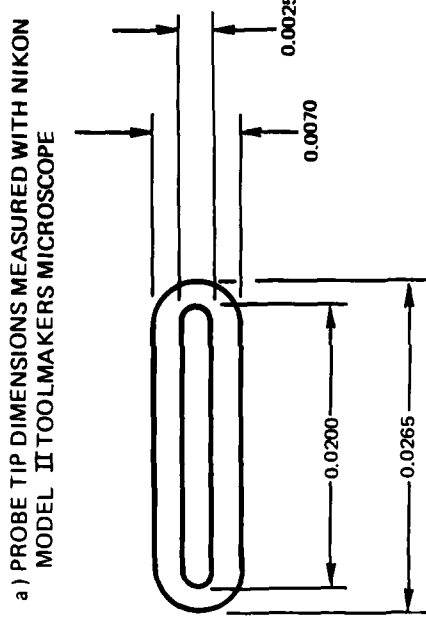
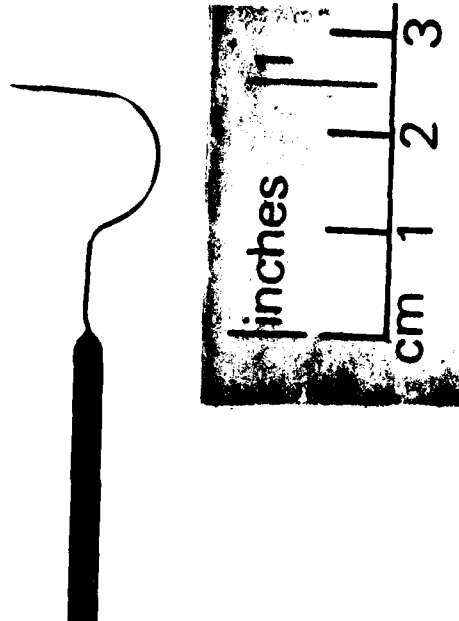


Figure 10. Photograph of Test Surface of the Uniform Heat Flux Flat Wall Model Prior to Coating with High Emissivity Paint

R80-914388-12



b) SIDE VIEW PHOTOGRAPH OF PROBE



c) MAGNIFIED VIEWS OF PROBE TIP USING JONES AND LAMSON
MODEL PC 14 SHADOWGRAPH

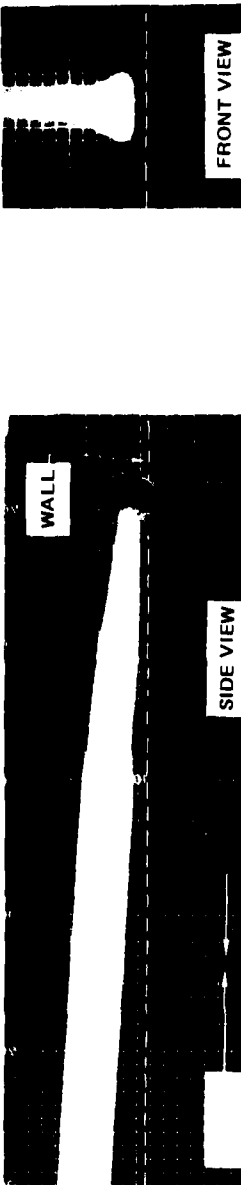
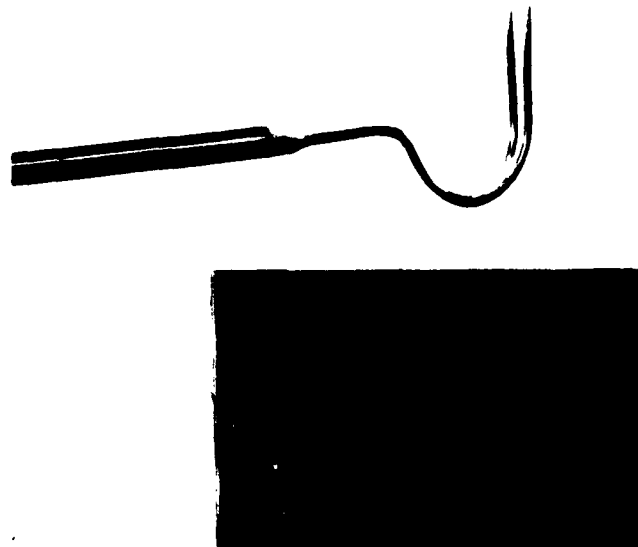
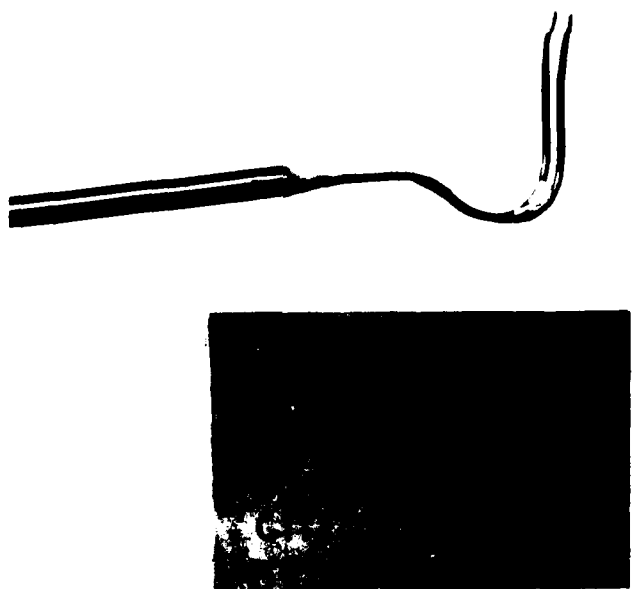


Figure 11. Typical Boundary Layer Pitot Probe Details

R80-914388-12



a) TEMPERATURE PROBE NO. 1



b) TEMPERATURE PROBE NO. 2

Figure 12. Typical Boundary Layer Thermocouple Probes

R80-914388-12

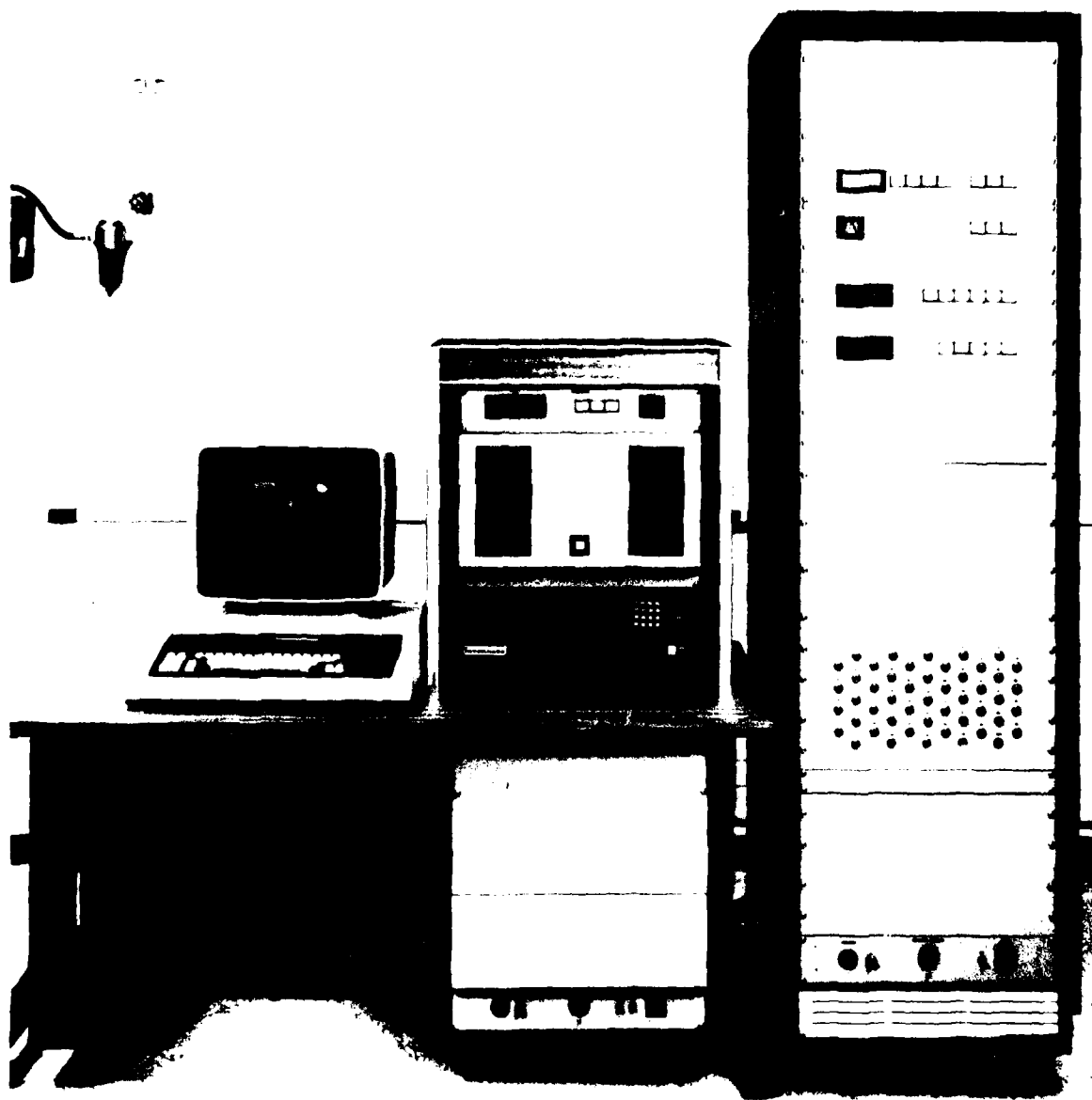


Figure 13. UTRC Boundary Layer Wind Tunnel Data Acquisition System

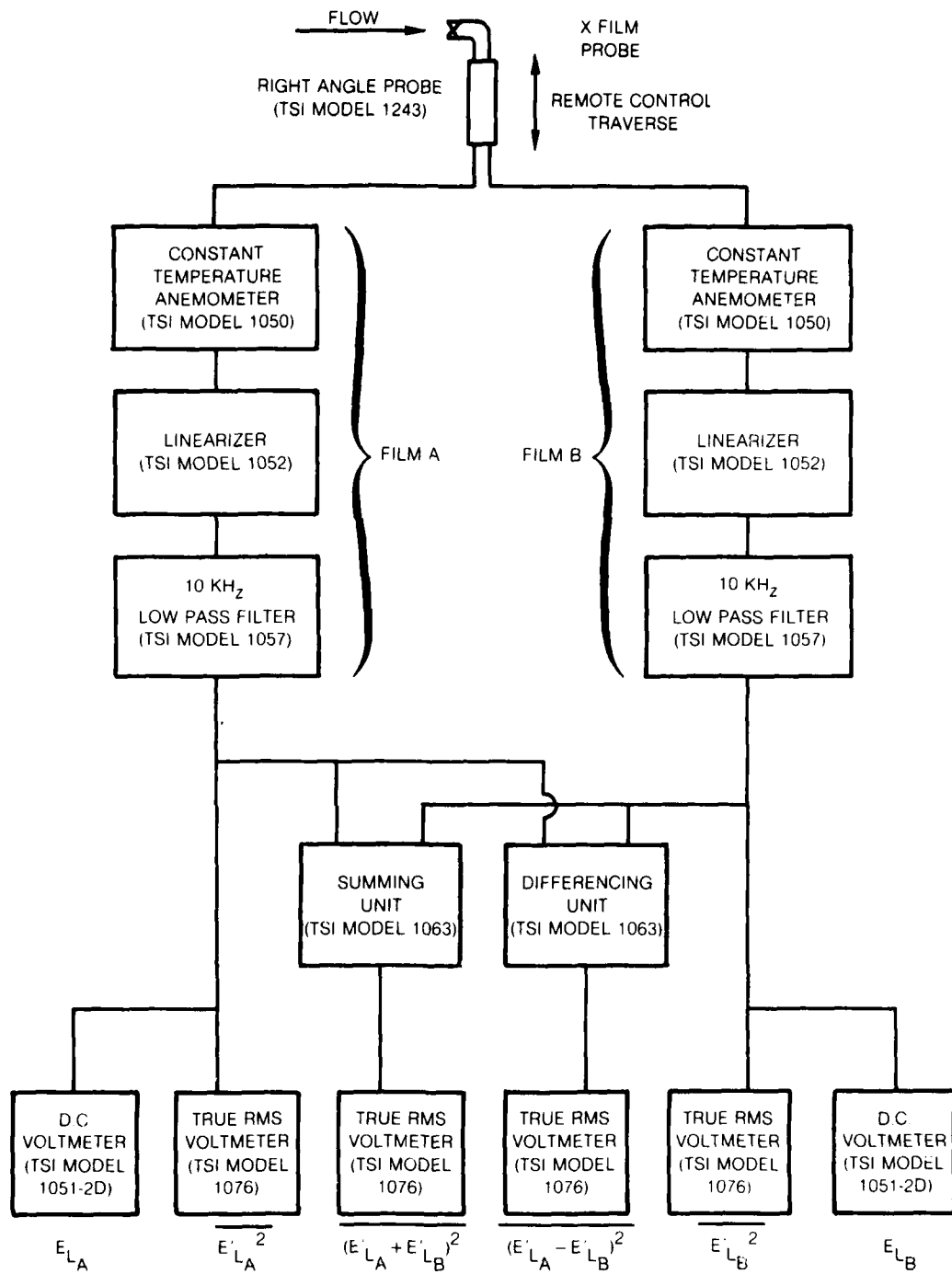


Figure 14. Block Diagram of Instrumentation Arrangement for Obtaining Multi-component Turbulence Measurements

AD-A101 094

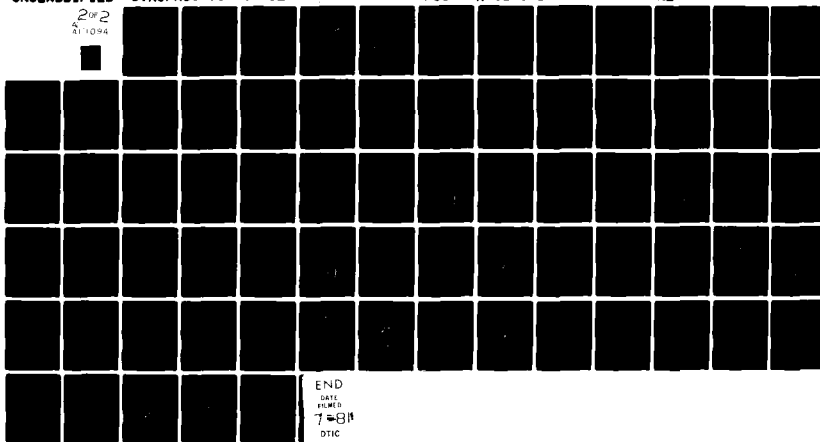
UNITED TECHNOLOGIES RESEARCH CENTER EAST HARTFORD CONN F/6 20/4
THE INFLUENCE OF FREE-STREAM TURBULENCE ON THE ZERO PRESSURE GR-ETC(U)
SEP 80 M F BLAIR, M J WERLE F49620-78-C-0064

UNCLASSIFIED

2 OF 2
A1094

AFOSR-TR-81-0514

NL



END
DATE FILMED
7-81
DTIC

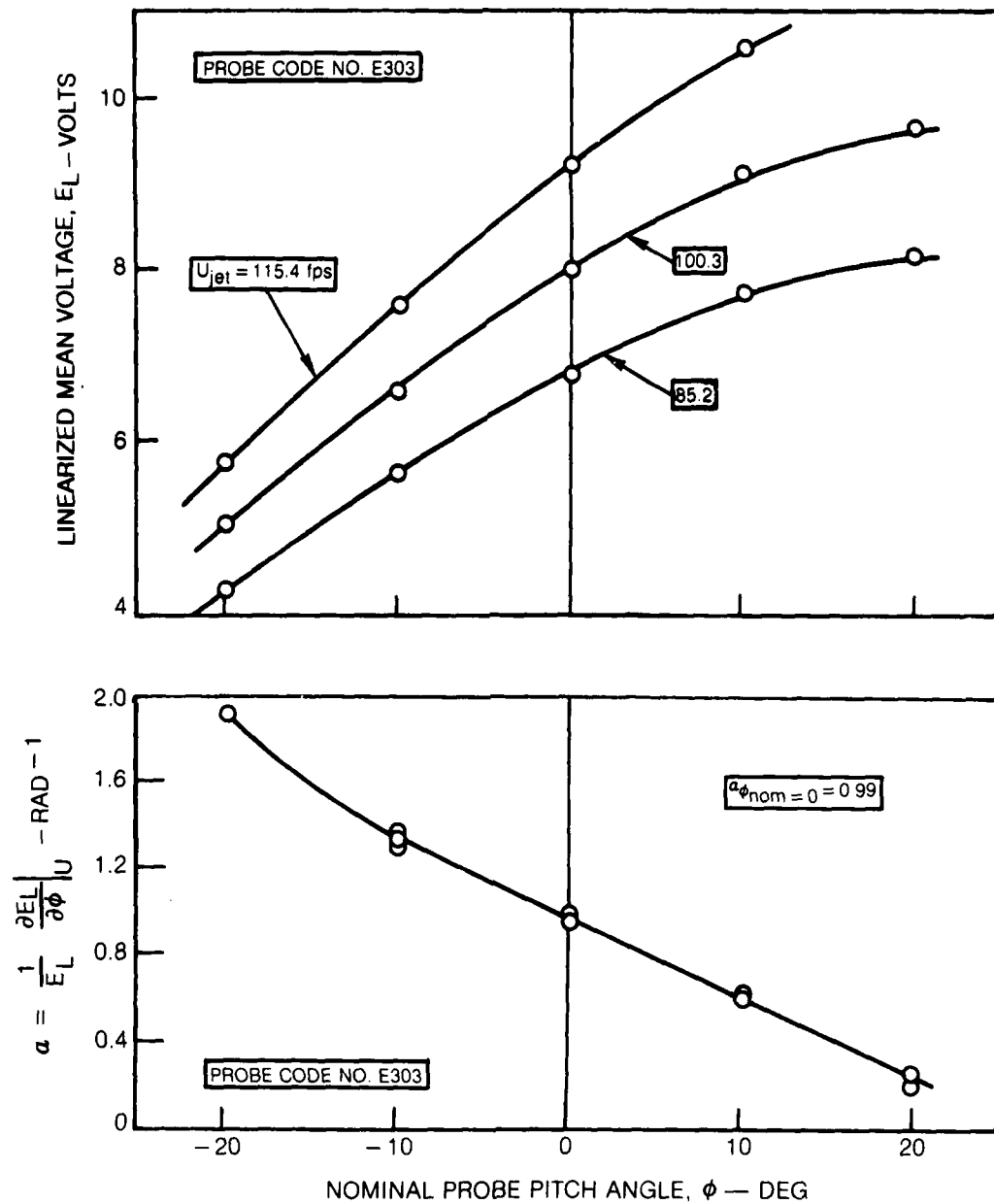


Figure 15. Sample Calibration Curves for an X Hot-Film Probe

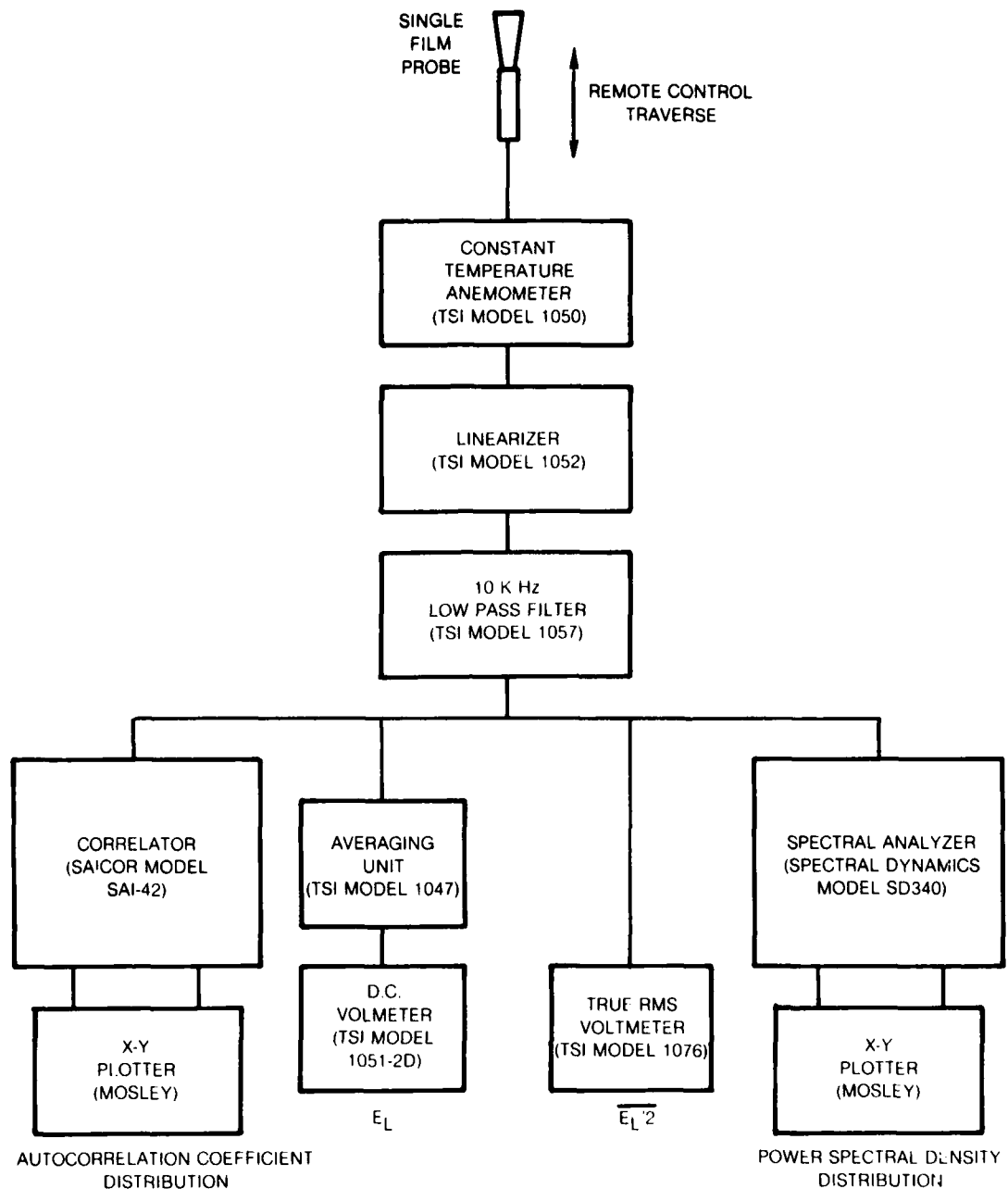


Figure 16. Block Diagram of Instrumentation Arrangement for Obtaining Length Scale and Spectral Distribution Data.

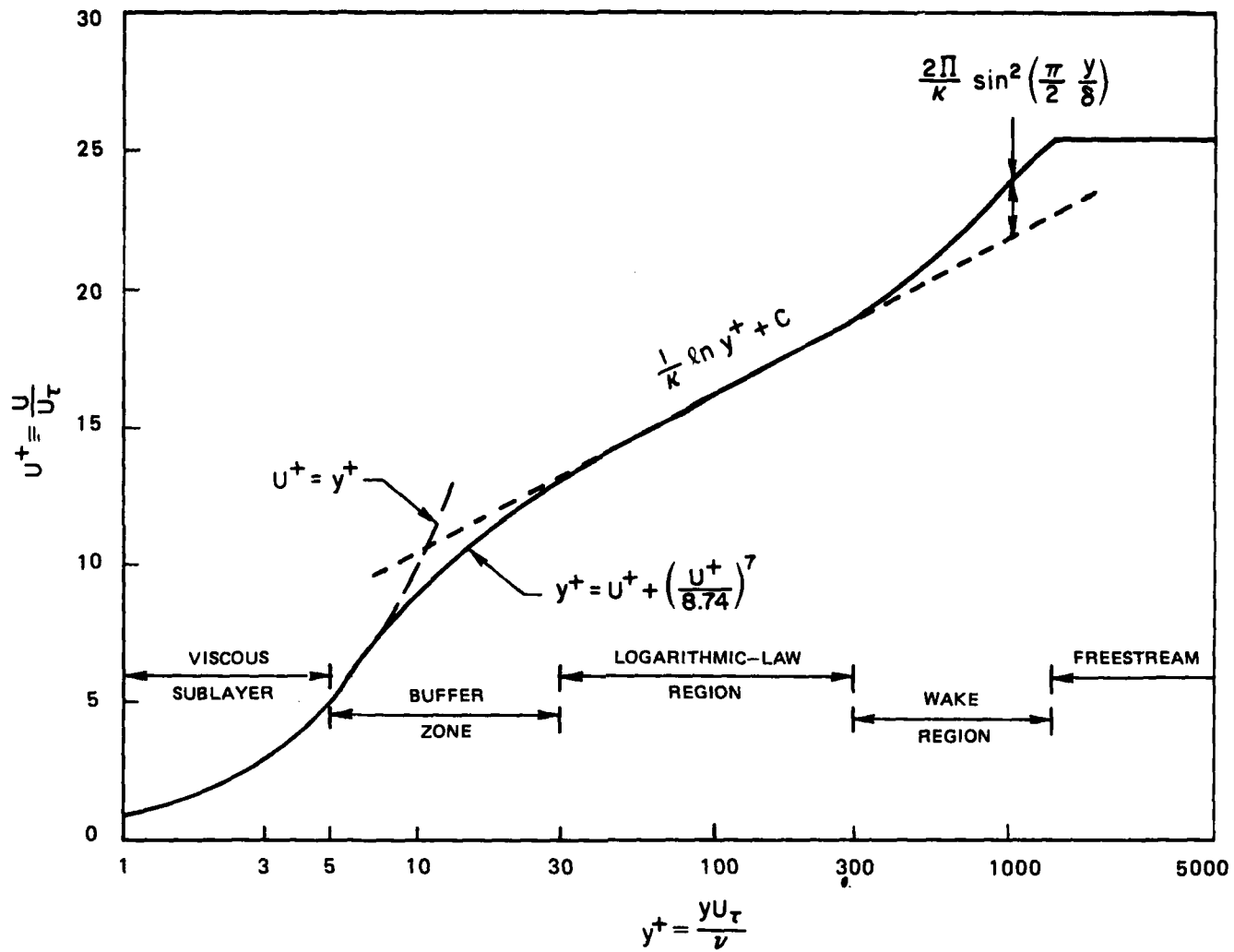
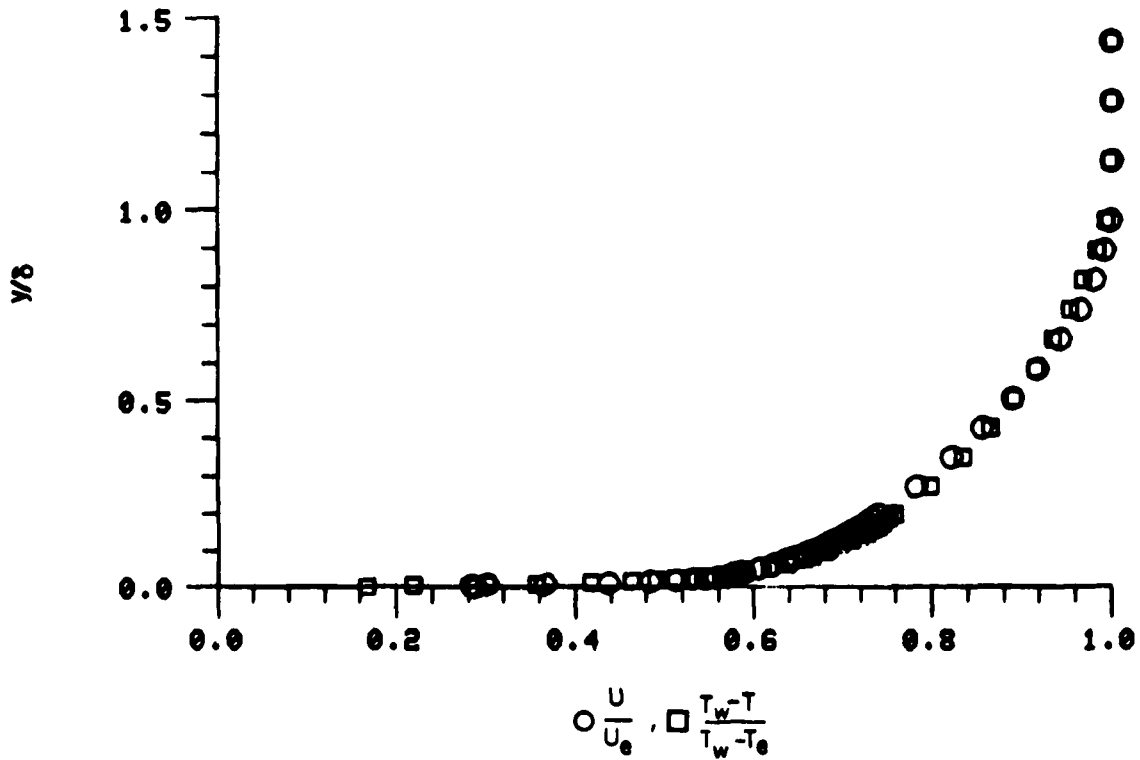


Figure 17. The Universal Velocity Distribution for Constant Pressure Turbulent Boundary Layers

R80-914388-12

VELOCITY AND TEMPERATURE RATIOS



VELOCITY AND TEMPERATURE DISTRIBUTIONS IN UNIVERSAL COORDINATES

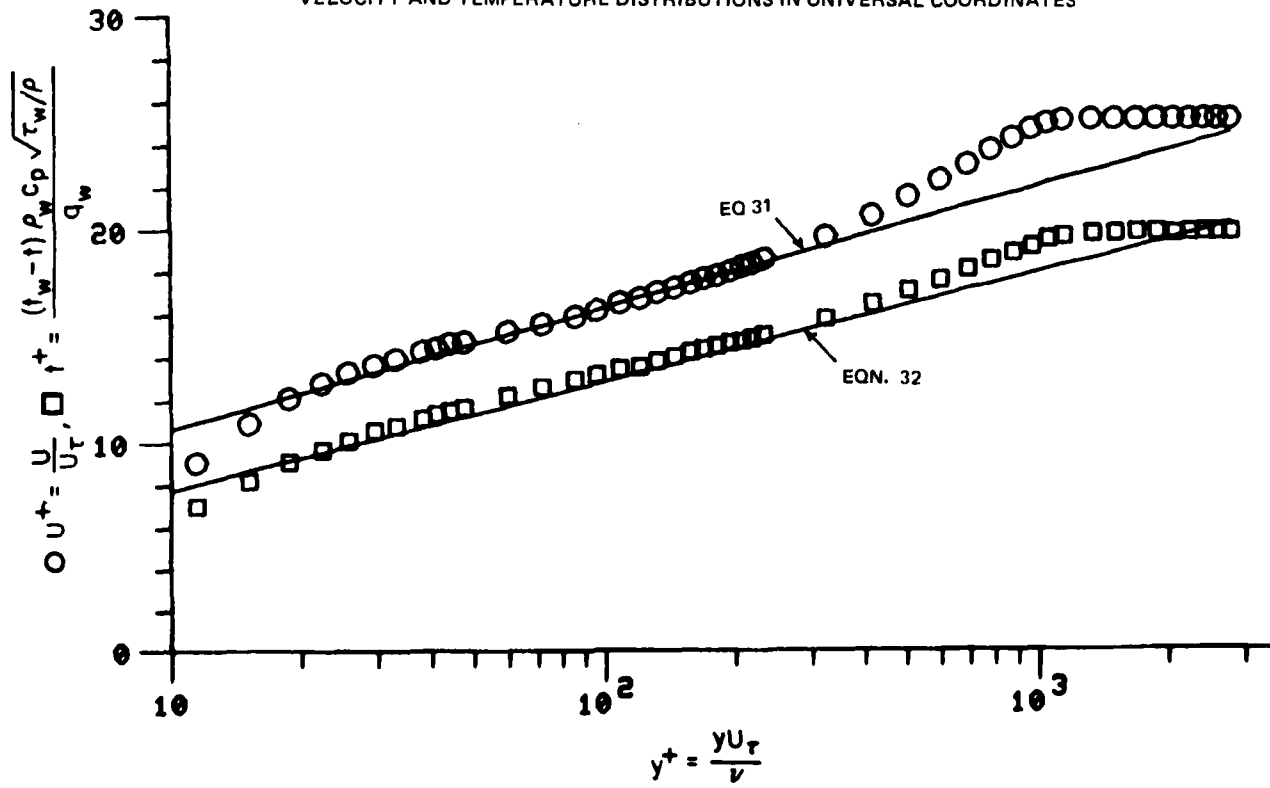
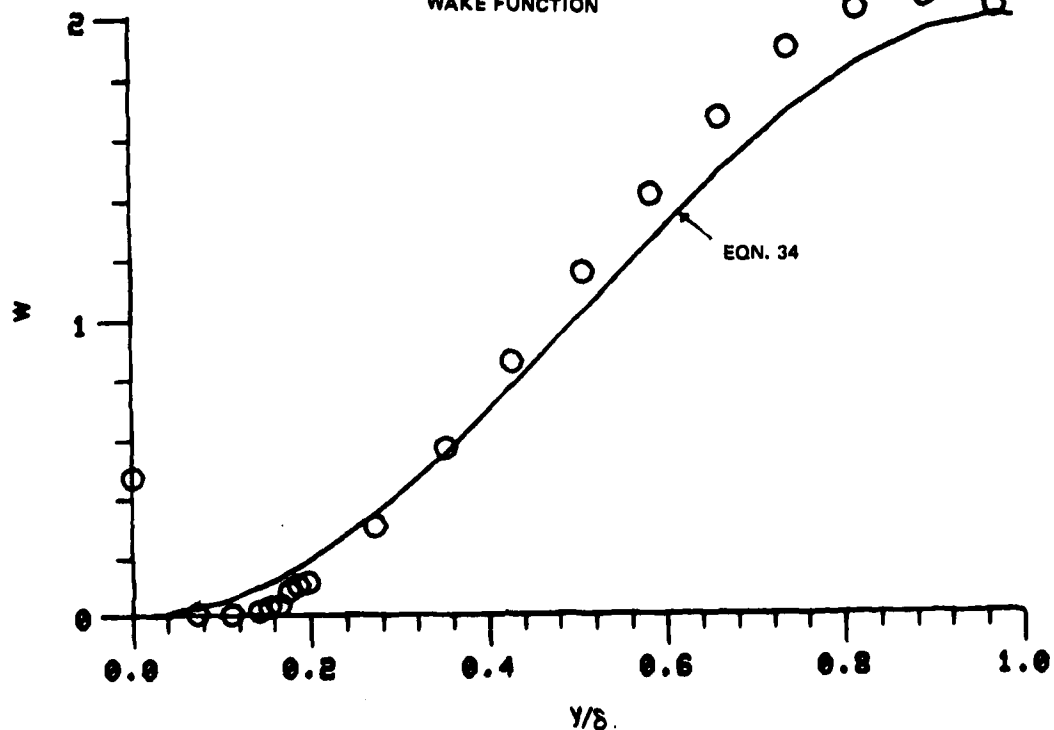


Figure 18a. Typical Boundary Layer Velocity and Temperature Profiles

78-12-100-1

R80-914388-12

WAKE FUNCTION



DEFECT VELOCITY

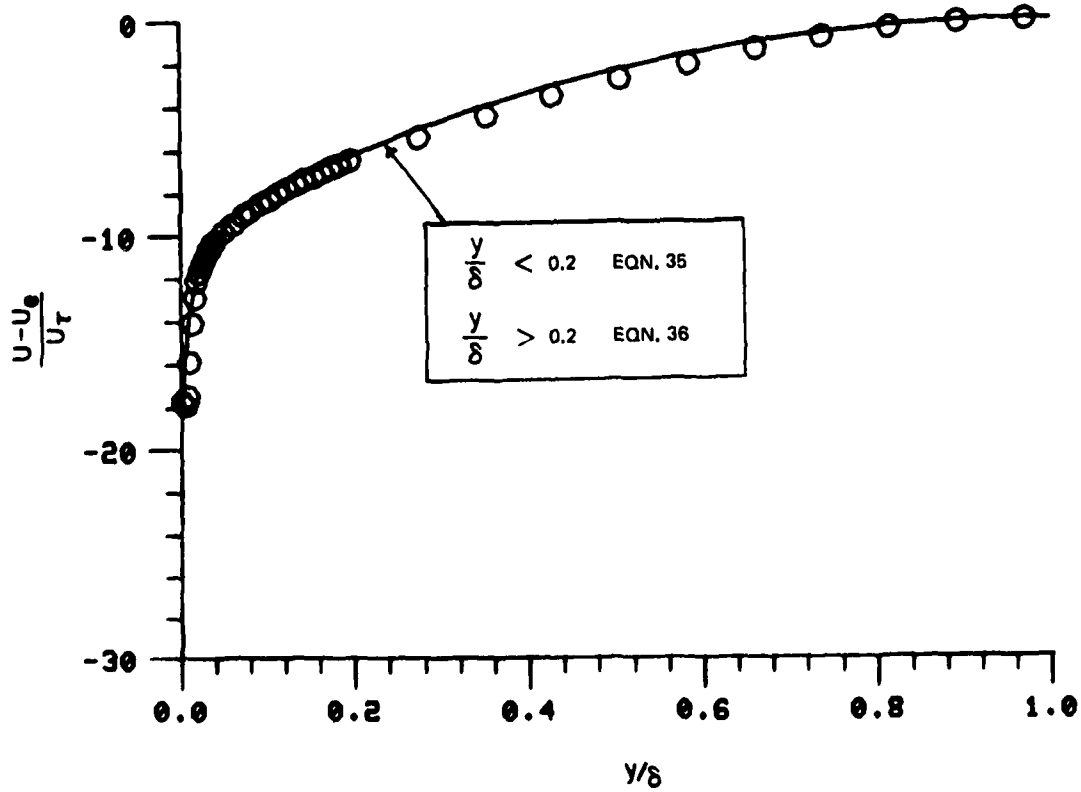


Figure 18b. Typical Boundary Layer Velocity Profiles

78-12-100-2

RECEIVED PROFILE DATA

THE JOURNAL OF CLIMATE

UNIT 1

11

11

Figure 19. Typical Tabulated Velocity and Temperature Profile Data

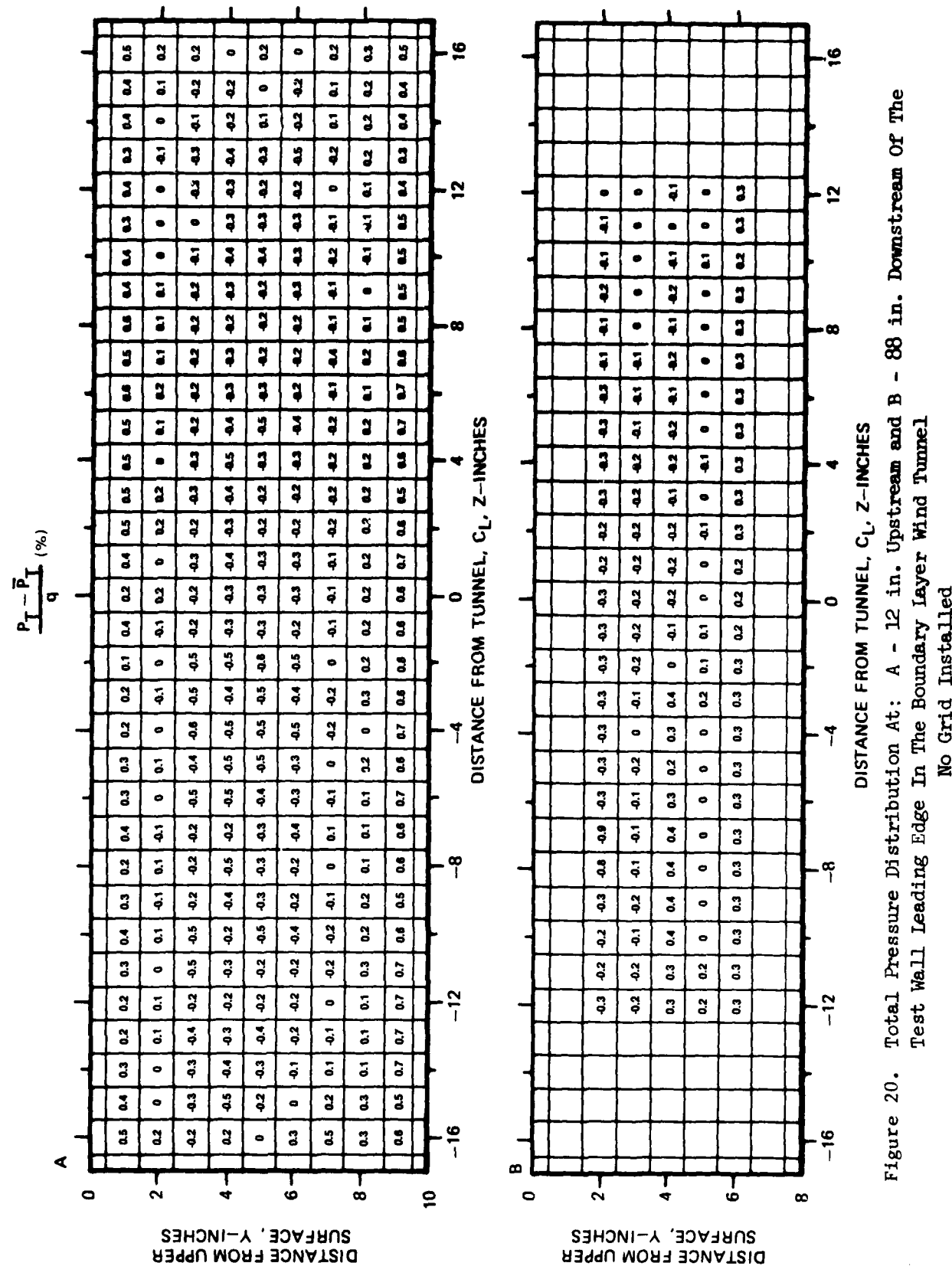


Figure 20. Total Pressure Distribution At: A - 12 in. Upstream and B - 88 in. Downstream Of The Test Wall Leading Edge In The Boundary Layer Wind Tunnel
No Grid Installed

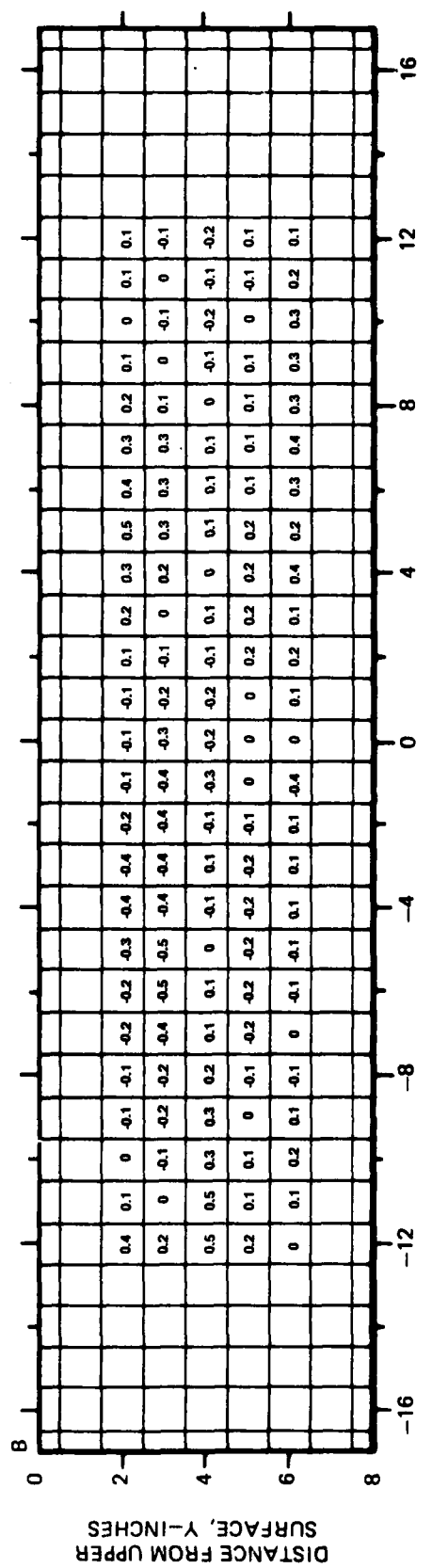
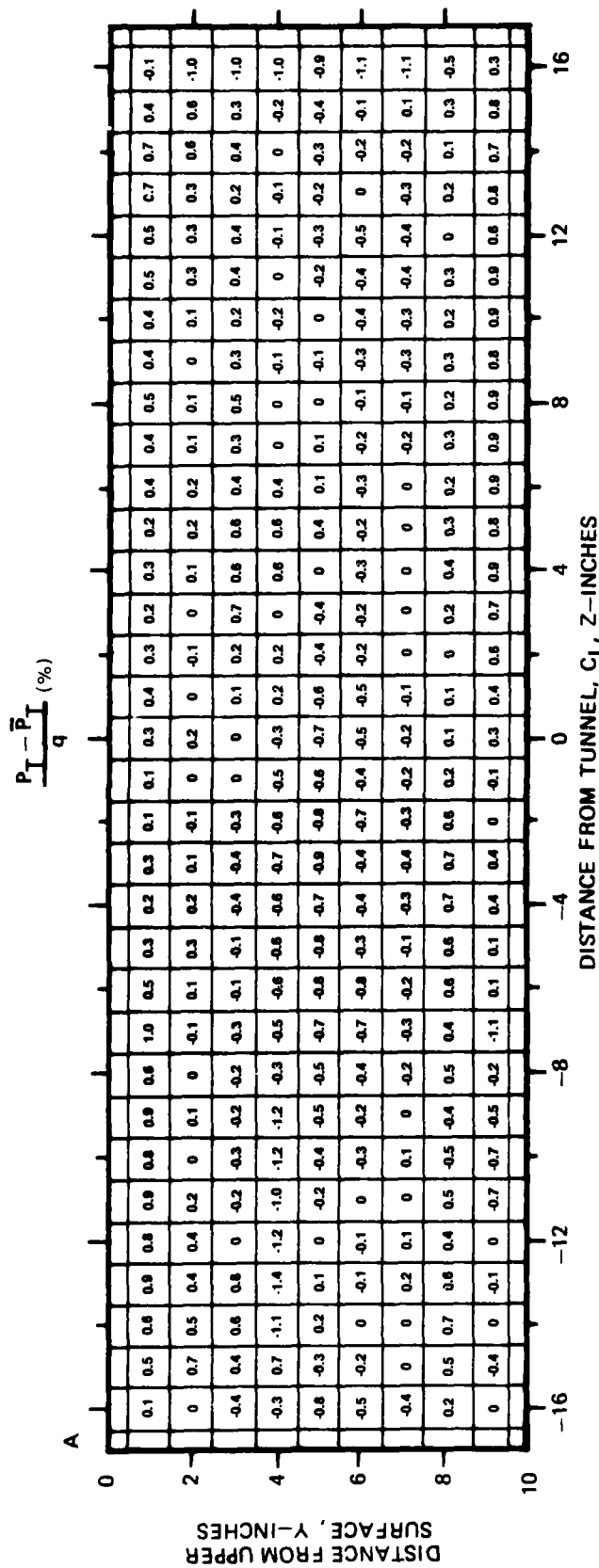


Figure 21. Total Pressure Distribution At: A - 12 in. Upstream and B - 88 in. Downstream Of The Test Wall Leading Edge In The Boundary Layer Wind Tunnel Grid Number 1 Installed

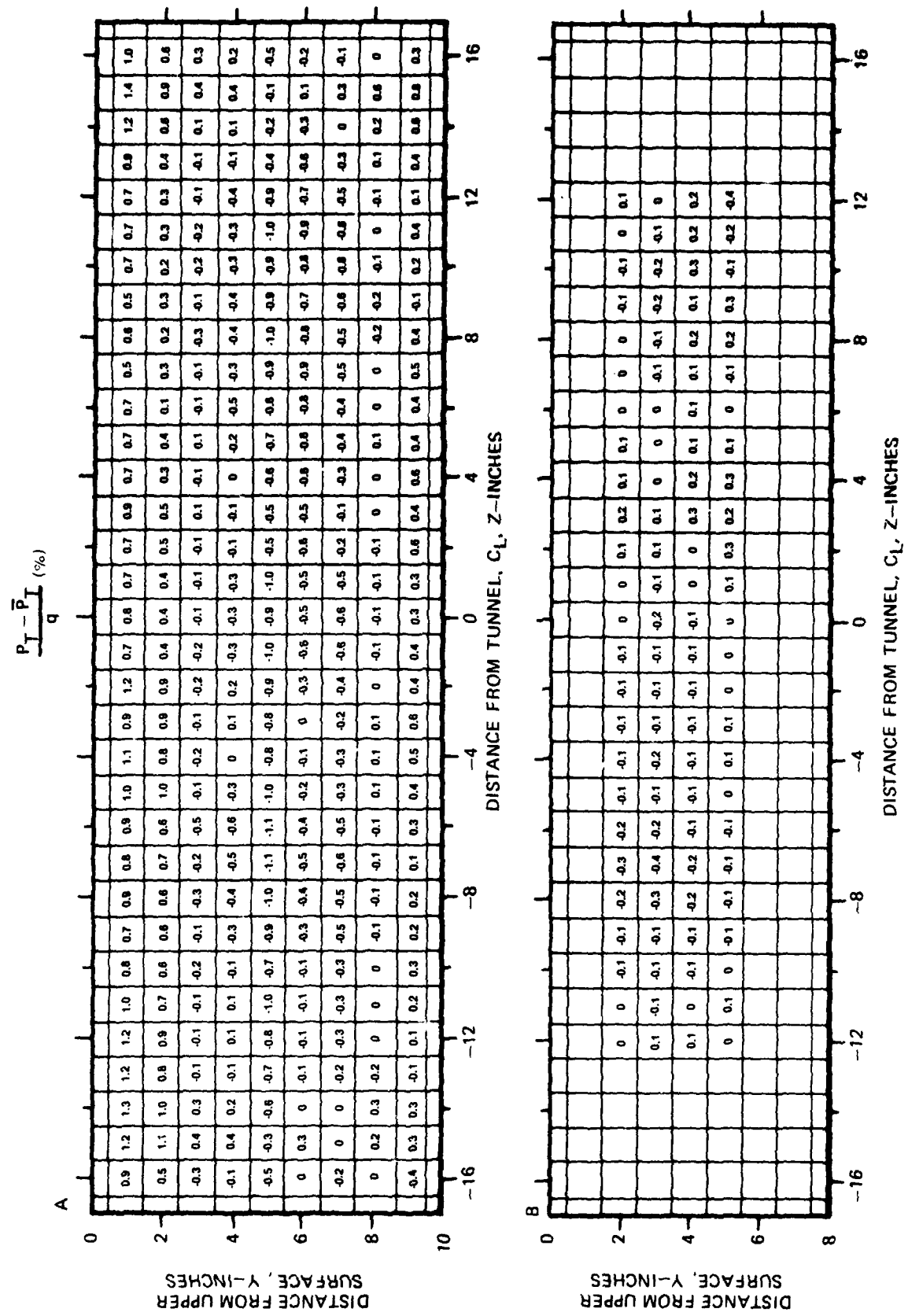


Figure 22. Total Pressure Distribution At: A - 12 in. Upstream and B - 88 in. Downstream Of The Test Wall Leading Edge In The Boundary Layer Wind Tunnel Grid Number 2 Installed

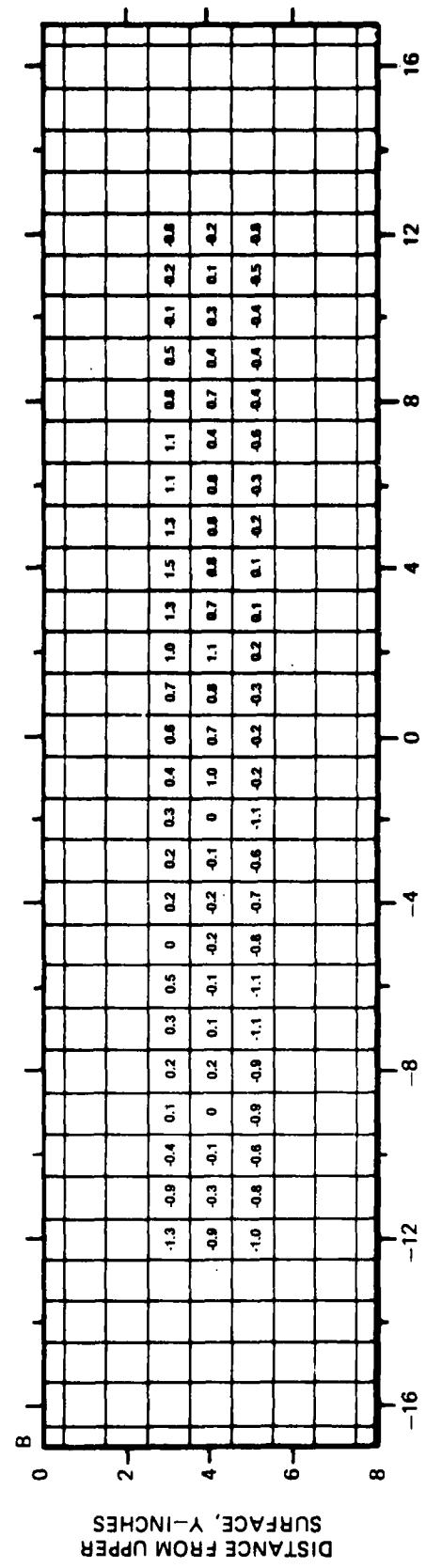
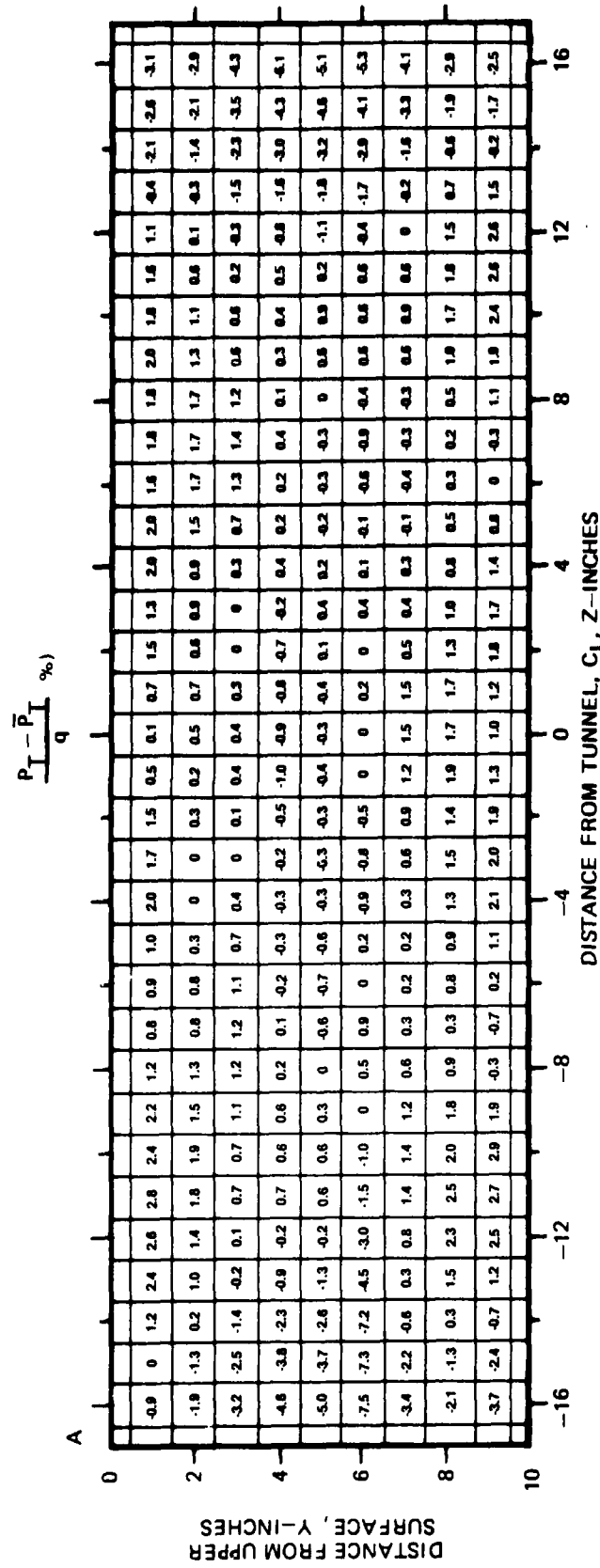


Figure 23. Total Pressure Distribution At: A - 12 in. Upstream and B - 88 in. Downstream Of The Test Wall Leading Edge In The Boundary Layer Wind Tunnel
Grid Number 3 Installed

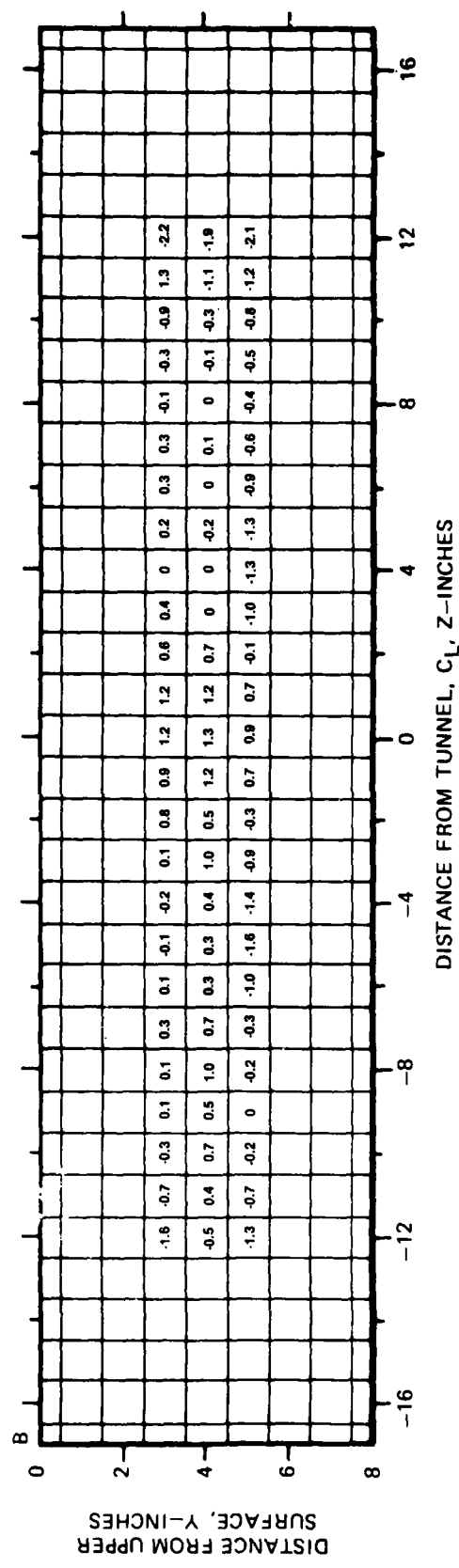
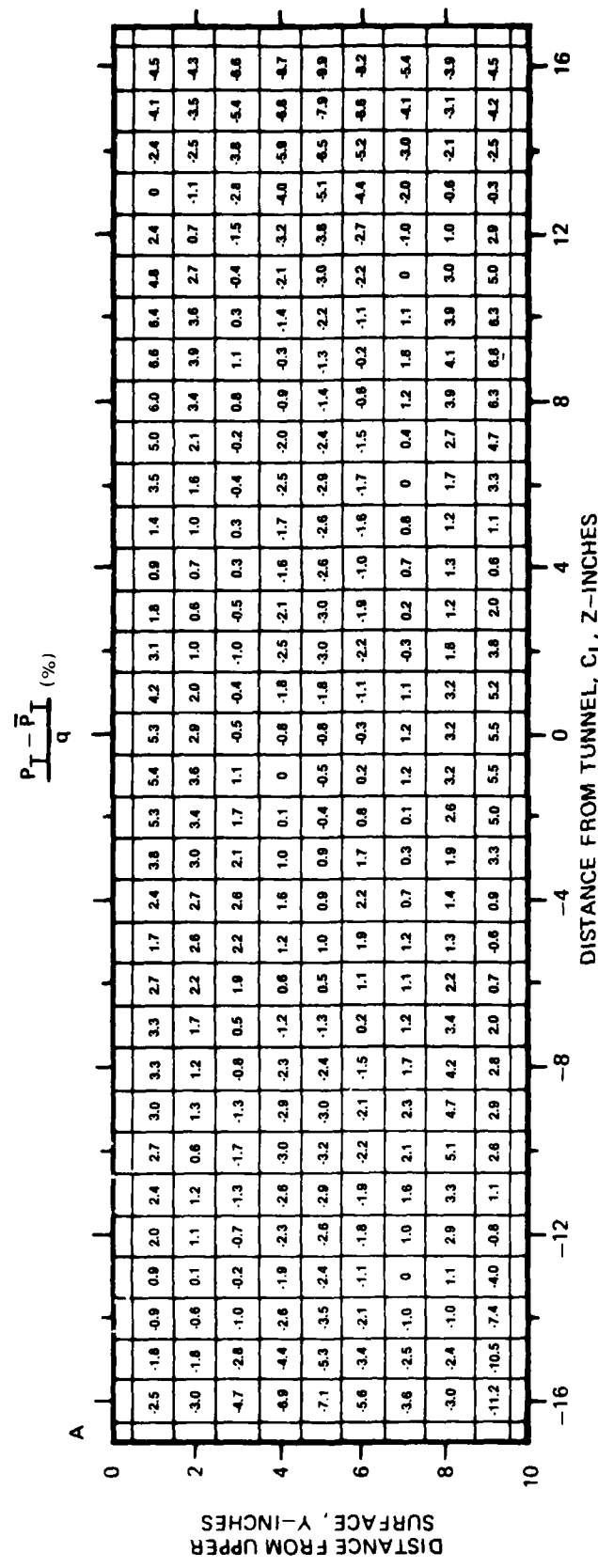


Figure 24. Total Pressure Distribution At: A - 12 in. Upstream and B - 88 in. Downstream Of The Test Wall Leading Edge In The Boundary Layer Wind Tunnel
Grid Number 4 Installed

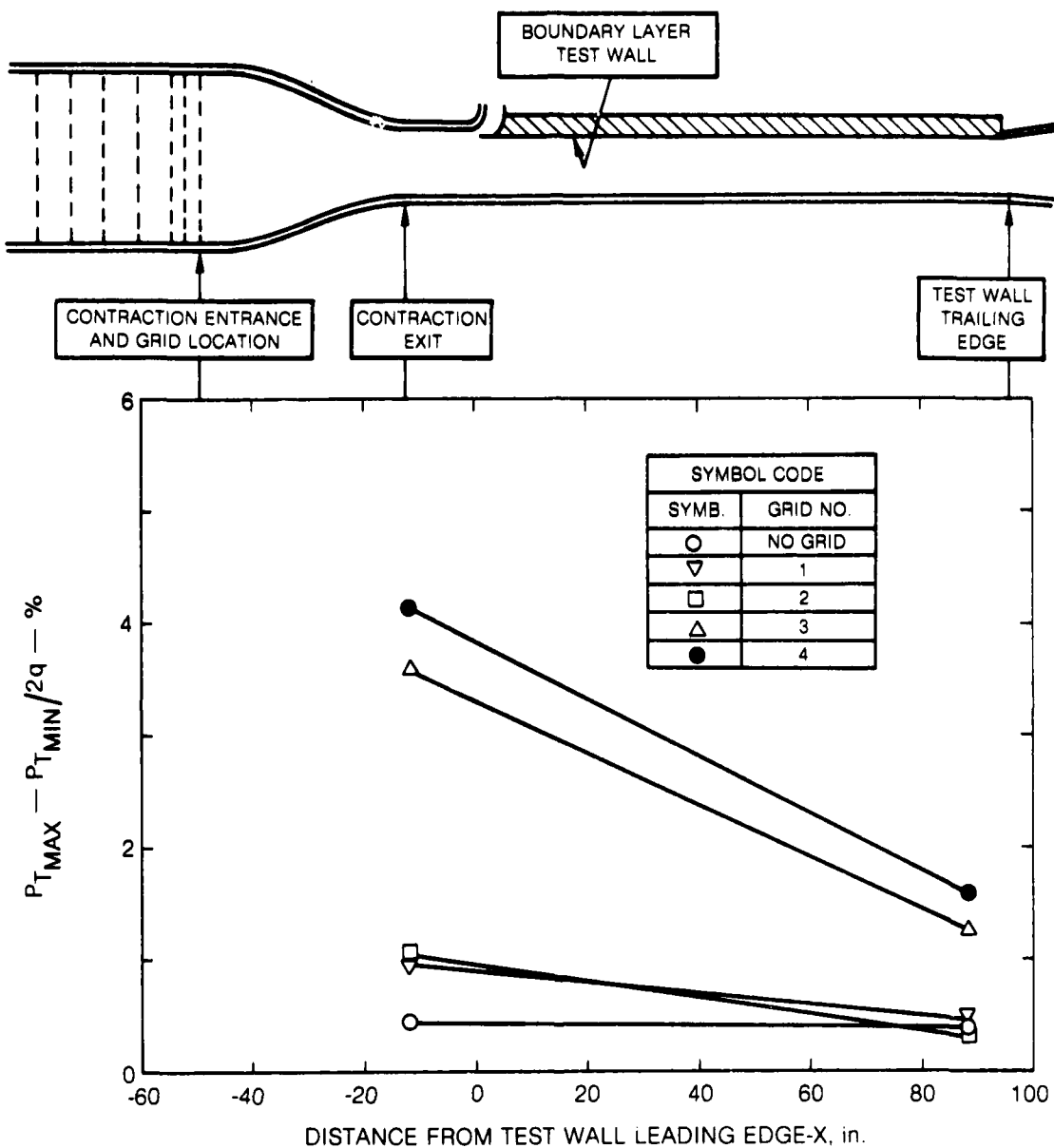


Figure 25. Total Pressure Nonuniformity In The Boundary Layer Wind Tunnel Test Section For Various Turbulence Generating Grids Installed At The Contraction Entrance.

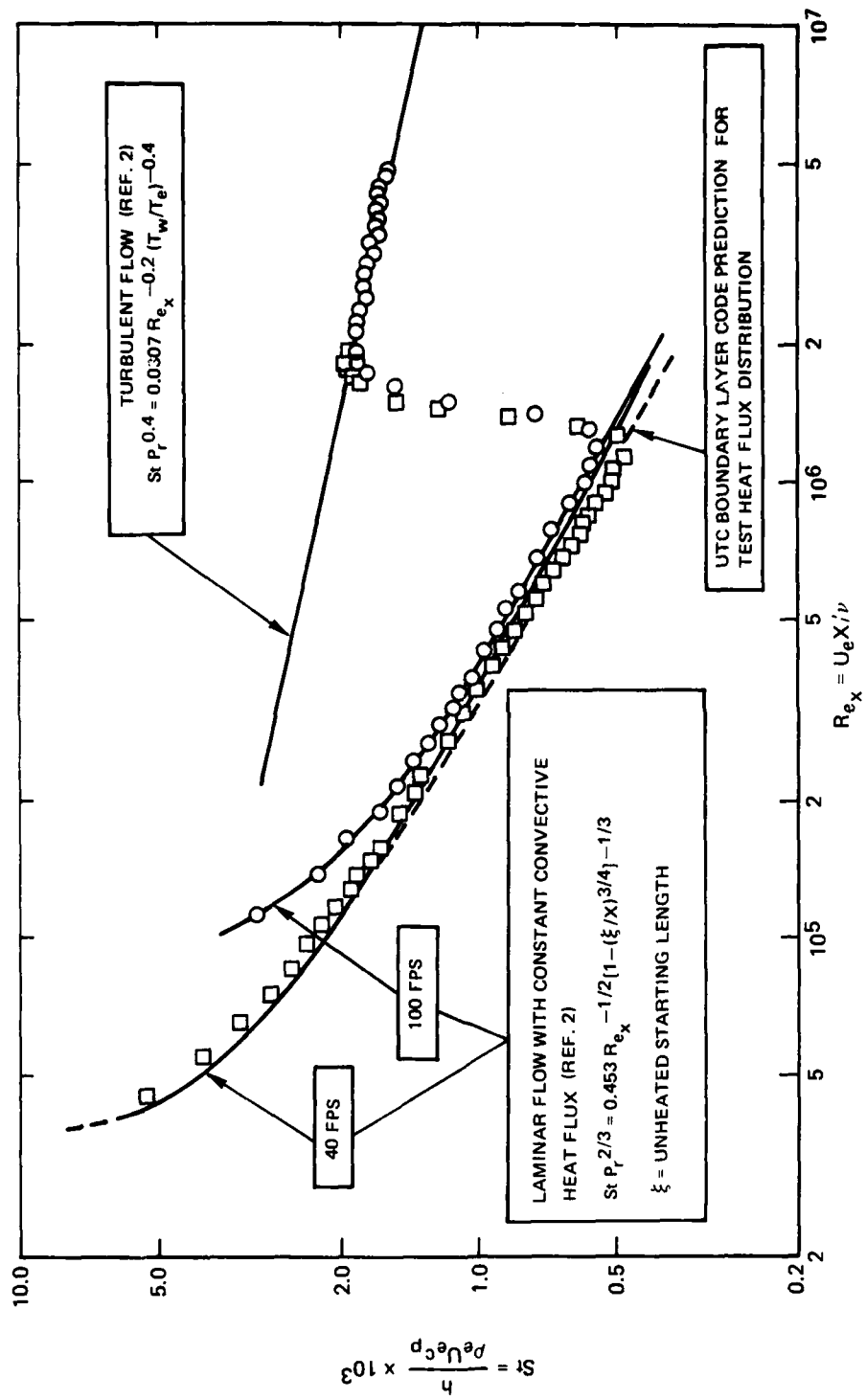


Figure 26. Heat Transfer Distribution Along the Uniform Heat Flux Test Wall For The Minimum Freestream Turbulence Configuration and Natural Transition of the Test Wall Boundary Layer

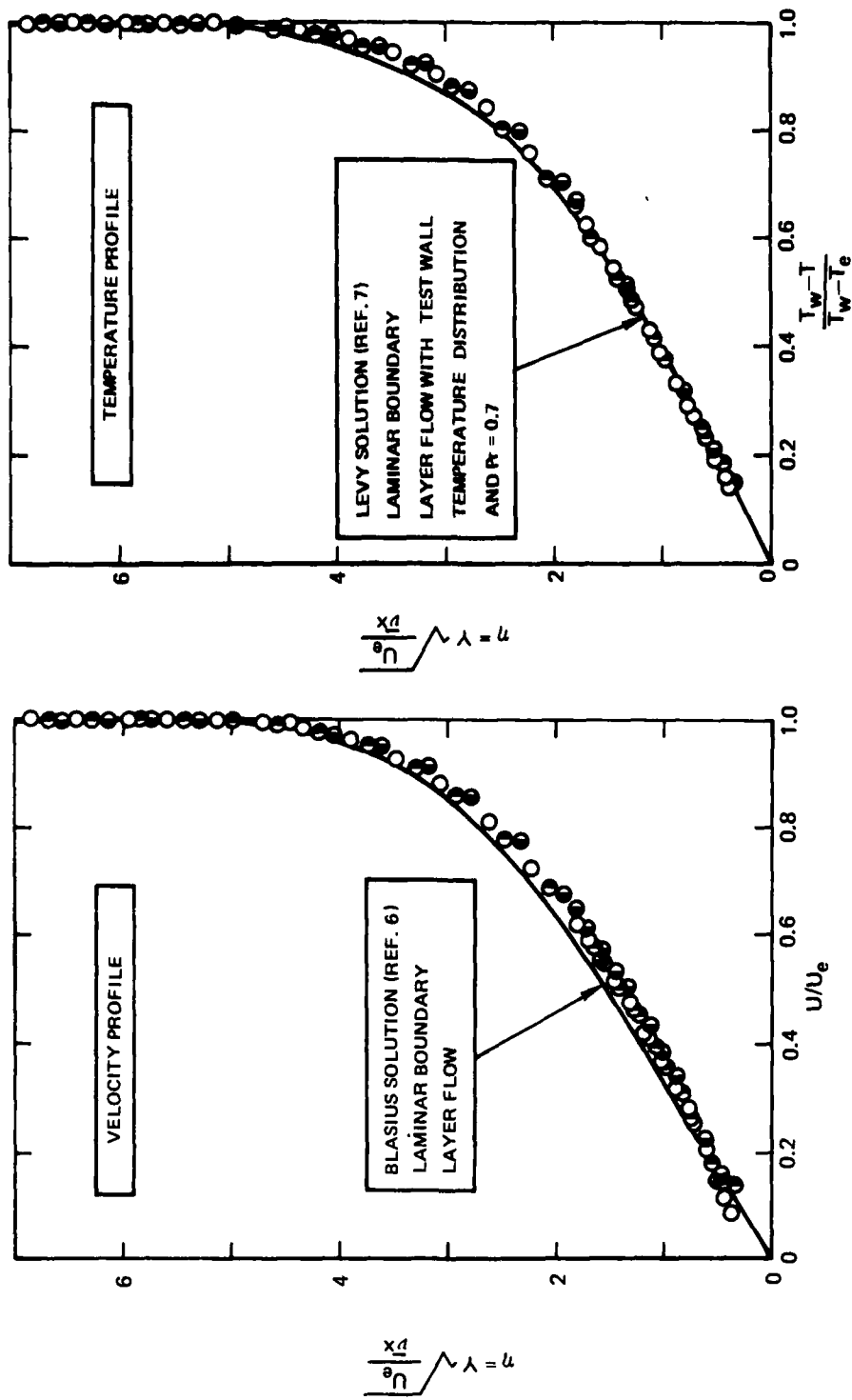


Figure 27. Velocity and Temperature Profiles Measured Upstream of Boundary Layer Transition For The Minimum Freestream Turbulence Test Condition ($Re_x = 0.63 \times 10^6$) at Three Transverse Locations O Tunnel C_L ; \bullet 6 in East of C_L ; \circ in West of C_L

R80-914388-12

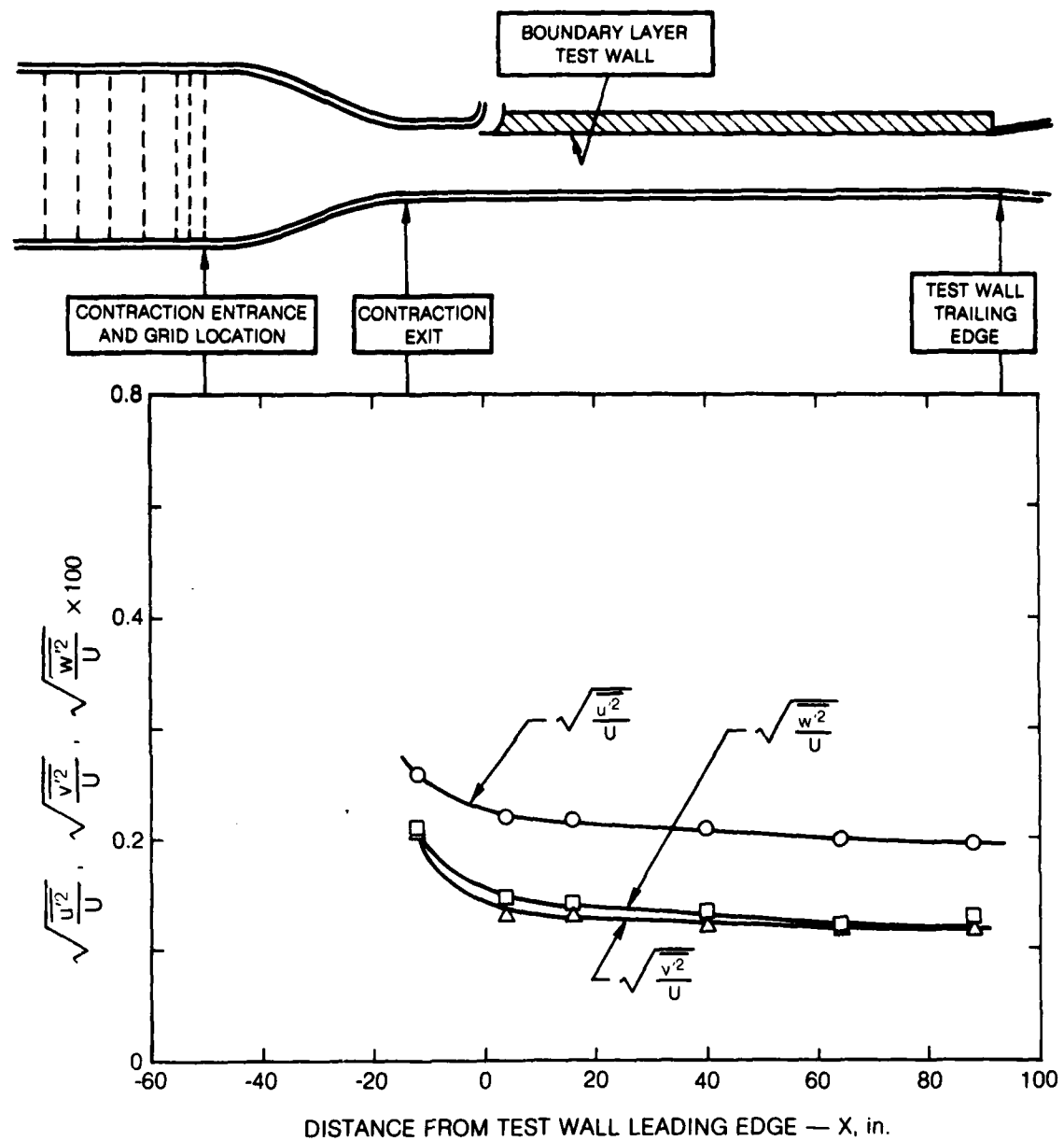


Figure 28. Distribution of the Components of the Turbulence In The Boundary Layer Wind Tunnel Test Section
No Grid Installed

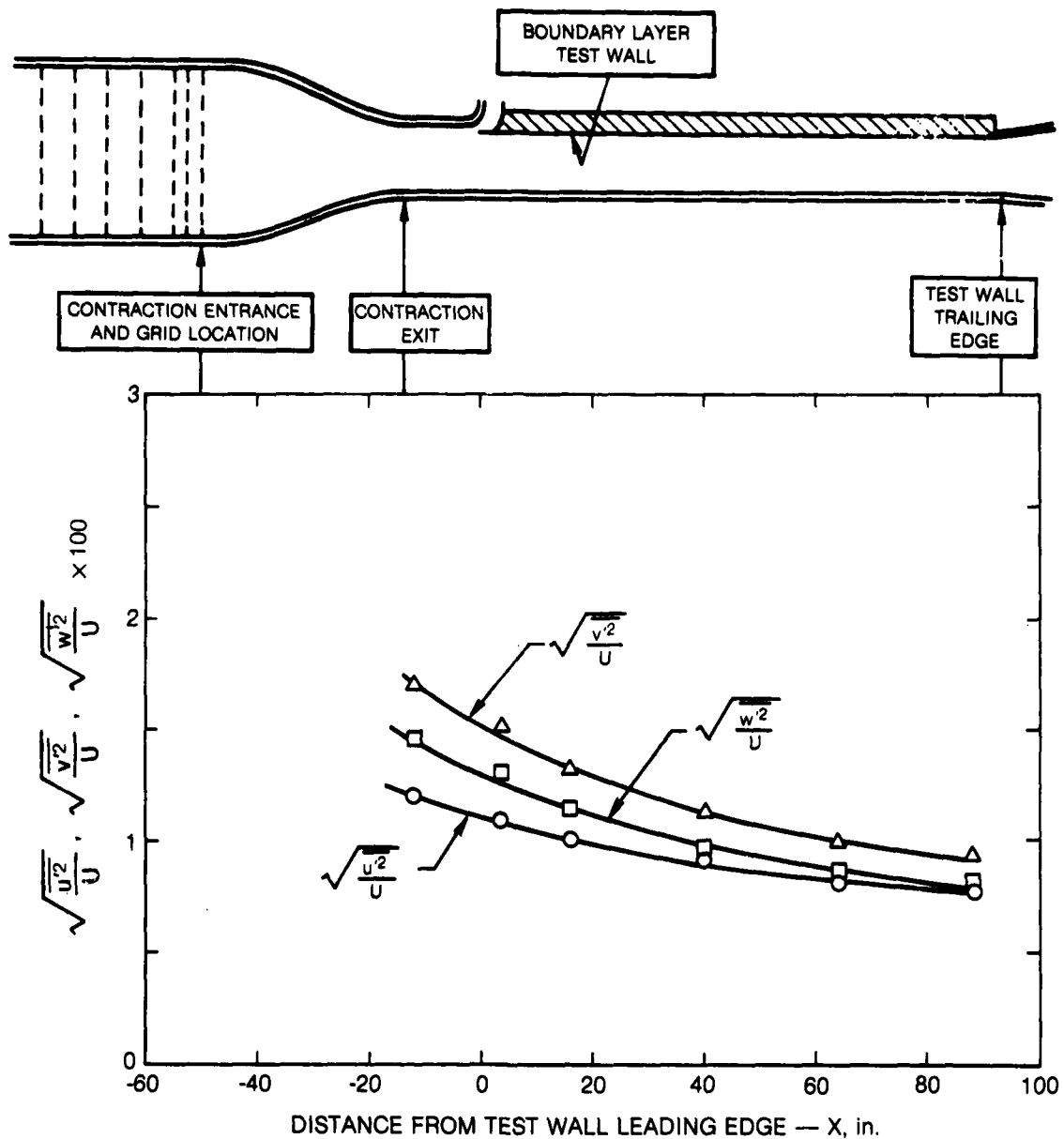


Figure 29. Distribution of the Components of the Turbulence In The Boundary Layer Wind Tunnel Test Section
Grid Number 1 Installed

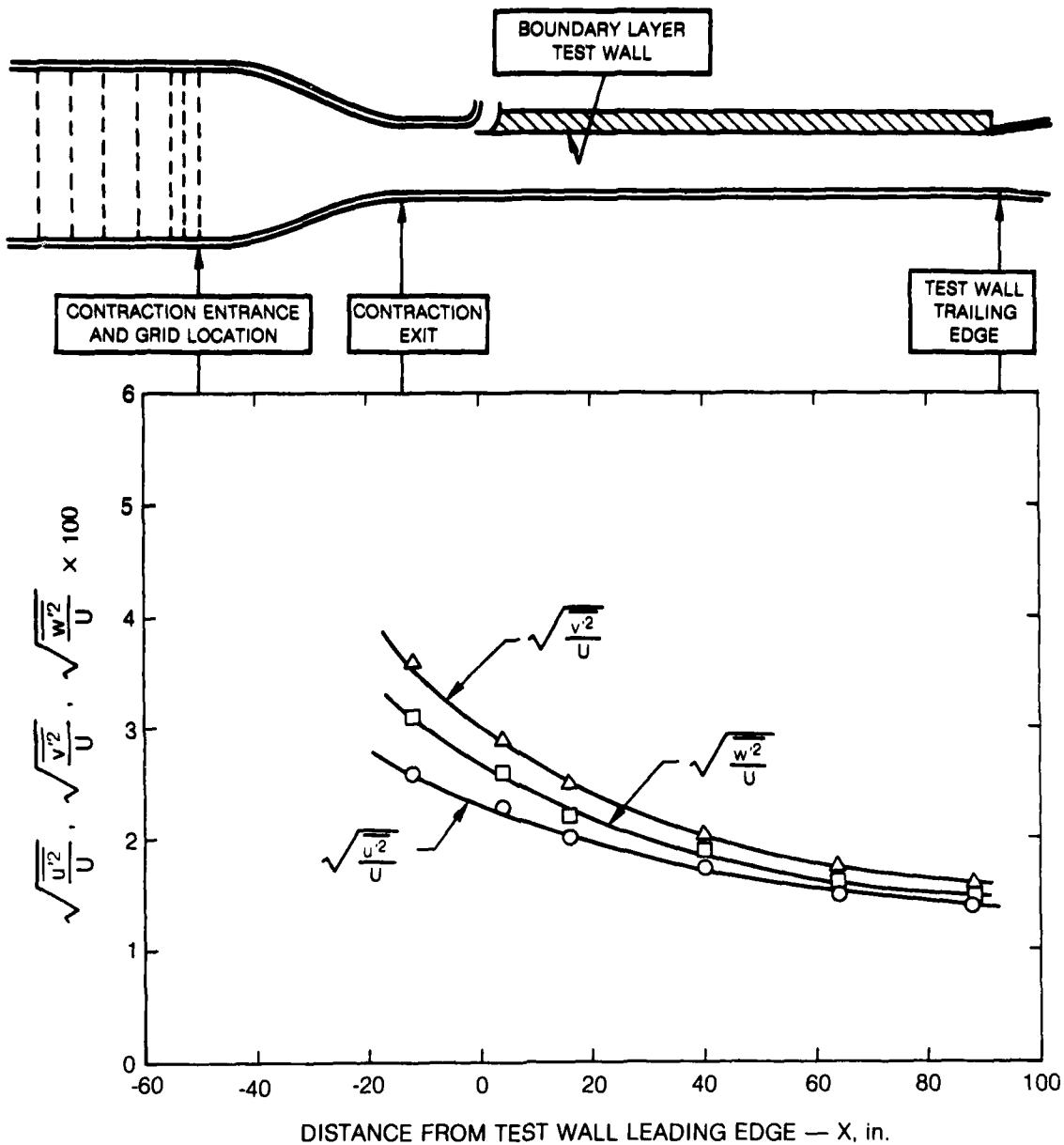


Figure 30. Distribution of the Components of the Turbulence In The Boundary Layer Wind Tunnel Test Section
Grid Number 2 Installed

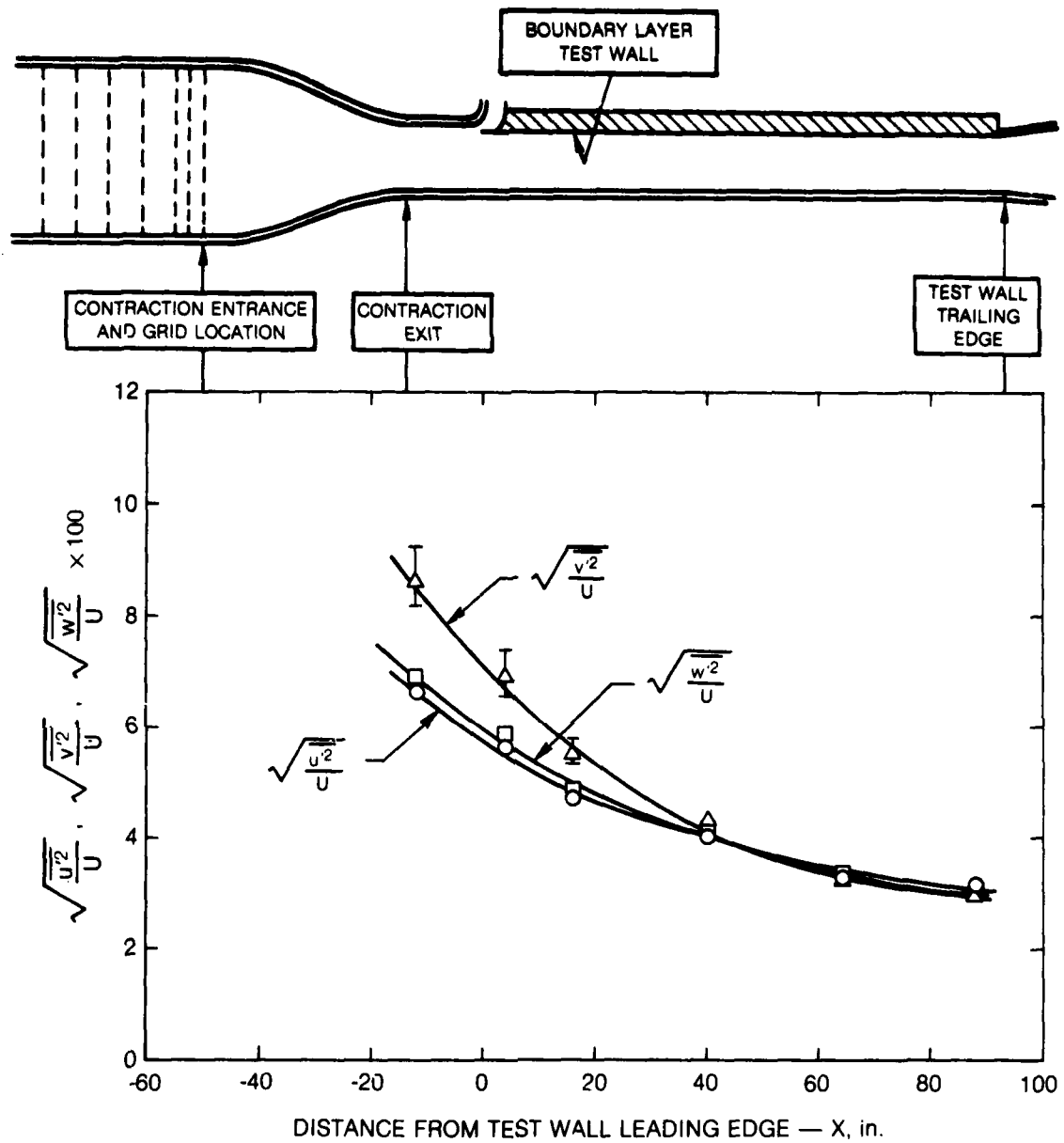


Figure 31. Distribution of the Components of the Turbulence In The Boundary Layer Wind Tunnel Test Section
Grid Number 3 Installed

R80-914388-12

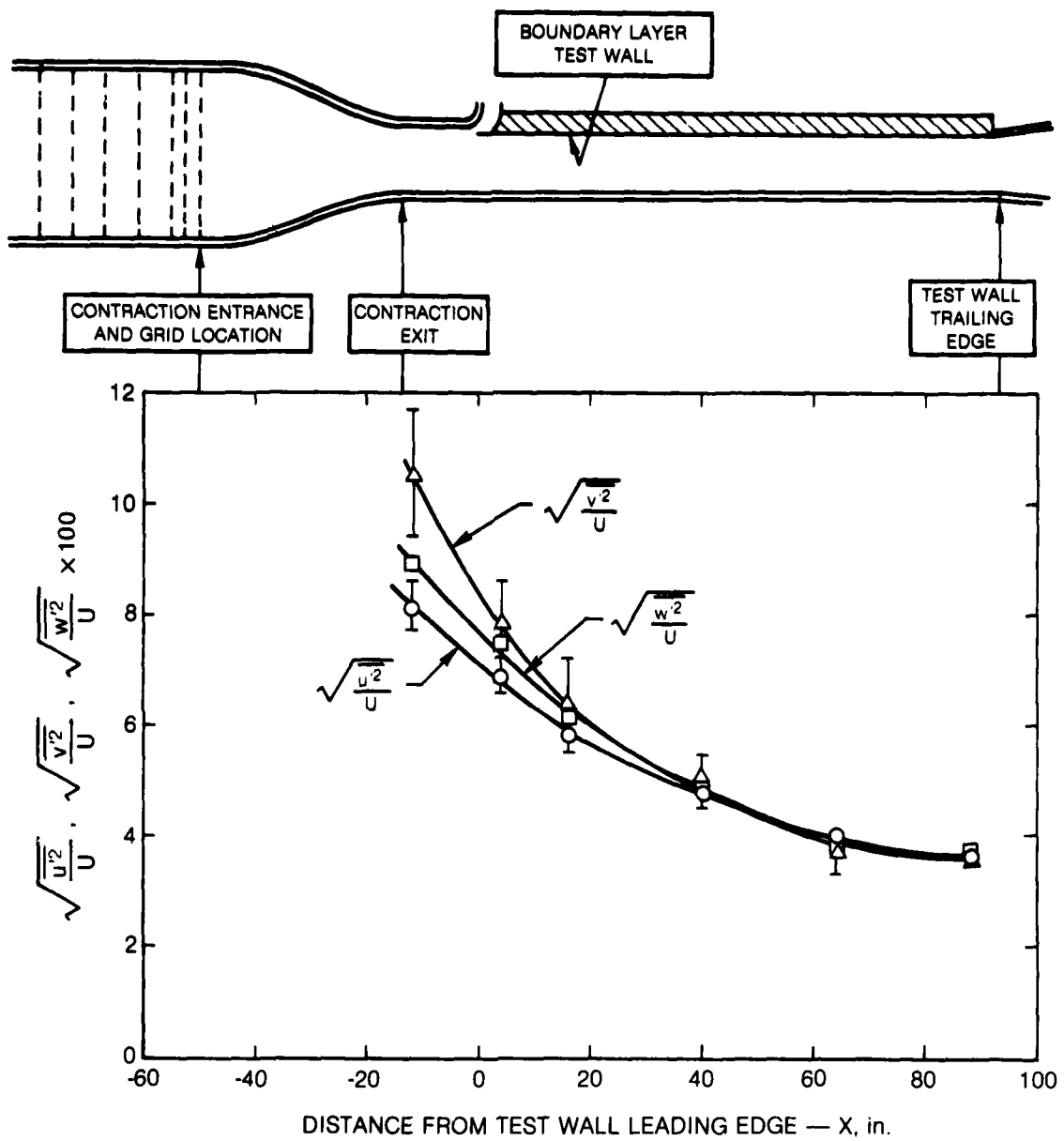


Figure 32. Distribution of the Components of the Turbulence In The Boundary Layer Wind Tunnel Test Section
Grid Number 4 Installed

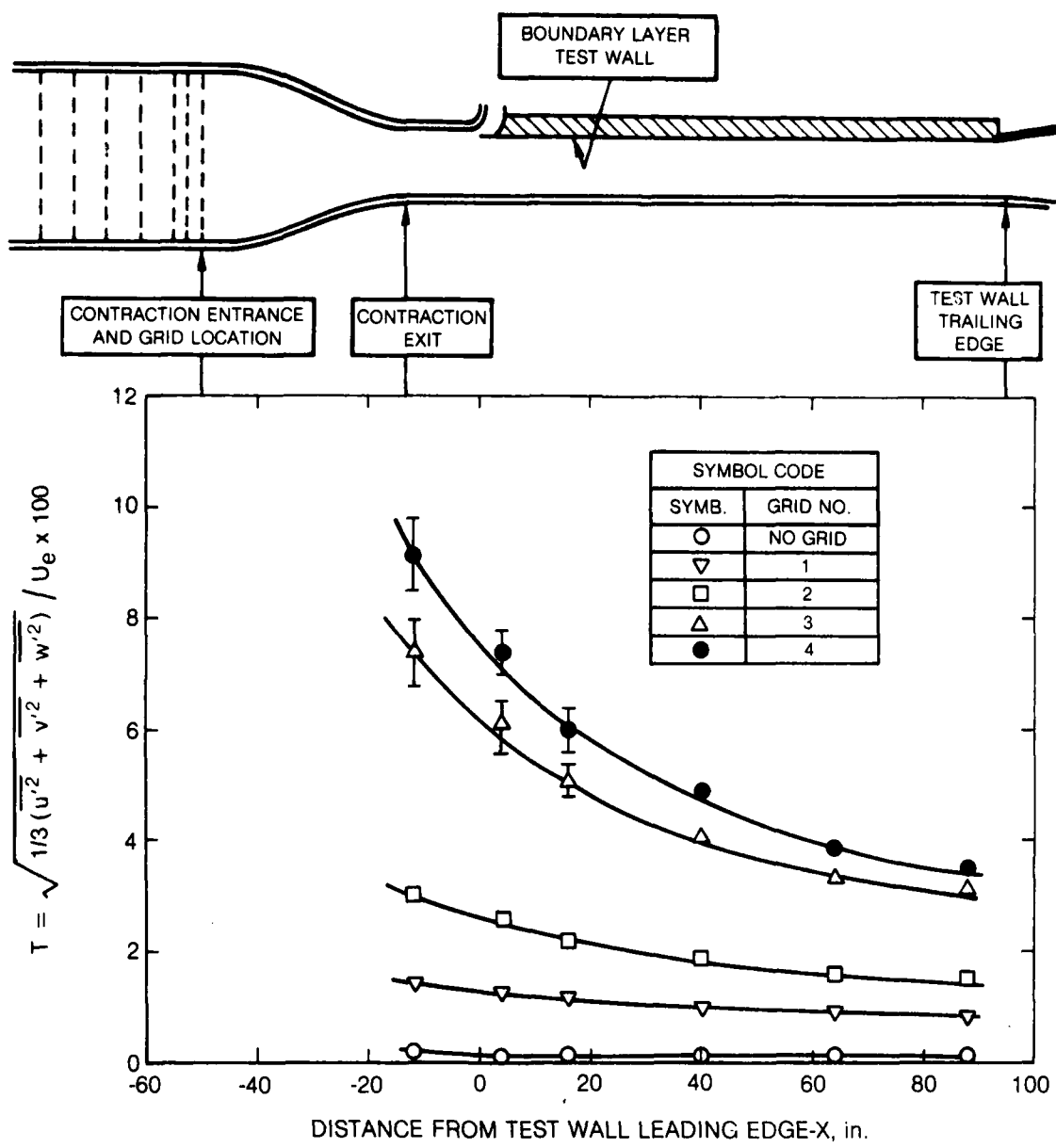
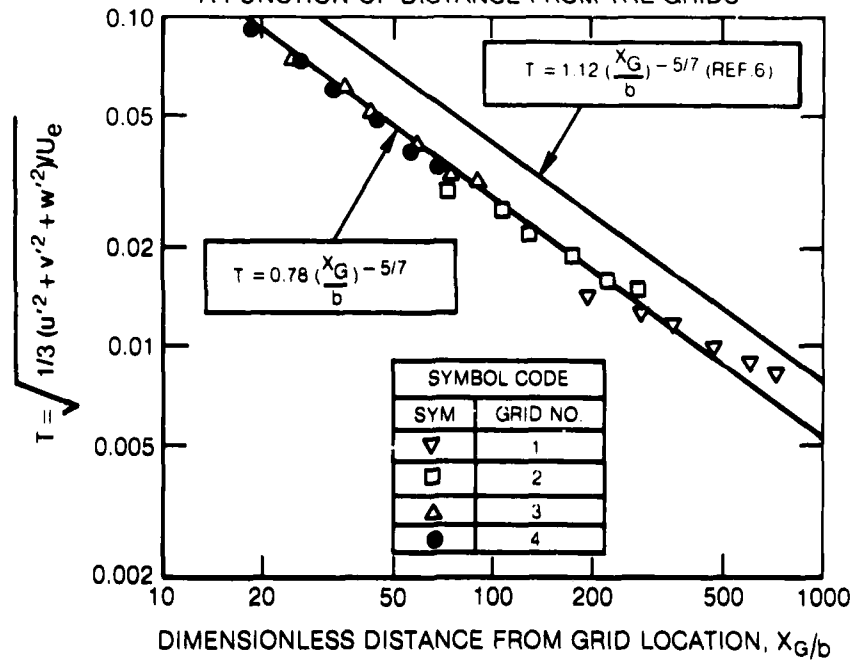


Figure 33. Distributions of Total Turbulence Intensity In The Boundary Layer Wind Tunnel Test Section For Various Turbulence Generating Grids Installed At The Contraction Entrance

a) TEST SECTION TURBULENCE DISTRIBUTION AS A FUNCTION OF DISTANCE FROM THE GRIDS



b) TEST SECTION TURBULENCE DISTRIBUTION AS A FUNCTION OF DISTANCE FROM THE "EFFECTIVE" GRID LOCATION

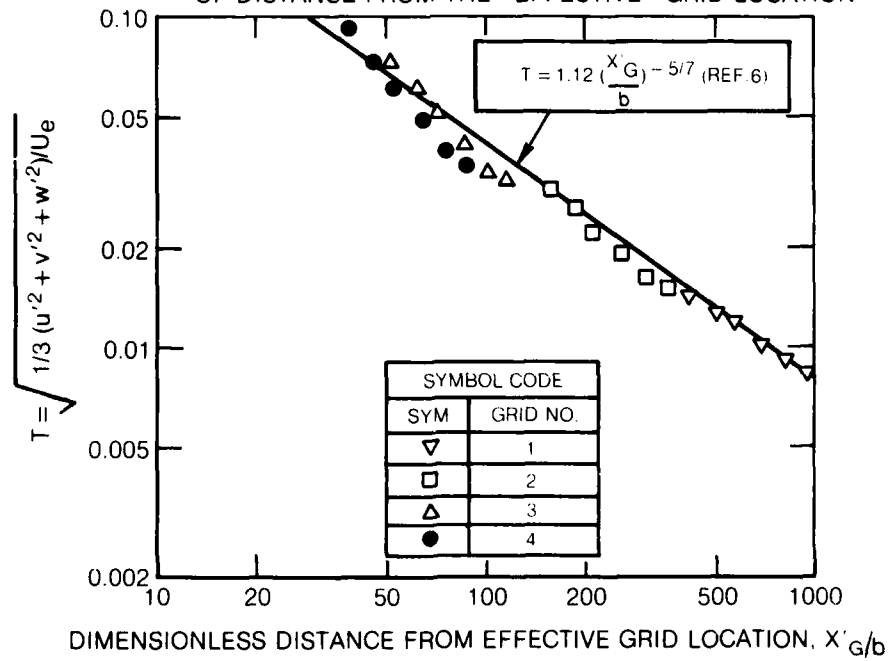


Figure 34. Distribution of Total Turbulence Intensity in the Boundary Layer Wind Tunnel Test Section Compared with the Results of Baines and Peterson (Ref. 6).

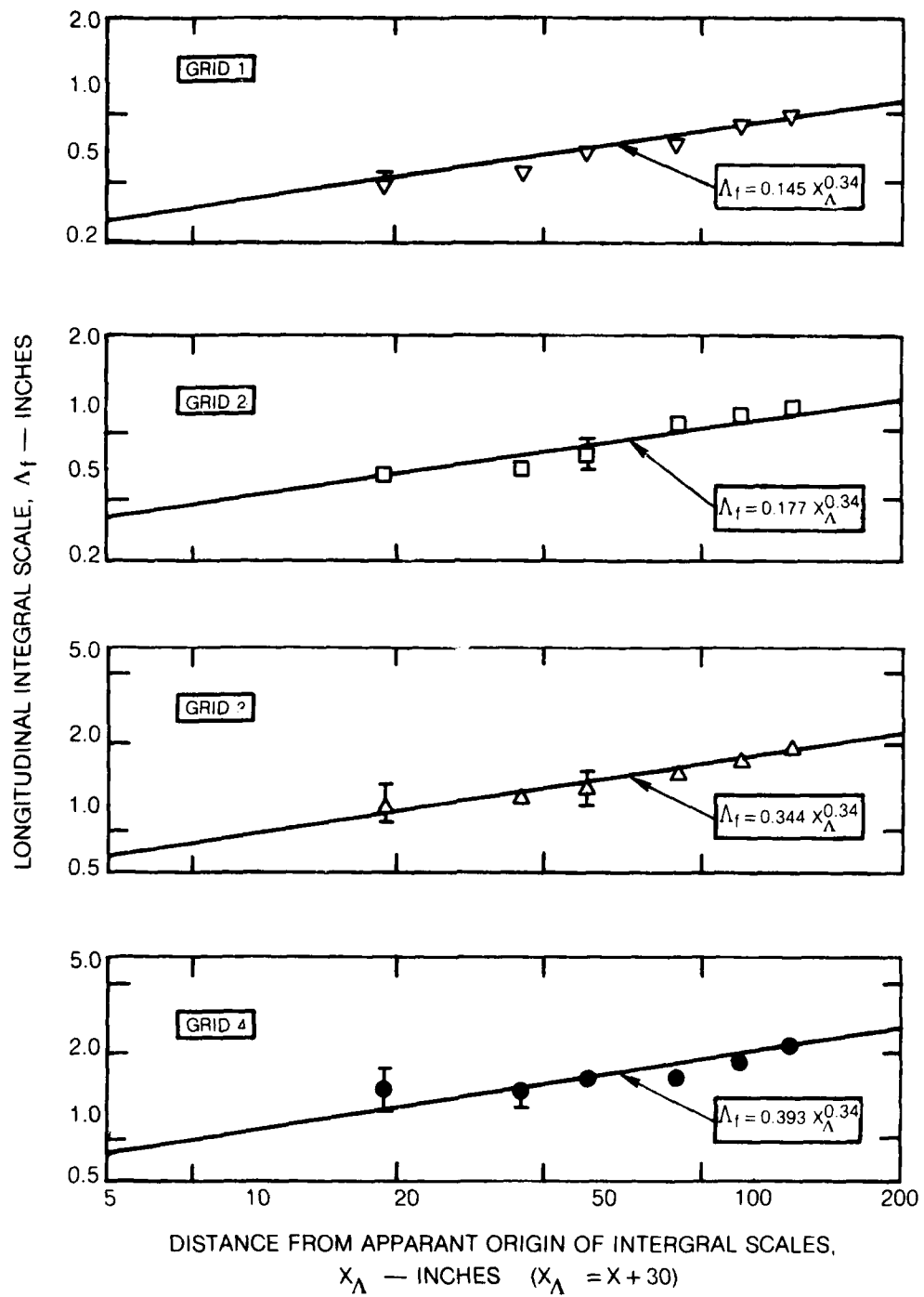


Figure 35. Growth of the Longitudinal Integral Scale Along the Test Section for the Various Turbulence Generating Grids - Logarithmic Plot

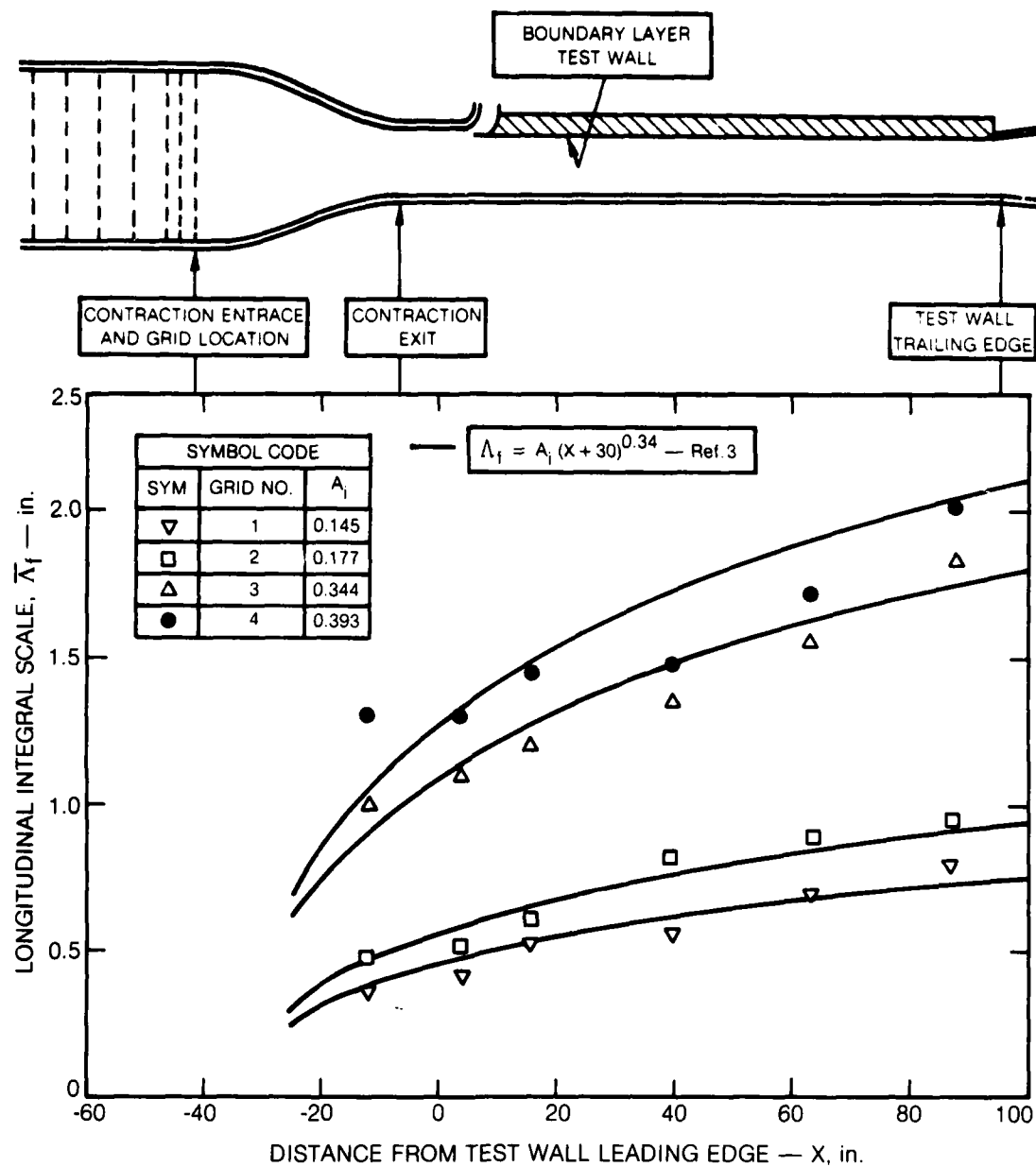


Figure 36. Growth of the Longitudinal Integral Scale Along the Test Section for the Various Turbulence Generating Grids - Linear Plot

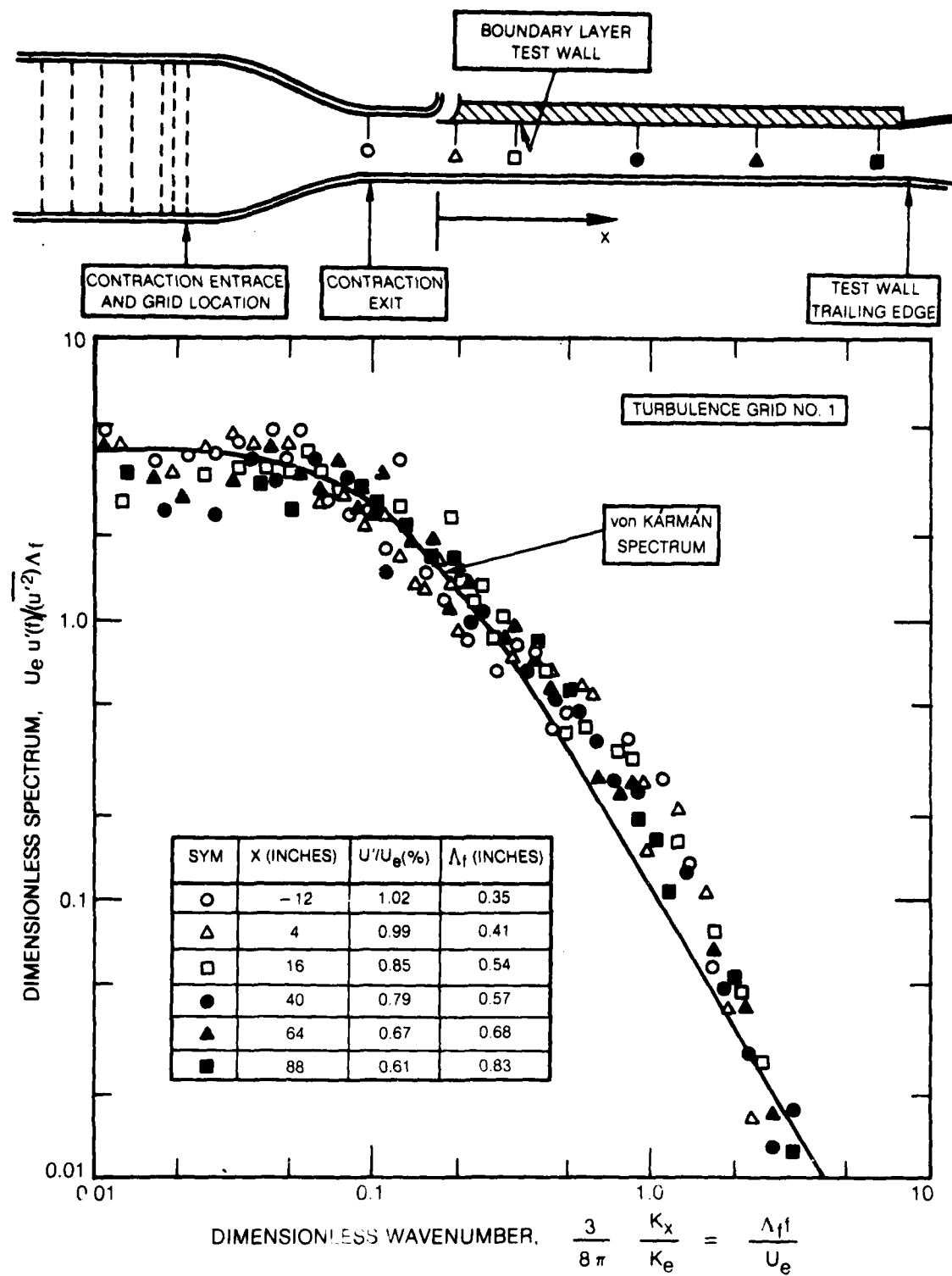


Figure 37. Free-Stream Power Spectral Density Distributions Measured at Various Streamwise Locations in the Test Section
Grid Number 1 Installed

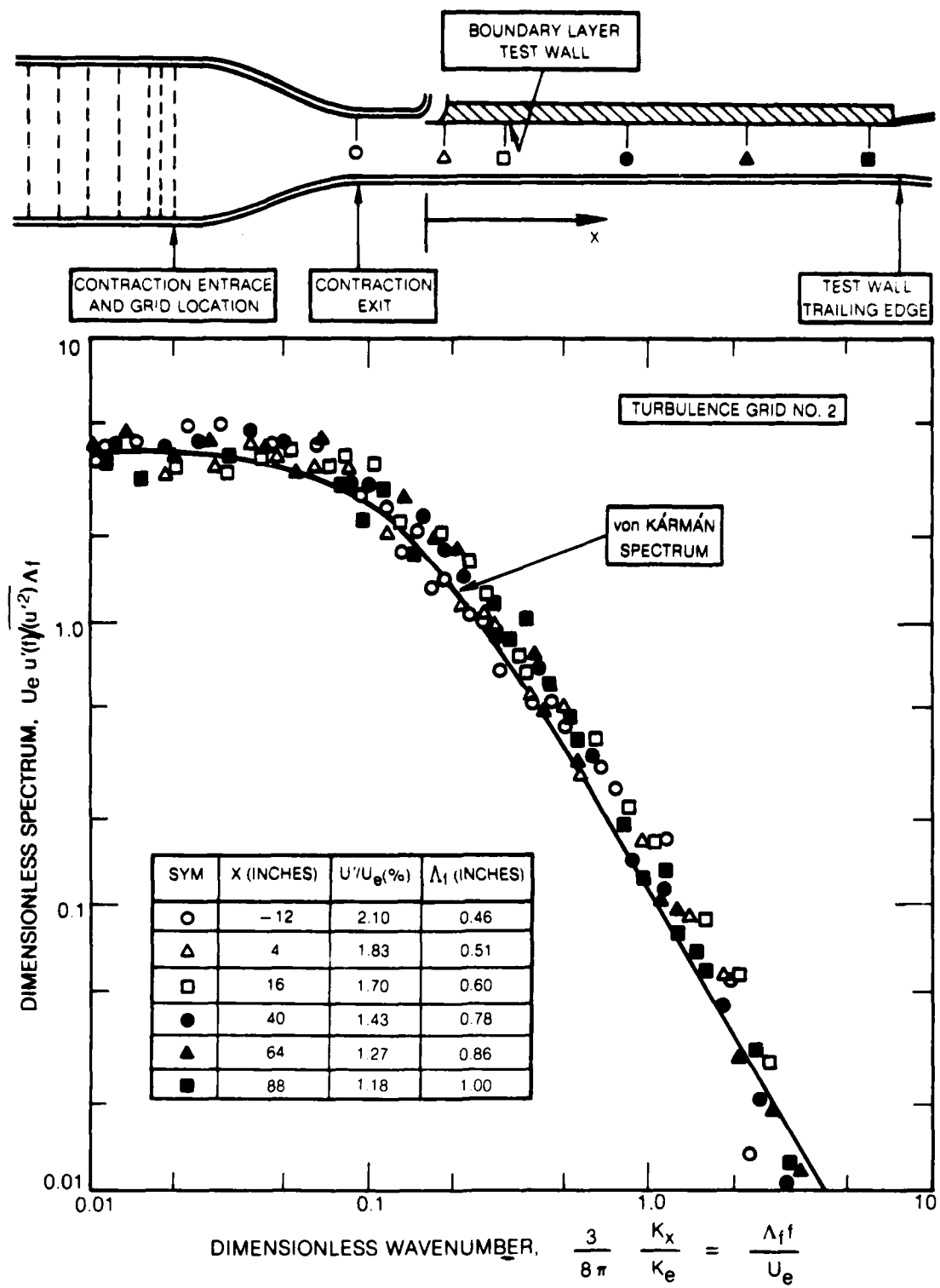


Figure 38. Free-Stream Power Spectral Density Distributions Measured at Various Streamwise Locations in the Test Section
Grid Number 2 Installed

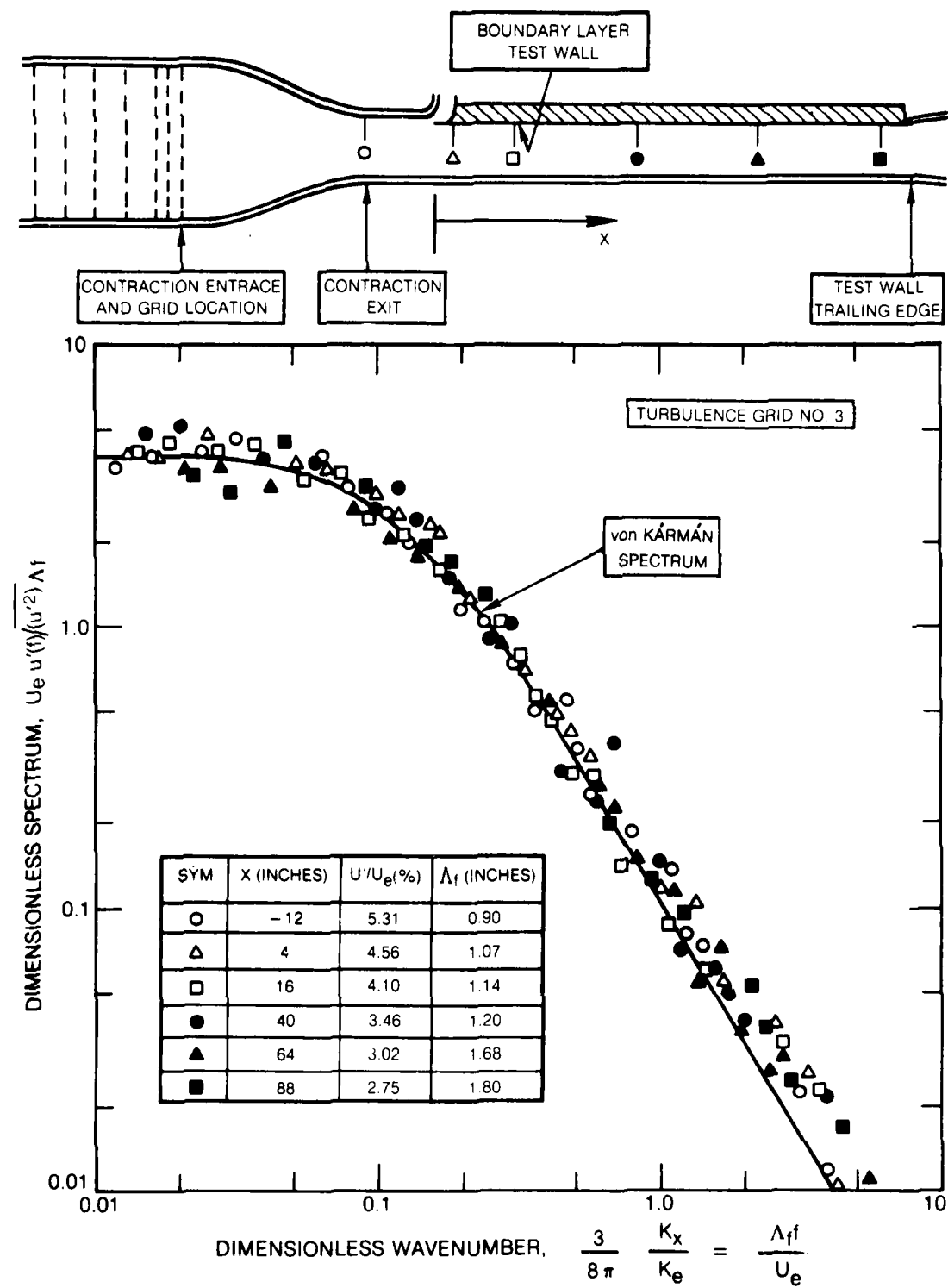


Figure 39. Free-Stream Power Spectral Density Distributions Measured at Various Streamwise Locations in the Test Section
Grid Number 3 Installed

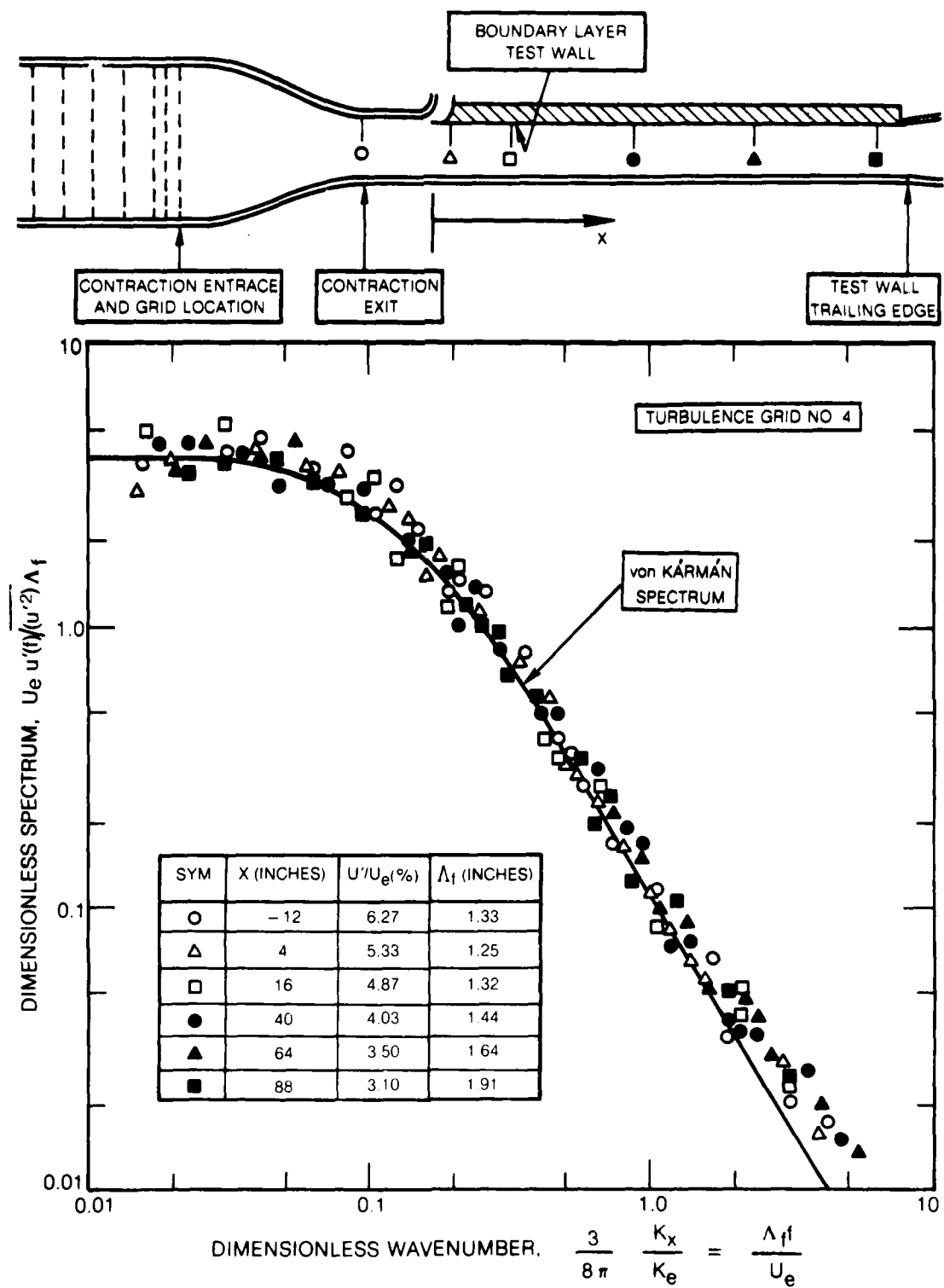


Figure 40. Free-Stream Power Spectral Density Distributions Measured at Various Streamwise Locations in the Test Section Grid Number 4 Installed

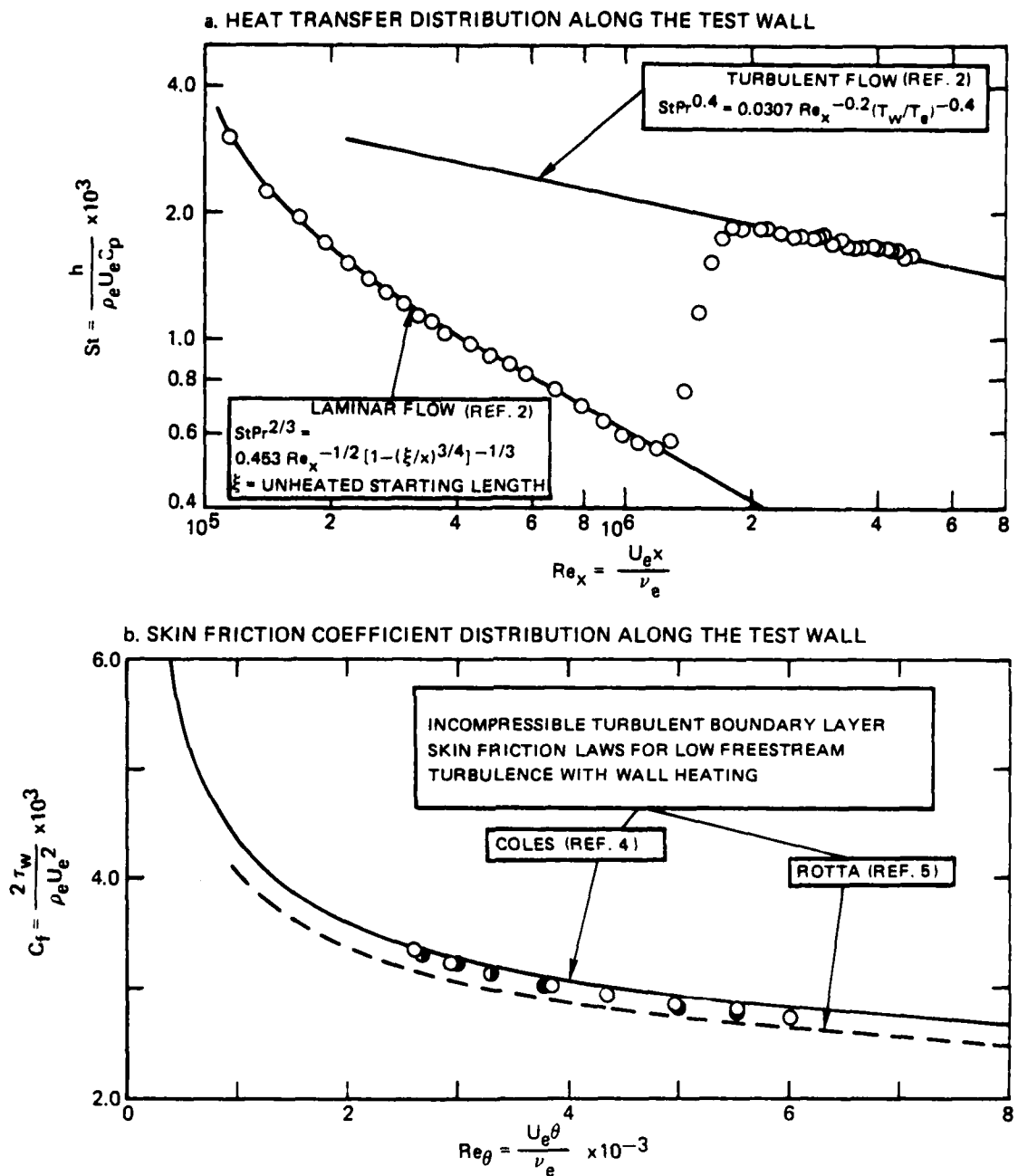


Figure 41. Heat Transfer and Skin Friction Coefficients Measured for the Minimum Freestream Turbulence Test Configuration with Natural Boundary Layer Transition \circ Tunnel C_L ; \bullet 6 in East of C_L ; \bullet 6 in West of C_L

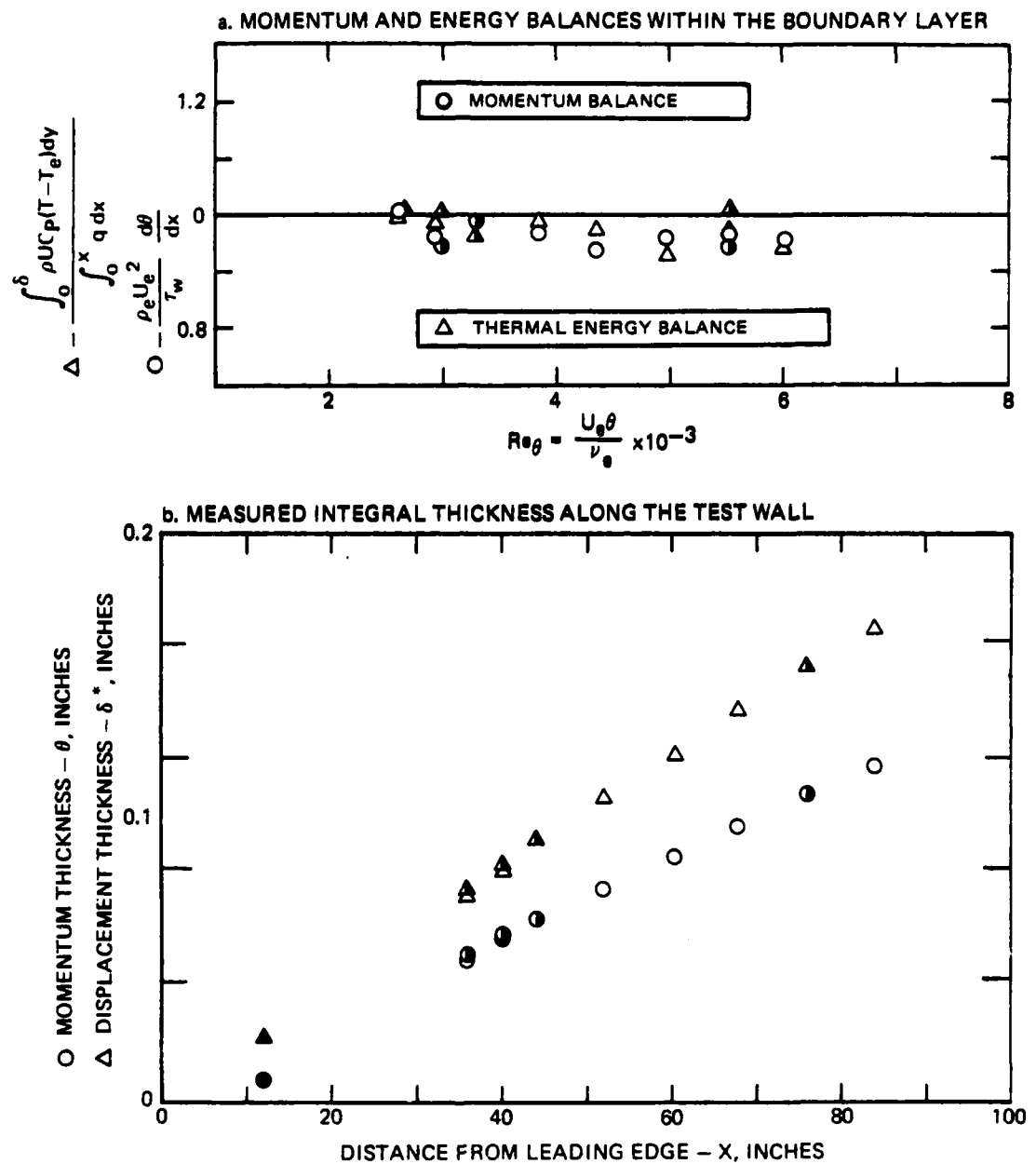


Figure 42. Boundary Layer Properties Measured for the Minimum Freestream Turbulence Test Configuration and Natural Transition of the Test Wall Boundary Layer
 ○ Tunnel C_L ; ● 6 in East of C_L ; ● in West of C_L

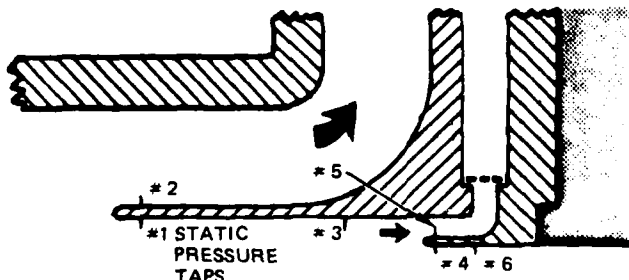
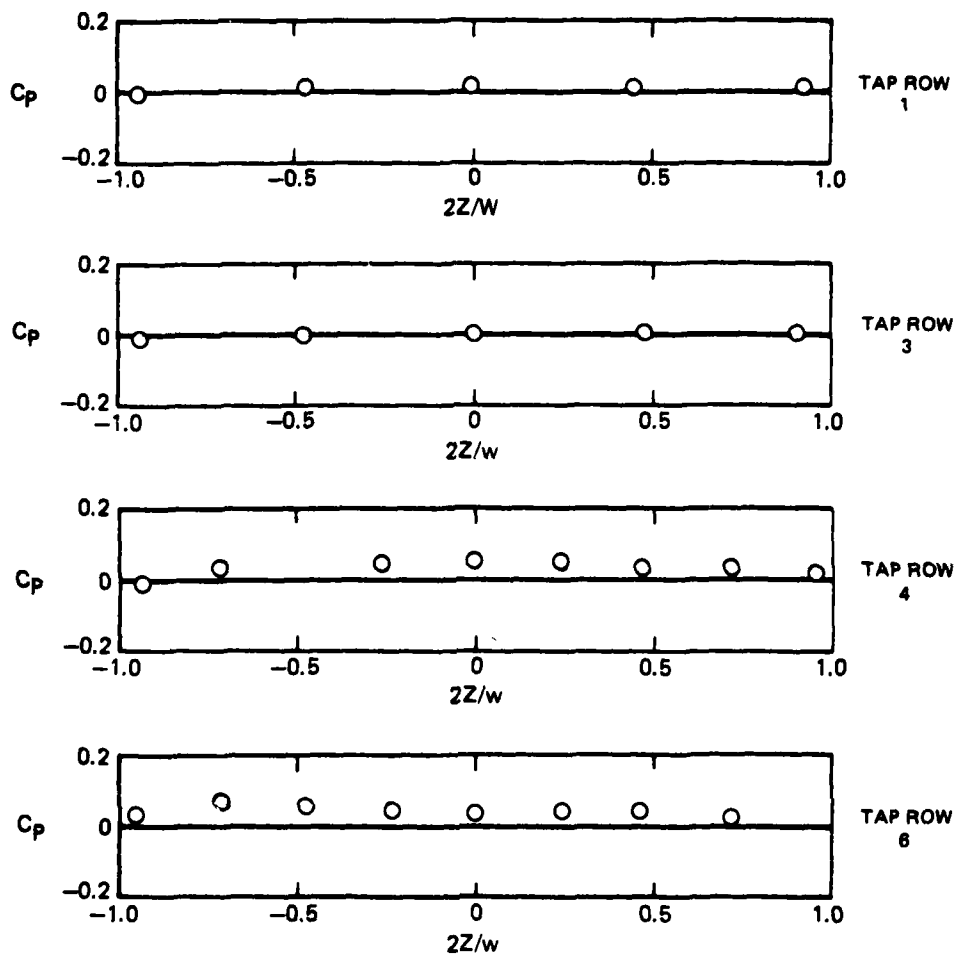


Figure 43. Transverse Distribution of Static Pressure along the Test Wall Leading Edge Bleed Scoop for the Minimum Freestream Turbulence Configuration and Natural Transition of the Test Wall Boundary Layer

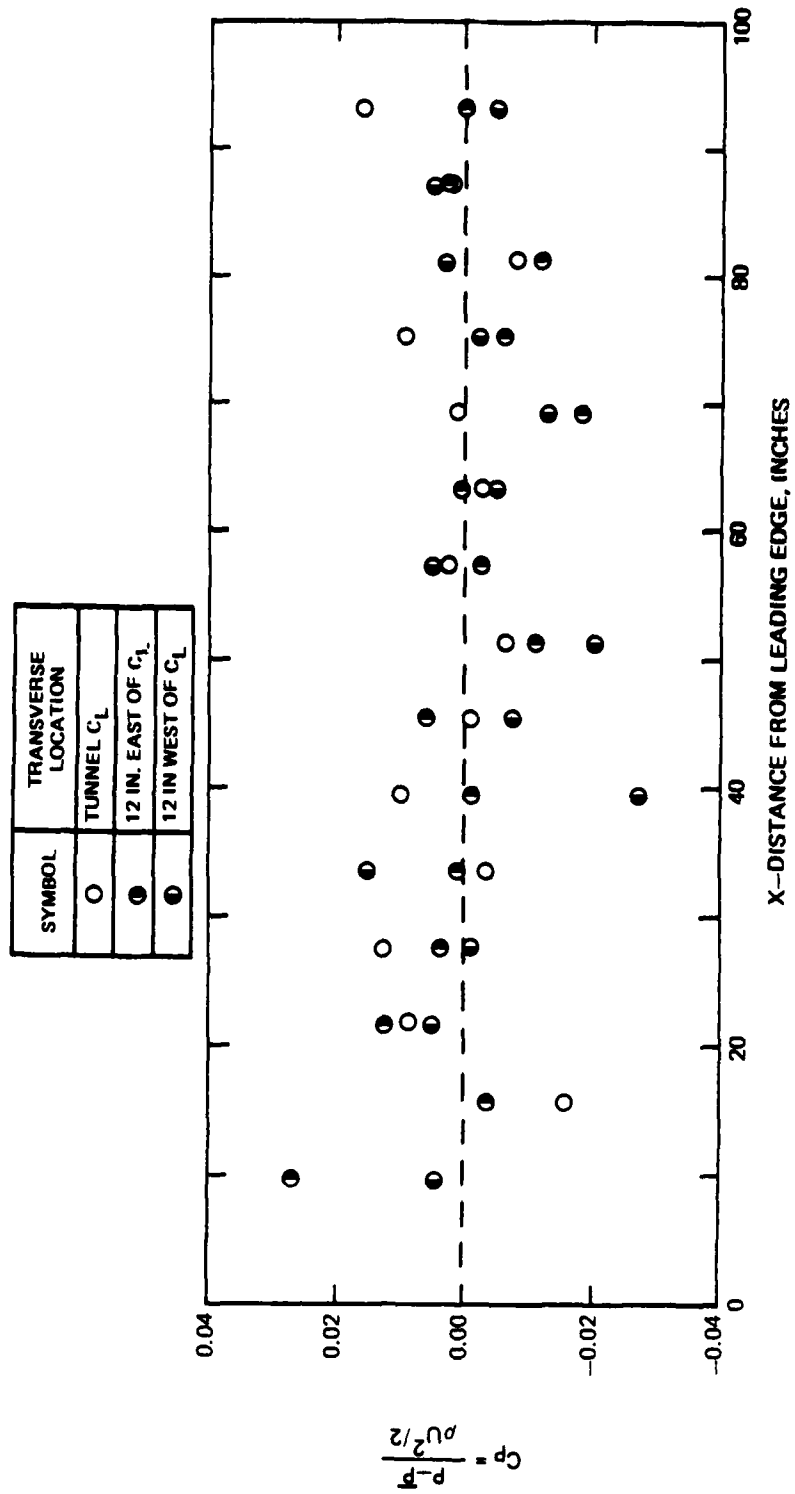
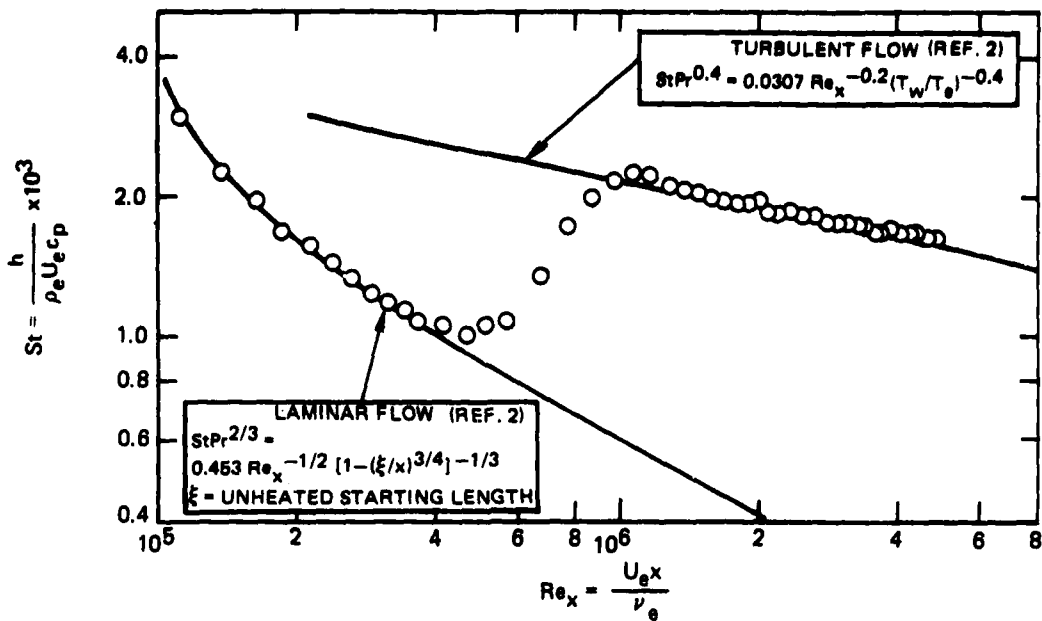


Figure 44. Static Pressure Distribution Along The Uniform Heat Flux Test Wall For The Minimum Freestream Turbulence Configuration and Natural Transition of the Test Wall Boundary Layer

R80-914388-12

a. HEAT TRANSFER DISTRIBUTION ALONG THE TEST WALL



b. SKIN FRICTION COEFFICIENT DISTRIBUTION ALONG THE TEST WALL

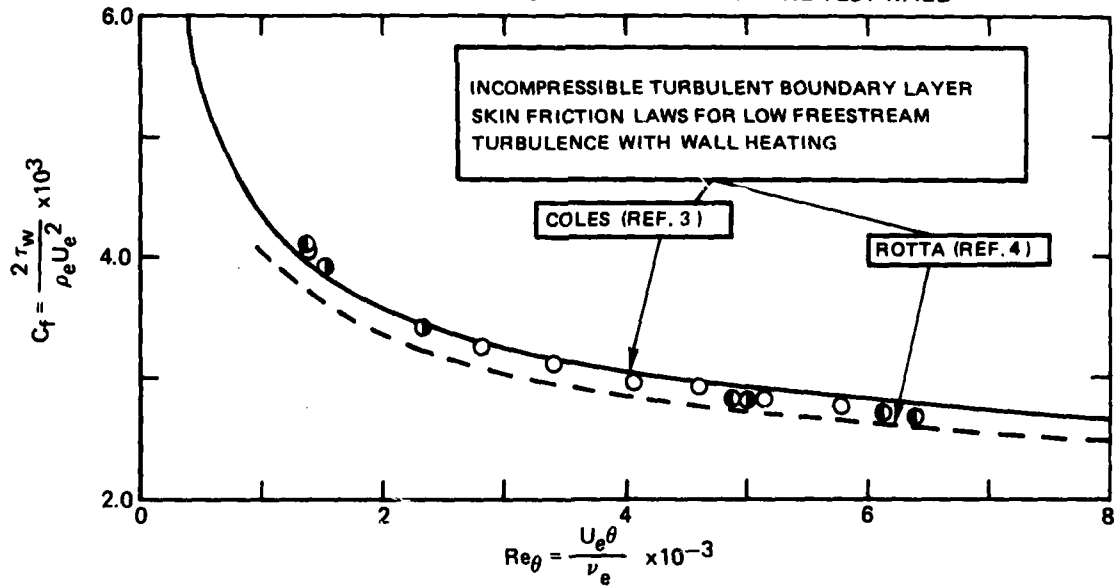


Figure 45. Heat Transfer and Skin Friction Coefficients Measured With Turbulence Generating Grid Number 1 Installed Tunnel C_L ; \bullet 6 in East of C_L ; \circ 6 in West of C_L

R80-914388-12

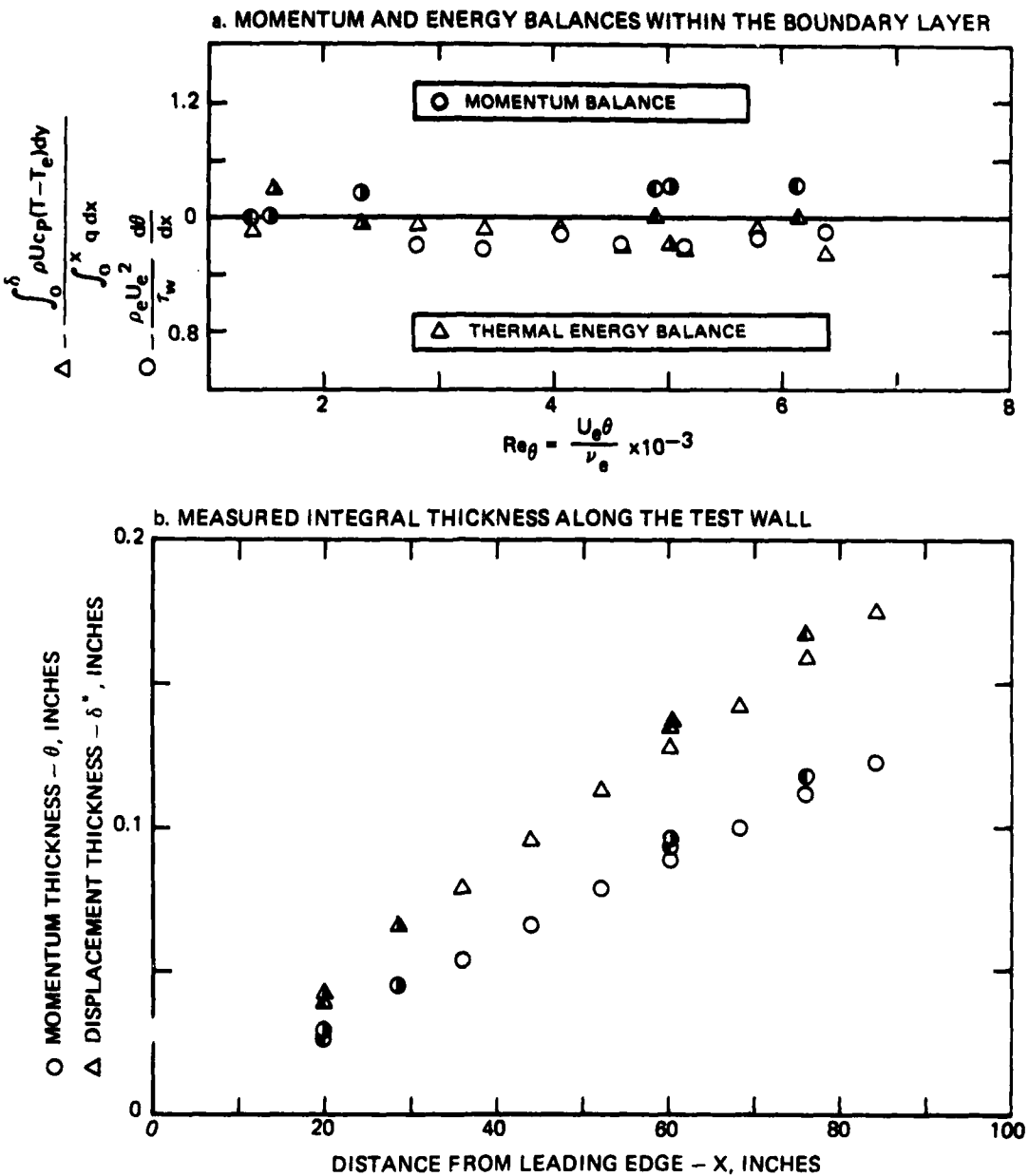


Figure 46. Boundary Layer Properties Measured With Turbulence Generating Grid Number 1 Installed
Tunnel C_L ; ○ 6 in East of C_L ; △ 6 in West of C_L

79-08-112-4

R80-914388-12

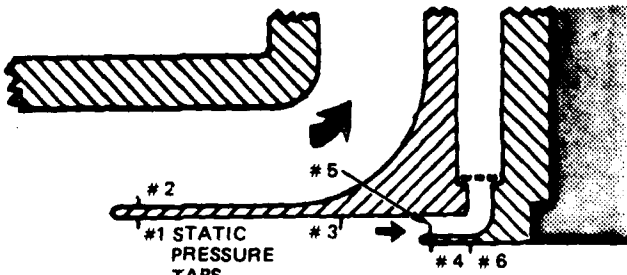
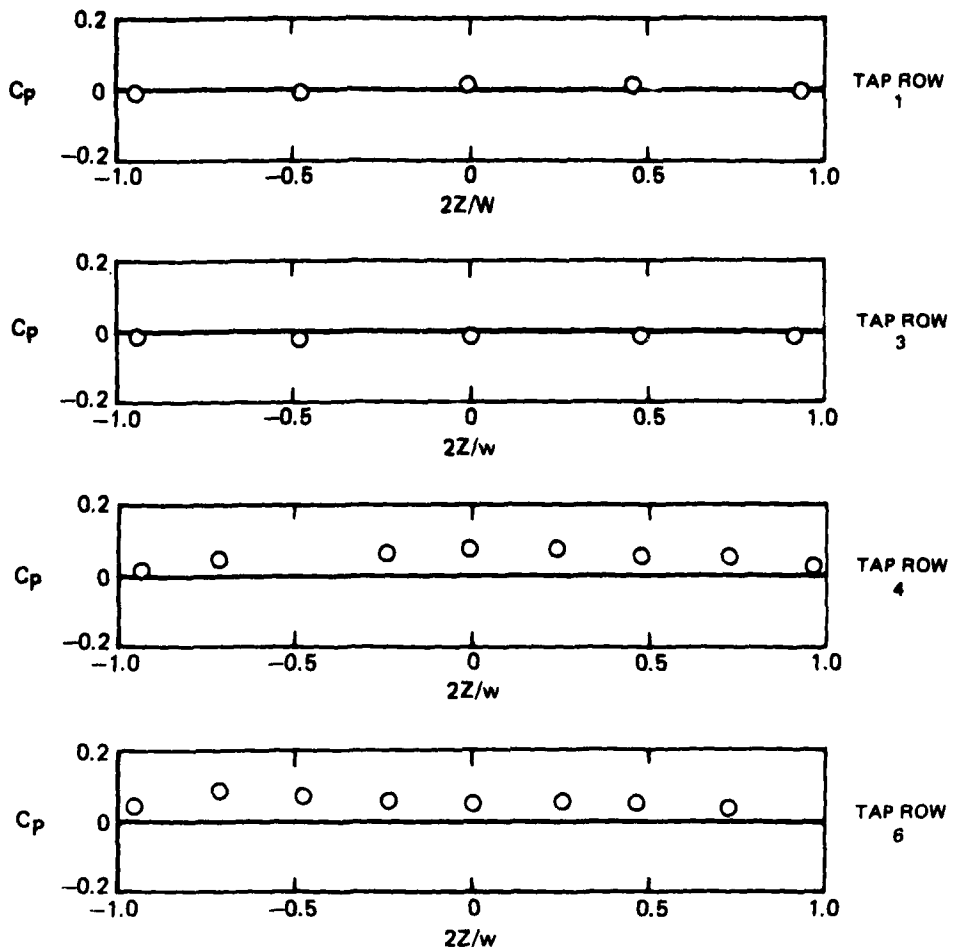


Figure 47. Transverse Distribution of Static Pressure Along the Test Wall Leading Edge Bleed Scoop with Turbulence Generating Grid Number 1 Installed

79-08-112-10

R80-914388-12

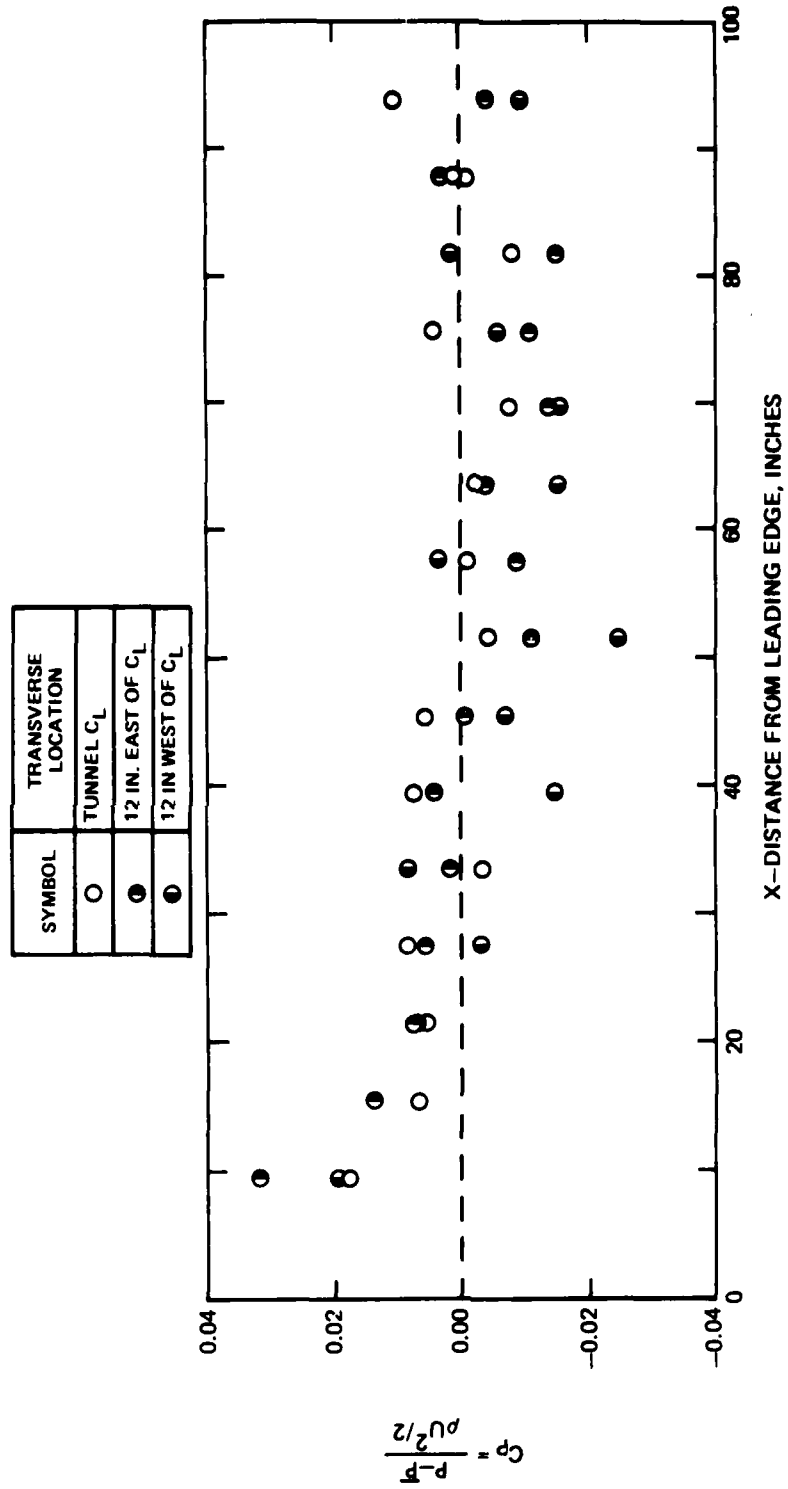
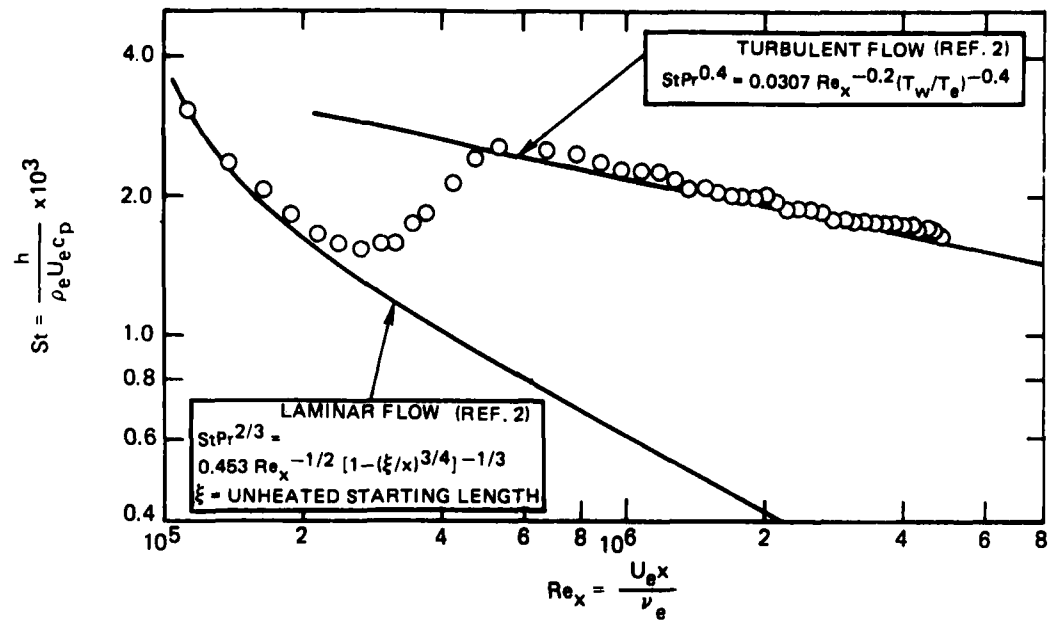


Figure 48. Static Pressure Distribution Along the Uniform Heat Flux Test Wall with Turbulence Generating Grid Number 1 Installed

79-08-112-7

a. HEAT TRANSFER DISTRIBUTION ALONG THE TEST WALL



b. SKIN FRICTION COEFFICIENT DISTRIBUTION ALONG THE TEST WALL

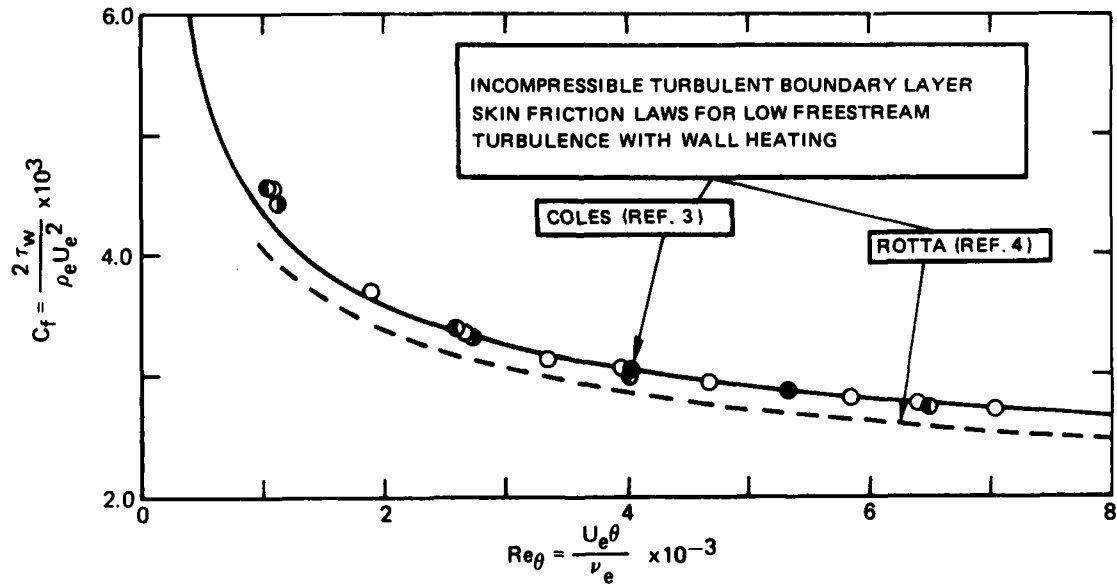


Figure 49. Heat Transfer and Skin Friction Coefficients Measured With
Turbulence Generating Grid Number 2 Installed
Tunnel C_L ; \bullet 6 in East of C_L ; \circ 6 in West of C_L

R80-914388-12

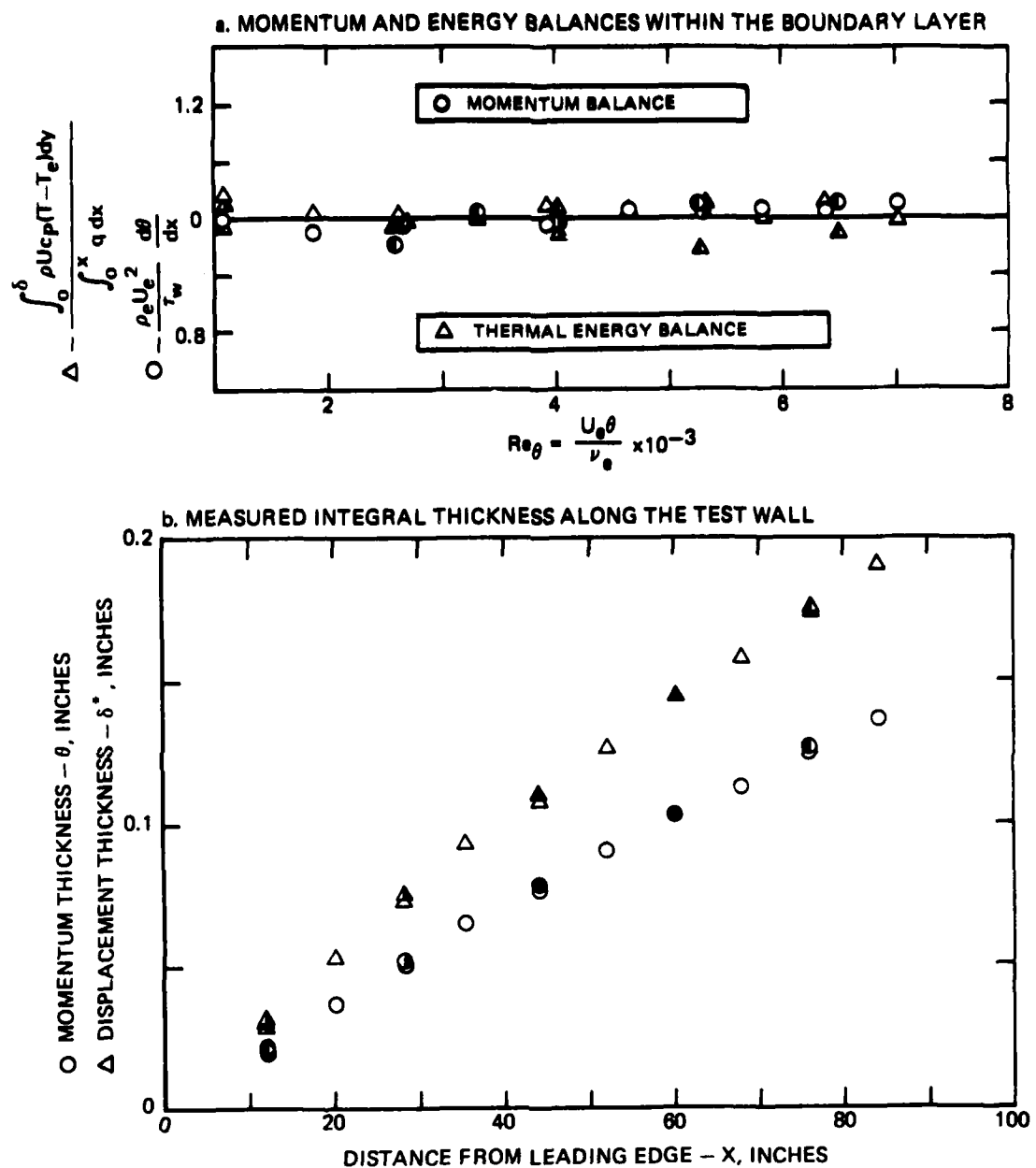


Figure 50. Boundary Layer Properties Measured with Turbulence Generating Grid Number 2 Installed
Tunnel C_L; ● 6 in East of C_L; ○ 6 in West of C_L

R80-914388-12

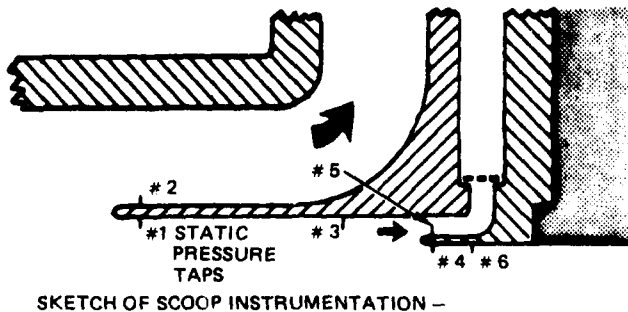
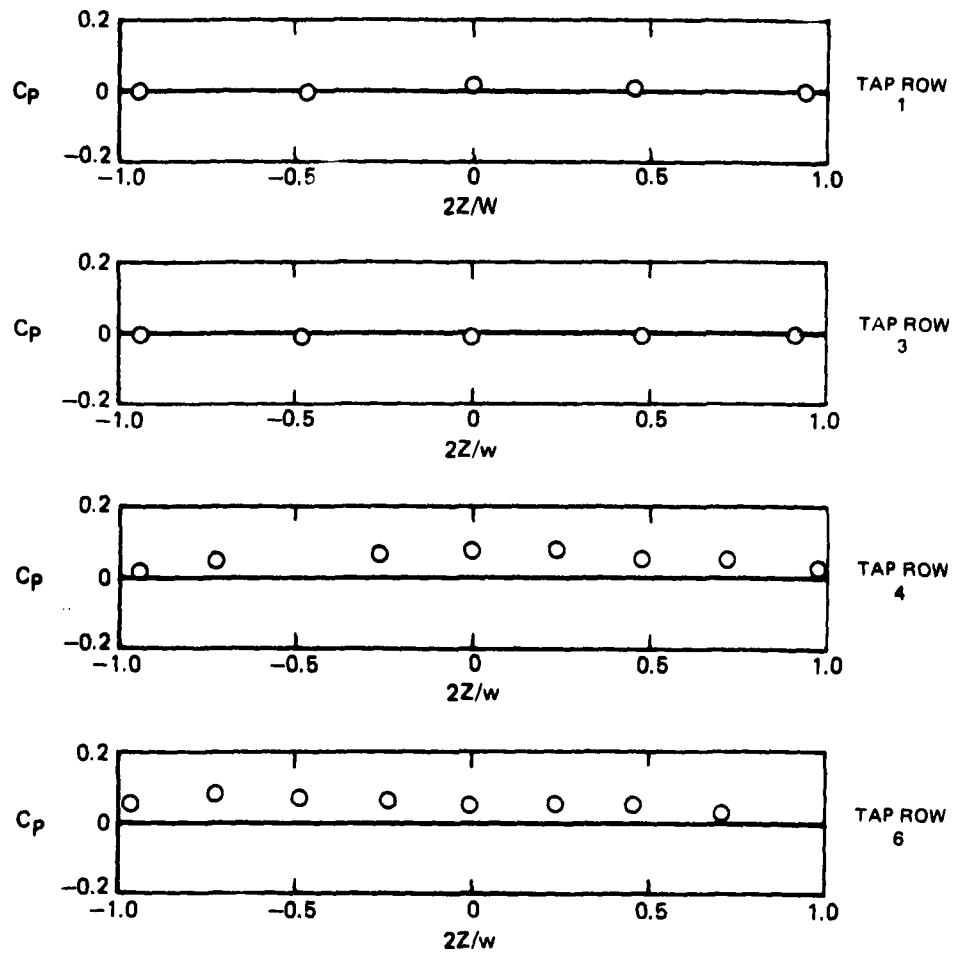


Figure 51. Transverse Distribution of Static Pressure Along the Test Wall Leading Edge Bleed Scoop with Turbulence Generating Grid Number 2 Installed

R80-914388-12

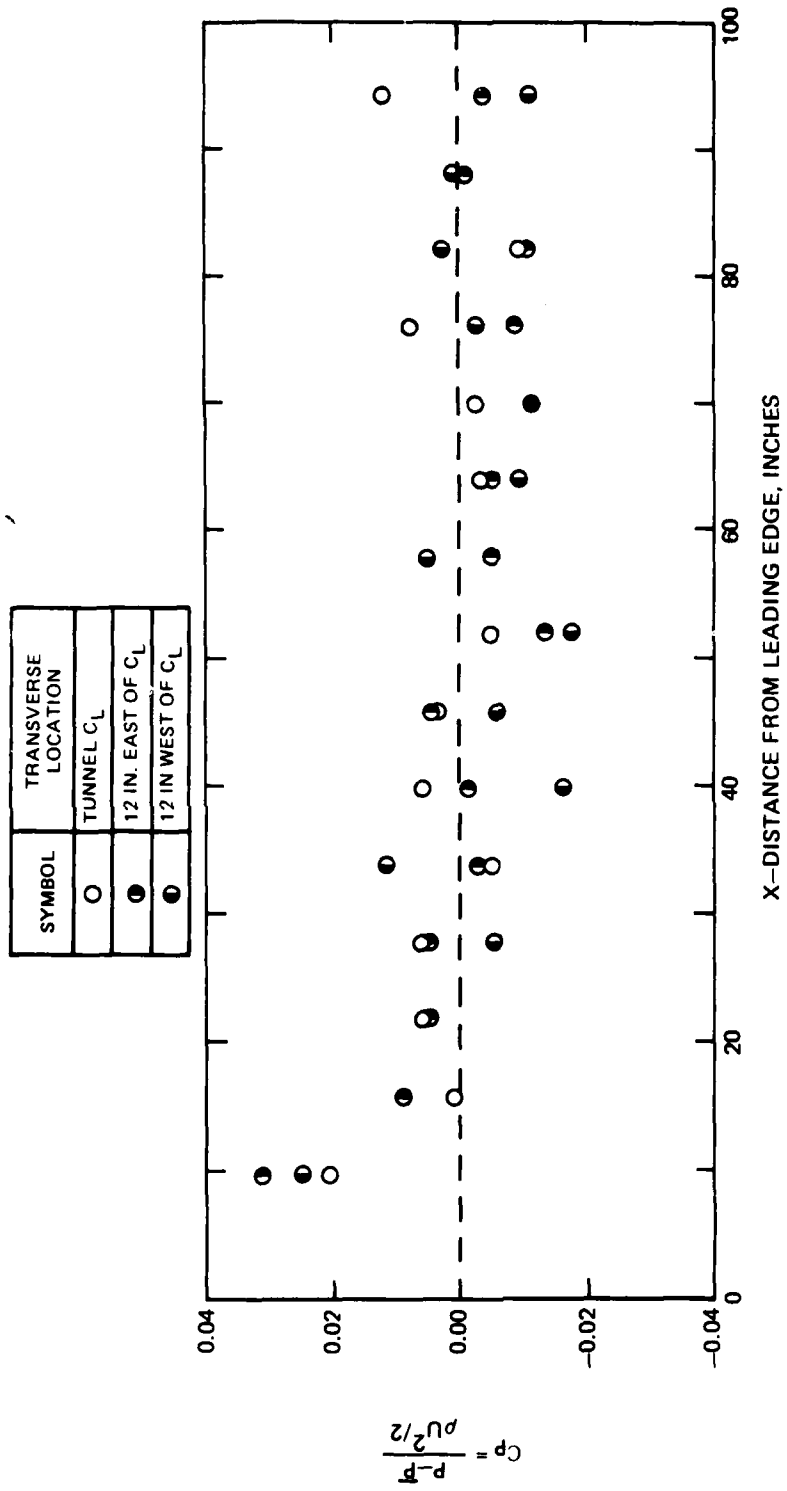


Figure 52. Static Pressure Distribution Along the Uniform Heat Flux Test Wall with Turbulence Generating Grid Number 2 Installed

79-08-112-8

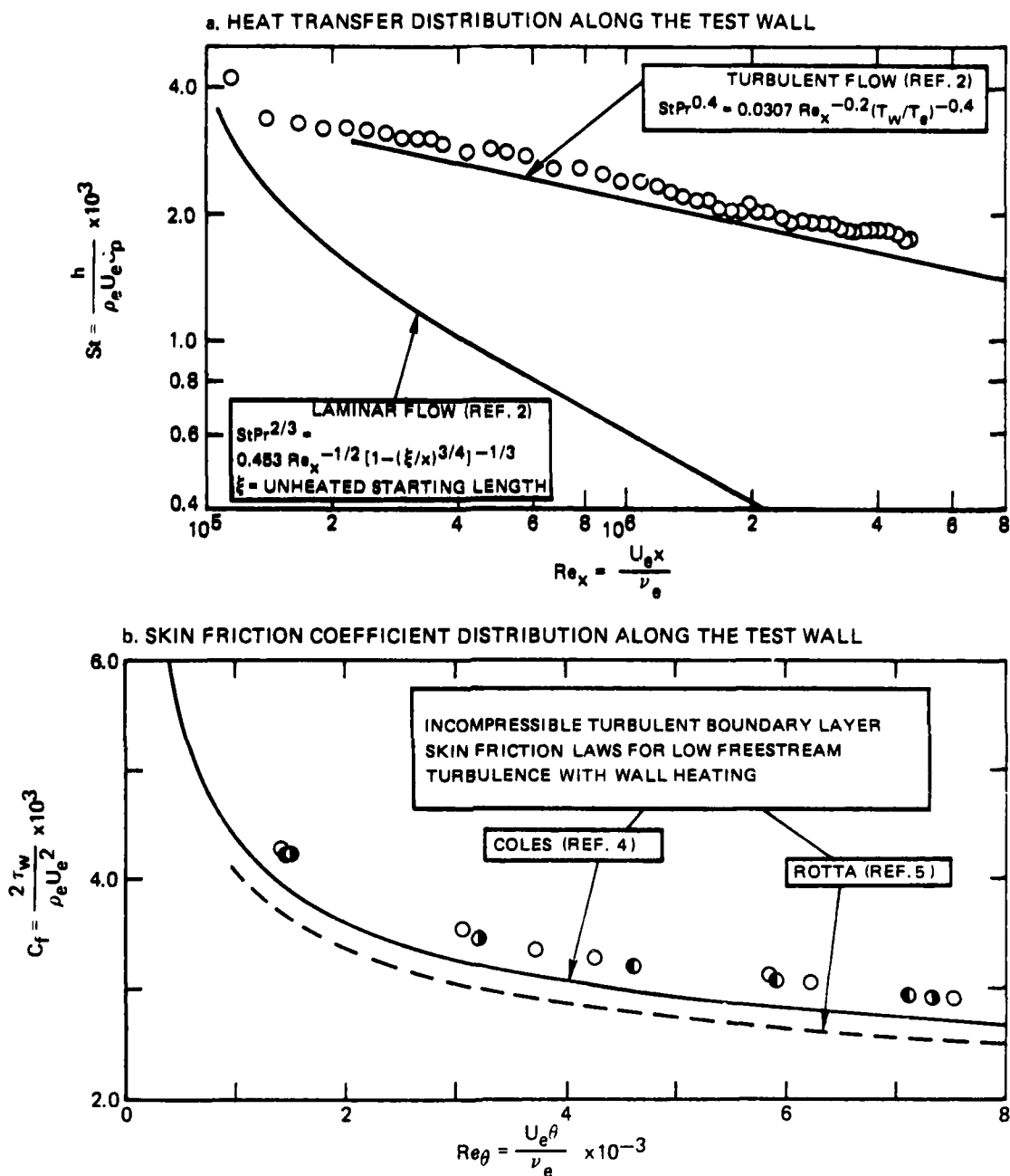


Figure 53. Heat Transfer and Skin Friction Coefficients Measured With Turbulence Generating Grid Number 3 Installed
○ Tunnel C_L ; ● 6 in East of C_L ; ● 6 in West of C_L

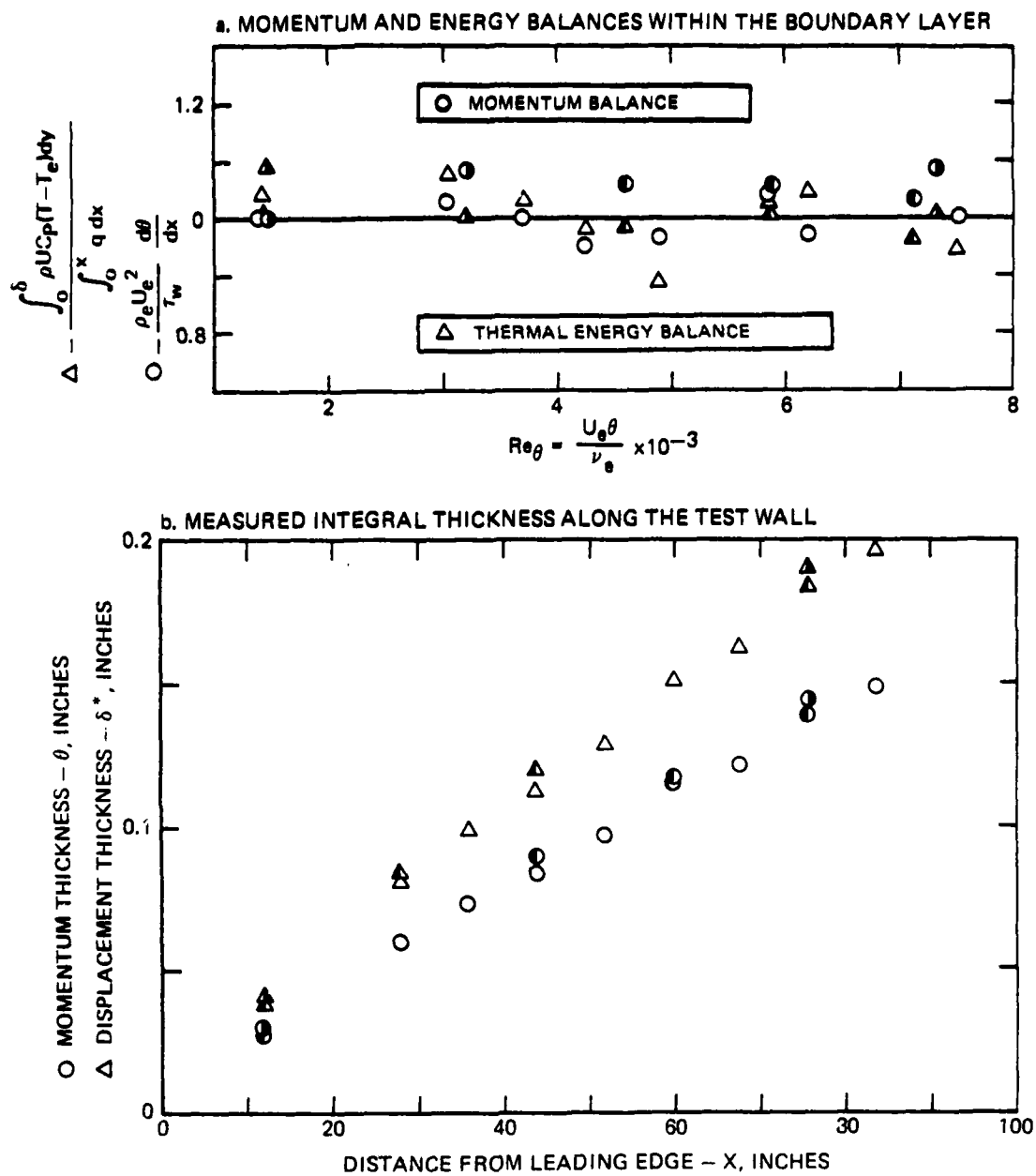


Figure 54. Boundary Layer Properties Measured with Turbulence Generating Grid Number 3 Installed
 ○ Tunnel C_L ; ● 6 in East of C_L ; ● 6 in West of C_L

R80-914388-12

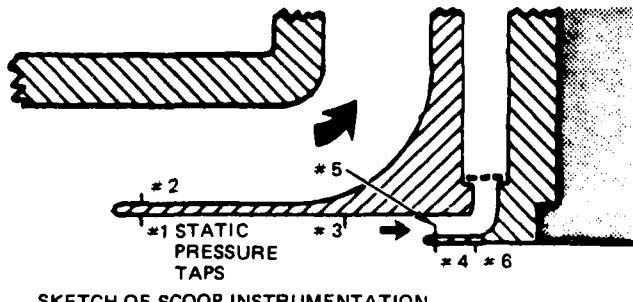
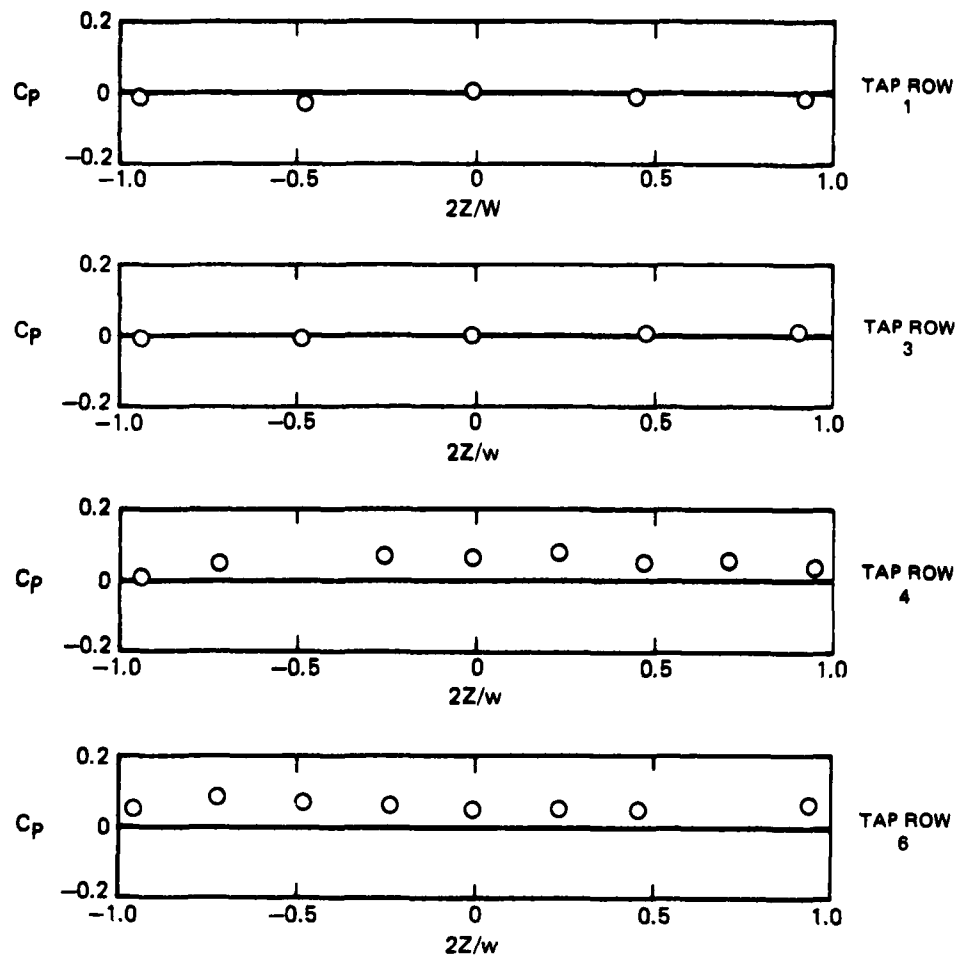


Figure 55. Transverse Distribution of Static Pressure along the Test Wall Leading Edge Bleed Scoop with Turbulence Generating Grid Number 3 Installed

79-06-70-10

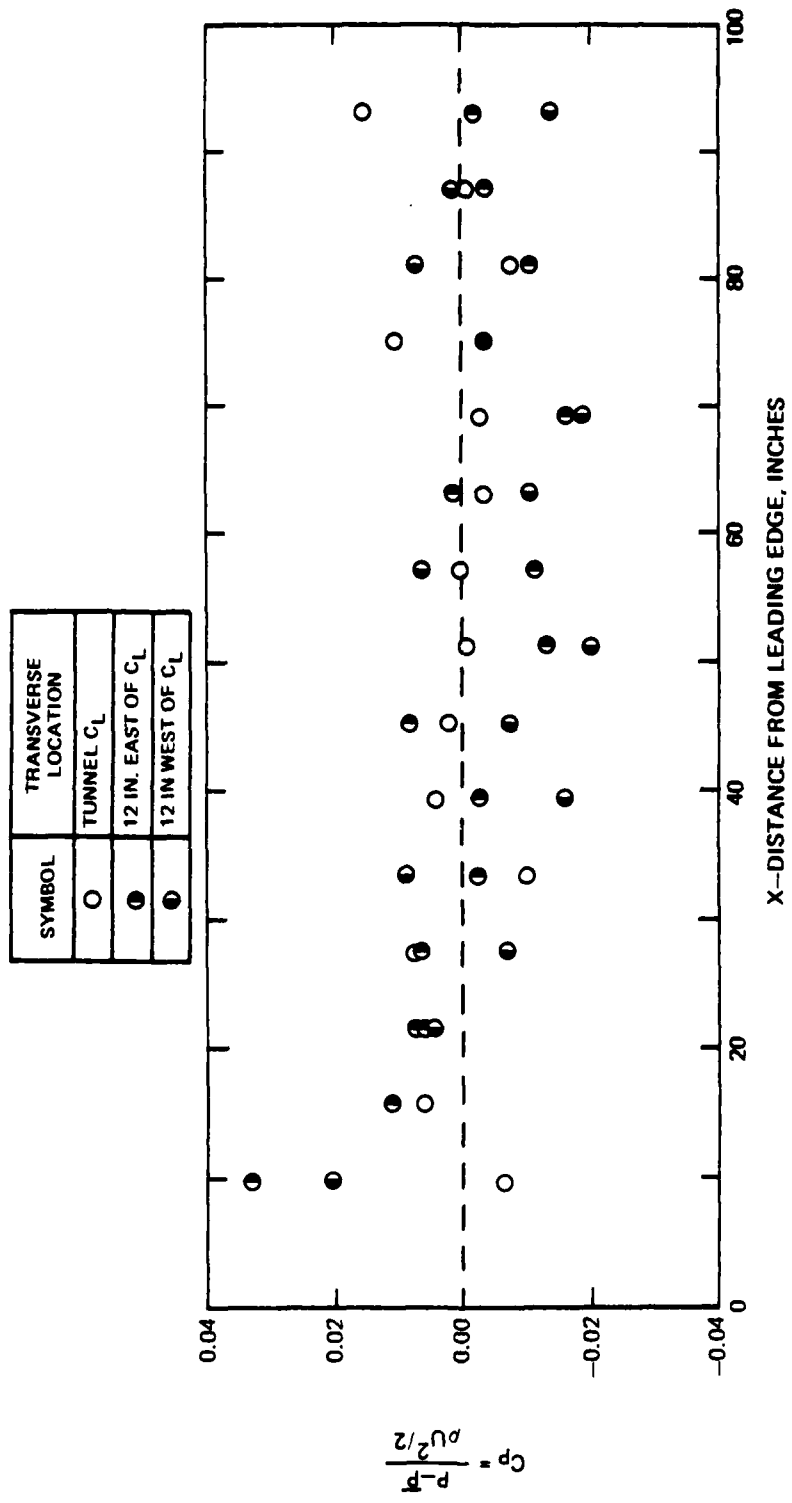
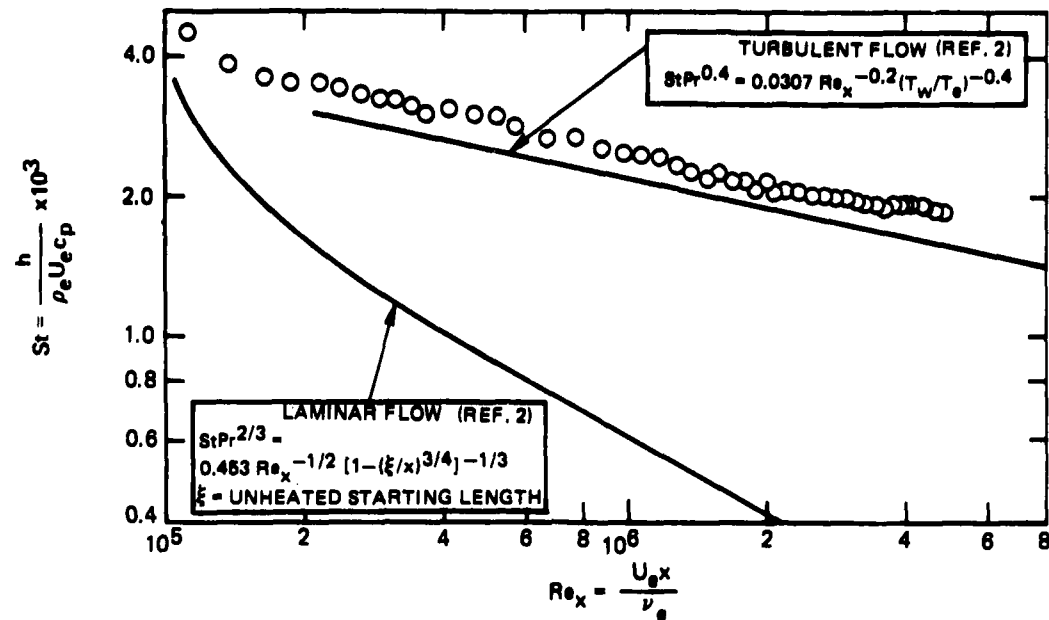


Figure 56. Static Pressure Distribution Along the Uniform Heat Flux Test Wall with Turbulence Generating Grid Number 3 Installed

a. HEAT TRANSFER DISTRIBUTION ALONG THE TEST WALL



b. SKIN FRICTION COEFFICIENT DISTRIBUTION ALONG THE TEST WALL

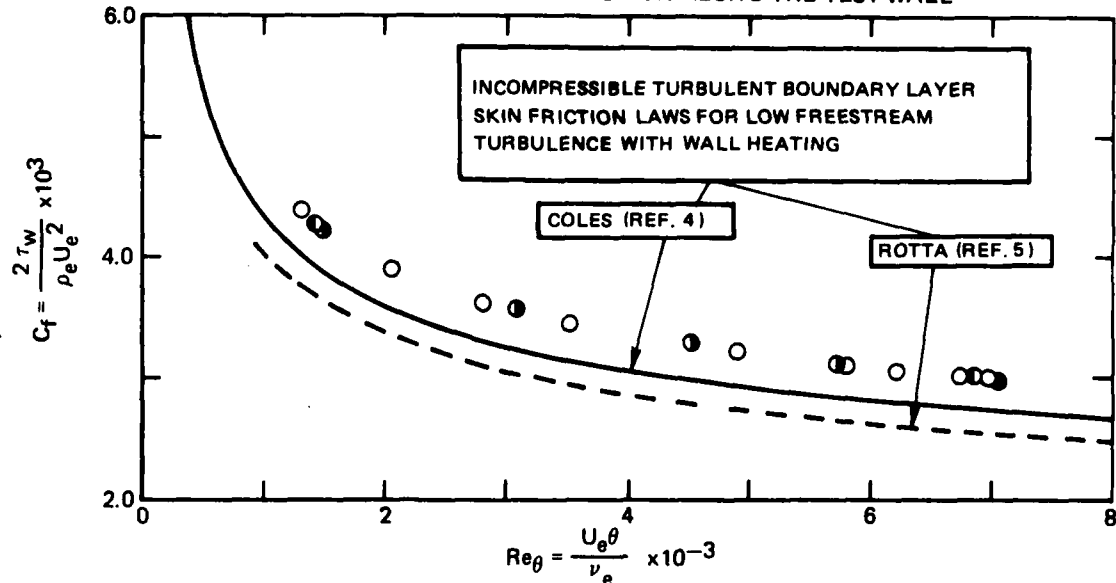


Figure 57. Heat Transfer and Skin Friction Coefficients Measured With Turbulence Generating Grid Number 4 Installed Tunnel C_L ; \bullet 6 in East of C_L ; \circ 6 in West of C_L

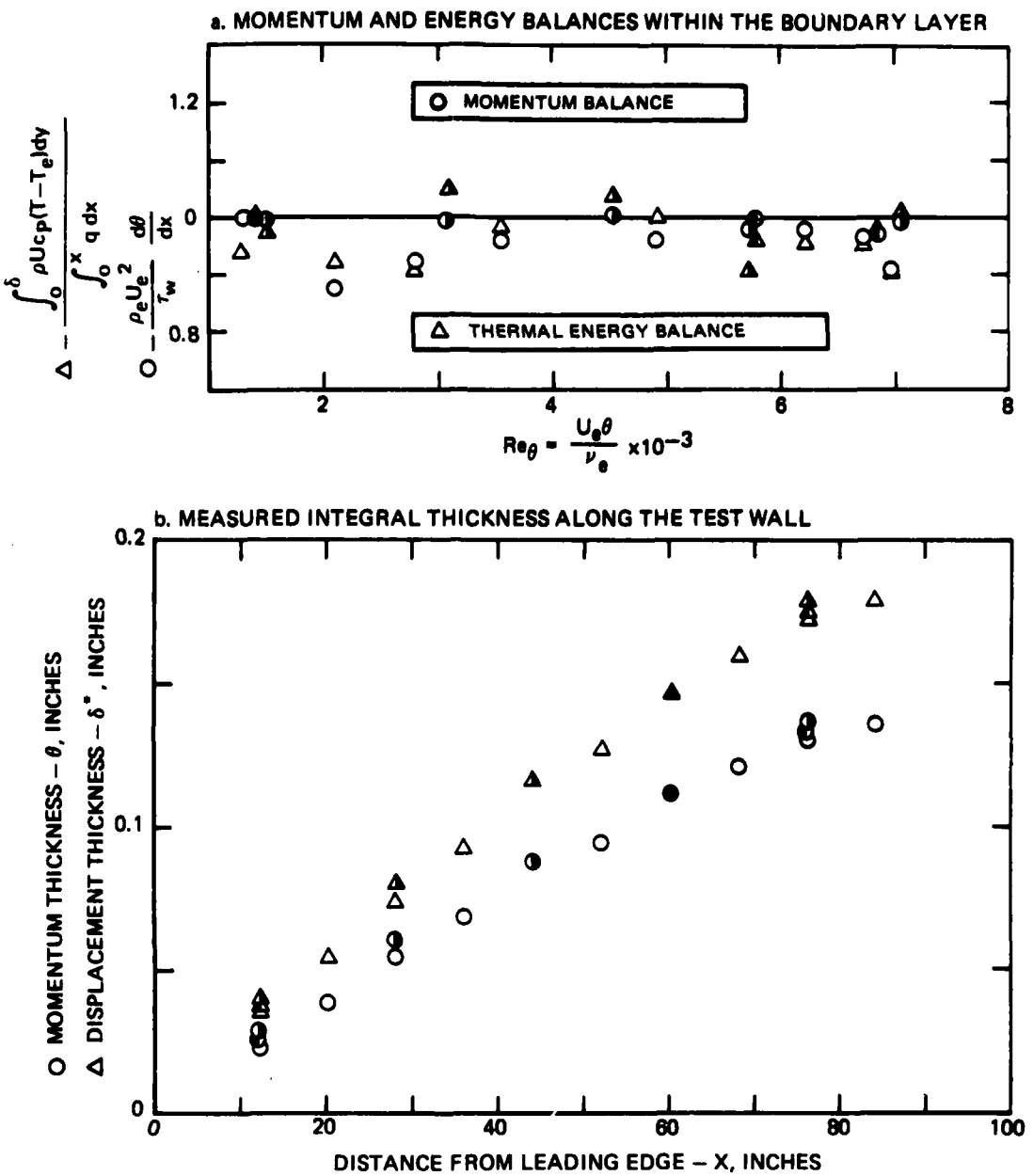


Figure 58. Boundary Layer Properties Measured with Turbulence Generating Grid Number 4 Installed
Tunnel C_L ; ○ 6 in East of C_L ; ● 6 in West of C_L

R80-914388-12

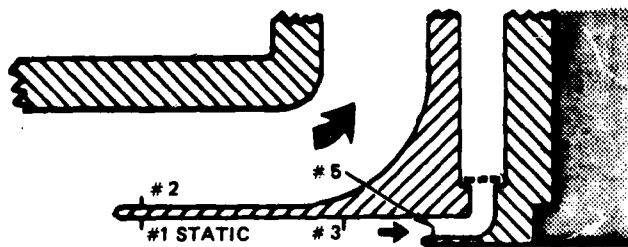
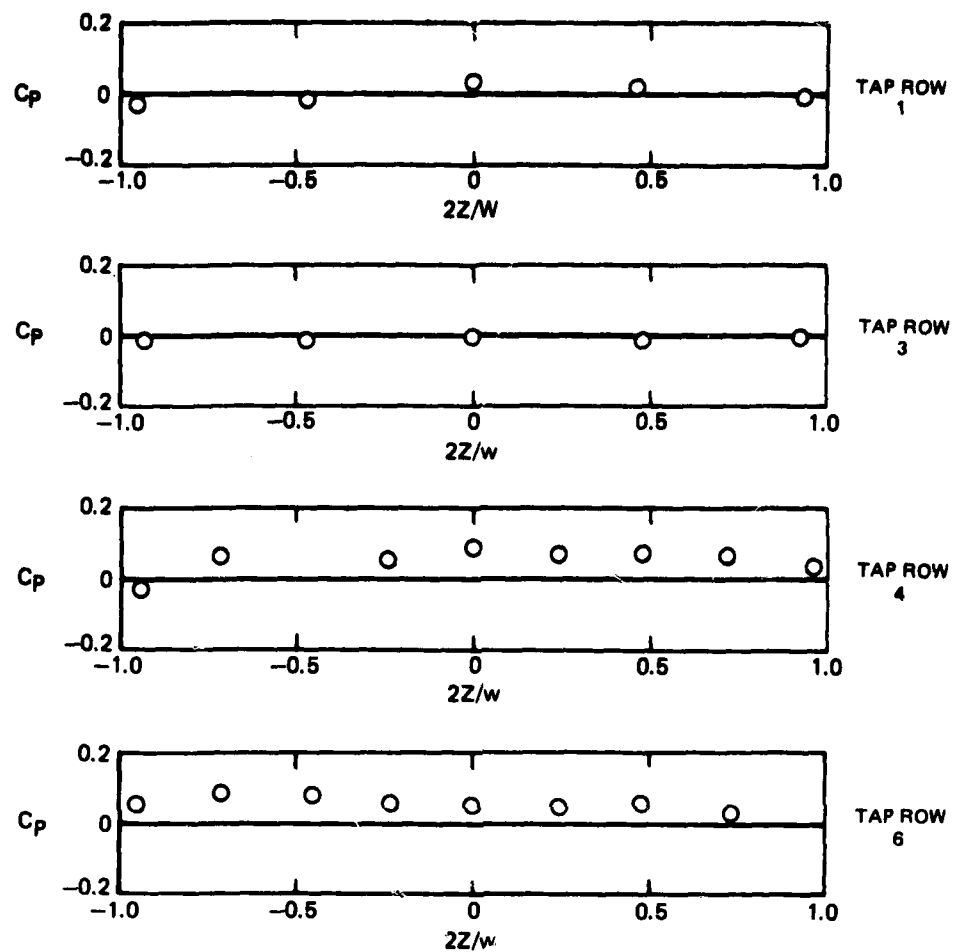


Figure 59. Transverse Distribution of Static Pressure Along the Test Wall Leading Edge Bleed Scoop with Turbulence Generating Grid Number 4 Installed

79-08-112-12

R80-914388-12

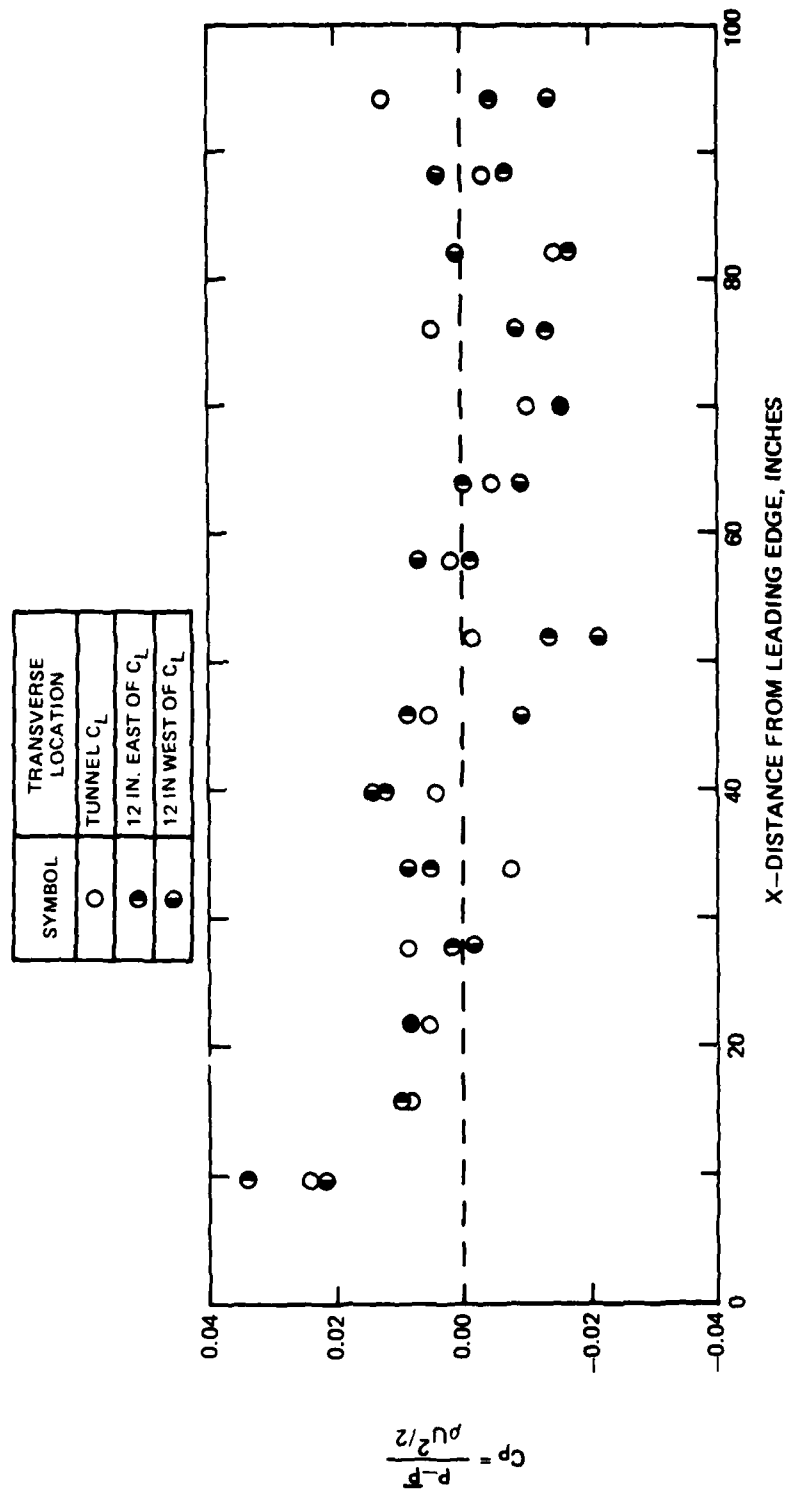


Figure 60. Static Pressure Distribution Along the Uniform Heat Flux Test Wall with Turbulence Generating Grid Number 4 Installed

79-08-112-9

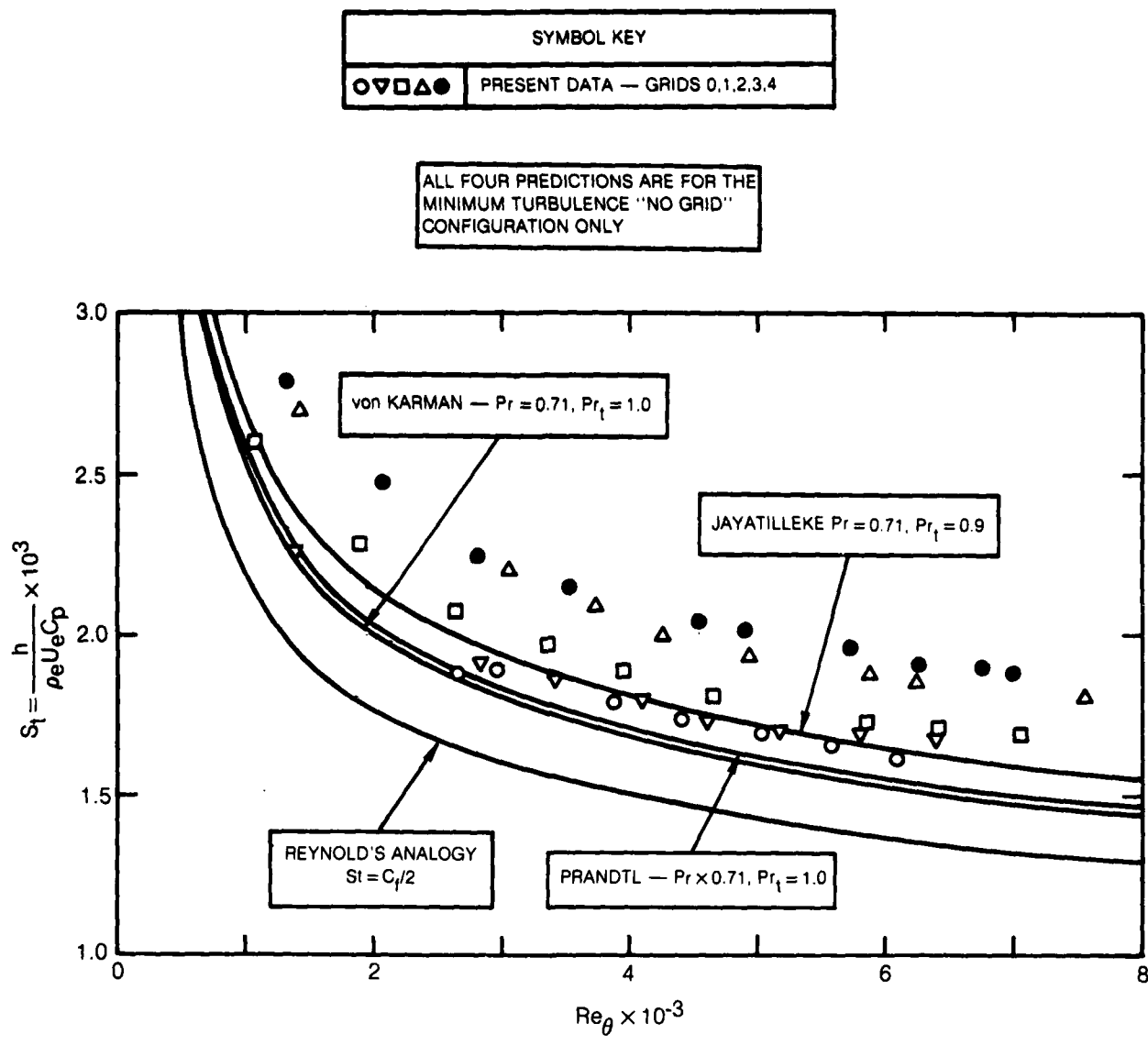


Figure 61. Heat Transfer Distributions for all 5 Turbulence Levels as a Function of Re_θ

SYMBOL KEY		Re _θ RANGE
▲	HUFFMAN et al (REF. 31)	4000-5300
■	CHARNAY et al (REF. 32)	700-2000
— - -	MEIER & KREPLIN CORRELATION (REF. 33)	3500-5400
— · —	SIMONICH & BRADSHAW CORRELATION (REF. 34)	1000-6500
○ ▽ □ △ ●	PRESENT DATA — GRIDS 0,1,2,3,4	1000-7500

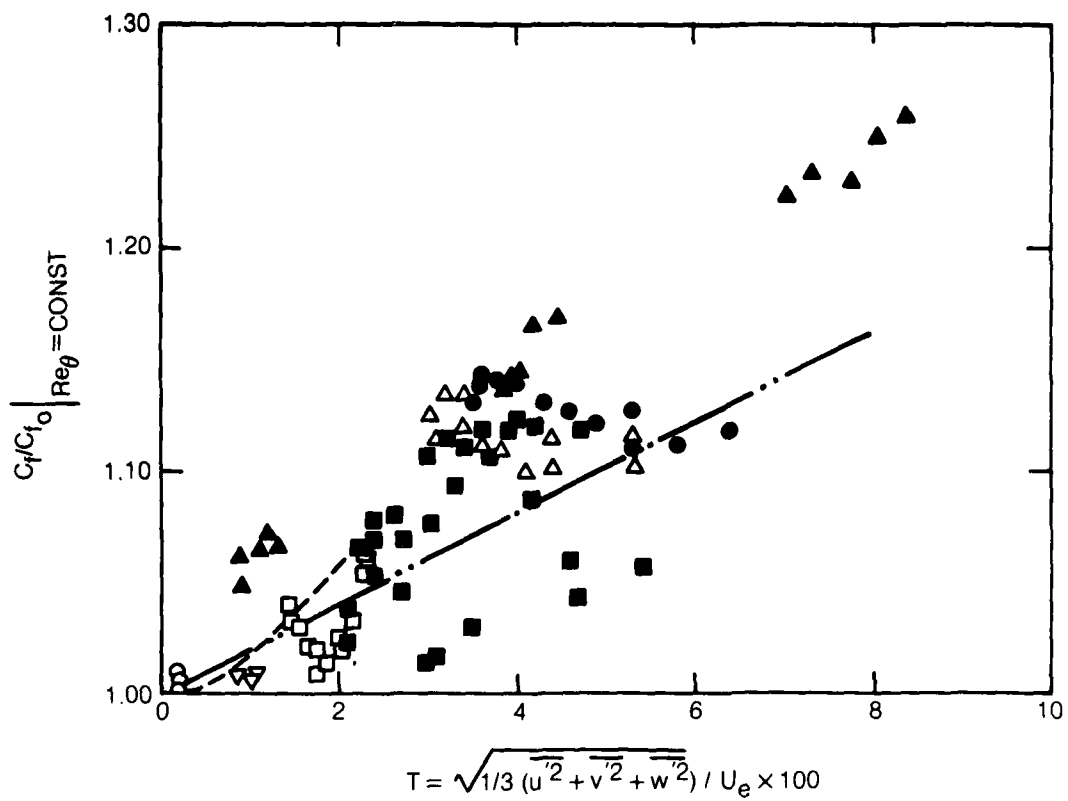


Figure 62. Influence of Turbulence Intensity on the Skin Friction Coefficient

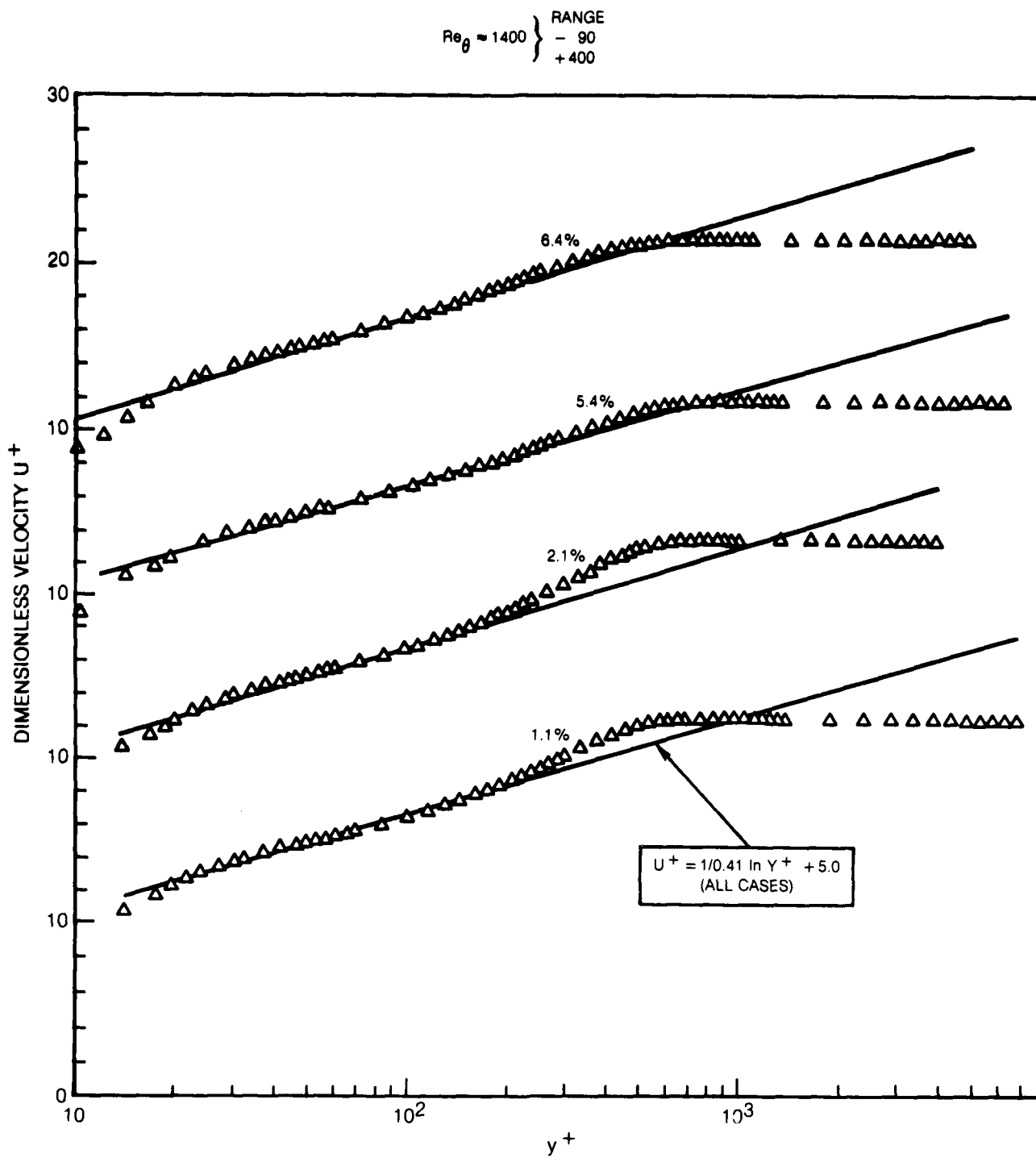


Figure 63A. Comparison of Mean Velocity Profile Shapes for Various Free-Stream Turbulence Levels for $Re_\theta \approx 1400$

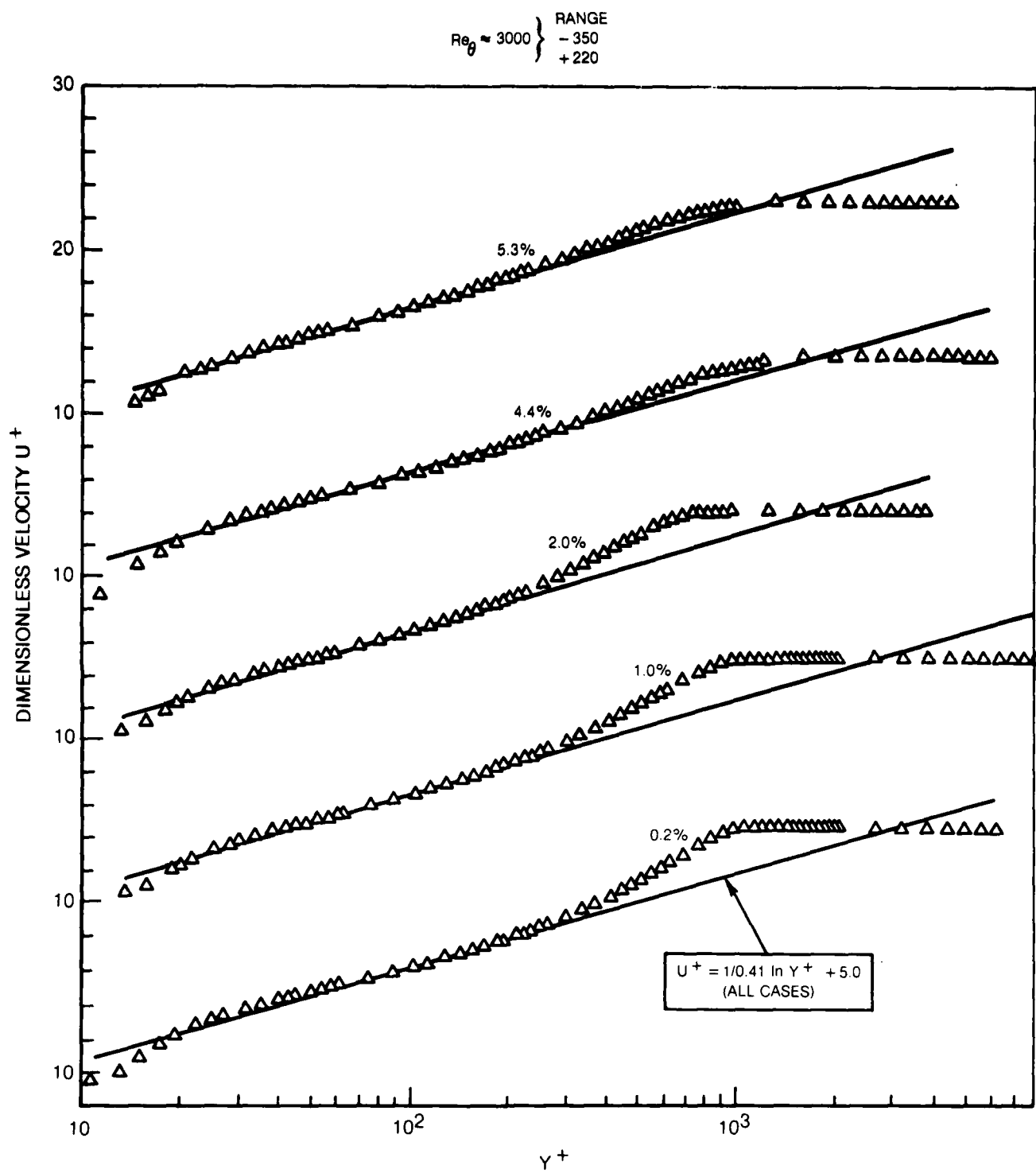


Figure 63B. Comparison of Mean Velocity Profile Shapes for Various Free-Stream Turbulence Levels for $Re_\theta \approx 3000$

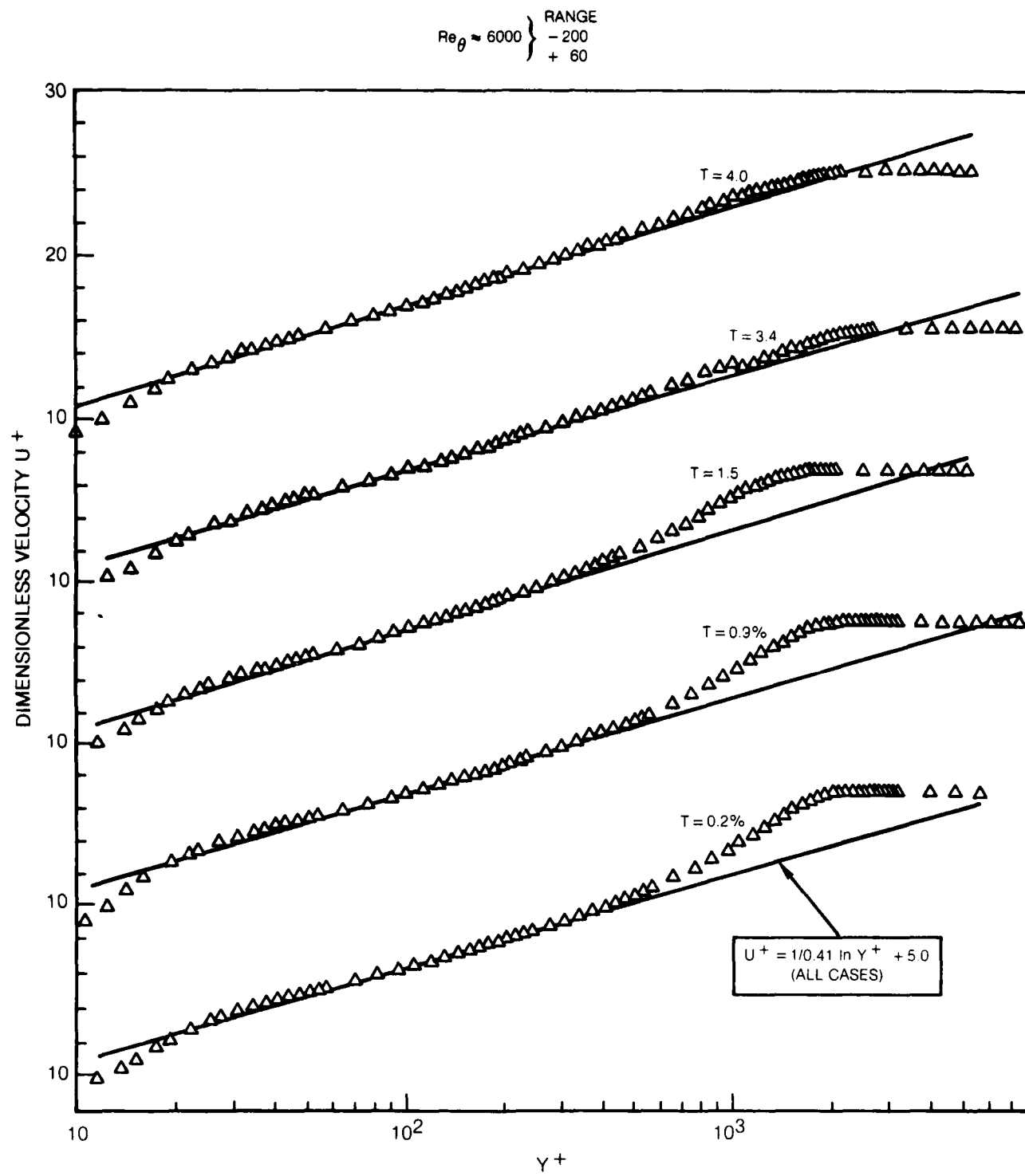
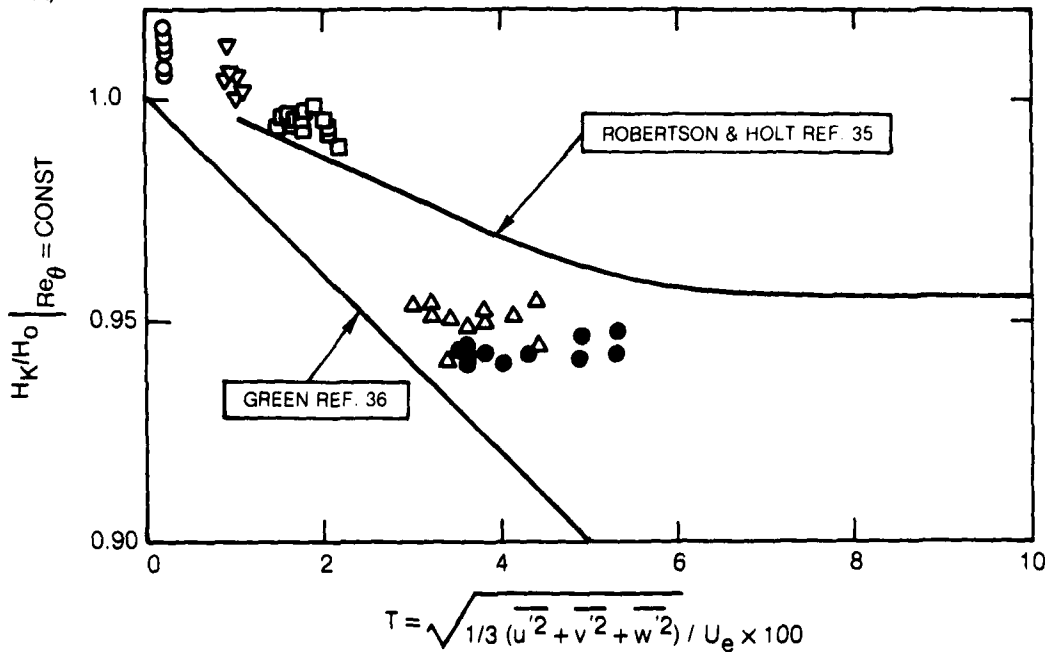


Figure 63C. Comparison of Mean Velocity Profile Shapes for Various Free-Stream Turbulence Levels for $Re_\theta \approx 6000$

SYMBOL KEY	
○▽□△●	PRESENT DATA — GRIDS 0,1,2,3,4

A)



B)

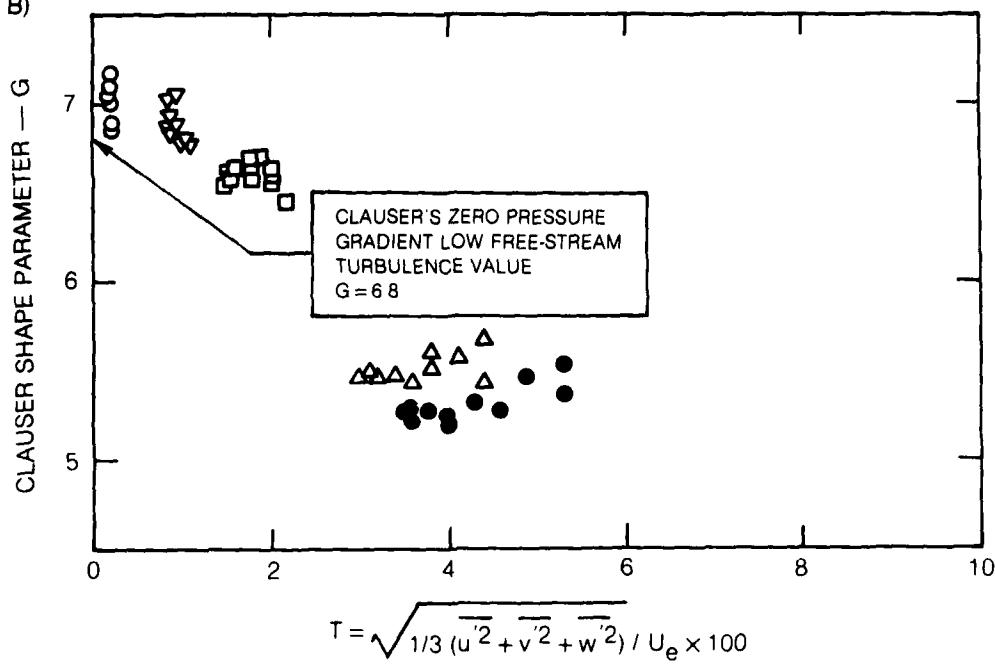


Figure 64. Influence of Total Turbulence Intensity on the Shape of the Mean Velocity Profiles

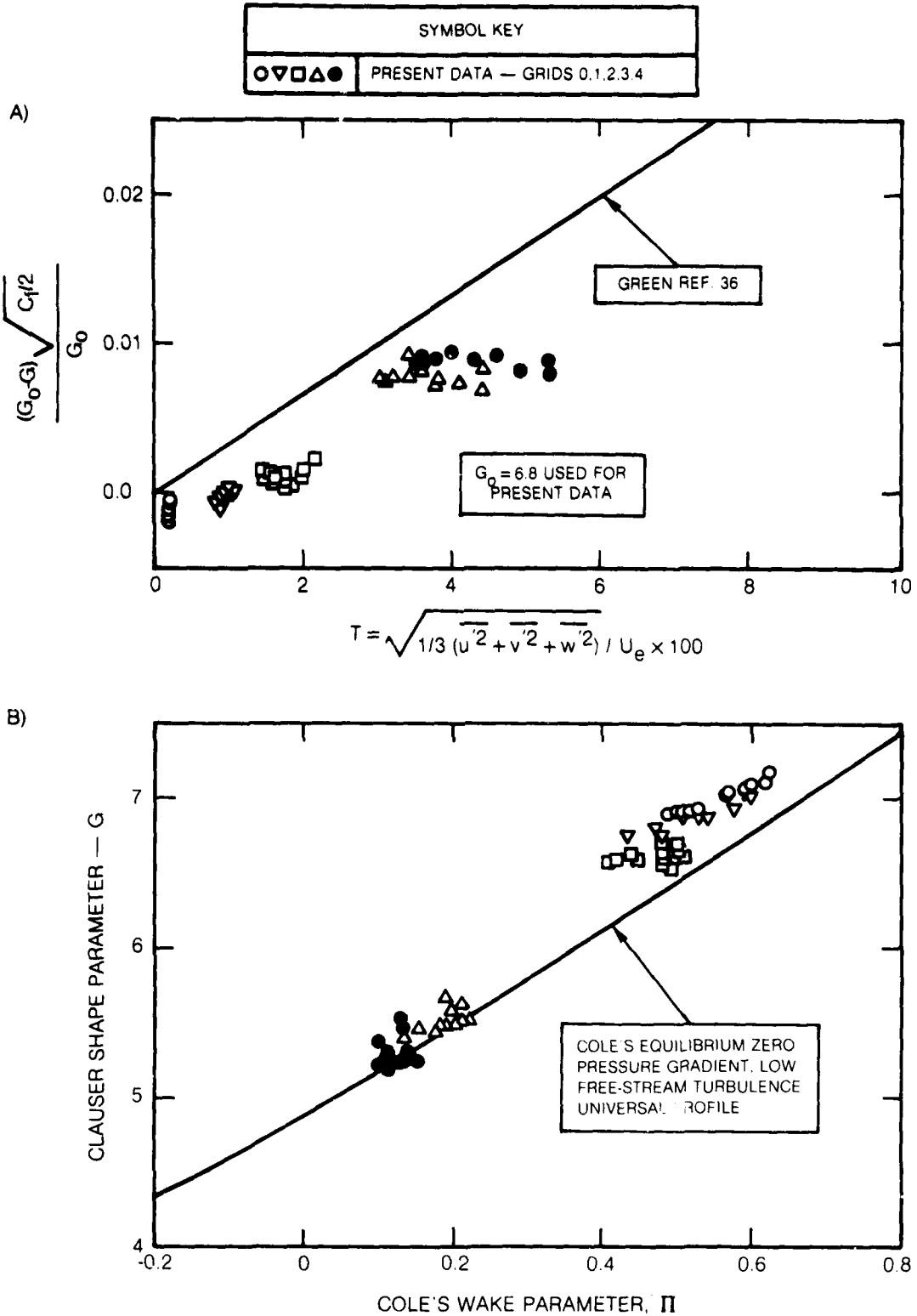


Figure 65. Influence of Free-Stream Turbulence on the Mean Velocity Profiles

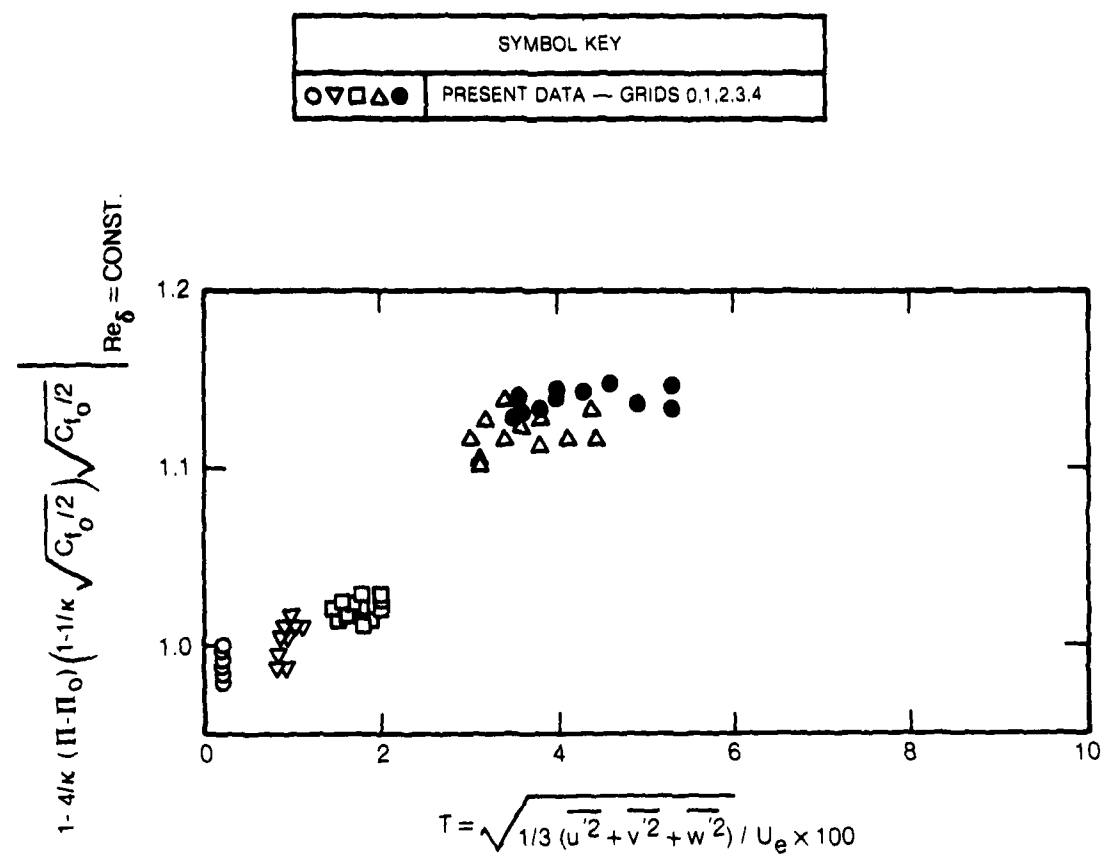


Figure 66. Influence of Free-Stream Turbulence Level on the Skin Friction Coefficient as Inferred From Reduction of the Profile Wake Component

SYMBOL KEY		Re_θ RANGE
— · —	SIMONICH & BRADSHAW CORRELATION (REF.34)	1000-6500
○ ▽ □ △ ●	PRESENT DATA — GRIDS 0.1,2,3,4	1000-7500

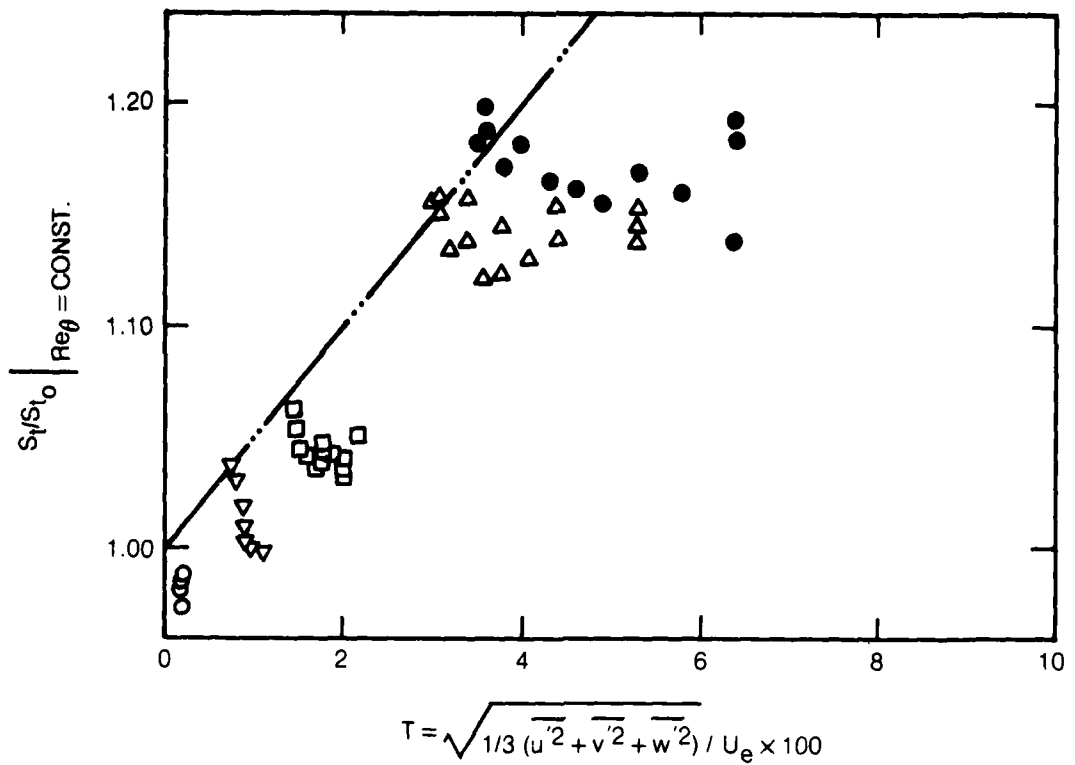


Figure 67. Influence of Turbulence Intensity on the Heat Transfer Coefficient

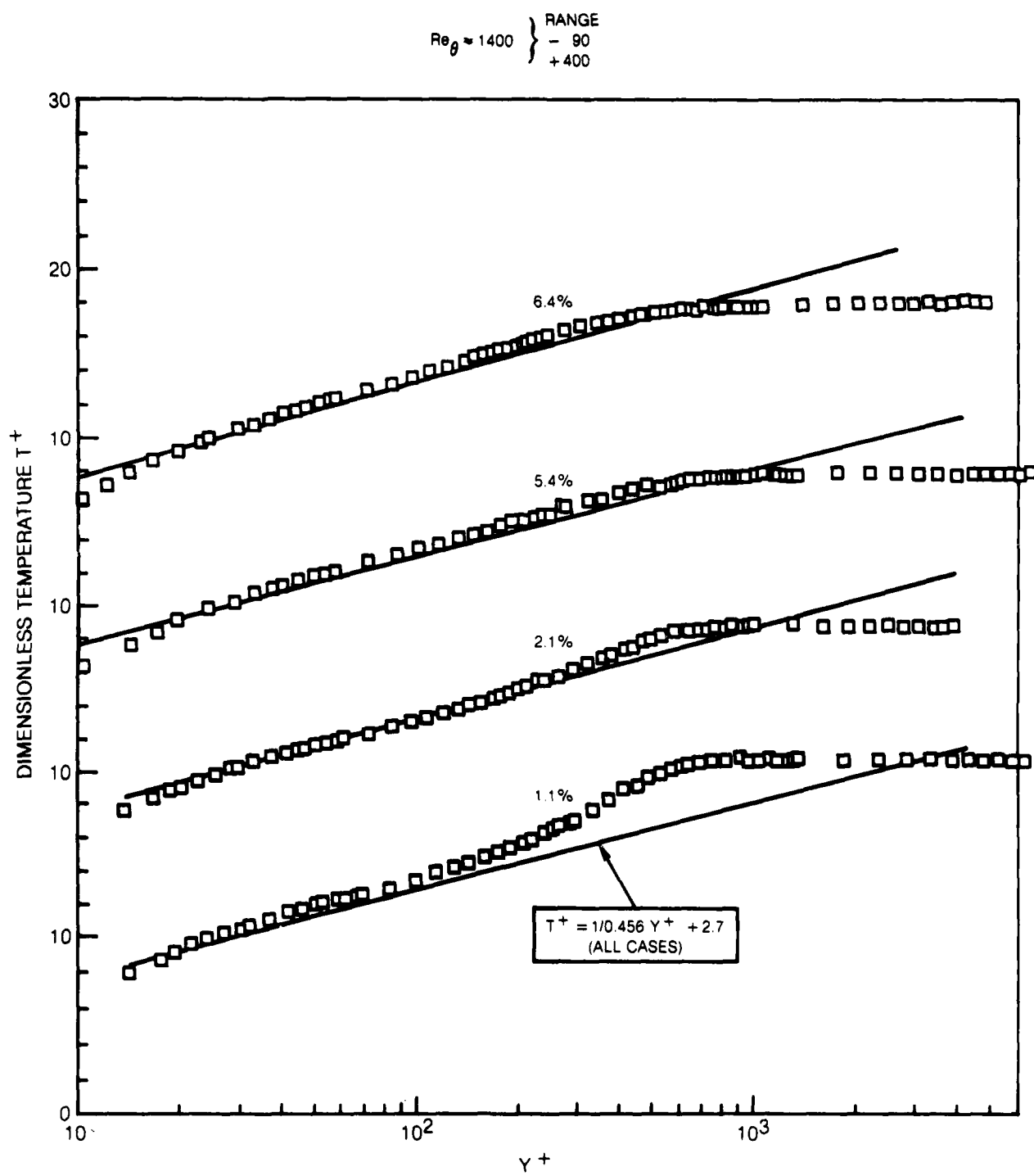


Figure 68A. Comparison of Mean Temperature Profile Shapes for Various Free-Stream Turbulence Levels for $Re_\theta \approx 1400$

R80-914388-12

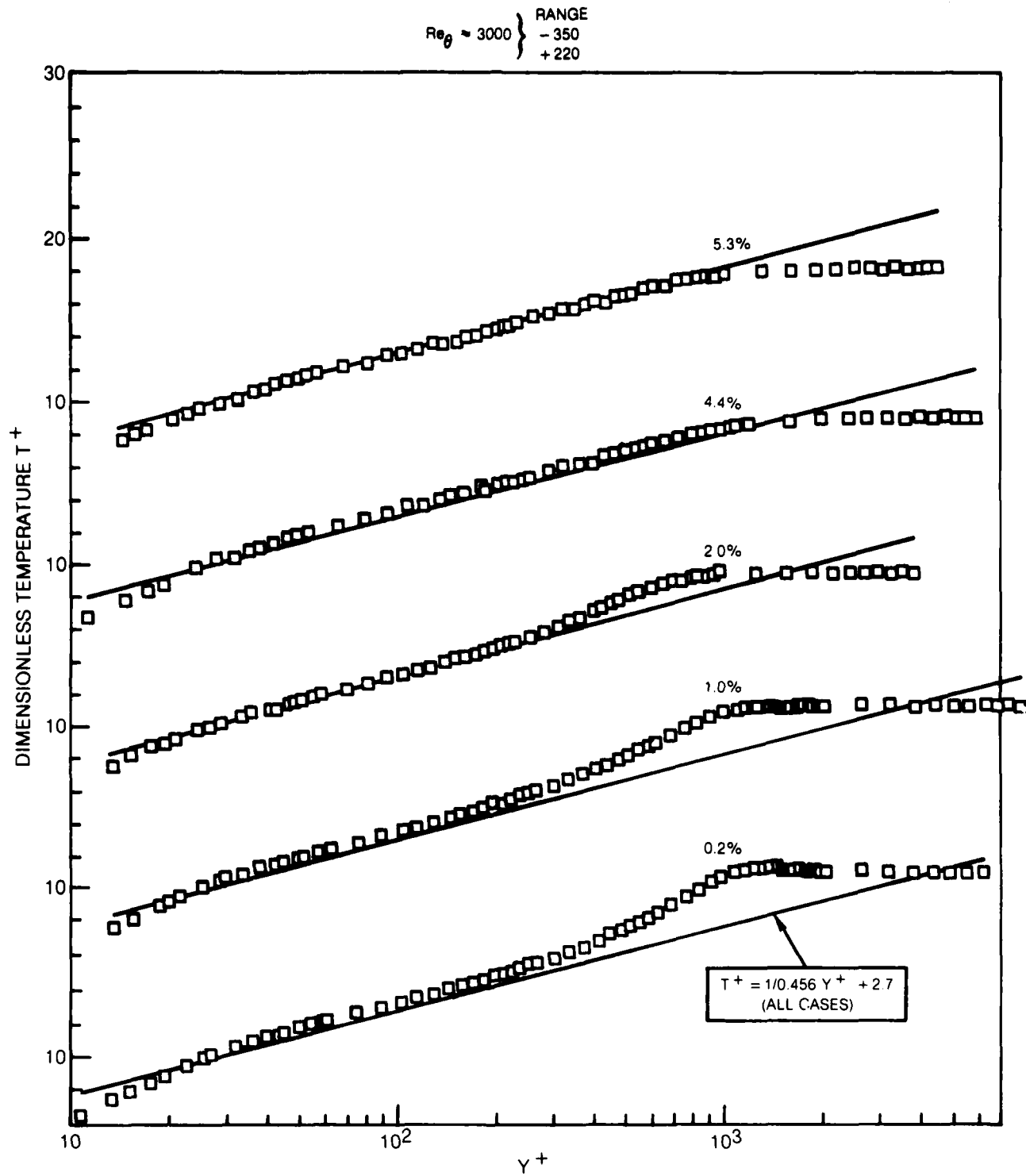


Figure 68B. Comparison of Mean Temperature Profile Shapes for Various Free-Stream Turbulence Levels for $Re_\theta \approx 3000$

R80-914338-12

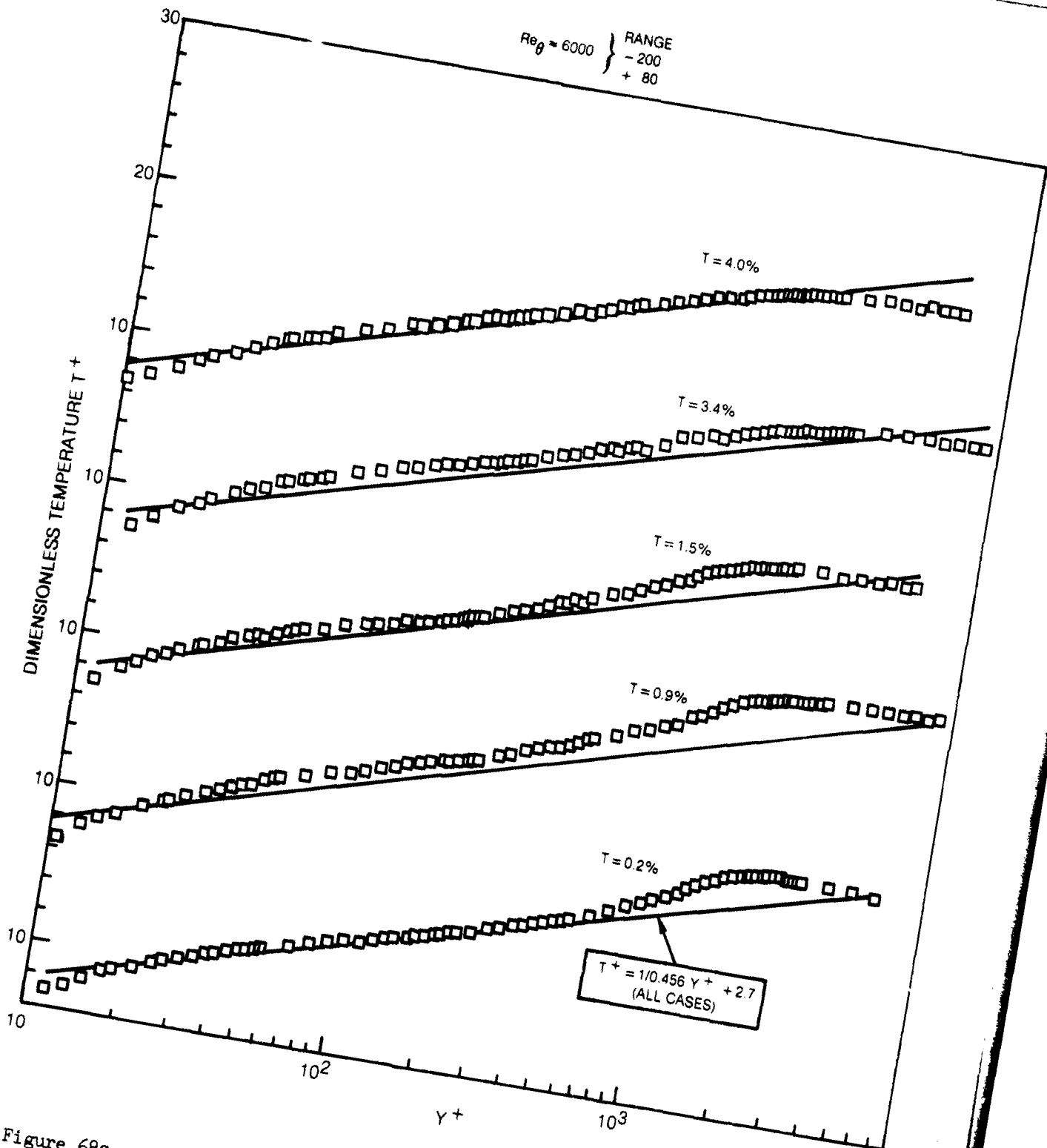


Figure 68C. Comparison of Mean Temperature Profile Shapes for Various Free-Stream Turbulence Levels for $Re_\theta \approx 6000$

80-07-11-14

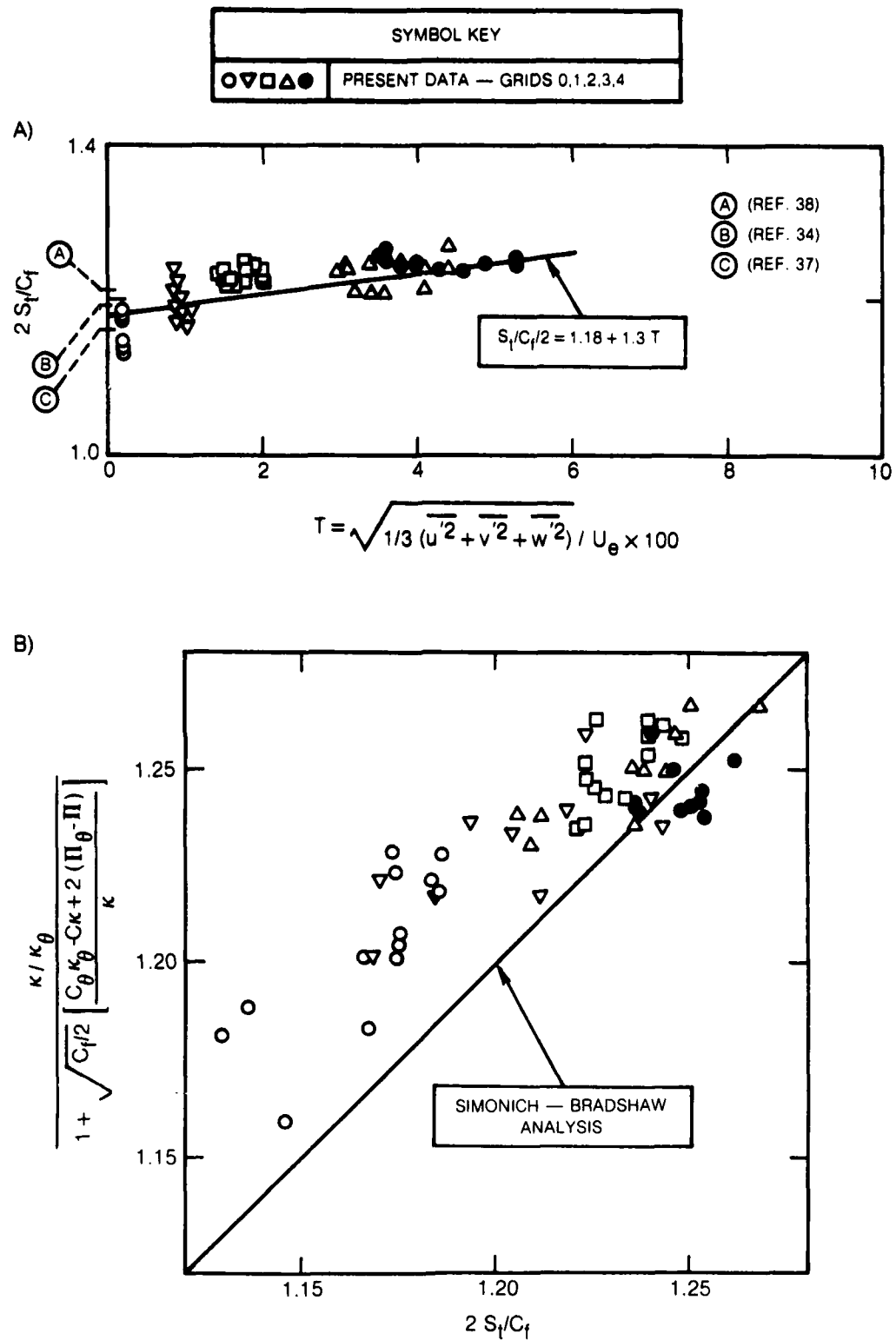


Figure 69. Influence of Free-Stream Turbulence on the Reynolds Analogy Factor

SYMBOL KEY		Re_{θ} RANGE
▲	HUFFMAN et al (REF. 31)	4000-5300
■	CHARNAY et al (REF. 32)	700-2000
— — —	MEIER & KREPLIN CORRELATION (REF. 33)	3500-5400
— · —	SIMONICH & BRADSHAW CORRELATION (REF. 34)	1000-6500
○ ▽ □ △ ●	PRESENT DATA — GRIDS 0.1.2.3.4	1000-7500

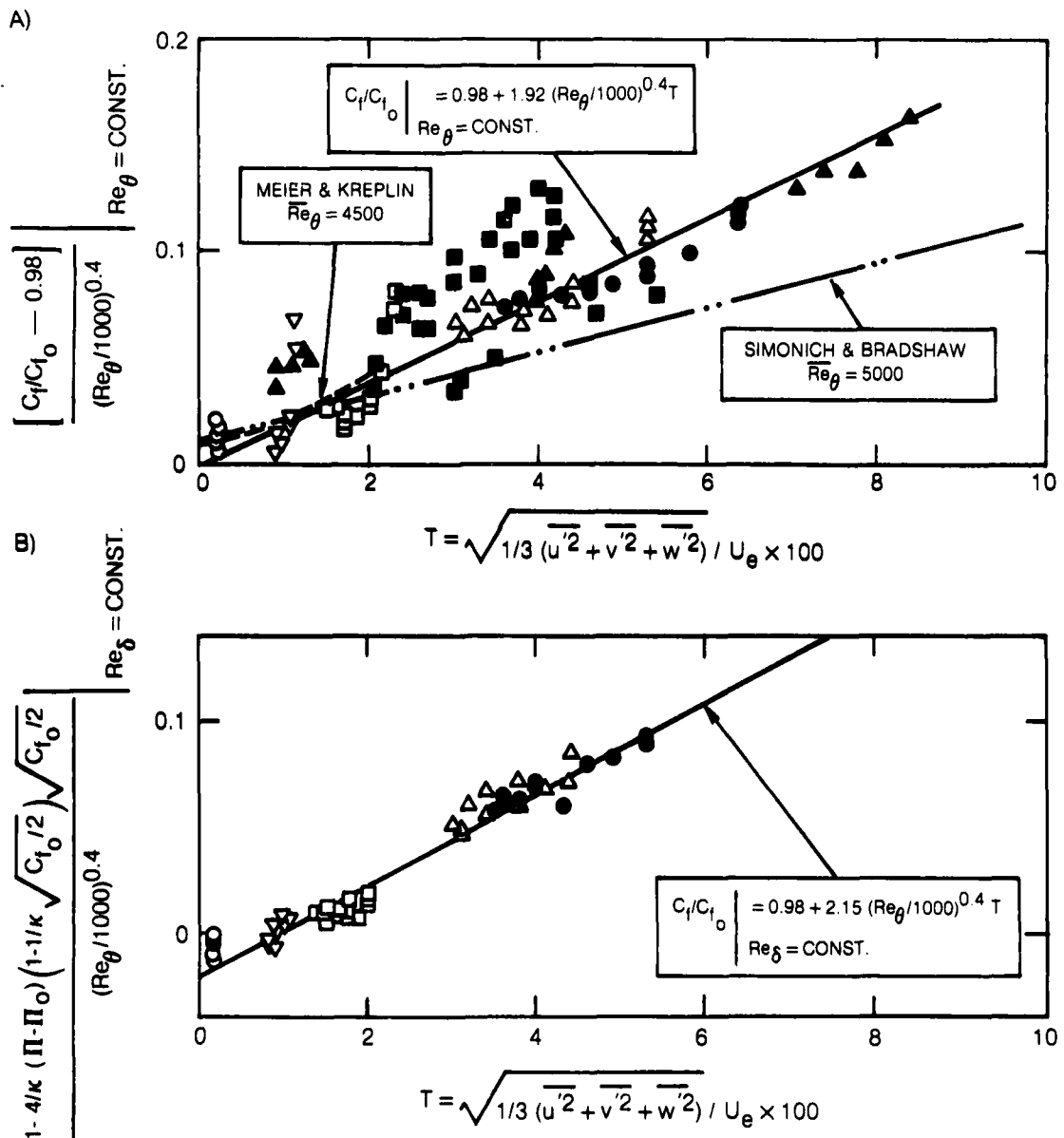


Figure 70. Influence of Free-Stream Turbulence Level and Re_{θ} on the Skin Friction Coefficient

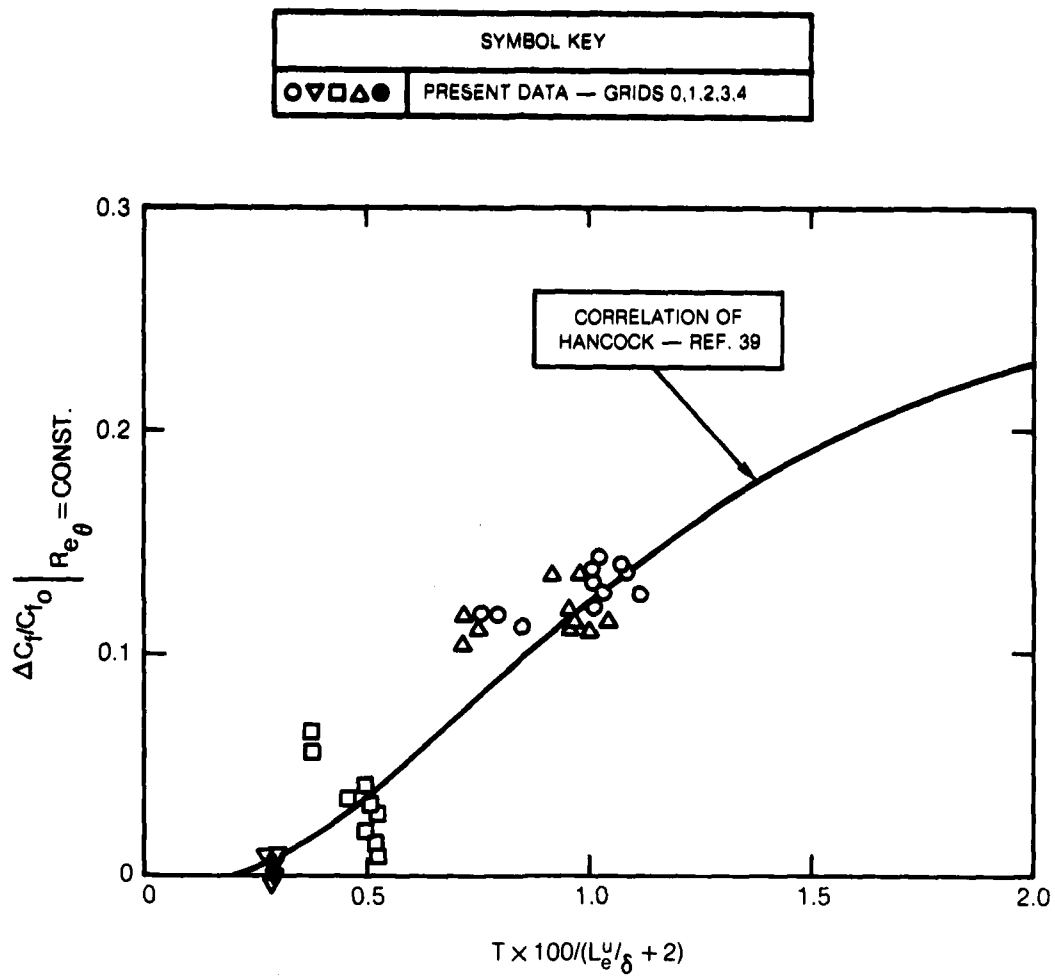


Figure 71. Present Data Plotted in the Coordinates of Hancock, Ref. 39

SYMBOL KEY		Re _θ RANGE
— · —	SIMONICH & BRADSHAW CORRELATION (REF. 34)	1000-6500
○ ▽ □ △ ●	PRESENT DATA — GRIDS 0,1,2,3,4	1000-7500

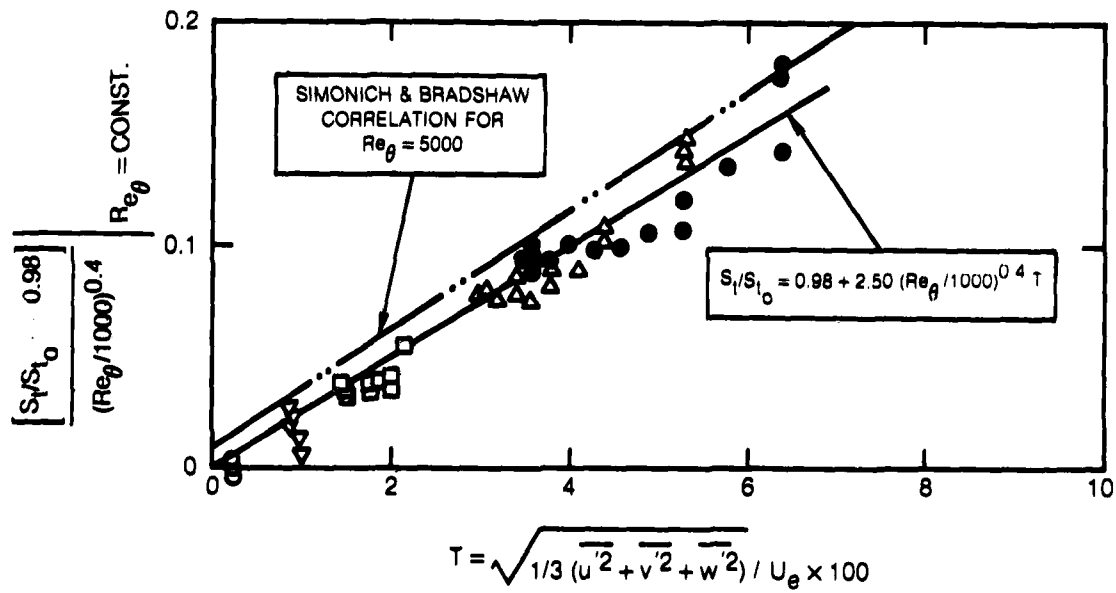


Figure 72. Influence of Free-Stream Turbulence and Re_{θ} on the Heat Transfer Coefficient

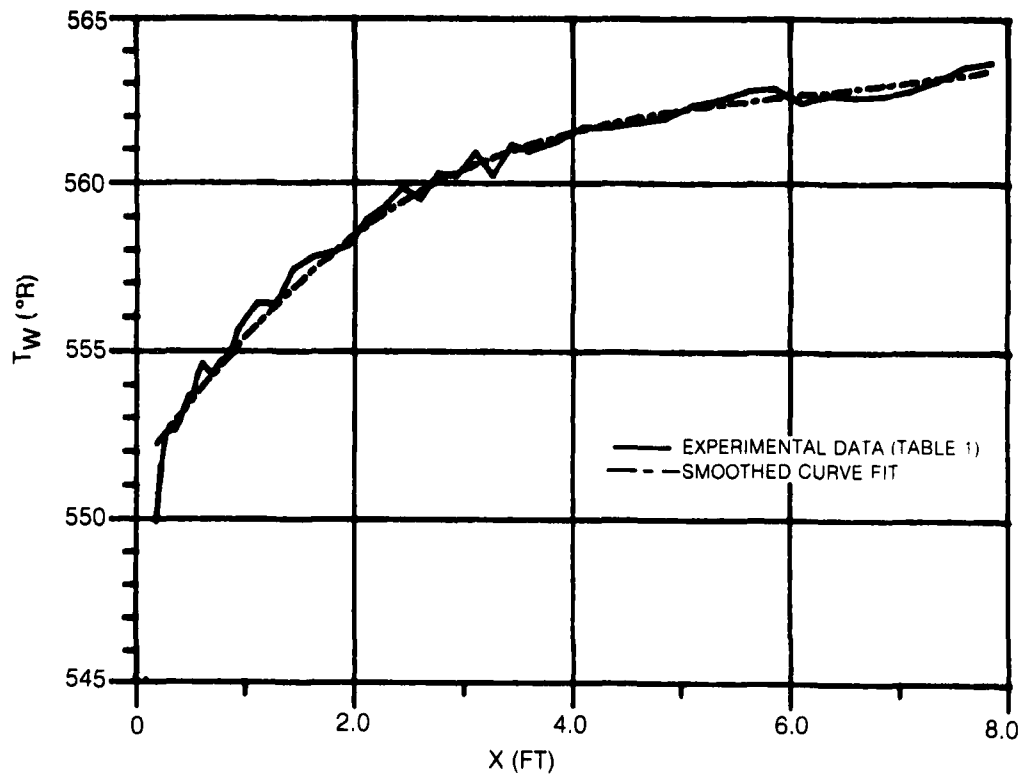
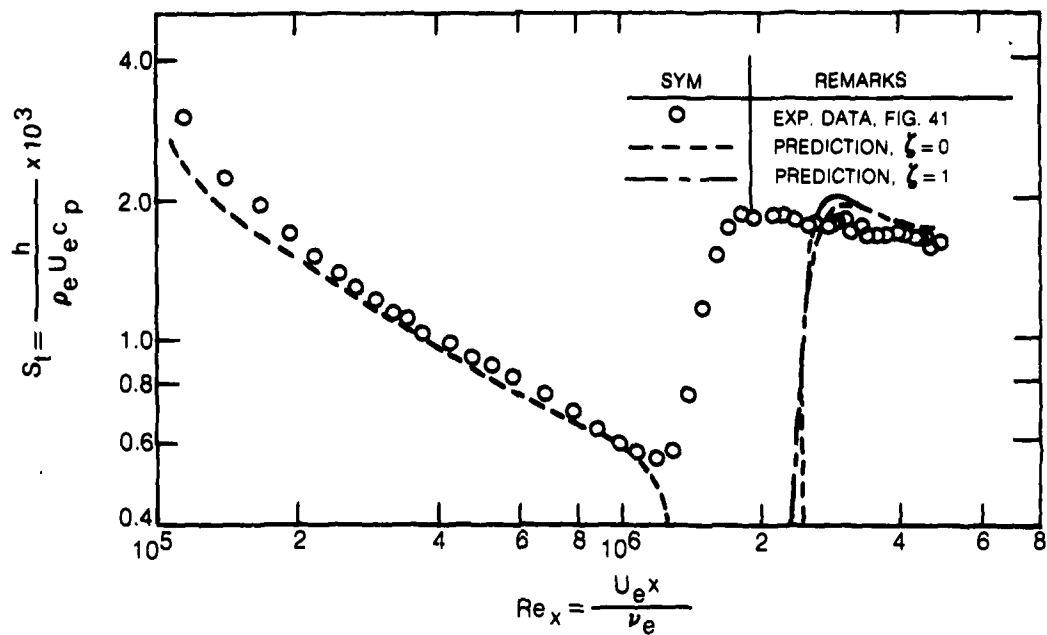


Figure 73. Numerically Smoothed Experimental Wall Temperature Data for Grid #4

a) HEAT TRANSFER DISTRIBUTION ALONG THE TEST WALL



b) SKIN FRICTION COEFFICIENT DISTRIBUTION ALONG THE TEST WALL

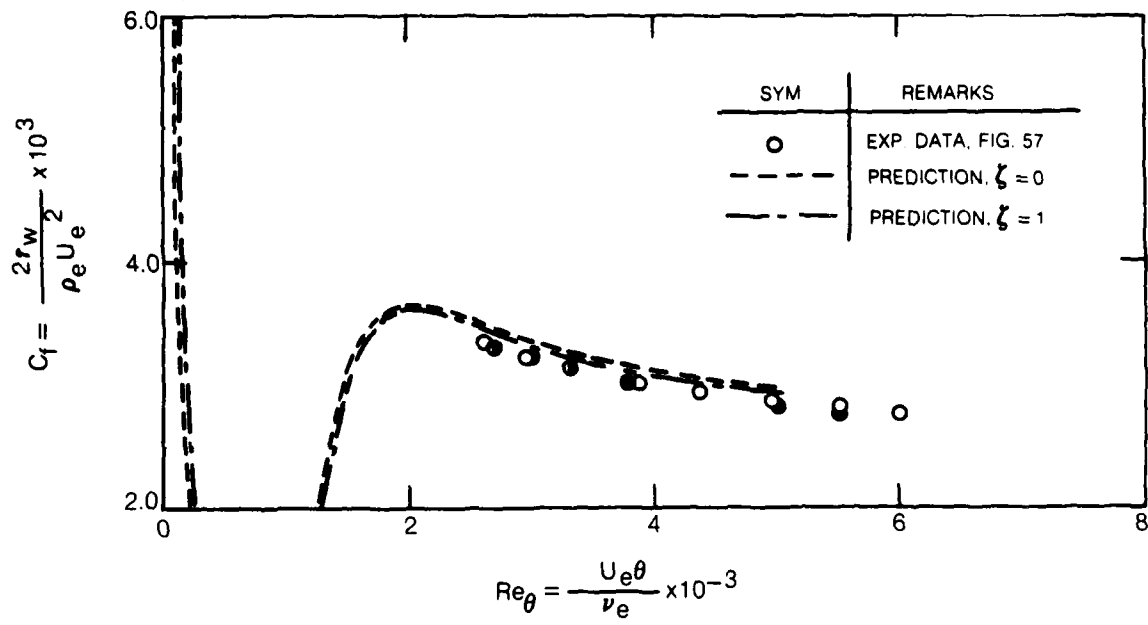
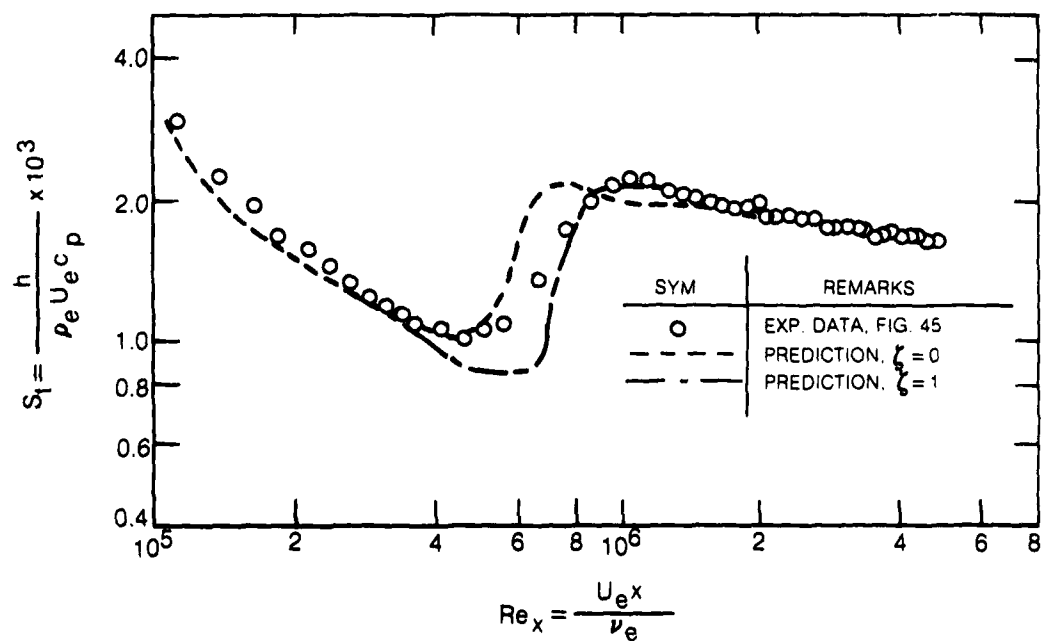


Figure 74. Comparison of Boundary Layer Code Predictions and Experimental Data, Minimum Turbulence

a) HEAT TRANSFER DISTRIBUTION ALONG THE TEST WALL



b) SKIN FRICTION COEFFICIENT DISTRIBUTION ALONG THE TEST WALL

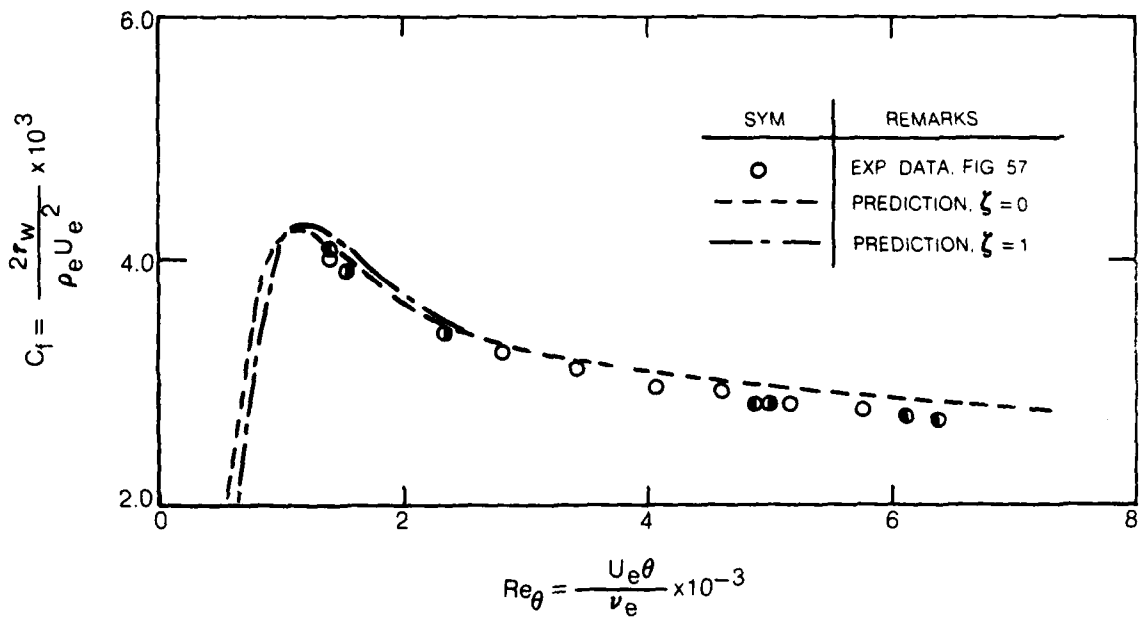
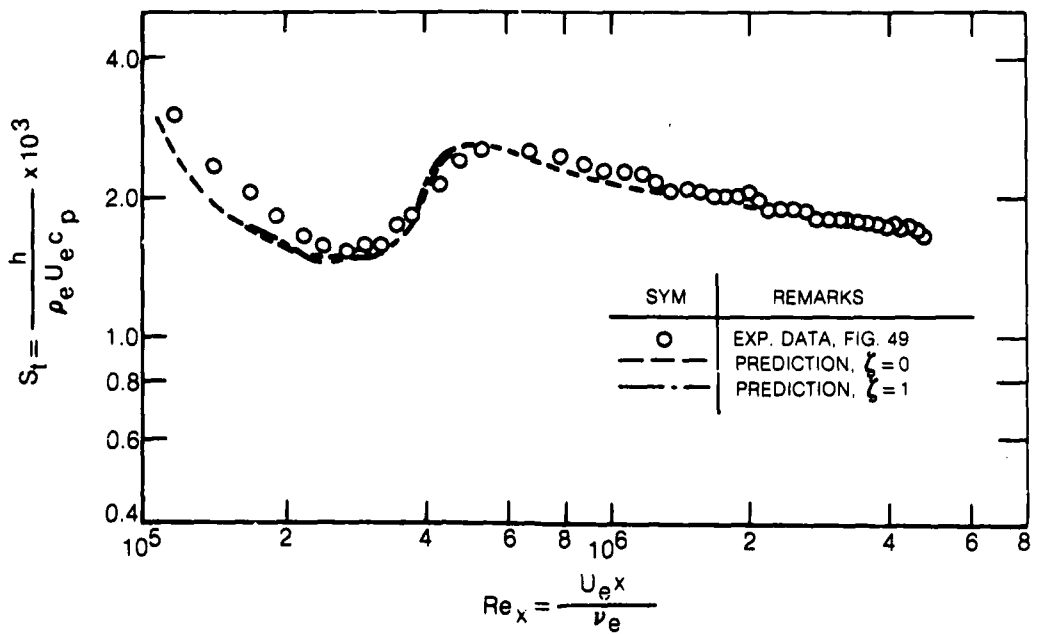


Figure 75. Comparison of Boundary Layer Code Predictions and Experimental Data - Grid #1

a) HEAT TRANSFER DISTRIBUTION ALONG THE TEST WALL



b) SKIN FRICTION COEFFICIENT DISTRIBUTION ALONG THE TEST WALL

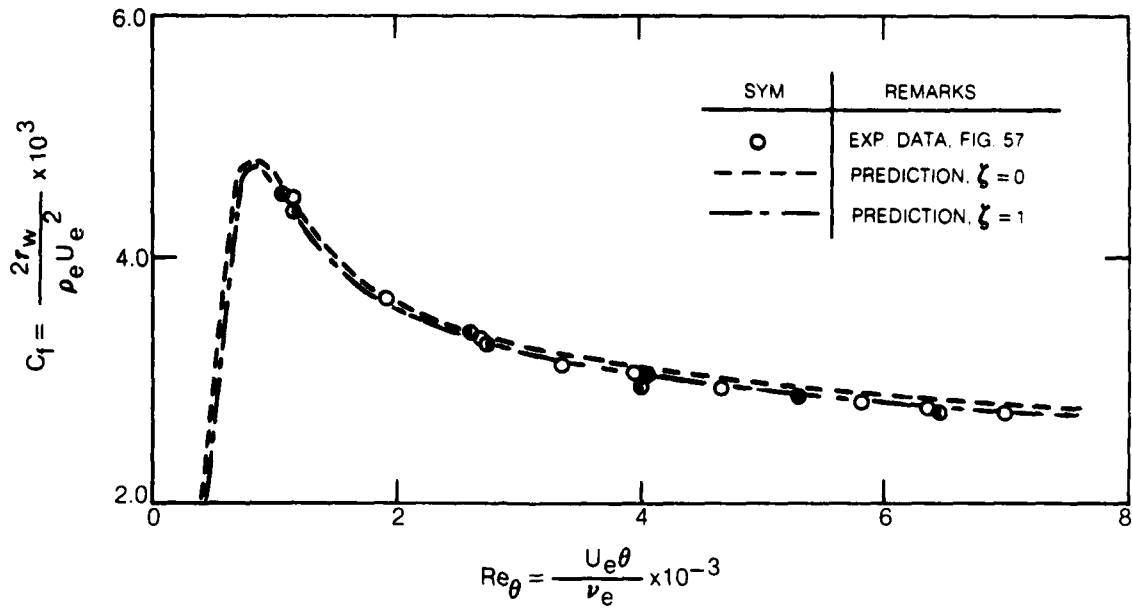
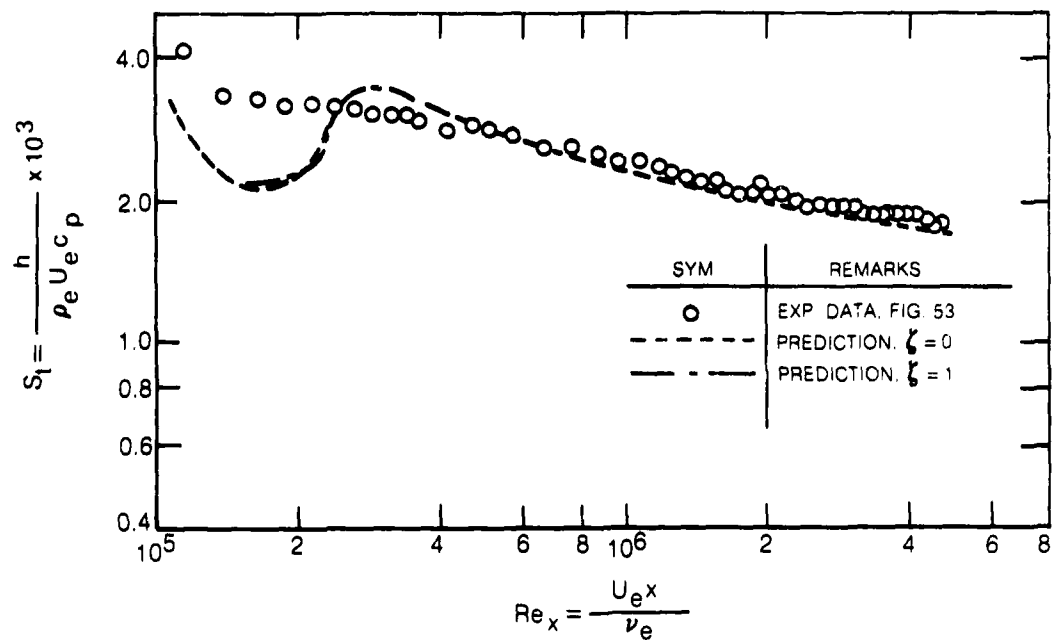


Figure 76. Comparison of Boundary Layer Code Predictions and Experimental Data - Grid #2

a) HEAT TRANSFER DISTRIBUTION ALONG THE TEST WALL



b) SKIN FRICTION COEFFICIENT DISTRIBUTION ALONG THE TEST WALL

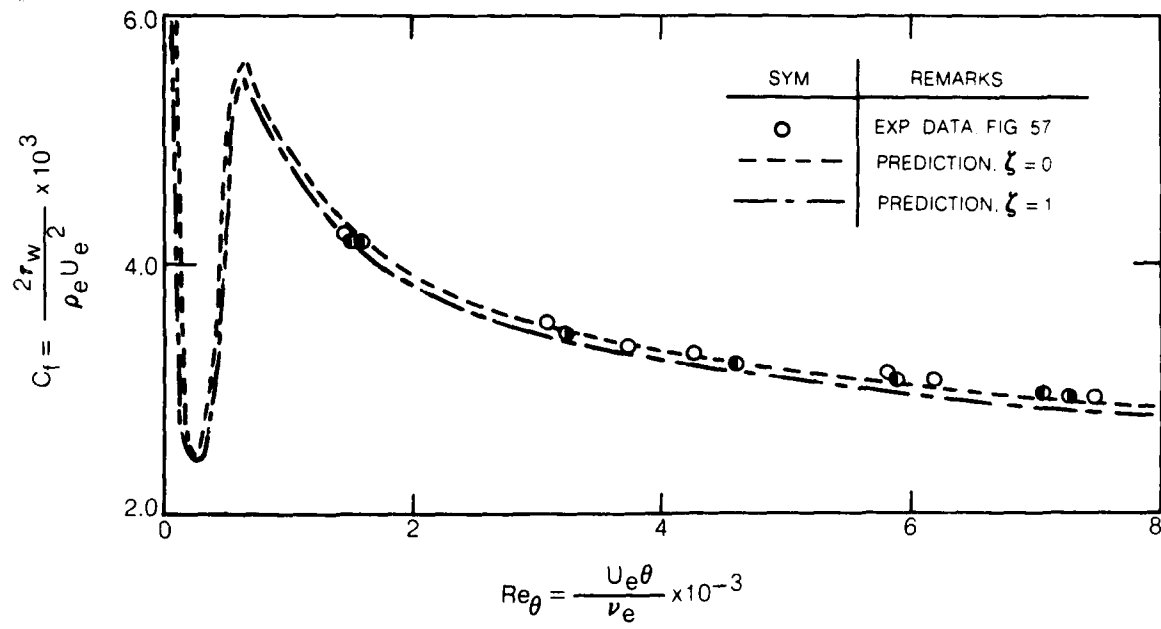
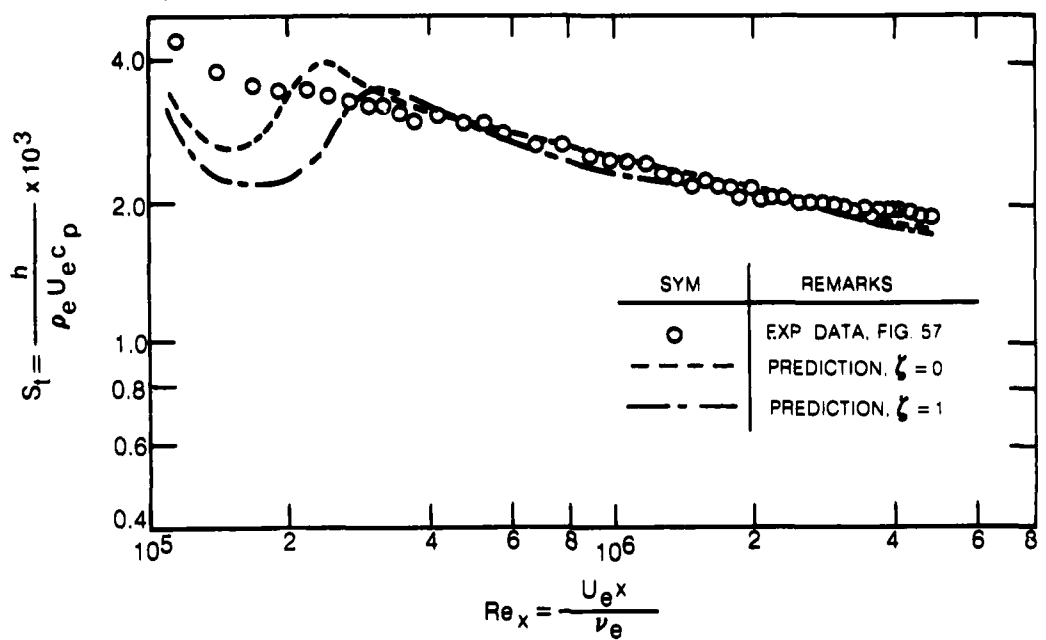


Figure 77. Comparison of Boundary Layer Code Predictions and Experimental Data - Grid #3

a) HEAT TRANSFER DISTRIBUTION ALONG THE TEST WALL



b) SKIN FRICTION COEFFICIENT DISTRIBUTION ALONG THE TEST WALL

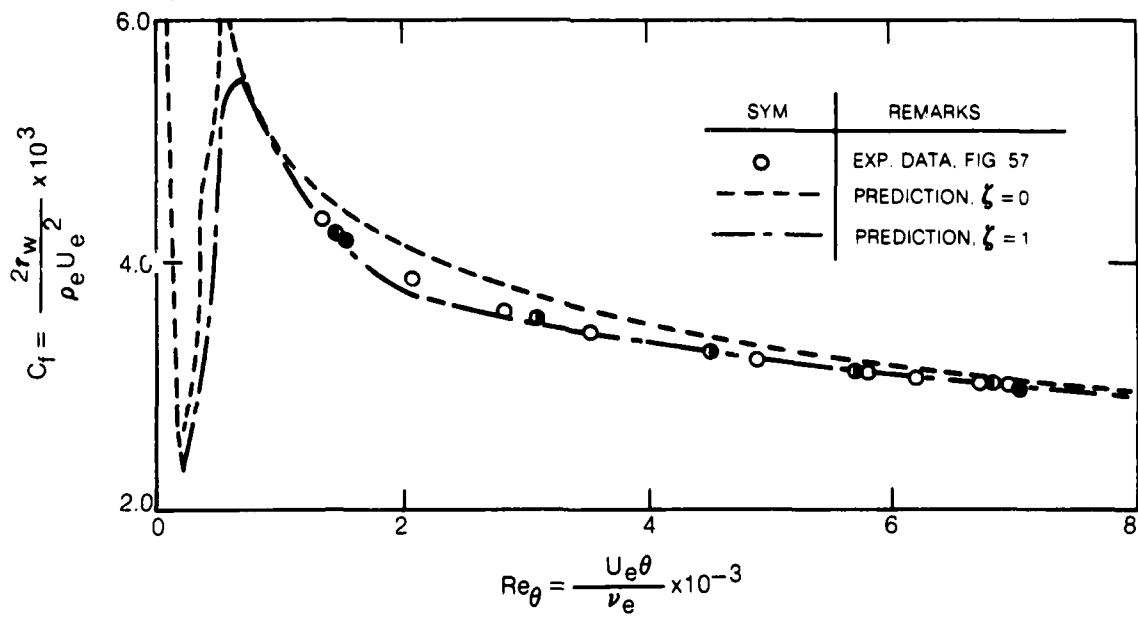


Figure 78. Comparison of Boundary Layer Code Predictions and Experimental Data - Grid #4

SYMBOL KEY		Re_θ RANGE
▲	HUFFMAN et al (REF. 31)	4000-5300
■	CHARNEY et al (REF. 32)	700-2000
○▽□△●	PRESENT DATA — GRIDS 0,1,2,3,4	1000-7500
—	THEORETICAL RESULTS	2000
\\\\\\\\	THEORETICAL RESULTS	4000-8000

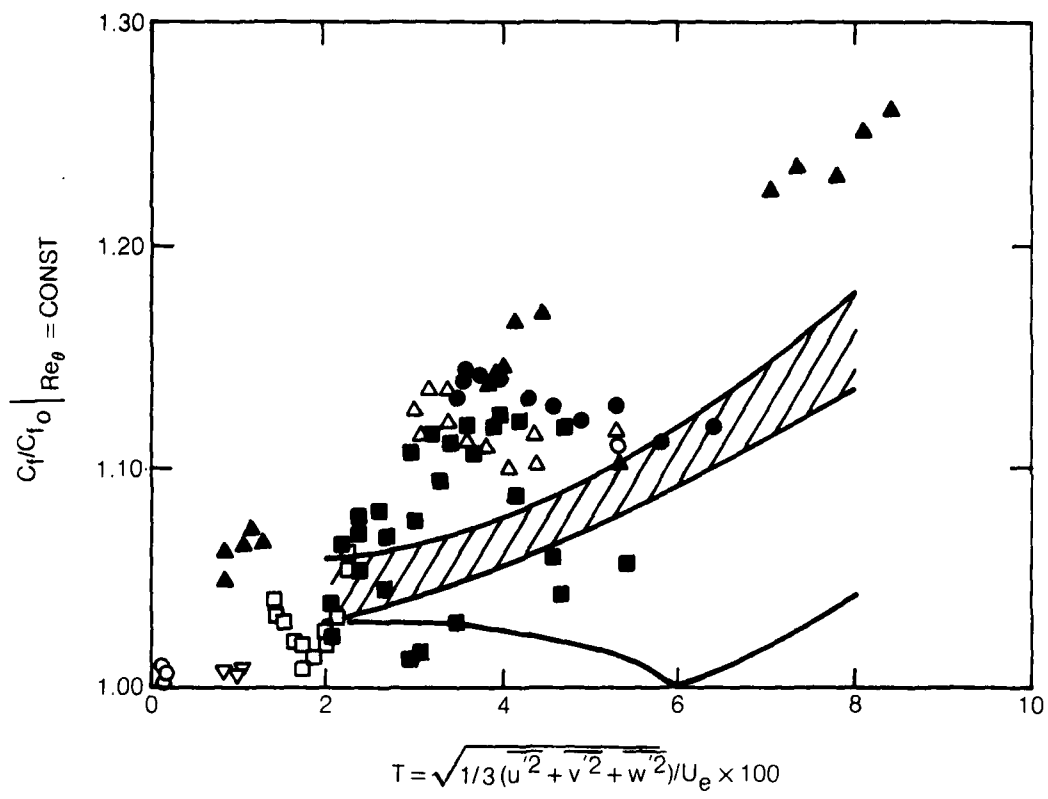


Figure 79. Theoretical Prediction of Surface Skin Friction
- Constant Edge Turbulence Level

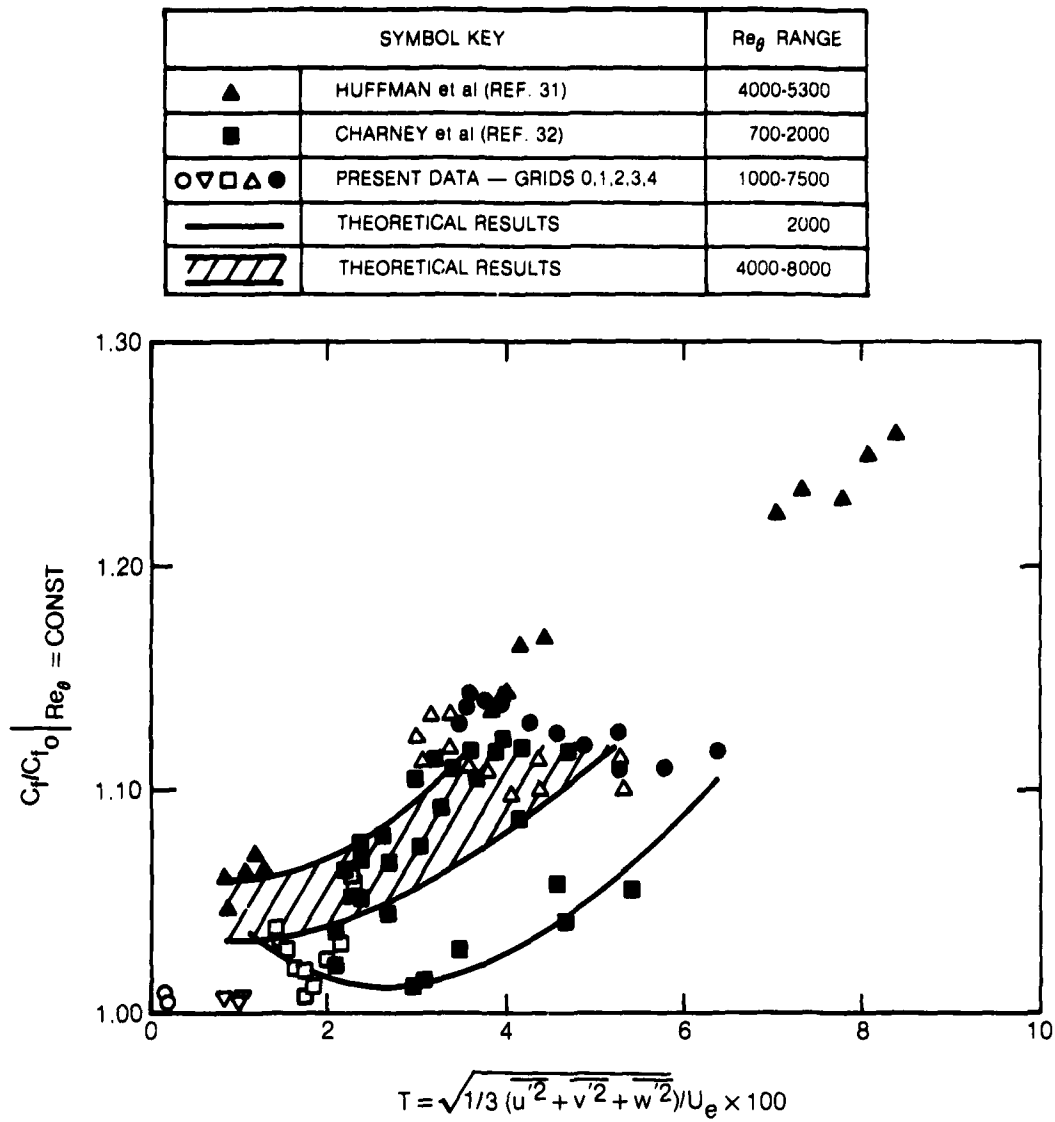


Figure 80. Theoretical Prediction of Surface Skin Friction
- Varying Edge Turbulence Level

SYMBOL KEY		Re_θ RANGE
○ ▽ □ △ ●	PRESENT DATA — GRIDS 0,1,2,3,4	1000-7500
—	THEORETICAL RESULTS	2000
\\\\\\\\	THEORETICAL RESULTS	4000-8000

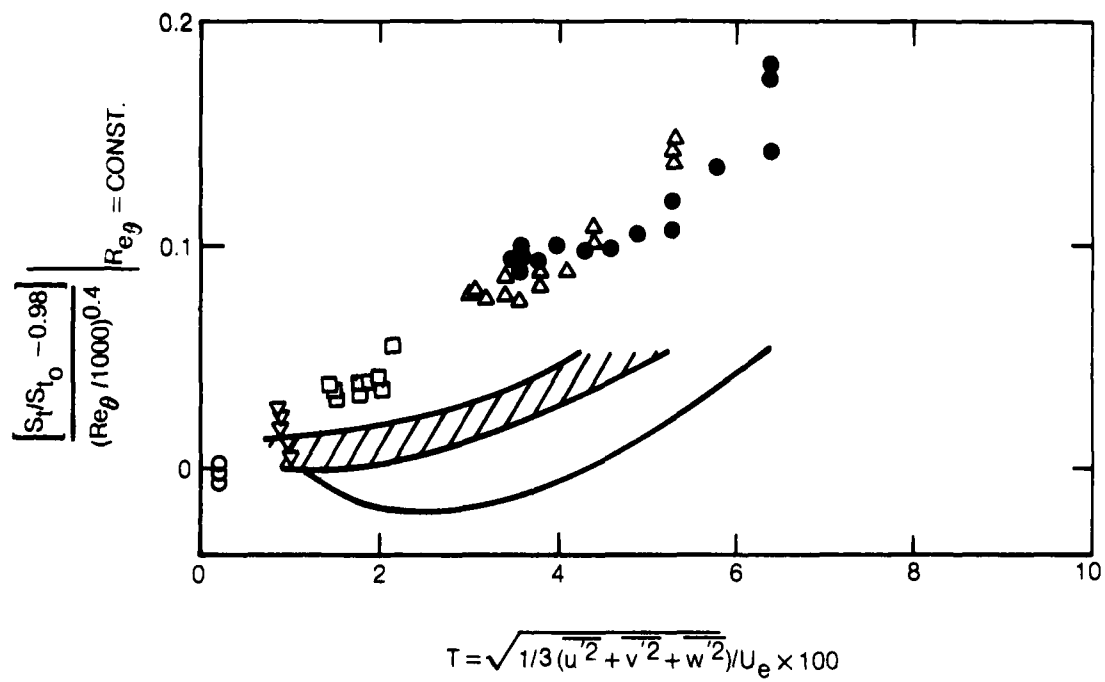


Figure 81 - Theoretical Prediction of Stanton Number
- Varying Edge Turbulence Level

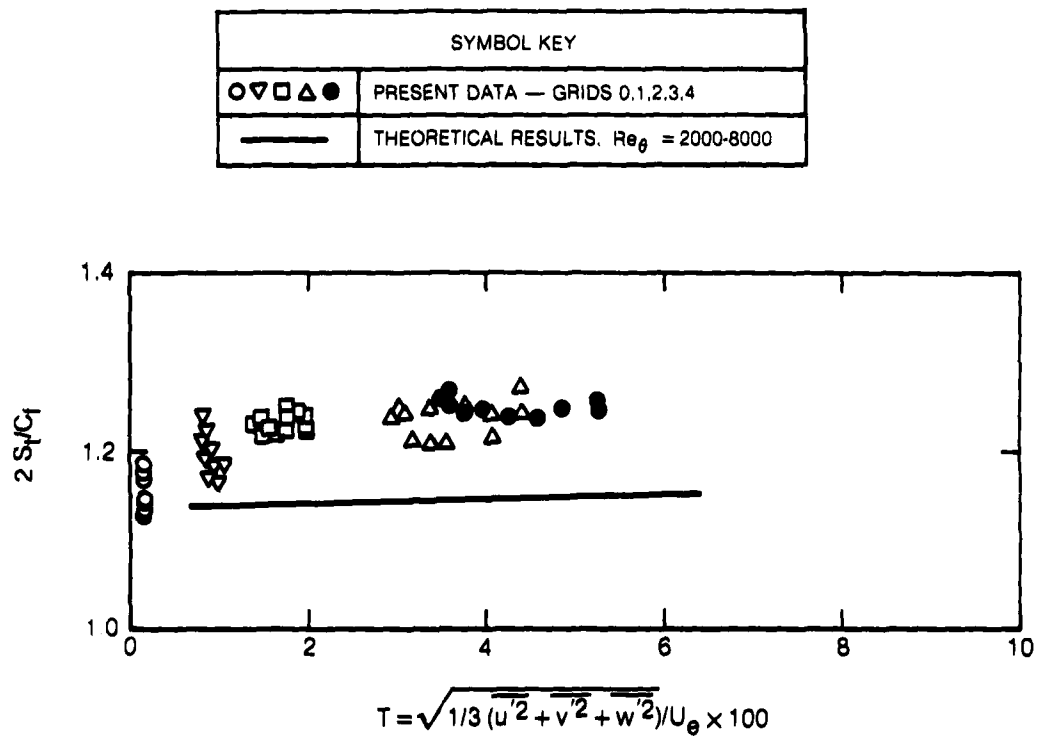


Figure 82 - Theoretical Prediction of Reynolds Analogy Factor
- Varying Edge Turbulence Levels